# Characterisation of FAST-DB - a Hybrid Solid-State Joining Process for Dissimilar Titanium Alloy Powder

Oliver Levano Blanch

A thesis submitted in partial fulfilment of the requirements for the degree of

Doctor of Engineering


Faculty of Engineering

Department of Materials Science and Engineering

Submitted: September 2021

# *Abstract*

This thesis explores the use of Field Assistant Sintering Technology (FAST) to join dissimilar titanium alloy powders into a multi-material component. The ability to produce multi-materials components will allow to improve the performance of certain components for key sectors such as the aerospace or the biomedical. For this manufacturing route to be successful, it is key to demonstrate that the diffusion bond is not the weakest part of the component. Therefore, there are three main areas of research present in this thesis: the study of the deformation in the diffusion bond, the residual stresses generated in the diffusion bond and the machinability of the multi-material components.

The deformation of the diffusion bond was studied under tensile conditions in the macro and meso scale with the technology digital image correlation (DIC). The DIC showed that each titanium alloy had a dissimilar deformation rate during the tensile test with a clear transition through the bond. Furthermore, the failure of these tensile samples always occurred in the weakest alloy, and this was not affected by the crystal orientation observed in the bond.

The residual stresses were measured with X-Ray diffraction and contour method in multiple titanium bonds and FAST-*forge* samples. The stresses measured in as FAST material were generally low, but residual stresses were observed in certain diffusion bonds made with two dissimilar alloys.

The machining of multi-material components is a key part of the manufacturing route. Hence, the damage and the forces generated in multiple bonds have been assessed. The results have shown that the surface finish is affected by the direction in which the diffusion bond is machined.

The positive results of this thesis contribute to increase the confidence in the use of FAST to diffusion bond dissimilar titanium alloy as well as producing multi material near-net shaped components.

“Strive for perfection in everything you do. Take the best that exists and make it better. When it does not exist, design it.”

- Sir Henry Royce

# *Dedication*

To my parents Gustavo and Silvia, and my brother Brandon. Your support and your encouragement have been vital to reach this goal. You have taught me to work hard, be ambitious and persevere. Without you, I wouldn't be where I am today. I will always be grateful for your patience, your humour and everything you have given me.

To Laura, who decided to leave everything behind and come to a new country just to be with me. You have always been there if I needed and you have made possible that I finished this thesis throughout the pandemic keeping a smile in my face.

# *Acknowledgment*

This thesis has been possible thanks to the support from a number of people. First and foremost, I would like to thank my supervisor Prof. Martin Jackson for his support throughout the project and all his valuable advises that have made this thesis better as well as made me better in my professional career. Thanks must also go to my industrial supervisor from Rolls-Royce plc, Dr. Gavin J. Baxter, for his continued support and the interesting discussions we had throughout the thesis.

Many thanks to the people in D1 for your support during the course of these four years; for all the interesting discussions, support and making it a great place to work in, particularly to Dr. Jacob Pope, Dr. Nick Weston and Dr. Ben Thomas for all your support at the start of the thesis and Dr. Daniel Suarez Fernandez for your support in the machining trials. I would also like to thank the technical staff of the department of material science and engineering in the University of Sheffield for being there when they are needed.

There have been several collaborations outside the university that I would like to thank. I am grateful to Adam Tudball at Kennametal and the staff from W.H. Tildesley for allowing the use of their equipment and all the support during the trials. I am also grateful to Dr. Ioannis Vitolatis from the AFRC for your support with the residual stresses work and to Dr. David Lunt from the University of Manchester for your support with the optical DIC work. I am appreciative to the staff at Rolls Royce plc and their continued support, which has been key to the completion of this thesis.

In addition to this, I would like to acknowledge the support of the industrial sponsors, Rolls-Royce plc, and EPSRC grant EP/L016273 Centre for Doctoral Training in Advanced Metallic Systems for supporting this research. The provision of materials and supporting information from Rolls-Royce plc. is gratefully acknowledged.

# Table of Contents

# List of Figures

# List of Tables

# 1. *Introduction*

## *1.1. Motivation for the work*

The aerospace sector has allowed society to travel around the globe in relatively short times, which has brought several advantages to the global economy. This has enhanced the connectivity between communities and businesses across the world and it is expected that the air traffic will continue to grow by 42% by 2040 compared with the number of flights in 2017 [1]. However, this revolutionary means of transport takes its toll on the environment, as it is estimated that the aerospace sector currently is responsible for 3% of global carbon emissions in Europe [1] and the USA [2].

In 2021, a coalition of European aviation trade associations published a report called 'Destination 2050' with a plan to achieve net zero carbon dioxide emissions by 2050 [3]. This report identified four pillars to achieve this aim, which are: (1) aircraft and engine technology, (2) air traffic management and aircraft operations, (3) sustainable aviation fuels and (4) smart economic measures. Materials play a key role in the "Aircraft and Engine Technology" pillar, as the development of new materials can help to reduce the overall weight of the engines and increase their efficiency by implementing higher pressures and temperatures within the combustor [1]. Ultimately, the engines will become more efficient, which means that they will require less fuel for the same amount of distance when compared to older engines. Consequently, there should be a reduction in the carbon dioxide emissions.

Many components in an aircraft and the jet engine have to withstand more than one type of failure mechanism. It is very difficult to have a single material with optimal performance for more than one type of failure mechanism. Hence, it would be very challenging to develop a new material with the desired mechanical properties. Nevertheless, another possibility is to

combine several well-known materials with the optimal mechanical properties to address each failure mechanism. That way, each of these optimal alloys can be used in specific subcomponent regions. With a multi-material component, it would be possible to improve the performance of these components as well as help to achieve net zero carbon dioxide emissions by 2050. A compressor blade is an example of an application where multi-material components could improve the actual performance by operating with higher stresses and temperatures. The root would be made of an alloy with better fatigue performance, such as Ti-64; and the aerofoil would have an alloy with better creep performance, such as Ti-6242.

Furthermore, the use of multi-material components is not limited to the aerospace sector, other sectors such as the automotive, defence or the biomedical devices would benefit too. A conrod is an example where the use of multiple materials could improve the performance of a component in the automotive sector. The conrod requires high strength in the rod, high stiffness in the stem, high wear resistance at the large and small ends and it needs to be as light as possible. This is very difficult to achieve with a single alloy because there is not an alloy that can meet all these demands. However, multiple alloys could be used in each subregion to improve the overall performance of a conrod, as well as reducing its weight. This example is shown in Figure 1.1.

For defence applications, the use of multiple alloys stacked one over the other could improve the ballistic performance of a shield. The front material could absorb the energy of the bullet while the second alloy would avoid the bullet passing through.

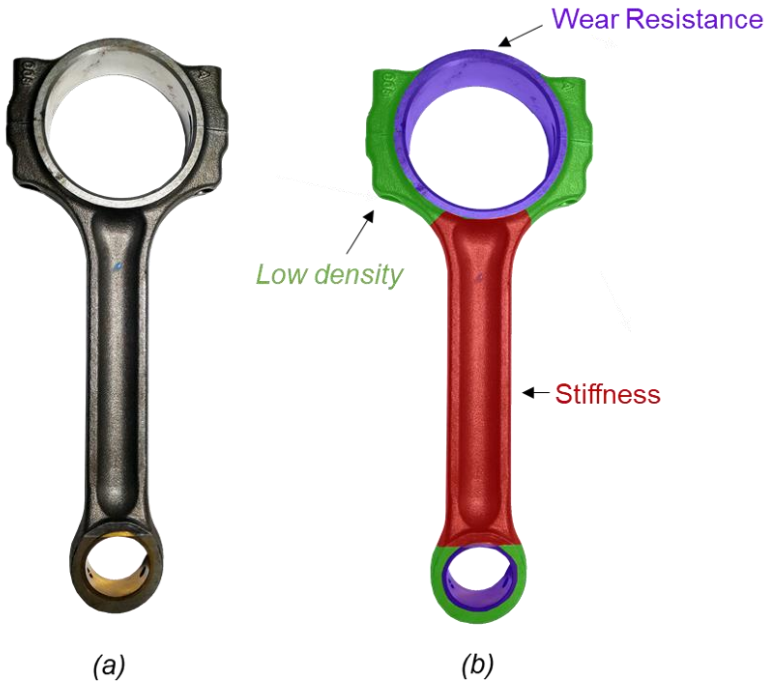


***Figure 1.1*** *- (a) photo of a conrod made of a single alloy, (b) coloured subregions of a conrod depicting where the use of different materials would be beneficial.*

Titanium has a high strength to weight ratio and it is capable to maintain its strength at relatively high temperatures. For that reason, titanium nowadays represents 25-30% of modern jet engines total weight [4]. Furthermore, titanium is also used for heavily-loaded airframe structures where aluminium or steels are not suitable. One of the main limitations for a more extensive use of titanium is its cost, that is inflated because of the difficulty in the extraction and thermomechanical processing. Moreover, conventional titanium production can have a buy-to-fly ratio over 95% [5], which represents a very high generation of waste material as well as an increase of the titanium components costs.

There are multiple technologies that can join dissimilar materials; however, it is common for some of these technologies to induce microstructure variation and defects in the bond such as heat affected zones and residual stresses [6,7]. In addition to this, the chemistry of the materials to be bonded needs to be carefully considered. Certain chemistries can create eutectic compounds or intermetallics in the bond that could affect the mechanical properties [8]. Therefore, it is necessary to have a good understanding of the materials that are going to be joined and the technology required to achieve this.

Field assisting sintering technology (FAST) or spark plasma sintering (SPS) has been used recently to join dissimilar titanium alloys (FAST-DB) [9], proving that the bond is not the weakest part of the FAST processed material. Furthermore, the processing route FAST-*forge* has demonstrated that it is possible to produce a near net shaped multi-alloy components from powder in only two steps [10]. The possibility of producing a multi-alloy titanium component in only two steps allows to reduce significantly the cost and the generation of waste.

FAST-DB is still in early stages of development and there is a drive to further understand the effect of the bond in the components for future applications in the aerospace sector. In this thesis, three main areas are going to be explored: (1) the deformation mechanism at the bond, (2) the formation of residual stresses in the bond and (3) the machinability of the bond. This knowledge will help the industrial sponsor of the project (Rolls-Royce plc) to determine if this is a technology worth investing in the future.

## *1.2. Aims and objectives of the thesis*

The aim of the thesis is to further understand the bond created with FAST-DB between dissimilar titanium alloys to determine if this technology has the potential to be used in the aerospace sector.

The underlying objective are as follow:

- To characterise the microstructure and chemistry of the bonds generated with FAST-DB.
- To study the deformation behaviour at the bond between two similar alloys and link it to the local grain orientation and the diffusion of alloying elements.
- To assess the degree and profile of residual stresses in the bond between dissimilar titanium alloys of as FAST material, as well as FAST-*forge* components.
- To study the effect of the bond on the machinability of multi-material components and determine the best approach to machine this type of component.

## *1.3. Thesis outline*

Following the introduction chapter, the literature review is divided into two main sections, one that covers a general overview of the production and properties of titanium alloys and another one that focuses on the powder metallurgy techniques and the joining of dissimilar titanium alloys. The relevant literature review of the residual stresses and the machinability can be found in the introduction of the Chapters 6 and 7 respectively.

Chapter 3 explains the general methods used to carry out the research in this thesis. The first part focuses on the FAST methodology followed by the forging of FAST material. Then, it is described the methodology used for the mechanical testing and the method used to analyse the samples produced for this work.

Chapter 4 presents all the powder used during the EngD with the corresponding properties for each one. This will be referenced in the results chapters.

There are three main results chapters. Chapter 5 is focused on the deformation behaviour of a FAST-DB bond between Ti-64 and Ti-6242 by using digital image correlation techniques. This chapter contains the content of a publication from MMTA from 2021 [11]. Chapter 6 is focused on the residual stresses generated in the FAST-DB bond between multiple titanium alloys as well as forged FAST-DB material. Chapter 7 studies the machinability of multi-materials components and the effect of the directionality when machining these types of components. Chapters 5-7 are structured in a similar way. To start, there is an introduction containing the specific literature review of the chapter, followed by the specific methods used in the chapter, the results and discussion and a summary of findings.

Finally, Chapter 8 presents the conclusions of the research and suggestions for future work.

# 2. *Literature Review*

## *2.1. History of Titanium*

Titanium is the fourth most abundant metal in earth after aluminium, iron and magnesium [12]. However, it was not until 1791 that titanium oxide was discovered by the British reverent William Gregor during the study of the mineral menaccanite. Menaccanite is a type of ilmenite found in the sand of the small river that goes through Tregonwell Mill, Cornwall. The element was also found 4 years later by a German chemist called M. H. Kalproth, who saw the element while he was analysing rutile from Budapest and decided to call it Titanium. However, he acknowledged Gregor as the first discover of titanium. Gregor decided to call the new element menaccanite or menachine, but the name was confusing because it was the same than the mineral, so Kalproth's name of Titanium became more popular [13].

Although titanium was discovered in 1791, it was not until 1887 that Nilson and Petterson used $TiCl_4$ combined with sodium in a metallic cylinder to produce pure titanium (~95%). The process was improved in 1910 by Hunter, who used a steel vessel able to resist very high pressures to obtain a high purity titanium [14]. However, it was in 1938 that Kroll [15] filled the patent of a new way to obtain pure titanium by reducing $TiCl_4$ with pure magnesium in a crucible coated with molybdenum at 1000°C under an argon atmosphere. The resultant product was known as "titanium sponge" due to its porous nature. Shortly after the end of the Second World War, DuPont started commercializing titanium as it was considered a key material for aerospace companies [16]. During the Cold War, the Americans saw in titanium a perfect material for aerospace applications, while the Soviet Union used it for submarines.

Nowadays, titanium's main application is the aerospace sector and the main extraction method is still the Kroll process [12]. The world total capacity of production of titanium sponge in 2017 was 277,000 tonnes, with China being the country with higher capacity, with a total of 110,00 tones [17].

## 2.2. Extraction of titanium

The most common way to extract titanium is with the conventional Kroll process. There has been lot of research trying to find a cheaper and less time-consuming alternative to Kroll process, but none have had success in producing high quantities of titanium in an industrial scale. The most common sources of titanium are rutile ($TiO_2$) and ilmenite ($FeTiO_2$) [18].

The extraction process starts by a chlorination process to reduce the $TiO_2$ with coke and $Cl_2$ to obtain $TiCl_4$. The $TiCl_4$ is further purified by fractional distillation before performing the Kroll process. Then, the $TiCl_4$ is reduced with Mg in an argon atmosphere at 1000°C to produce a titanium sponge[19]. Figure 2.1 shows a diagram of the chlorination and the Kroll process.

The titanium sponge is then crushed and mixed with any additional elements required to obtain the desired alloy. The resultant material is cold pressed and joined together by electron beam welding to make a vacuum arc remelting (VAR) electrode, which produces the final titanium ingot after the remelting process [12].

## 2.3. Titanium Metallurgy

Titanium alloys are commonly used in the aerospace, chemical and biomedical applications due to the high strength to weight ratio, its resistance to corrosion and its biocompatibility [20]. Section 2.3 introduces the fundamental metallurgy of titanium.

### 2.3.1. Crystal structure

Titanium has an allotropic phase transformation with two crystal structures in the solid state. Commercially pure titanium has a body-centred cubic crystal structure (BCC) at temperatures above 882°C and an hexagonal close-packed crystal structure (HCP) at temperatures below 882°C [12,16]. The phase with the BCC crystal structure is known as β-phase and the phase with the HCP crystal structure is known as α-phase. The temperature for the allotropic transformation is known as $\beta$ transus and it varies depending on the alloying elements in the substitutional and interstitial positions of the crystal structure.

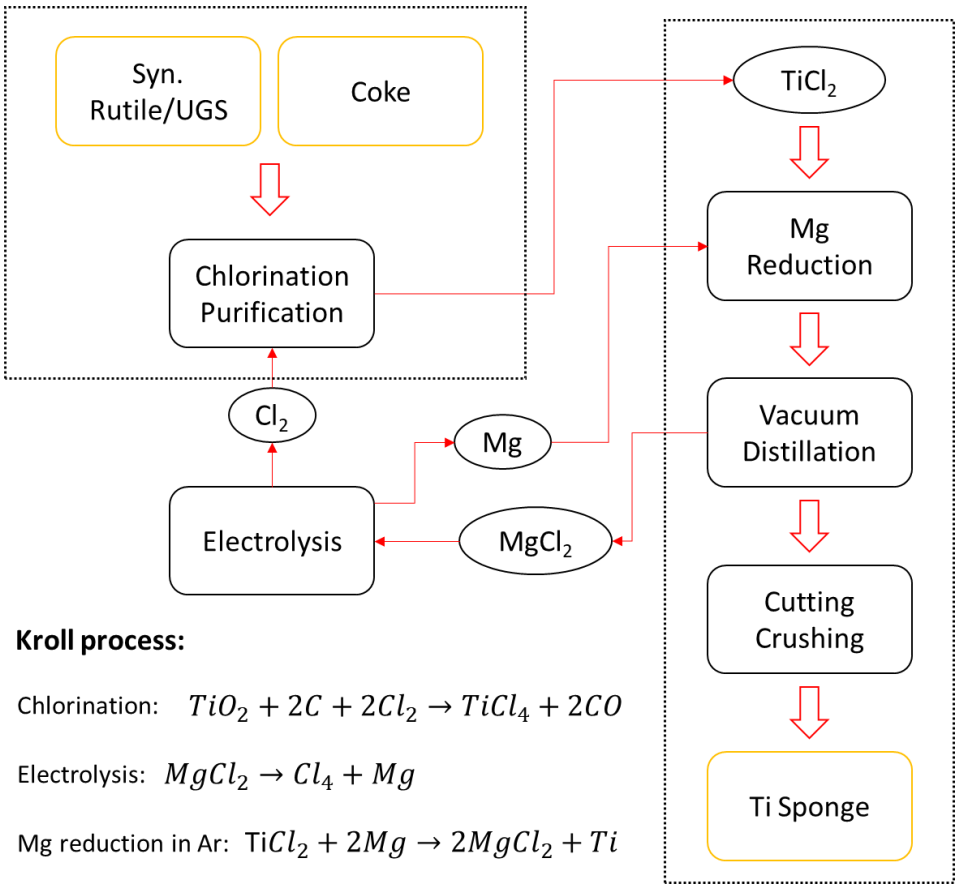


***Figure 2.1*** *– Illustration of the main processing steps of the Kroll process, chlorination and reduction of $TiCl_4$. (Redrawn from* [21]*).*

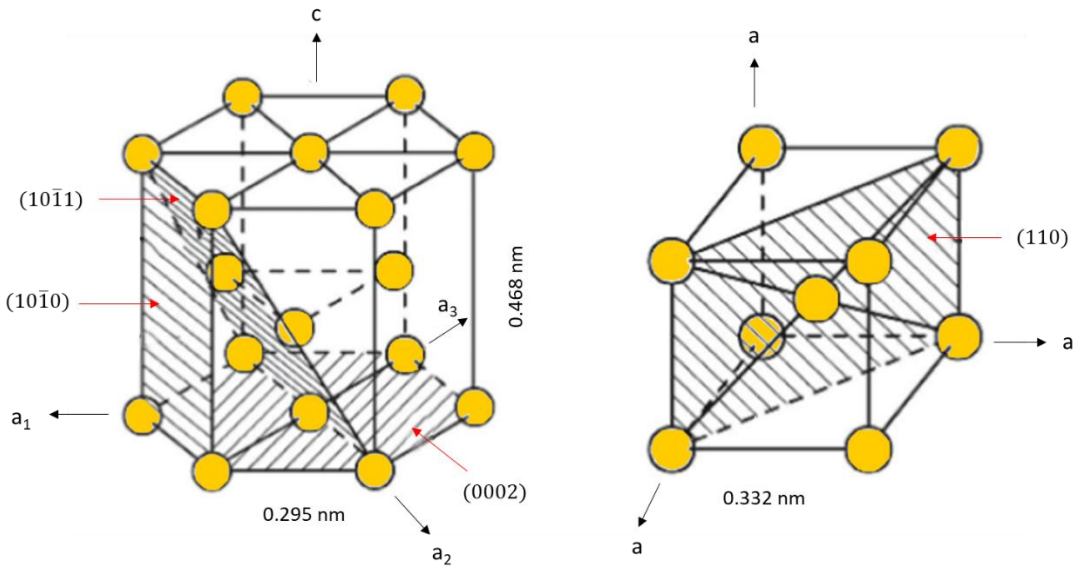


***Figure 2.2*** *– Crystal structure and corresponding planes for HCP (left) and BCC (right) phase (Redrawn from* [16]*).*

Figure 2.2 shows a schematic of the HCP and the BCC structure for titanium. The ideal ratio for an HCP crystal structure at room temperature is 1.663. However, for titanium this value is lower with a c/a of 1.587 [16].

### *2.3.2. Mechanical deformation*

The mechanical deformation of titanium depends on the crystal structure. The plastic deformation becomes easier when the structure changes from HCP $\alpha$-phase to BCC $\beta$-phase because the BCC crystal structure has 12 slip systems compared to the 3 slip systems in HCP. The slip systems are determined by the multiplication between the slip planes and the slip directions in the crystal structure. For the dislocations, it is energetically easier to move through close-packed planes and directions, because the energy required to move a dislocation is conditional to the minimal slip path. For this reason, although the HCP packing density is higher than the BCC lattice, the minimum slip path is smaller for BCC. Hence, the higher plastic deformation for these structures.

The HCP lattice has an anisotropic response that depends on the orientation from which the material is being deformed. The young modulus can vary from 145 GPa when the stress is parallel to the c-axis, to 100 GPa when the stress is perpendicular to the stress axis [12]. However, for polycrystals materials this effect is less evident.

### *2.3.3. Slip and twinning*

It has been mentioned in Section 2.3.2 that dislocations occurs in the close pack planes and directions of a crystal structure. Figure 2.3 shows the close packed planes and directions with the corresponding axis for an HCP crystal. The HCP cell has three planes that are the most densely pack: the basal plane $\{0002\}$, three prismatic planes $\{10\bar{1}0\}$ and six pyramidal planes $\{10\bar{1}1\}$. The packed direction is the $\langle 11\bar{2}0\rangle$ which corresponds to an $\vec{a}$ type Burges vector [12,16]. The prismatic plane has a higher density than the basal plane, and that makes the prismatic plane preferential for dislocations to move. This is caused because the c/a ratio in α titanium is lower than the ideal, which increases the atomic spacing in the prismatic plane and increases its packing density [16]. There are a total of 12 slip systems, however, only 4 of them are independent of each other. The von Misses criteria says

that it is necessary to have at least 5 independent slip systems to produce a homogenous plastic deformation [22]. Therefore, there has to be an alternative slip system when a strain is applied in the c-axis. At high temperatures, the alternative mechanism is the $\vec{c} + \vec{a}$ slip that have the slip direction $\langle 11\bar{2}3 \rangle$ and the slip plane $\{11\bar{2}3\}$ for the 1st order pyramidal slip and $\{11\bar{2}2\}$ for the 2nd order pyramidal plane. The 5 independent slip systems are summarised in Table 2.1.

At lower temperature, twinning is the alternative mechanism of deformation in $\alpha$ titanium and the main modes are $\{10\bar{1}2\}$, $\{11\bar{2}1\}$ and $\{11\bar{2}2\}$. Under a tension force parallel to the c-axis, the $\{10\bar{1}2\}$ and $\{11\bar{2}1\}$ twins are activated while under compression force, the $\{11\bar{2}2\}$ is activated [23].

***Table 2.1*** *– Summary of the slip systems in alpha titanium.*

| **Slip System** | **Burger's vector** | **Slip Plane** | **Slip Direction** | **Number of Slip Systems** | |
|---|---|---|---|---|---|
| | | | | Total | Independent |
| **Basal** | $\vec{a}$ | $\{0001\}$ | $\langle 11\bar{2}0 \rangle$ | 3 | 2 |
| **Prismatic** | $\vec{a}$ | $\{10\bar{1}0\}$ | $\langle 11\bar{2}0 \rangle$ | 3 | 2 |
| **Pyramidal** | $\vec{a}$ | $\{10\bar{1}1\}$ | $\langle 11\bar{2}0 \rangle$ | 6 | 4 |
| **1st order Pyramidal** | $\vec{c} + \vec{a}$ | $\{10\bar{1}1\}$ | $\langle 11\bar{2}3 \rangle$ | 6 | 5 |
| **2nd order Pyramidal** | $\vec{c} + \vec{a}$ | $\{10\bar{2}2\}$ | $\langle 11\bar{2}3 \rangle$ | 6 | 5 |

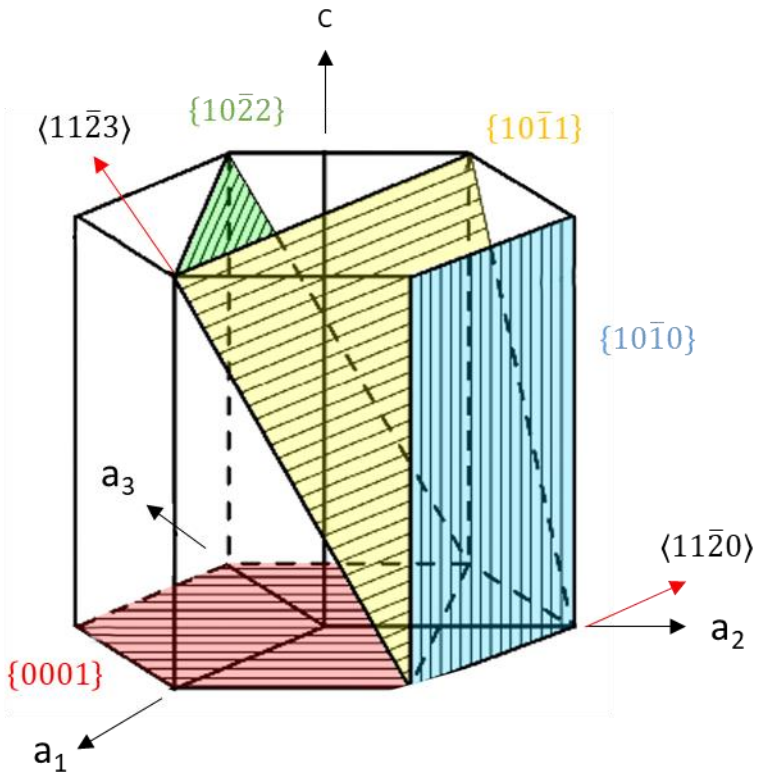


***Figure 2.3*** *– Illustration of the slip systems for a HCP lattice (Redrawn from* [12]*).*

### *2.3.4. Schmid factor*

The slip in a grain will occur when the shear stress on a slip plane that is resolved in the direction of the slip reaches certain value, known as critical resolved shear stress ($\tau_c$ or CRSS). The CRSS can be calculated with the Schmid law shown in Equation (2.1).

$$\tau_c = \sigma_y \cos\varphi \cos\lambda \qquad \textbf{(2.1)}$$

Where $\sigma_y$ is the yield stress of the material, $\varphi$ is the angle between the slip plane and the normal to the slip plane and $\lambda$ is the angle between the slip plane and the slip direction. The quantity $\cos\varphi \cos\lambda$ is known as Schmid factor and has a maximum value of 0.5 and a minimum of 0 [24,25]. The Schmid factor does not take into account the local stress state but it has been observed that the activation of slip systems correlate well with the highest Schmid factor [26]. Nevertheless, at the subgrain scale more complex deformation can take place [27]. Figure 2.4 shows a diagram of the Schmid law planes and directions.

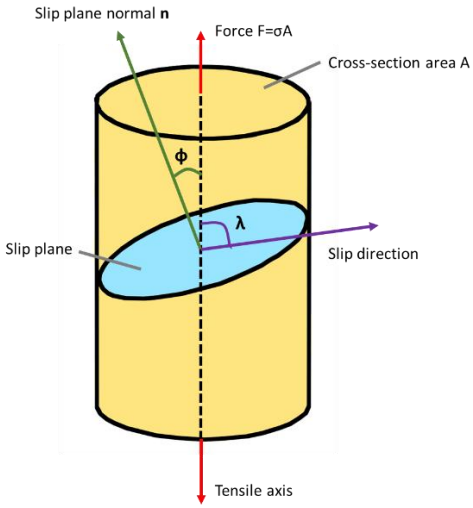


***Figure 2.4*** *– Diagram of the Schmid law planes, angles and directions. (Redrawn from* [28]*)*

The value of the CRSS will change for different alloys and slip planes. For example, Figure 2.5 shows how the CRSS is higher for pyramidal slip in comparison to basal or prismatic. For Ti-64, the CRSS in the pyramidal plane is considered at least two times higher than the prismatic CRSS [29]. In addition to this, there has been previous work that have demonstrated lower values of CRSS in the prismatic plane compared to the basal plane [26,30,31]. It has been suggested the possibility to add a hardening effect to the CRSS calculation for polycrystalline material to take into account the interaction between neighbouring grains.

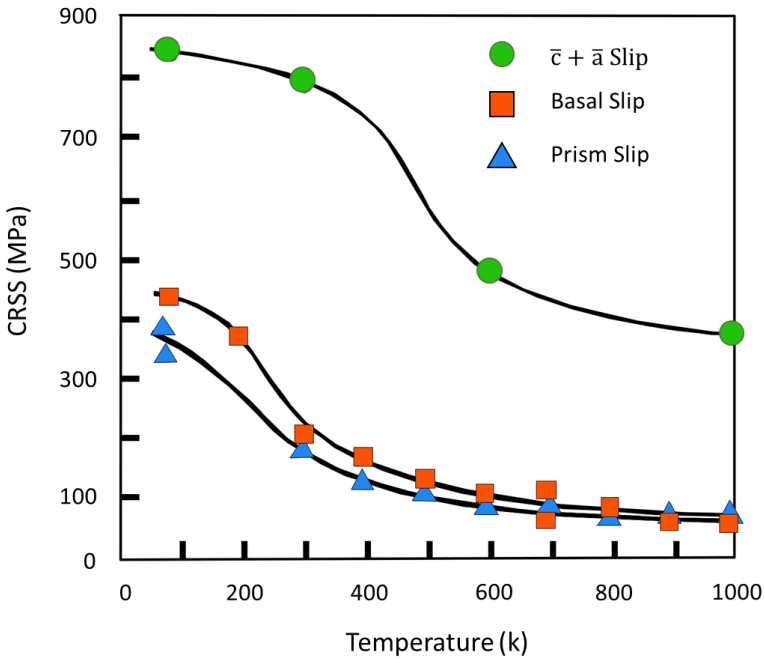


***Figure 2.5*** *– Graph of the CRSS value at certain temperatures of basal, prism and <$\vec{c} + \vec{a}$> slip for a single crystal Ti-6Al-4V (Redrawn from* [12]*).*

## 2.4. Titanium Alloying elements

Titanium is classified in α alloys, β alloys and α+β alloys classes and the difference between these categories is defined by the quantity and type of alloying elements in the titanium. The β transus in titanium is the key to obtain a titanium alloy with a specific microstructure. The alloying elements can increase or decrease the β transus to obtain the desired class of titanium alloy. Additionally, there are other elements that are considered neutral and they do not influence the temperature of the β transus. Figure 2.6 shows a graph that reflects the different types of titanium alloys when the amount of β stabilizer in the titanium is increased.

There are two additional classes called near α alloys and metastable β alloys. The α alloys are created by adding a small amount of β stabilizer; and metastable β alloys are created by increasing the content of β stabilizer until it is not possible to create martensitic structure.

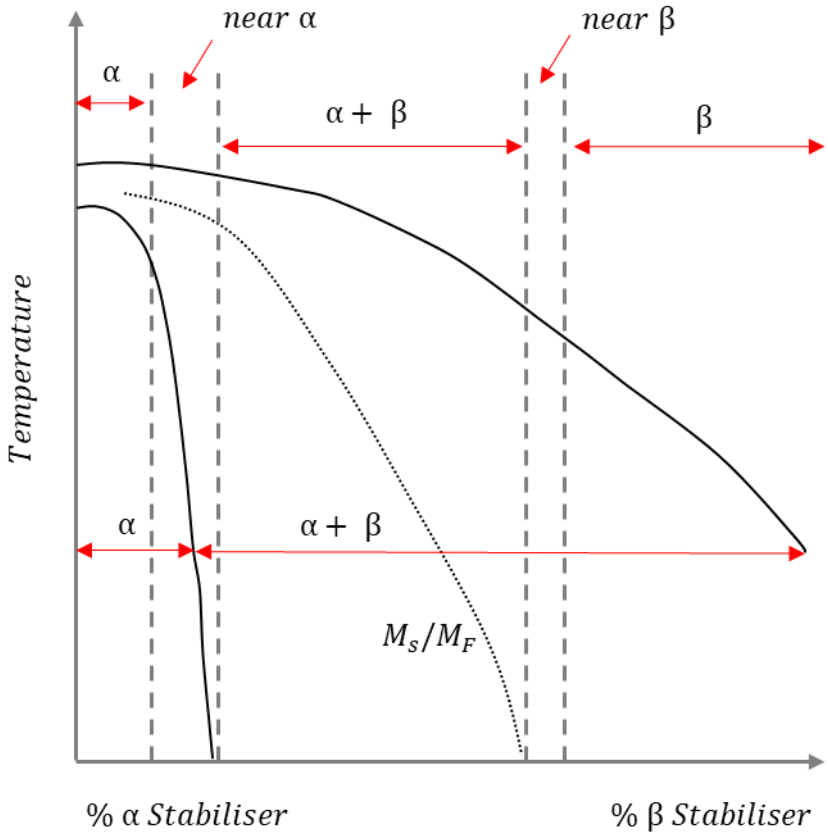


***Figure 2.6*** *– Graph showing the influence in the final phases when increasing the β content in a titanium alloy. (Redrawn from* [32]*)*

### 2.4.1. $\alpha$ alloys

The alpha alloys have an HCP lattice like it was mentioned in Section 2.3.1. In the lattice, the $\alpha$ stabilizers can be positioned at substitutional positions like Al, or at interstitial positions like O, C and N. The three subclasses of $\alpha$ alloys are: commercially pure titanium, $\alpha$ alloys and near $\alpha$ alloys.

The commercially pure titanium can be divided in 4 different grades, which depends on the content of interstitial alloying elements. Grade 1 has high corrosion resistance and ductility while grade 4 shows better strength in the alloy. Due to the good corrosive properties, the CP-Ti is common in the construction for chemical and petrochemical processing equipment that does not require high mechanical properties.

Near $\alpha$ alloys have a small amount of $\beta$ stabilizing elements, usually lower than 2%. The $\beta$ phase helps to control the grain size of the $\alpha$ phase and improves the processing window at high temperatures. One common near $\alpha$ alloy in the aerospace sector is the Ti-6Al-2Sn-4Zr-2Mo ,which shows an improved mechanical performance at high temperatures [12].

### 2.4.2. $\alpha$+$\beta$ alloys

The $\alpha$+$\beta$ alloys contain $\alpha$ and $\beta$ stable phases at room temperatures, which allow them to have very attractive properties in the aerospace sector. These alloys can have martensitic microstructure if they are quenched from the $\beta$ field at enough speed, as shown in Figure 2.6. The $\alpha$+$\beta$ alloys have three main types of microstructures depending on the way is processed: fully lamellar, fully equiaxed and bi-modal. The critical feature in the fully lamellar microstructure is the $\alpha$ colony size because it establishes the effective slip length, hence, a fine $\alpha$ colony will increase the yield stress [12]. Similarly, the mechanical properties of a fully equiaxial microstructure are defined by the $\alpha$ grain size. The critical feature in the bi-modal microstructure is the $\beta$ grain size and the element partitioning effect. The most common alloy in the $\alpha$+$\beta$ class is the Ti-6Al-4V due to a good balance of mechanical properties.

### 2.4.3. β alloys

The β alloys do not transform in martensitic structures when they are quenched from the α+β regions, as shown in Figure 2.6. One of the major advantages of the β alloys is that they can have very high strength and they can be processed at lower temperatures. Furthermore, the β alloys have good corrosion resistance, especially in high hydrogen environments. There are two main types of β alloys, the "high strength" alloys that have high content of α phase and the "heavily stabilized" alloys with a low content of α phase.

## 2.5. Phase transformation

When titanium is cooled from above the β transus, there is a transformation from a BCC crystal structure to an HCP crystal structure. In function of the cooling rate, the transformation can be martensitic, or it can be controlled by a diffusion and grain growth process. Burges [33] determined the crystallographic relation during the transformation shown below:

$$(110)_\beta \,||\, (0002)_\alpha$$

$$[1\text{-}11]_\beta \,||\, [11\text{-}20]_\alpha$$

One BCC crystal can have 12 HCP cells with different orientations. The transformation occurs in the closed packed BCC plane, and it transforms into the basal plane of HCP.

### 2.5.1. Diffusion controlled nucleation growth

When a titanium alloy is cooled down slowly form the β phase to the α+β, it is possible to avoid the martensitic structure and obtain α colonies in a β grain. In the β phase the titanium microstructure is made of β grains only. When the alloy reaches the α+β phase, the α phase starts nucleating in the grain boundary of the β grains. The α phase grows creating a continues layer in the grain boundaries of the β grains. Then, the primary alpha starts to nucleate from the grain boundaries to the centre of the β grain creating the first plates. The plates that grow

from the same region of the grain boundary usually are parallel to each other and receive the name of $\alpha$ colonies. These $\alpha$ colonies grow to the centre of the $\beta$ grain until they reach other colonies. The thickness of these colonies depends on the cooling rate of the material where higher cooling rates will produce thinner plates. This kind of diffusion-controlled nucleation growth is only applicable to near $\alpha$ and $\alpha$+$\beta$ alloys.

### *2.5.2. Martensitic transformation*

The martensitic transformation is diffusionless represented with $\alpha$' and it takes place when the material is quenched in water or oil from the $\beta$ field. This transformation is based in a shear system of the planes and directions $[2\bar{1}\bar{1}3]_{\alpha}(\bar{2}112)_{\alpha}$ and $[2\bar{1}\bar{1}3]_{\alpha}(\bar{1}011)_{\alpha}$. The microstructure obtained in this transformation is very fine and the possible shapes of the $\alpha$' are plate-like or acicular.

## *2.6. Diffusion*

### *2.6.1. Fick's 1st Law*

Diffusion is the random movement of atoms from one part of the system to another part of the system [25]. Diffusion is driven by a reduction of the Gibbs free energy in the system and it stops when the chemical potentials of the atoms are the same in the hole system [34]. The atoms have a vibration energy of $3k_bT$ where $k_b$ is the Boltzmann constant and the T is the temperature. Consequently, at higher temperatures, the diffusion increases because the atoms will have a higher frequency of vibration, which will allow them to move to a vacant position [34]. The movements of the atoms is contrary to the concentration gradient in the material and in a steady state it can be described with Fick first law of diffusion shown in Equation (2.2) [35].

$$J = -D\frac{dc}{dx} \qquad \textbf{(2.2)}$$

Where $J$ is the amount of atoms that diffuse against the gradient in a specific amount of time [ atoms $m^{-2}$ $s^{-1}$], $D$ is the diffusivity coefficient [$m^2$ $s^{-1}$] and $\frac{dc}{dx}$ is the amount of atoms per surface [atoms $m^{-4}$]. The diffusivity coefficient follows an Arrhenius relation and it is dependent of the temperature like is shown in Equation (2.3).

$$D = D^0 e^{\frac{-Q}{k_B T}} \quad \textbf{(2.3)}$$

Where $D^0$ is a frequency factor, $Q$ is the activation enthalpy of diffusion, $T$ is the temperature and $k_B$ is the Boltzmann constant.

### 2.6.2. Fick's 2nd Law

In reality, the diffusion takes place under unsteady state conditions. Fick's second law takes into consideration the change of the concentration gradient over time and can be defined with Equation (2.4).

$$\frac{\partial C}{\partial t} = D \frac{\partial^2 C}{\partial x^2} \quad \textbf{(2.4)}$$

Where C is the concentration, $t$ is the time, $D$ is the diffusivity coefficient and $x$ is the distance to the interface. This equation has several solutions that depend on the boundary conditions. A common solution to this equation is the one shown in Equation (2.5).

$$c(x,t) = c_0 \,\mathrm{erf}\left(\frac{x}{2\sqrt{Dt}}\right) \quad \textbf{(2.5)}$$

Where $c$ is the element concentration, $c_0$ is the initial element concentration, erf is the error function, $x$ is the distance to the interface, D is the diffusion coefficient and t is the time the system has been at a specific temperature. This equation is obtained for a one dimension semi-infinite system with the boundary conditions c(0,t) = 0 and $\partial c/\partial x = 0$ for x = ∞,t and an initial condition of c(x,0) = 0 [36].

### *2.6.3. Diffusion in titanium*

The diffusion in titanium can vary in function of the crystallographic structure. As shown in Figure 2.7, the β titanium self-diffusion is three times higher than the α titanium. Similar observations can be made for the rest of the elements, where the diffusivity is always higher in β titanium [12,16]. The diffusion in the α titanium is anisotropic due to the HCP crystal structure, and it depends on the angle created with the c-axis.

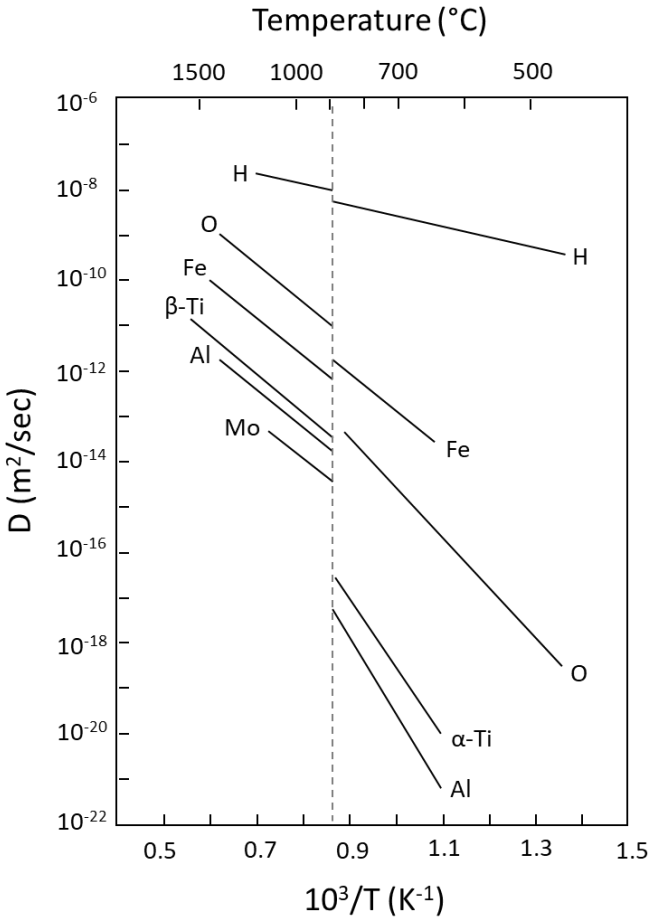


***Figure 2.7*** *– Influence of the diffusivity with the temperature and the crystal structure in a titanium alloy (Redrawn from* [12]*).*

## 2.7. Thermomechanical processing

### 2.7.1. Primary working

The most common method to shape titanium components for structure applications is by the hot forging route. This route deforms the ingots generated via vacuum arc remelting (VAR) through a series of thermomechanical processes with the aim to break up the cast microstructure [16]. Before the thermomechanical processing, it is necessary to condition the ingot for the primary forging stage to reduce the stresses concentrators that could generate cracks in further processes. To produce large deformations with a small application of force, titanium ingot is forged above the β transus at first. Furthermore, the final stage of the primary working consists in processing below the β to reduce the size of the β grains generated during the casting process [12]. There are a number of intermediate forging steps where a combination of sub and supertransus forging takes place depending on the alloy and the final shape desired. An example of a primary working route is shown in Figure 2.8. It is important to take into account the cooling rate in (c) prior to the final forging because it can modify the α lath thickness and have a direct impact on the gran size and mechanical properties. At the end of the primary working, there are three main products generated: billet, bar and flat rolled sheet.

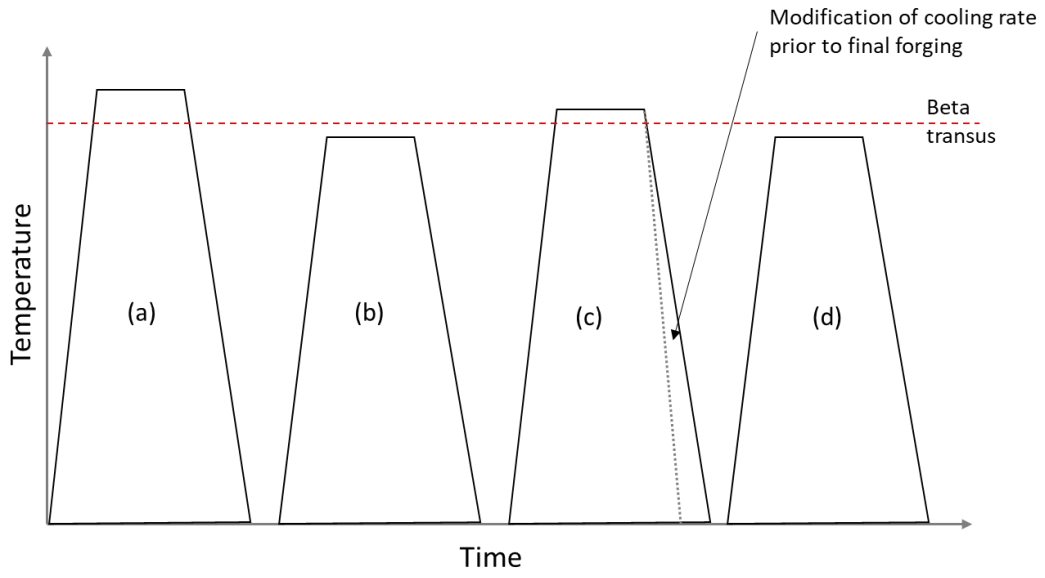


***Figure 2.8*** *– Schematic diagram of a titpical primary working processing route. The different steps are: (a) inicial β forge, (b,c) intermediate forgning steps and (c) final α/β forging step. (Redrawn from [12])*

### *2.7.2. Secondary working*

To produce a near-net shape component further thermomechanical processing is required. There are a number of processes that can produce the final shape such as: forging, rolling, wire drawing, ring rolling and extrusion. Furthermore, the final geometry can be heat treated to further refine the desired microstructure and mechanical properties. This section will only focus on the forging process because this is the only technique used in this work.

#### *2.7.2.1.* Forging

Forging consists in the deformation of a metal at high or medium temperatures by applying mechanical pressure with a hummer or large presses. The number of forging processes and blows will depend on the alloy and the final geometry. One disadvantage of titanium is that it is necessary to apply higher forces than other materials, like aluminium, because it has a higher resistance to deform (flow stress) when forging. Furthermore, the development of texture, when forging HCP crystal structure, increases the anisotropy in the material and makes it more difficult to forge.

The most common types of forging are open and close die forging. In open die forging there are no constrains in the side of the die and the working piece can flow to the sides during the

forging process. However, in the close die forging, there are constrains in the sides of the die and the workpiece cannot flow to the sides. Therefore, close die forging allows more flexibility to create complex geometries [12].

Hot forging takes place close to the β transus in titanium and the workpiece can be heated above or below this temperature depending on the desired microstructure for the component. The strength coefficient at high temperature is lower than at low temperature; hence, it is possible to make large deformations while applying lower forces. Weiss et al. [37] demonstrated for a β titanium a decrease of the flow stress when increasing the forging temperature of the workpiece. One of the key aspects in the reduction of the flow stress is the change of crystal structure from HCP to BCC that occurs in titanium alloys and how the BCC deforms in comparison to HCP.

In supertransus conditions, the cooling rate defines the colony sizes and the formation of α in the grain boundaries. At temperatures below the β transus, the workpiece is usually cooled down in air and the microstructure obtained is an equiaxed shape. It has to be taken into account the adiabatic heat generated during the forging process while processing below the β transus because the component could reach temperatures above the β transus.

### *2.7.3. Dynamic deformation mechanisms*

The microstructure during the forging process suffers from different dynamic mechanism that allows the formation of new microstructures. This is caused because the strain applied to the workpiece increases the dislocation density. Then, the interaction between the dislocations produces a higher strain energy in the workpiece that allows a dynamic recovery and recrystallization to occur during the forging process.

The dynamic recovery process (DRV) is one of the dynamic mechanisms that can occur during a forging process in high stacking-fault-energy materials. This mechanism lowers the total energy of the system by reducing the density of dislocations. The reduction of the dislocation density takes place when two dislocations with opposite sign annihilate each other through gliding in active slip [38]. Nonetheless, the flow curve of a DRV process first shows an increase of strength due to the flow hardening occurring in the workpiece followed by a steady state,

which represents the point where dislocation density hardening and dynamic recovery balance each other. This is shown very clearly in Figure 2.9.

In low staking-fault-energy materials, the dynamic mechanism dominating the behaviour of the material is the discontinuous dynamic recrystallisation process (DDRX). There is a high dislocation density in the material produced by the fact that mobile dislocations are dissociated, which makes the climb of the dislocations more difficult. The DDRX process takes place when there is nucleation and growth of equiaxed strain free grains caused by the combination of higher density movement at high temperatures and dissimilar dislocation densities in the grain boundaries [39]. This process is in a continuous loop while the workpiece is being forged. The DDRX graph in Figure 2.9 shows a similar steady state caused by the balance of the DDRX and DRV process, with the main difference that, in this case, there is a peak of stress followed by a flow softening.

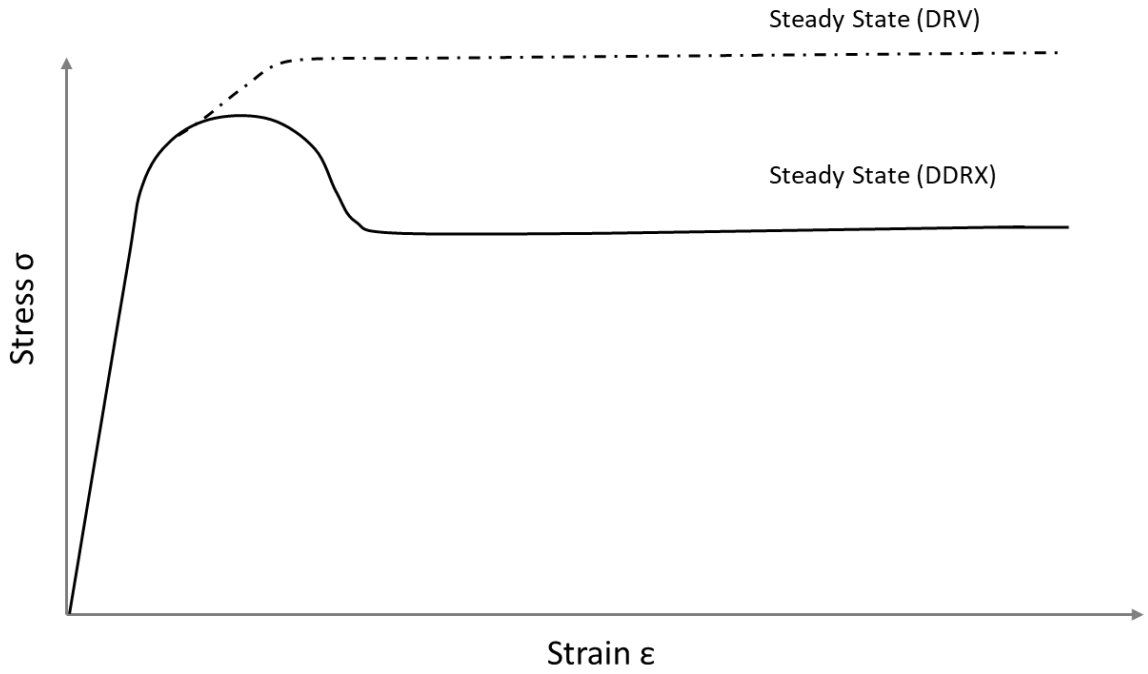


***Figure 2.9*** *– Schematic representation of the work hardening behaviour at high temperatures when titanium is undergoing dynamic recrystallization. (Redrawn from* [40]*)*

## 2.8. Powder Metallurgy

### 2.8.1. Introduction

Powder metallurgy consists in producing a near net shape component from powder. This process does not require melting the material and allows to reduce the amount of scrap produced with other methods. The most common feedstocks to produce powders comes in forms of Ti sponge, billet or ingot material. There are two main routes to produce titanium alloy powder: the pre-alloying (PA) or the blended elemental (BE) approaches [41]. The pre-alloyed route contains the desired alloy before the production of the powder while the blended elemental route the alloying elements are added to titanium as elemental powders. The PA powders tend to have more strength than BE powders [21].

### 2.8.2. Types of powders

Nowadays, most of the powder available are produced through gas atomized (GA), plasma atomized (PA), the hydride-dehydride (HDH) or plasma rotating electrode process (PREP) [21,42].

- *Gas Atomisation (GA):* The process consists in melting the metal at the top of a crucible. Then, the molten metal is poured through a refractory nozzle to a high - pressure argon gas stream. The aim is to break up the melt into a fine spray that will convert into powder when solidifies. Titanium can also be produced by a variation of the gas atomisation process, called electrode induction gas atomisation (EIGA). The main variation of this process is that it melts the metal through drip melting an electrode and the drops of molten titanium falls into a gas atomising nozzle [43]. In general, the gas atomized powders tend to be spherical with some defects and satellites in the exterior or the particles. The formation of the satellites is due to the fine particles colliding with partially molten particles. Furthermore, the high-pressured gas tends to cause more porosity in the powder in comparison to other techniques [42].

- *Plasma Atomisation (PA):* This technique uses titanium wire as a feedstock. The spool of wire is melted and atomised by plasma torches and gas jets inside the atomisation chamber. The melted droplets solidify in powder particles at the bottom of the chamber [44]. The type of powder produced from PA tends to be spherical with some satellites and high level of purity because the particles are not in contact with the atomisation chamber. The main disadvantage of this technique is the high cost of the titanium wire and the fact that some titanium alloys are not available in this format [42].
- *Plasma Rotating Electrode Process (PREP):* This process is similar to PA process and the main difference is that PREP uses a rotating bar for feedstock instead of the wire. The end of the bar is melted by the plasma torches, which causes droplets of fuse material to eject from the surface due to the high rotating speed (3000-15000 RPM) [45]. PREP process tends to create the best quality powder because as mentioned with the technique PA, the powder is not in contact with the chamber before cooling down. Furthermore, PREP powder has low internal porosity because the process uses centrifugal forces to create the powder [42].
- *Hydride-Dehydride (HDH):* This is a cheaper method to produce titanium powder because it can be produced directly from Ti sponge, ingot or mill products. The titanium is embrittled by heating the material in a hydrogen atmosphere and crushed to desired PSD. The excess of hydrogen in the powder is removed by heating the powder in a vacuum environment [46]. HDH powder particles have an angular morphology caused by the crashing stage of the solid components. This technique can only be applied to materials that are sensitive to hydrogen embrittlement [47].

### *2.8.3. Particle Size Distribution (PSD)*

The particle size distribution (PSD) obtained from these processes is very wide and this can be a problem for some technologies such as additive manufacturing (AM) where it is required that the powder particle have small diameters [48]. Figure 2.10 shows the typical PSD of a gas atomized powder and the PSD required for different powder metallurgy processing techniques. It is possible to see that most of the techniques require small PSD, which represents a small percentage of the powders produced with GA. Consequently, the powders

have to be sieved to different PSD before they can be processed. However, there is still large amount of oversize powder that is considered waste for the additive manufacturing sector.

The PSD is also dependent on the processing technique used. A clear example is shown in Figure 2.11, where PA produces some of the finest powders while PREP or FFGA produces courser powder. Furthermore, other techniques such as the EIGA process, produce a wide range of PSD. The high cost of fine powders produced with processes such as PREP powder is related to the quality of the powder and the amount feedstock required to produce the small PSD.

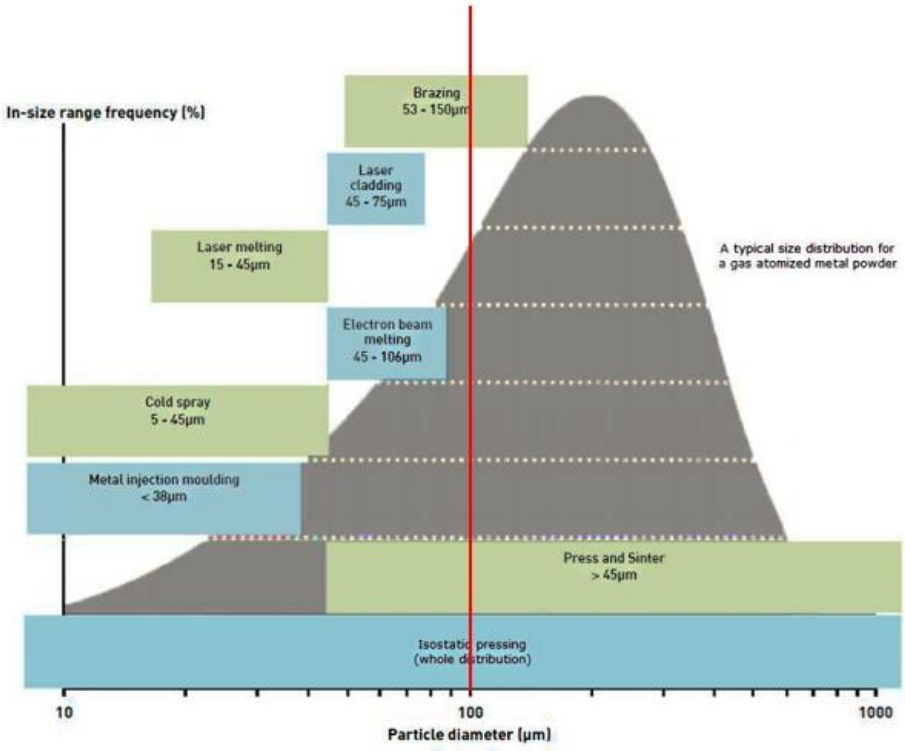


***Figure 2.10*** *– Graph of a typical PSD for a GA powder with the PSD required for several powder technologies (Adapted from* [48]*).*

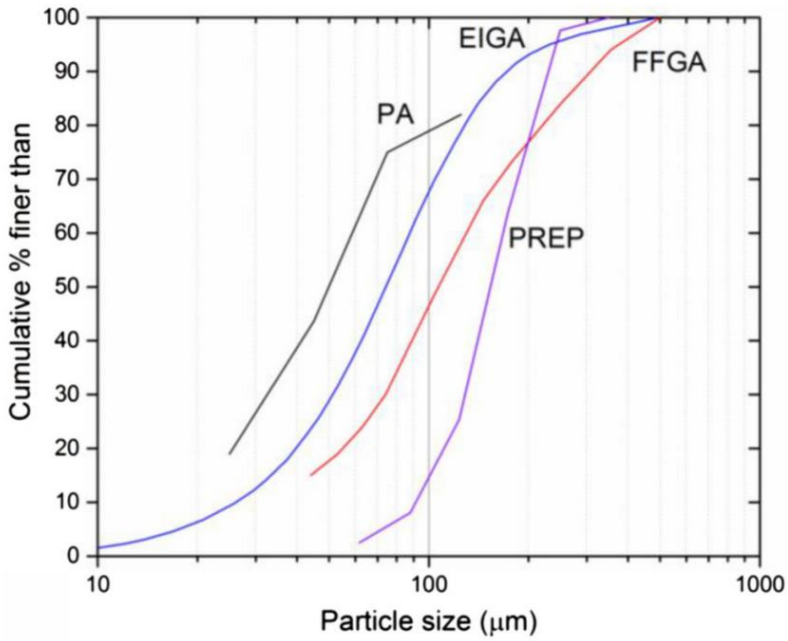


***Figure 2.11*** *– Graph with the typical PSD of titanium powder produced with different methods* [42]

## *2.9. Common powder metallurgy techniques*

### *2.9.1. Additive Manufacturing (AM)*

Additive manufacturing is a technique capable of building components with complex geometries layer-by-layer, which are not possible to create with any other technique. Furthermore, it reduces the number of steps required to produce a component because AM has the freedom to create any near-net shape in a single step.

According to the ASTM International, the AM processes can be classified into seven categories, which are: Material jetting, binder jetting, direct energy deposition, VAT photopolymerization, material extrusion and powder bed fusion [49]. Nevertheless, only powder bed fusion, binder jetting and direct energy deposition are the categories that uses powder as a feedstock [7]. Some of the most common AM processes in the aerospace technology are direct energy deposition (DED) [50] and powder bed fusion (PBF) [51]. DED and PBF can use a laser or electron beam to melt the powder. The main difference between these two techniques is that the powder in DED is delivered and melted through a nozzle in

the desired location while in PBF the powder is in a bed layer, and it is the nozzle with the heat source that melts the powder in the desired location.

Although additive manufacturing is a relatively novel technique with unique characteristics that make it very promising for the industry, it has a number of issues that need to be solved before it is used more widely in industry. The two most common defects found in additive manufacturing are porosity and lack of fusion [52]. The pores are caused by gas trapped inside the melt pool and the lack of fusion is related to low temperatures in the melt pool or an excess of power [50]. The defects can be minimized with a posterior hot isostatic pressing (HIP) treatment, but this increases the cost and the time required to create the component. In addition to this, the rapid changes or temperature while melting the powder create high residual stresses in the AM part, which required further treatment to remove them [53]. Other possible issues are dimensions inaccuracy and oxidation of the powder [51].

### *2.9.2. Pressure less sintering*

The process consists of sintering metallic powder without applying pressure during the sintering process. The powder has been previously pre-pressed at room temperature to obtain a green part. Then, the green part is placed in a furnace at a temperature of 1200°C or higher to make sure the component is fully sintered and the BE powder have been fully homogenised [54]. The sintering process needs to occur under vacuum conditions or with an argon atmosphere to avoid picking up oxygen and nitrogen.

The advantage of this technique is that it is capable of producing a high number of samples because no mould is required during processing. However, besides the issues with oxygen and nitrogen pick up, the average density of the final component is 98% of the theoretical density for BE powder. The final density of the component is even lower for PA powder [21].

### *2.9.3. Hot Isostatic Pressing (HIP)*

HIP is one of the most common methods used for consolidating powders such as titanium [55]. The principle of the process consists in applying isostatic pressure to the powder at certain temperature for a range of time until the powder is fully consolidated. The most

common way of applying the isostatic pressure is with argon gas. This pressure is transmitted to the powder with the aim to deform the material and remove the pores [56]. To avoid any oxidation, the process takes place in a hermetically sealed HIP vessel. Moreover, the powder needs to be inside a leak-free container that has to be machined once the metal is fully processed. Figure 2.12 shows a schematic overview of a HIP unit.

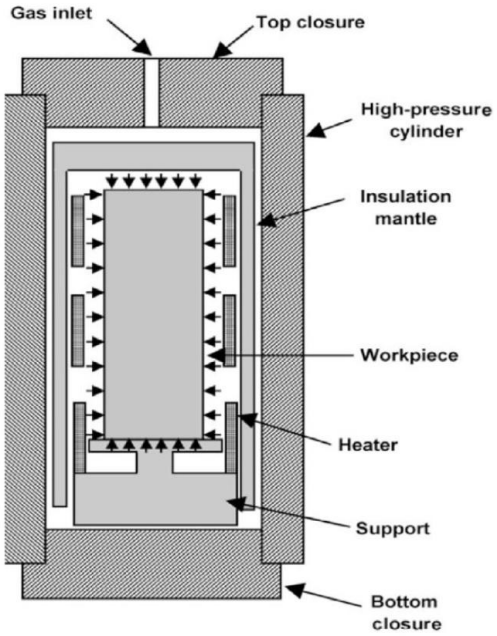


***Figure 2.12*** *– Illustration of the basic parts and mechanisms used in HIP to fully consolidate powder* [57]

The microstructure and the mechanical properties of HIP material depend on the processing temperature. Further refinement of the microstructure is possible by combing HIP with a thermo mechanical processing [58]. However, this could increase the performance/cost ratio of the HIP component [59].

The advantages of HIP are that it is capable of producing near-net shaped components with a 99.9% theoretical density [60]. Furthermore, the use of isostatic pressure allows to obtain fully consolidated components at temperatures below the beta transus for titanium. HIP also has a high repeatability of microstructure and mechanical properties in comparison to other technique [61].

HIP also have some disadvantages such as long dwell time (~ 4-6 hours), which reduces the number of possible components produced in an industrial environment. Furthermore, there is a potential risk of producing residual stresses in the component caused by thermal stresses due to non-uniform densification of the powder [62,63]. The canning of the HIP process is

also challenging because the container shrinkage is not isotropic and depends on multiple parameters [61]. Also, the development of a canning is expensive and has to be machined away after every use.

### *2.9.4. Vacuum Hot pressing*

Vacuum hot pressing (VHP) is a technique used to consolidate all ranges of metallic powder. The assistance of pressure allows to obtain better consolidation than pressure less sintering, especially with PA powder. The powder is processed inside graphite tools and is heated with an induction coil or a radiated furnace. At the same time, there are two uniaxial pistons that apply the pressure to the powder. All this process is done inside a vessel in vacuum conditions to avoid any oxidation of the powder.

This technology has some limitations in comparison to similar techniques, such as field assisted sintering technology (FAST). The vacuum hot pressing requires longer times to fully consolidate powder in comparison to FAST [64,65]. Therefore, the mechanical property of FAST material is better than VHP when processed in the same conditions [66]. Furthermore, it has been demonstrated that substituting HP for FAST can increase the production up to 33,200 components more per year with a significant cost saving [67].

## *2.10. Field Assisted Sintering Technology*

In 1996, Inoue published the first pattern [68] of what is known nowadays as field assisted sintering technology (FAST), spark plasma sintering (SPS) or pulsed electric current (PECS). The technology combines low-voltage electrical current with mechanical pressure to obtain a fully consolidated solid from powder. The original name was spark plasma sintering but there are not enough evidences of plasma formation during the processing of the powder [69]. Therefore, the name field assisted sintering technology (FAST) has become more popular over the past years.

The use of FAST has several advantages compared to similar techniques described in Section 2.9. One of the biggest advantages of FAST is that it can produce high heating rates as well as

shorter processing times and lower sintering time, which helps to retain a small smaller microstructure [70,71]. More importantly, shorter processing times mean that it is possible to produce more samples in the same amount of time and reduce its cost compared to similar techniques [69,72–74]. Furthermore, the graphite tools used in FAST to consolidate the powder can be reused between 30-50 times, reducing the tooling cost of the process.

Techniques such as AM require a specific PSD to minimise the defects generated during the production, as shown in Section 2.9. FAST has a high tolerance to the size and shape of the feedstock with little effect to the final density of the component [75]. A clear example is the consolidation into a fully dense part of titanium swarf [76].

O. Guillon et al. [77] pointed out that FAST provides a better control of the operation mode and the sintering energy in relation to the conventional methods, which allow the obtention of consistent microstructure.

However, the FAST technique also has some disadvantages. The temperature in the material can have a difference of 5% approximately from the centre to the edge for large samples, which can have an impact in the mechanical properties. The microstructure can also be affected if processed at temperatures close to the beta transus. This issue can be minimized by using a good thermal isolation around the graphite ring and the application of boron nitride (BN) spray in the graphite foil to concentrate more current in the material. Additionally, a good design of the mould can be critical, especially when producing more complex geometries because a good geometry can distribute the current homogeneously to avoid hot and cold regions in the powder [78,79].

Another limitation with FAST is the little research about scaling up the technology for industrial applications. Most of the current research focuses on small scale work, which allows very high heating rates as well as rapid cooling of the sample. However, it is more challenging to have high heating and cooling rage for larger samples, causing the microstructure to differ from similar processing conditions in the small scale [80,81]. For this reason, it can be misguiding to draw conclusions from results obtained in a small-scale equipment to an industrial level.

In addition to this, it is still challenging to create complex near-net shape directly with FAST. It is important to ensure that the pressure is applied homogeneously as well as avoid affecting the current path with sudden changes of geometry.

### *2.10.1. FAST sintering mechanism*

Sintering consists in reducing the system energy through a diffusion process by reducing the surface areas of the powder or solid and reducing the total percentage of grain boundaries. The sintering process tends to occur at the homologous temperature, which is between 0.5 and 0.8 of the material's melting temperature [82].

The conventional sintering process starts by the rearrangement of the powder particles in a pre-pressure stage, that helps improves the compaction and activates de densification mechanisms. If the stress is higher than the yield stress of the material, it can produce a plastic deformation that can improve the densification of the component [82,83]. With the application of heat, there is an initial stage with the formation of necks between particles, as the one shown in Figure 2.13. These necks start growing with time and temperature and start connecting with other neighbours' necks to start consolidating the powder as well as reducing its surface area. At the same time, the grain boundaries start growing from the necks to reduce the overall energy of the system.

The sintering of the powder takes places because there are several mass transportation mechanisms that contribute to densify and coarsen the particles. It is important to take into account that during the sintering of the powder, some mechanisms contribute to the coarsening of the particles while other contribute to the densification of the part. In Figure 2.13 (a), the typical types of mass transport mechanisms for FAST are shown. The evaporation and the surface diffusion mechanisms contribute to the coarsening of the powder while the grain boundary and the volume diffusion mechanism contribute to the densification of the powder. Each of these mechanisms have different activation energies and by modifying the processing parameters of FAST, it is possible to favour one mechanism over the other. For example, high heating rates with FAST contribute the densification of the powder rather than the coarsening. The reason is that the surface diffusion mechanism is more active than the other mechanisms at low temperature due to its low activation energy. However, at high

temperature the dominant mechanisms are the grain boundary and volume diffusion. Therefore, by increasing quickly the temperature, the sintering will be dominated most of the time by densification mechanisms.

Another factor that contributes to the densification is the application of pressure. As shown in Figure 2.13 (b), the application of pressure rearranges the particles, which improves the compaction and activates the densification mechanisms.

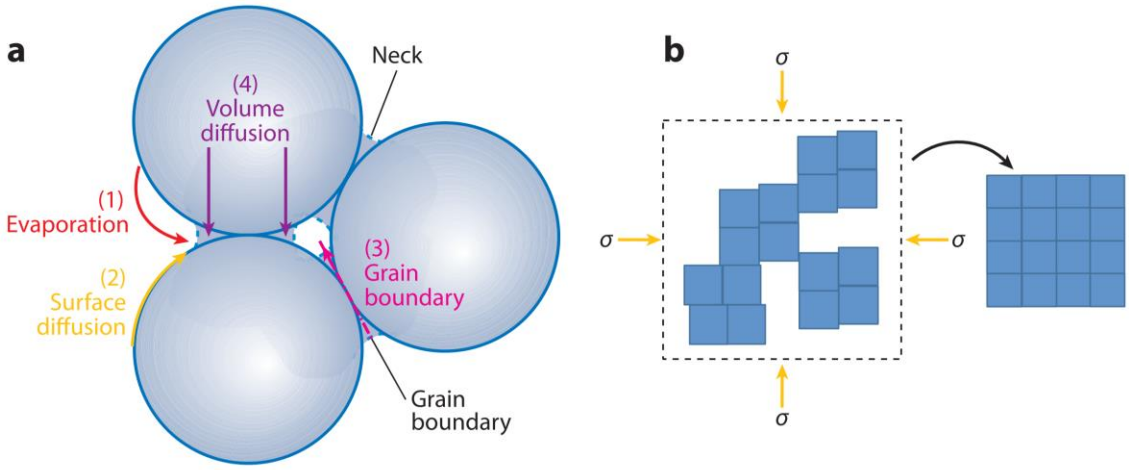


***Figure 2.13*** *– (a) mass transport mechanisms involved in sintering. (b) rearrangement of the powder when pressure is applied* [83].

### *2.10.2. Effects of the electrical current*

The application of electrical current is one of the main characteristics of the SPS. There are three main types of currents that can be applied: constant direct current (DC), pulsed DC and alternating current (AC). The type of current may depend on the material being sintered; however, the most common method is to use pulsed DC. There has been work comparing the different types of current and what effects produce in the materials while consolidating. For example, it has been observed in ceramics that the only way to obtain a fully consolidated sample is with pulsed DC current instead of constant DC [84].

The pulsed current can influence the properties and microstructure of the powder being sintered. It has been stated that pulsed current can remove from surface the oxide layer and other impurities from the particle [85] but the amount of cleanliness of the surface could be influenced by the heating rate [86]. In addition to this, there have been several studies that

have shown a higher diffusion with FAST, which is caused by the high-density currents can enhance vacancy defect migrations [87–89]. The electrical current can also reduce the flow stress of metals [90] to obtain a rapid consolidation of the powder. Furthermore, the current can influence the solid-state phase transformations by accelerating or delaying the phase transformations. This is dependent on the original powder used, the processing conditions and the current density [91].

### *2.10.3. Effect of electric field*

The electric field produced with FAST is another physical effect that can influence the densification of the component as well as grain boundary migration or grain growth [92]. Some studies have shown a grain refinement caused by a reduction in the driving force due to a decrease of the grain boundary energy [93]. Additionally, an increase of the electric field improves the sintering rate, with a more significant improvement for AC field compared to DC field [94].

### *2.10.4. Effect of pressure*

The pressure is also a key parameter to obtain a fully dense component and the use of it has multiple advantages. The pressure can reduce the sintering temperature threshold [95] as well as induce phase transformations [96]. Furthermore, the application of pressure rearranges the powder at the early stages of processing, which reduces the initial porosity in the powder and reduces the sintering time required to obtain a fully consolidated component. However, for more complex geometries, there is also a possibility that stress gradients are produced during the FAST process. Consequently, the components produced with FAST could have an inhomogeneous microstructure [97].

## *2.11. Use of FAST in titanium*

FAST is a novel route to process titanium powder that has begun to become more popular in the last years because it is possible to reduce the cost of titanium components when

compared to a conventional processing route. This reduction of cost can be achieved by reducing the amount of steps required in the thermomechanical processing, using lower sintering temperatures or short dwell times as well as cheaper feedstock [80]. Two of the most common titanium powders sintered with FAST are made of CP-Ti and Ti-64.

Research by Zadra et al. [98] obtained a fully dense CP-Ti at 800˚C, proving that it is not required to use temperatures as high as other processes to obtain a fully dense component. Furthermore, the work showed little variation of carbon, oxygen and nitrogen content before and after processing the powder with FAST. The mechanical testing done in the samples obtained a similar values to the ones in the ASTM standards. Chaudhari and Bauri [99] also obtained similar mechanical properties to the ASTM standards of CP-Ti powder consolidated via FAST. Lower cost feedstock has also been exploited by Pascu et al. [100] and Sharma et al. [101] where titanium hydride ($TiH_2$) powder was used with the aim to desorption the hydrogen at high temperatures. Weston et al. [75] studied the consolidation of spherical gas atomised and angular hydride dehydride CP-Ti powder, showing full consolidation for both types. Additionally, it was observed that the hold temperature and pressure were the critical parameters to obtain a fully consolidated sample. Weston et al. [75] produced a 250 mm billet with FAST and showed a similar microstructure from centre to edge. In the centre of the sample the grains are slightly bigger than on the edge. One of the reasons is that the temperature is measured from the centre of the sample and this is where the maximum temperature is reached. The other reason is that the edge will cooldown quicker than the centre, which allows the formation of finer microstructure. The work proves that the FAST process can be scaled up for more industrial applications if a small variation of the microstructure does not affect the final geometry shape. This is shown in Figure 2.14.

There have also been multiple studies focused on consolidating Ti-64 with FAST. The pressure to obtain a fully consolidated sample from Ti-64 is not required to be extremely high as shown by Garbiec et al. [102], where a full dense component was made with a pressure of 25 MPa. Menapace et al. [103] showed that is possible to hot forge Ti-64 preforms made via FAST in a similar way to titanium obtained through the conventional methods. It was observed that the stress necessary to deform the component varied in function of the as FAST material, were subtransus material required less stress than the supertransus. Weston et al. [104] further developed Menapace et al. [103] study and proved a novel route to create titanium near-net

shape called FAST-*forge,* which consists in combining FAST with one step forging. FAST-*forge* was first proven for Ti-64 with two different routes. The first route was to produce a shaped component with FAST and then forge it and the second route was to machine the shape from FAST material and forge it. The result showed small differences in the microstructure between both methods. A schematic of the process FAST-*forge* process is shown in Figure 2.15. To increase the densification rate of titanium components an approach is to use blended elemental powder, as shown by Yang et al [105]. Long et al. [106] and Vajpai et al. [107]. They used FAST to create bimodal microstructures with FAST, however, this was only achieved after milling the powder for several hours.

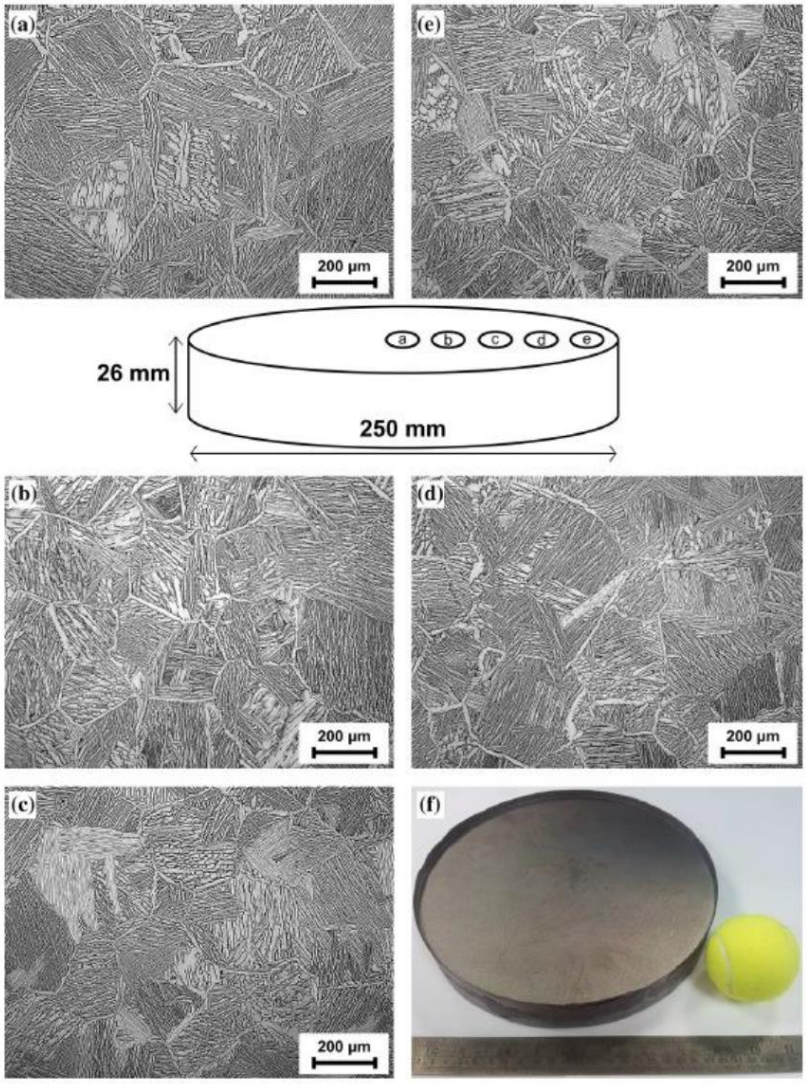


***Figure 2.14*** *– Micrograph proving that the microstructure in a 250mm diameter cylinder is the same in all parts* [75]*.*

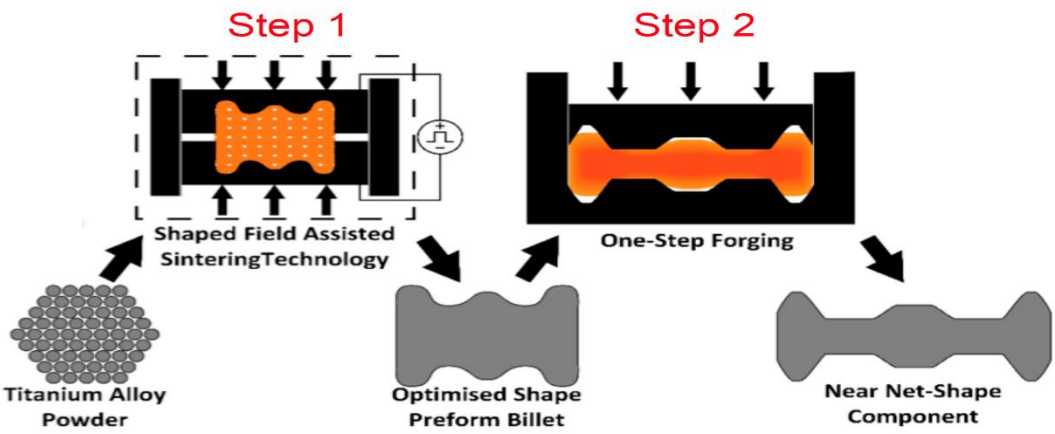


***Figure 2.15*** *– Schematic of the* FAST-*forge process where a near net shape is produced from powder with only two steps* [104].

With FAST it is also possible to consolidate other titanium alloys. Calvert et al. [108] processed Ti-5Al-5Mo-5V-3Cr powder and the results showed full consolidation of the sample as well as producing similar microstructures and mechanical behaviour to conventional processed titanium. Similar results were presents by Yang et al. [109] but with blended elemental Ti-10V-2Fe-3Al.

The aerospace industry has also been very interested in developing titanium aluminide (TiAl) due to their lower density compared to conventional titanium alloys. There has been several studies undertaken at CEMES in Toulouse with these alloys [110–113]. The studies showed the final components had good mechanical properties as well as a refined microstructure caused by the presence of borides at high temperatures.

### *2.11.1. Upscaling FAST for titanium applications*

The production of near-net shaped components made directly from FAST is possible but there are still some challenges within it. It is important to have a good understanding of the current flow through the graphite tooling because there is a risk of creating heterogeneous heating in the component. In addition to this, it is important to have a homogeneous pressure throughout the sample to avoid porosity in the final component. The use of finite elements to support the tool designs is essential for a good understanding of the current and pressure distribution.

An example of a near-net shape component is shown in Figure 2.16, where Voisin et al. [114] made a near-net shape gamma titanium aluminide (γ-TiAl) turbine blade directly from FAST. Nevertheless, the final density of the component was not disclosed in the study. It is likely that the root of the turbine blade had a high amount of porosity because the airfoil is thinner and will reach full density before the root. Therefore, heterogenous strain will be applied to the final component. This is an issue discussed in Section 2.10.4 and demonstrated by Mainere et al. [97]. To solve this issue, Maniere et al. [115] proposed to use sacrificial material to allow the near-net shaped component to fully consolidate. Another approach to produce near net shaped specimens was shown by Maniere et al. [116] and consisted of producing the desired geometry with the graphite foil inside a round mould. Then, the mould was filled with powder in both sides of the graphite foil.

There is a lack of confidence from the industry point of view because FAST is seeing as a discontinues process with little control of the process. However, the control in FAST is very precise and can be used in chain productions. New approaches with FAST equipment have been developed to improve the processing speed. For example, the new FAST machine at the University of Sheffield has a secondary chamber to cool down the samples. This chamber is capable to cool down a 200 mm disk from 1000°C to room temperature in less than an hour. With a dwell time of 30 min, it would be possible to produce a 200 mm disc with 30mm thickness every hour. Another approach is to create multiple samples in a single run as shown in Figure 2.17, this combined with a cooling chamber would allow to increase the productivity of FAST [77].

One of the limitations in FAST is the control of the cooling rate once the dwell time finishes. A 250 mm cylinder can take up to 5 or 6 hours to cool down to room temperature. Zhang et al. [117] explored the possibility to have rapid cooling capabilities in FAST by having multiple nozzles inside the vessel combined with high pressure argon. With this method it was possible to cool down the sample with a cooling rate of $6.9^{\circ}Cs^{-1}$.

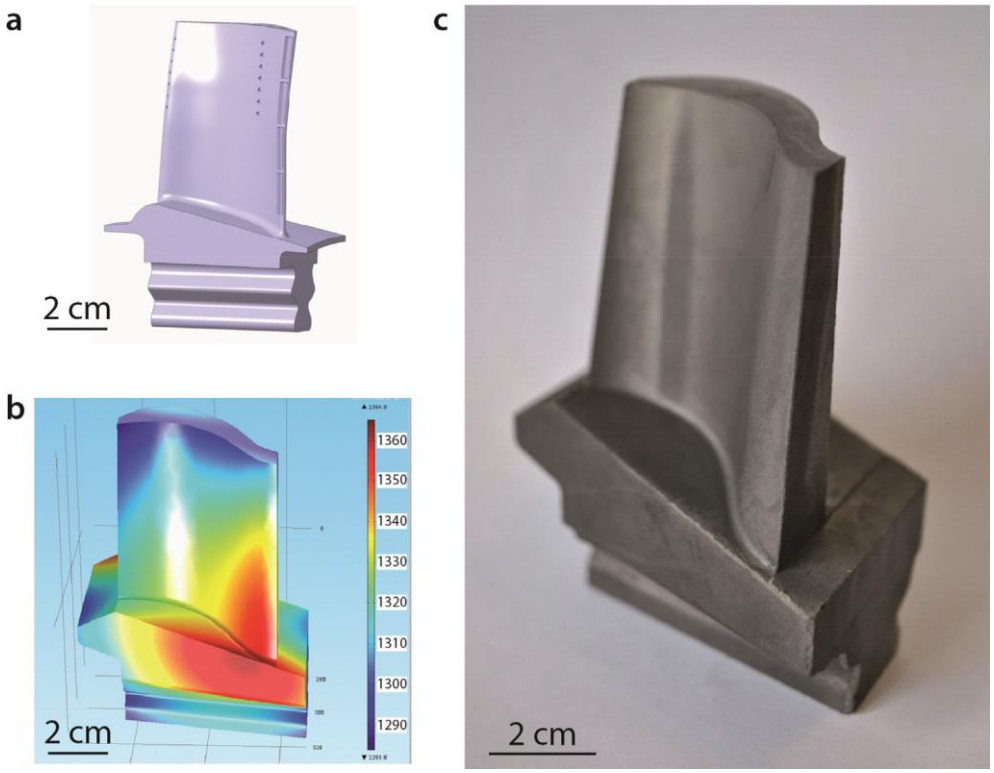


***Figure 2.16*** *– A pre-alloyed 48-2-2 powder was used to make a compressor blade directly with FAST. (a) The cad file of the final component. (b)A simulation of the expected temperatures inside the die. (c) The compressor blade made via FAST* [114].

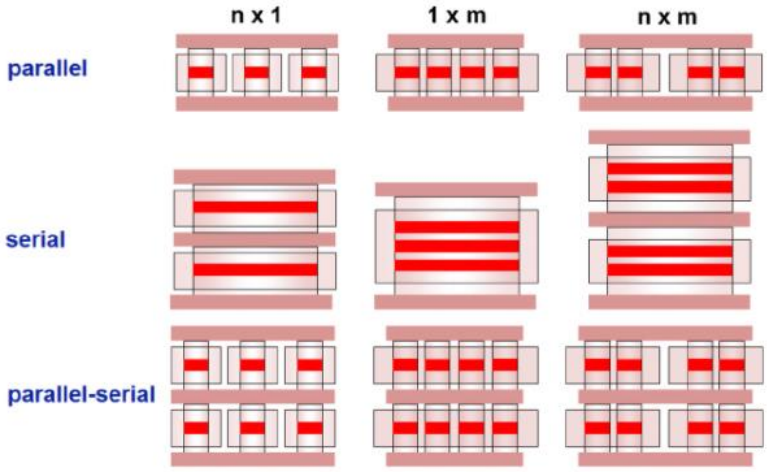


***Figure 2.17*** *– Illustration of tools for the production of multiple components with the FAST technology* [77].

## *2.12. Method to join different titanium alloys*

There are two main methods to join dissimilar titanium alloys, by fusion welding or solid-state welding methods. The fusion welding method consists of melting metal and solidifying it to

join the two alloys, this can be done with or without the use of an external electrode. The fusion welding group can be divided in two subgroups, more conventional techniques such as tungsten inert gas (TIG) and more advanced techniques such as additive manufacturing processes. The solid-state welding method consists of joining the two dissimilar alloys through a diffusion process. Most of the powder metallurgy techniques presented in Section 2.9 can be used to join dissimilar alloys because the densification mechanism is based in a diffusion process. In addition to the techniques presented in Section 2.9, this section includes other technologies, such as powder interlayer bonding (PIB), that are still in early phases of development.

### *2.12.1. Conventional fusion welding method*

The conventional fusion welding methods has a number of techniques that uses different electrodes, environment protection or heat sources, but the bases are very similar for all of them. The method consists in melting an electrode between two independent solid plates, these plates will be joined together once the melted metal solidifies. The whole process has to be done under vacuum conditions or with an inert gas to reduce interstitial pickup and segregation issues.

The issue with this technique is the formation of a heat affected zone (HAZ) that can affect the microstructure and the mechanical properties of the bond [118,119]. Furthermore, it is common to have formation of pores in the weld due to absorption or entrapment of the gas as well as contamination in the surfaces [120]. In addition to this, the rapid cooling of the melted metal tends to generate high residual stresses that have a direct impact on the mechanical properties [121].

### *2.12.2. Alternative fusion welding methods*

The additive manufacturing technology has been introduced in Section 2.9.1. This technology can be used to join dissimilar titanium alloys by using more than titanium powder. However, not all the additive manufacturing techniques to produce metallic structures use powder, wire arc additive manufacturing (WAAM) uses metallic wire to build the structure. It is possible to combine wires made of different alloys to produce the multi material component.

### *2.12.3. Solid-state joining methods.*

Multi material components can be created with the powder metallurgy technologies such as FAST, HIP or vacuum HP, which have been described in Section 2.9 and 2.10. This can be done by distributing the dissimilar powder alloys in different regions of the moulds. Another powder metallurgy technology that could be used to join dissimilar components is the technology powder interlayer bonding (PIB). This technology consists of joining two solid components by applying mechanical pressure, perpendicular to the union, and heat through induction heating. In the region where the two components are going to be joined, a small amount of powder is added to act as the "glue" between the two parts. With the application of temperature and pressure, the powder fully consolidates and joins the parts by diffusion bonding. One of the major advantages of this technique is the small generation of HAZ in comparison to other welding techniques [122].

Similar to PIB, resistance heating can also be used to join dissimilar material. This technique consists in using mechanical pressure and electrical current to join two components. It is required a layer of powder between the two components that are going to be joined.

Another technique extensively used in the aerospace sector is linear friction welding (LFW). The LFW technique consists in joining two solid components by a reciprocating motion with a small frequency of one of the components against the other. The friction generated in the interphase produces heat that softens the material and joins the two components. Although the mechanical properties of LFW joints tend to be good [6], the residual stresses tend to be high in the weld [123]. Friction stir welding (FSW) and rotary friction welding (RFW) are similar techniques to LFW with the difference that for FSW it is an external tool that creates the friction between the two materials and for RFW the movement of the workpiece is rotation instead of lineal.

## 2.13. Bonding of titanium

### 2.13.1. Fusion welding methods

#### 2.13.1.1. Conventional fusion welding methods

There have been multiple studies joining dissimilar titanium alloys with conventional fusion welding methods such as laser beam welding (LBW), electron beam welding (EBW) or TIG-laser hybrid welding.

Several pieces of research that have studied the mechanical properties of the joint made with EBW. Wang et al. [124] joined the titanium alloys Ti-64/Ti-17 and Ti-64/BT9 with EBW and the bond had higher strength than Ti-64. However, the failure in the fatigue testing occurred on the HAZ for both bonds. Tan et al. [125] observed similar results for the tensile test of Ti-22Al-25Nb/TC11 but showed a reduction of fracture toughness of the bond caused by the formation of B2 phase in the HAZ. Meanwhile, Zhang et al. [126] showed a decrease of hardness in the bond between $Ti_3Al$/TC4 and the failure of the tensile tests also occurred in the bond.

The TIG – laser hybrid welding was used by Turichin et al. [127] to join two titanium plates made with the alloys Ti-1.5Al-1Mo and Ti-64. The analysis of the mechanical properties of the bond is limited in the study but the microhardness test shows an intermediate hardness in the centre of the joint compared to the bulk material. Zhang et al. [128] also used TIG – laser hybrid technique to join TI-22AL-27Nb to TA15 showing that the failure on the tensile test occurs in TA15 instead of the bond. For the same bond, Li et al. [129] observed a reduction of microhardness occurring in the join.

Fomin et al. [130] joined Ti-64/CP-Ti in a T-join with laser beam welding as shown in Figure 2.18. There were five distinct zones in the weld and the microhardness of the fusion zone had a higher value than the bulk material.

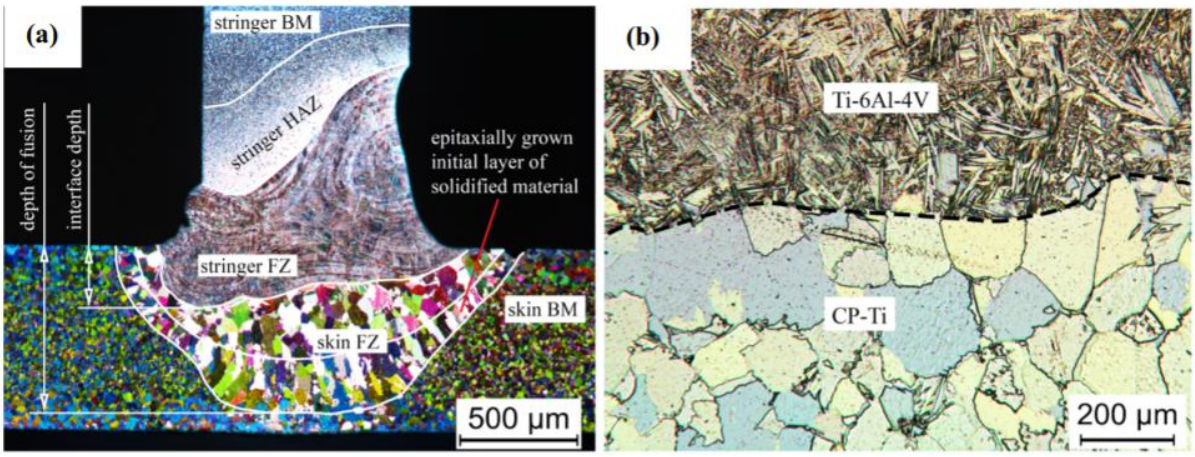


***Figure 2.18*** *– (a) Optical micrograph of the welded zone between Ti-64/CP-Ti after applying Weck's tint etchant. (b) Optical micrograph of the union between CP-Ti and Ti-64* [130].

### *2.13.1.2.* Alternative Fusion welding methods

Additive manufacturing technologies have also been used to produce multi materials components. The versatility of the technology allows to be very flexible with the location of both alloys. However, there are a number of parameters to take into account in order to obtain a good bond.

Liu et al. [131] produced a TiAl alloy in the bond by starting with a 100% Ti-64 composition and transitioning into an AlSi10Mg alloy. However, it was observed the formation of cracks due to brittle phases generated in the alloy. Yan et al. [132] also produced a functionally graded TiAl alloy with CP-Ti/Ti-48Al-2Cr-2Nb and the results showed an increase of hardness when increasing the content of Ti-48Al-2Cr-2Nb. The same approach was used by Schneider-Maunoury et al. [133] to investigate functionally grading Ti-64/Mo. The results showed good bonding between Ti-64 and Mo, nevertheless, it was detected unmelted Mo in the sample. Liang et al. [134,135] and Qian [136] studied the bond between CP-Ti and Ti-6Al-2Zr-1Mo-1V showing a smooth transition of chemistry and microhardness between both alloys. The mechanical tests done of the functionally graded material presented better strength than CP-Ti but very little plastic deformation. The formation of microcracks was also observed close to the joint. Finally, Ren et al. [137] demonstrated that a graded bond between Ti-6Al-4V and Ti-6.5Al-3.5Mo-1.5Zr-0.3Si has similar tensile properties than a wrought bar made of Ti-6Al-4V.

### *2.13.2. Solid state joining process*

The use of techniques such as hot pressing or hot isostatic pressure have not been widely explored to join dissimilar titanium alloys. However, other techniques such as LFW and FSW have been used to produce multi material components with good mechanical properties in the bond. The company TWI Ltd. used FSW to join Ti-6Al-4V with Ti-15V-3Cr-3Al-3Sn to make propellant tanks for the European Space Agency (ESA) [138]. FSW was also used by Gangwar et al. [139] to join the dissimilar titanium alloys TIMET-54M and ATI-425. The results showed a good bond between both alloys with no clear defects in it. However, the mechanical properties were dependent on the alloy positioned in the advancing side of the FSW because the failure always occurred in the retreating side.

The use of LFW to create multi material components has been studied for potential aerospace applications. Guo et al. [140] used LFW to demonstrate a multi material blade made with Ti-6Al-2Sn-4Zr-6Mo and Ti-6Al-4V but the mechanical properties of the bond were not tested. Ji et al. [141] assessed the mechanical performance of a bond made with Ti-6Al-4V/Ti17. The results showed that the bond had better tensile properties than the bulk material but worse impact testing performance. Rajan et al. [142,143] studied the bond between Ti-6Al-4V and Ti-6Al-2Sn-4Zr-2Mo, as shown in Figure 2.19. The results presented no defects in the bond, but the hardness decreased in the HAZ and reached a maximum value at the weld line. The tensile tests obtained similar results to the AMS specifications, and the failure occurred in the Ti-6Al-4V region for all the tests. The fatigue performance of the joint after applying a heat treatment was similar to the performance of the bulk material, and the failure always occurred far from the bond. The fatigue results are in agreement with Wen et al. [144] research for a bond made with Ti-6Al-4V and Ti-6.5Al-3.5Mo-1.5Zr-0.3Si. Yang et al. [145] also studied the performance of a dissimilar titanium bond made of Ti-6.5Al-3.5Mo-1.5Zr-0.3Si and Ti-5Al-2Sn-2Zr-4Mo-4Cr. The fatigue life decreased when increasing the pressure and welding time. Furthermore, an initial increase fatigue life and posterior decreased was observed with the increase of the frequency, which is in agreement with Zhao et al. [146] observations.

The use of resistance bonding to join dissimilar alloys was investigated by Pleydell-Pearce's thesis [147]. In this work, the alloy Ti-6Al-4V is joined to several dissimilar materials such as

In718 and steels. Overall, the bond produced with this technique has poor quality because the thermo-physical / electrical properties are too dissimilar. Additionally, with this technique a heat affected zone (HAZ) is generated, which affects the mechanical properties of the union and the deformation behaviour.

Powder interlayer bonding is another technology that has been used to bond titanium alloys. Watkins et al [122] also studied the union of Ti-6Al-4V by modifying some of the parameters in the PIB process. The results showed that the increase of temperature and pressure improved the densification of the powder in the bond. Davies et al [148] showed high integrity bond between two Ti-6Al-4V components made via additive manufacturing. Davies et al. [149] also obtained good bonding integrity in the bond when joining titanium aluminides via PIB. Davies et al [150] studied the fatigue performance of forged Ti-6Al-4V and Ti-6Al-2Sn-4Zr-6Mo alloys when joined by PIB. The fatigue life for the bond made of Ti-6Al-4V outperforms the fatigue life of the base material. Nevertheless, the bond made of Ti-6Al-2Sn-4Zr-6Mo had shorter fatigue life than the base material.

Powder interlayer bonding has also been used to join dissimilar titanium alloys. Davies et al [151] joined the titanium alloys Ti-6Al-2Sn-4Zr-6Mo and Ti-6Al-4V, obtaining a reduction of 10% of strength in the bond when compared to the strength of the base alloys. Other dissimilar materials have been bonded with PIB, an example is the work of Stanners et al. [152] where dissimilar nickel-based superalloys were joined successfully.

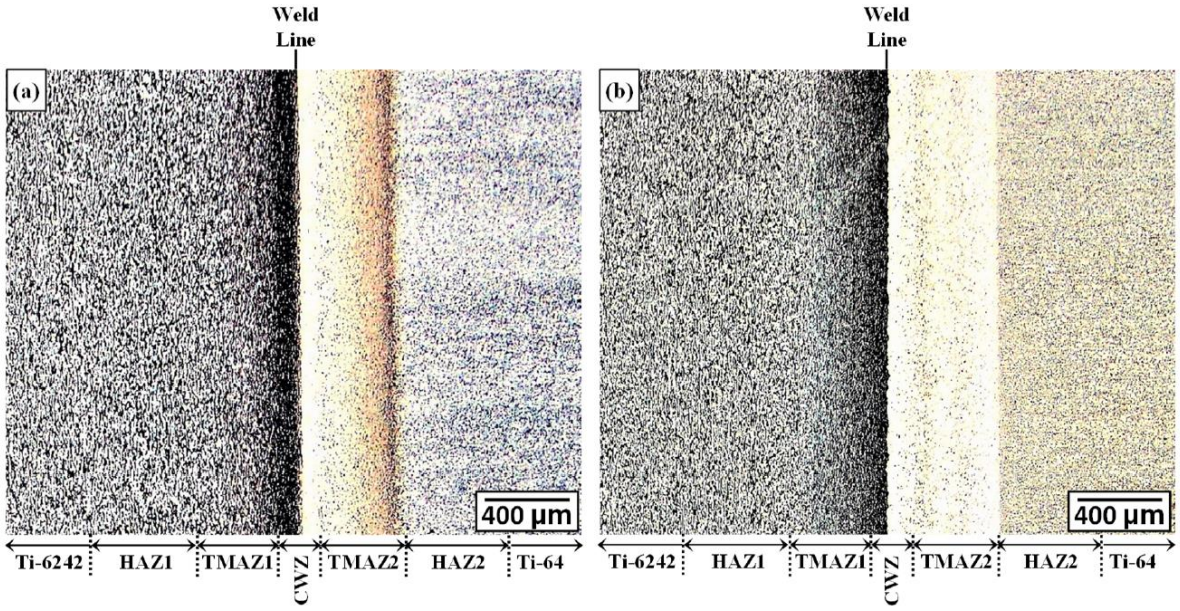


***Figure 2.19*** *– Micrographs of a LFW bond made of Ti-6242 and Ti-64. (a) as-welded (b) stress relief annealed conditions* [143].

### *2.13.3. FAST*

This section is adapted from the conference paper published by Levano et al. [153] in the proceedings of the *14th World Conference on Titanium.* This conference paper is open access under the terms of the Creative Commons Attribution License 4.0.

FAST has been used to produce multi material components because it is a relatively simple and quick process that allows to obtain good bonding. Most of the research has been focused on joining two solid components but there has also been some work done joining dissimilar titanium powders. He et al. [154] were some of the first authors to use the FAST process to bond two solid blocks of titanium, as opposed to powder. The results of the mechanical test performed in the join showed that failure occurred in areas near the bond. A similar experiment was performed by Miriyev et al. [155] in which Ti-6Al-4V was bonded to AISI4330 steel. The bond between the two materials failed by brittle fracture due to the formation of titanium carbides. Similarly, Kumar et al [8] joined two flat pieces of CP-Ti and AISI304L, obtaining a tensile strength of 260 MPa. Nevertheless, the strength increased to 400 MPa when threads were used in the bond. Pripanapong et al. [156,157] observed that the

formation of the intermetallic $Ti_3Al$ improved the properties of the bond when joining Mg alloys with CP-Ti. Vincente [158] used FAST to bond the titanium alloy CP-Ti grade 2 with Co-28Cr-6Mo and observed that the roughness of the interface is influenced by the hardness of the two materials. The effect of the temperature, pressure and time in the mechanical properties when joining pre-sintered billets of Ti-45Al-7Nb-0.3W was studied by Zhao et al. [159]. It was observed that at higher temperatures the material failed in the base material while at higher pressure the material failed at the bond interface. Martin et al. [160] used an innovative approach to bond two titanium alloys using FAST: The method consisted of bonding a Ti-6A-4V 3D structure made with by electron beam melting (EBM) to CP-Ti grade 2 powder. This method generated a fully consolidated component with 99.5% of density.

Recently, Pope et al. [9] studied the integrity of the diffusion bond (DB) of dissimilar titanium powders such as Ti-5553, Ti-6Al-4V and CP-Ti grade 2 processed with FAST. Such FAST bonds of dissimilar alloys displayed excellent mechanical integrity under tensile testing, with failure occurring in the base material of the lowest strength alloy, as opposed to the bond region like is shown in Figure 2.20. Furthermore, Pope and Jackson et al. [10] produced a multi material near-net shape component via FAST-*forge*, showing no damage in the bond after the forging stage.

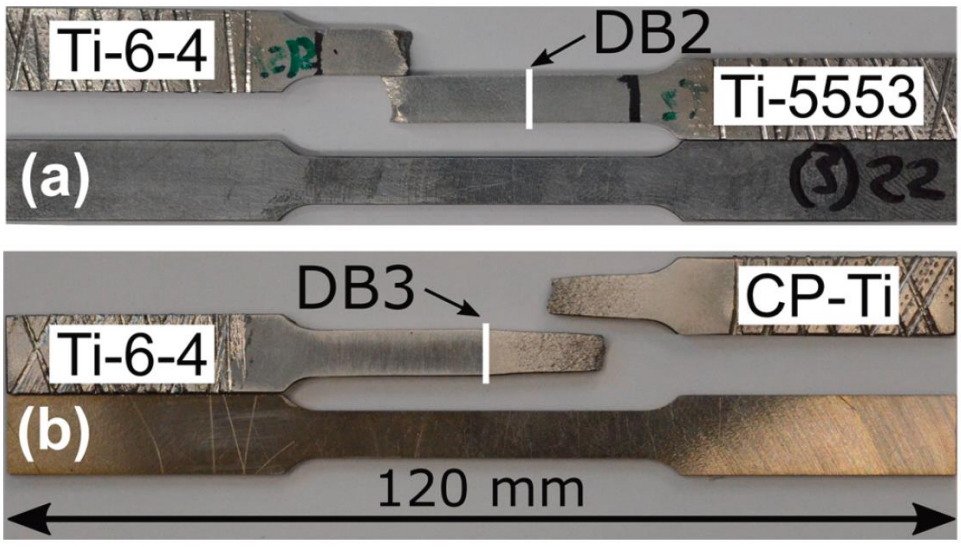


***Figure 2.20*** *– Tensile specimens made via FAST-DB showing that the failure occurred in the weakest material instead of the bond* [9].

# 3. *Methodology*

## *3.1. Introduction*

The aim of this chapter is to describe the experimental methods used in this thesis. Specific experimental methodology will be provided in the corresponding chapter.

The first section will explain the general methodology for FAST given the importance of this technology throughout the thesis. Then, the hot forging processes and the mechanical testing will be described, including tensile testing and microhardness testing. The following sections will focus on the general characterization techniques for solid material and powder. The final section describes the analysis carried out during the machining trials.

## *3.2. FAST*

The production of bonds made of dissimilar titanium alloys was carried out using the solid-state processing technology - FAST. There are two machines that were used in this work, one was located at the University of Sheffield and the second at Kennametal in Newport, UK. The main difference between the machines is the maximum dimensions of the billets that they are capable of producing. The machine at the University of Sheffield is capable of producing billets up to 80 mm diameter, while the larger machine at Kennametal can produce billets up to 250 mm diameter. The large billets were produced to machine FAST specimens larger than 80 mm, as described in Chapter 6 and Chapter 7.

### *3.2.1. General methodology*

The FAST process uses electrical current and mechanical pressure to fully consolidate the powder. The mechanical pressure is applied in a uniaxial direction by a water-cooled ram while the temperature is measured by a pyrometer that reads the temperature at the top of

the sample. To process the powder, graphite tools are used because they can withstand the pressure at high temperatures, which means that the tools can be re-used.

The tools are made of two main parts, the graphite ring and the punches (top and bottom), as shown in Figure 3.1 (a, d). The punches have a hole in the middle to enable a pyrometer to measure the temperature close to the workpiece powder. For the graphite rings, the width of walls is critical as it defines the amount of pressure and powder that can be withstood, for that reason, the rings have to be checked before every run to ensure they are free from cracks. To avoid the powder sticking to the graphite tools, it is important to cover the punches and the ring with graphite foil, as shown in Figure 3.1 (b,c). In some cases, graphite discs were added between the punch and the powder with the aim of protecting the punches. In addition to this, before processing the powder, it is a requirement to add supports to make sure the pressure from the pistons is distributed homogenously across the punch. Furthermore, it is necessary to put a felt jacket around the graphite ring, for two reasons; (1) to protect the FAST vessel from the heat of the dies and (2) to retain the maximum amount of heat with the aim of reducing the amount of power required. For samples greater than 40 mm diameter, additional CFC plates have to be added between the supports and the pistons to optimise the current path; otherwise, the equipment would struggle to attain a high heating rate. Furthermore, the CFC plates act as a thermal insulator between the graphite tools and the rams, thus preventing the pistons from getting too hot. The CFC plates, the graphite supports and the felt jacket are shown in Figure 3.2 (b,c).

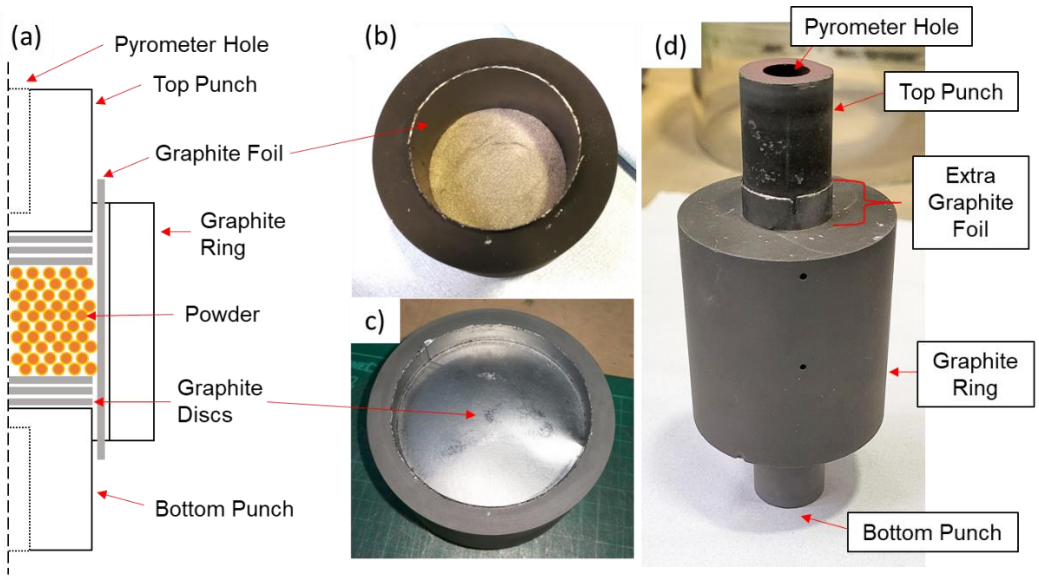


***Figure 3.1*** *– (a) A cross section schematic of the FAST process and part. The photograph of the moulds after (b) pouring the powder, (c) adding the three top graphite foils discs and (d) introducing the top punch.*

The steps followed to prepare a sample using FAST were always the same. First, the graphite foil was placed covering the interior face of the graphite ring, then the bottom punch was introduced into the ring until one quarter of the punch was inside. The next step was to introduce three graphite discs over the bottom punch to make sure no powder particle had direct contact with the tools. Before pouring the powder into the mould, it was necessary to calculate the amount of powder required to obtain a specific height in the final sample, which was done through Equation (3.1).

$$m = V\rho = h\pi r^2\rho \qquad \textbf{(3.1)}$$

Where $m$ is the mass of powder, $V$ the volume, $r$ is the radius of the tooling and $\rho$ represents the density of titanium powder, which is 4.4 g/cm$^3$. Most of the moulds had a cylindric shape, therefore, the volume can be calculated with $h\pi r^2$ where $h$ is the high of the final component. Although different powders have different levels of compaction, the final component is fully consolidated when processing with FAST. Consequently, the calculation in Equation (3.1) is a good approximation.

For multi-material components, a divider was introduced into the die before pouring the powder into the graphite mould. Once poured, the powder was flattened by tapping the graphite ring until the top surface was completely flat and then the divider was carefully

removed. Next, three graphite circles were added over the powder and the top punch was introduced until it touched the powder. To make sure the powder was well compacted, an initial pressure of 20 MPa was applied with a mechanical press. Once the supports and the felt jacket were added, the sample was positioned inside the FAST machine.

The final steps consisted of closing the vessel and uploading the recipe to the FAST machine control system with the required processing parameters. To reduce oxygen pick up in the workpiece, all the FAST runs were done under vacuum.

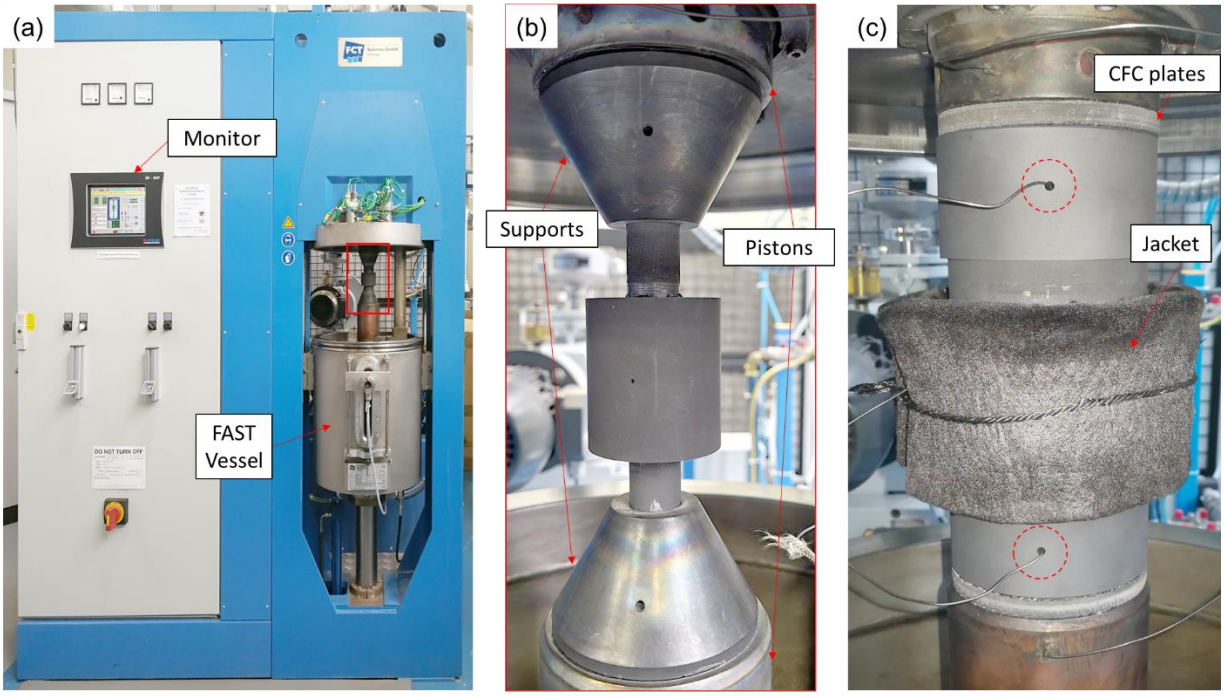


***Figure 3.2*** *– Photograph of (a) the FAST machine at the University of Sheffield, (b) the graphite tooling of a 20mm mould inside the FAST vessel and (c) the graphite tools for a 60mm mould inside the FAST vessel with the corresponding felt jacket and CFC plates.*

### *3.2.1. Small Scale FAST - General Method*

The work carried out at the University of Sheffield was done with an FCT Systeme GmbH SPS Furnace Type HP D 25, which is shown in Figure 3.2 (a). This machine can process samples up to 80 mm in diameter and a mass of 400 g of titanium powder. The temperature was measured with a pyrometer 3 mm away from the interface between the powder and the upper punch.

Polymeric dividers made with a 3D printer were used in order to produce the multi-material components. The most common divider shape employed was a cross, as shown in Figure 3.3

(a). The cross shape ensured that the divider could be removed in a 90° angle from the powder and as a result, the resultant bond will be a straight line. In more complex shapes, it was important to make sure the divider was touching the graphite walls to obtain a straight bond line. An example of a complex divider is shown in Figure 3.3 (b), which represents the Sheffield Titanium Alloy Research (STAR) logo. Figure 3.3 (c, d) shows the dissimilar titanium powders once the divider has been removed.

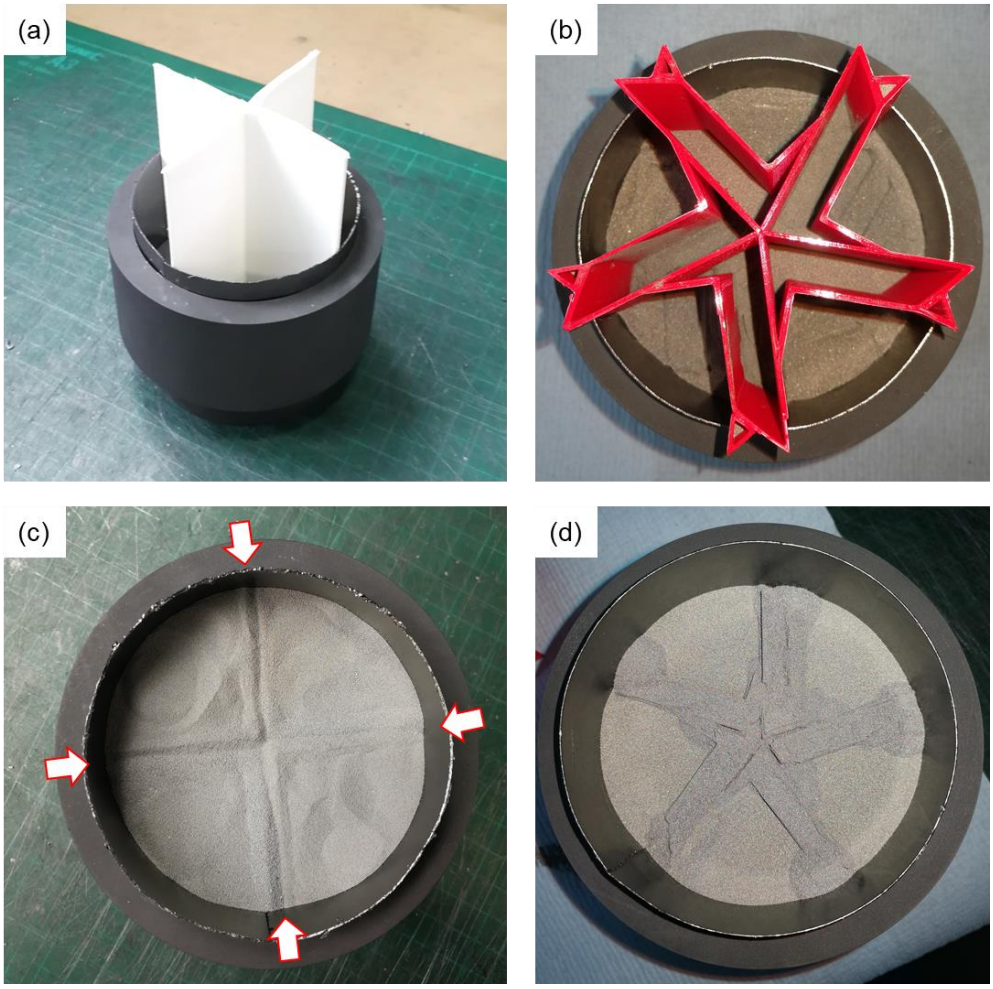


***Figure 3.3*** *– Photograph of the graphite tools while preparing the mould before and after removing the divider for (a, c) a cross shape divider and (b, d) the STAR logo divider.*

### *3.2.2. Large Scale FAST at Kennametal facility*

The 250 mm FAST billets were processed on the larger FCT System GmbH SPS Furnace Type H-HP D 250 at Kennametal UK Ltd., in Newport, South Wales, UK, which is shown in Figure 3.4. Although the machine is three stores high, the process to prepare and process the sample

was the same as the smaller FAST machine at the University of Sheffield, which is described in Section 3.2.1.

The dividers used for large samples were fabricated from aluminium instead of a 3D printed polymer because at the time of the experimentation it was not possible to 3D print a divider for a 250 mm mould. The main challenge with the aluminium dividers was to remove them at a 90° angle (without tilting) in order to maintain a straight bond. Figure 3.5 shows photographs of the aluminium divider inside the graphite ring.

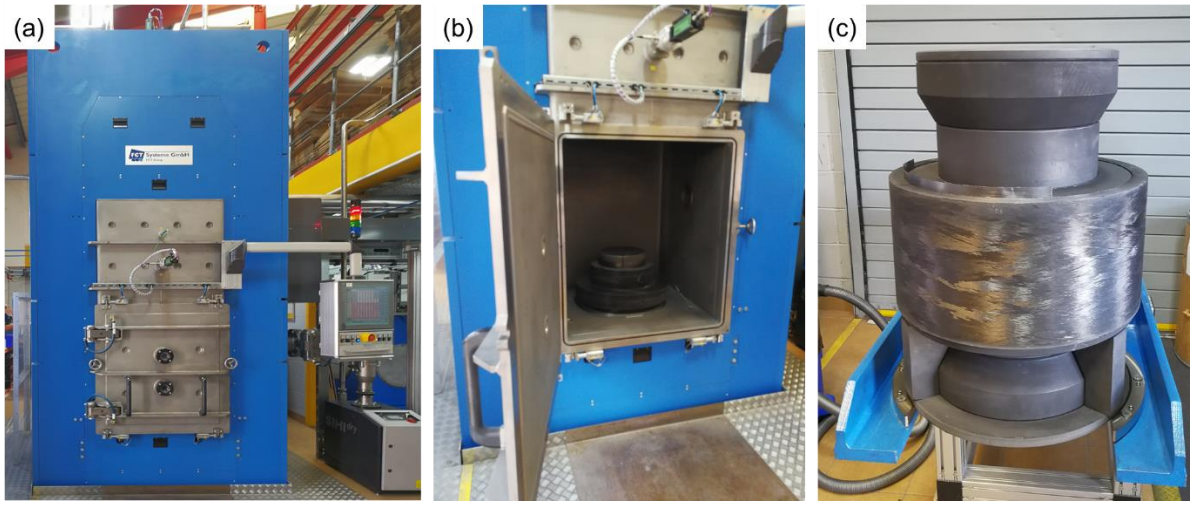


***Figure 3.4*** *– Photograph of the FCT Systems GmbH SPS Furnace Type H-HP D250 at Kennametal. (a) Photograph of the front of the machine, (b) photograph inside the FAST processing chamber with the bottom piston and (c) photograph of the graphite tool before processing it with FAST.*

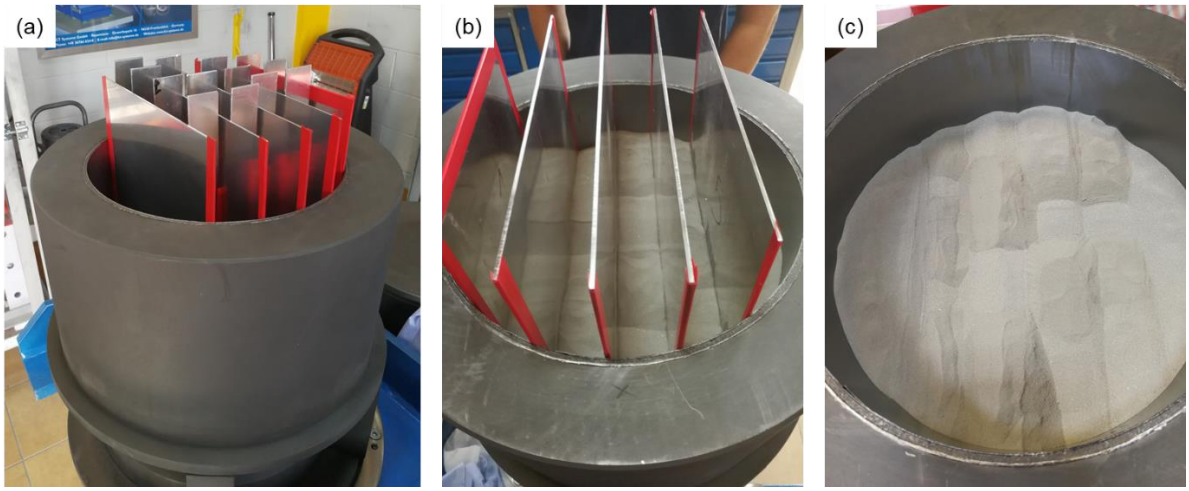


***Figure 3.5*** *– Photographs of (a,b) the aluminium dividers used for the 250 mm moulds inside the graphite ring and (c) the multiple powders inside the graphite ring after the dividers were removed.*

## 3.3. *Hot forging of FAST billets (*FAST-*forge)*

### 3.3.1. *FAST preforms*

The FAST-*forge* components were hot forged from preform bars made of two titanium alloys, Ti-6242 and Ti-64. The preforms were machined from a 250 mm FAST billet produced on the equipment described in Section 3.2.2. The FAST billet was processed at 970°C for 1 hour at a pressure of 32.5 MPa and it was left to cool down slowly inside the FAST chamber.

Figure 3.6 illustrates the process followed to obtain the multi-material preforms. Once the FAST billet was removed from the graphite tools (Figure 3.6 (a)), the top and bottom surface were machined to determine the exact position of the bond lines (Figure 3.6 (b)). Then, the preforms were wire-EDM'ed from the 250 mm billet and machined to obtain the final shape of the preforms, which were solid bars of 20 mm diameter (Figure 3.6 (c)). Additionally, in Figure 3.6 (c), it is depicted how the two titanium alloys were distributed inside the FAST billets together with the final preforms.

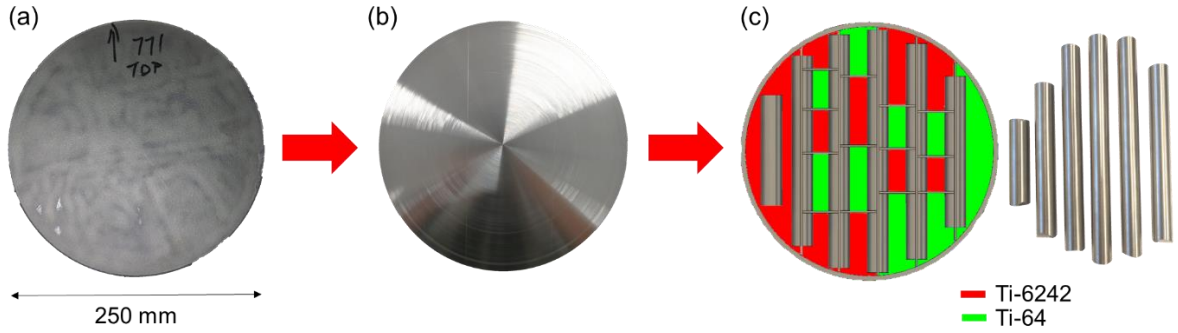


***Figure 3.6*** *– Image of the multiple steps required to machine hot forging preforms from FAST billets. (a) An image of the FAST billet after is removed from the graphite tools, (b) an image of the FAST billet after a face turning operation and (c) is an illustration of the FAST disc with the location of the preforms and the multiple alloys in combination of an image of the preforms.*

### 3.3.2. *Hot closed-die forging*

The closed-die hot forging was conducted at W.H. Tildesley, Wolverhampton, UK, on an industrially used Massey 1.1 MSC drop hammer forge with foot pedal control and 11 kJ blow energy. The preforms were heated with a gas furnace to a temperature below the β transus

and the dies were heated to minimise any die chilling effects. For the forging process, the dies were lubricated through intuition by the 40 year experienced forgemaster and a total of 3 to 4 blows were required to obtain the near-net shaped component. At the end of the forging process, the flash was crimped off and the components were water quenched. Figure 3.7 shows the equipment used for the forging trials, while Figure 3.8 shows the preform bar before and after one hammer blow as well as the final near-net shaped of the multi-material component.

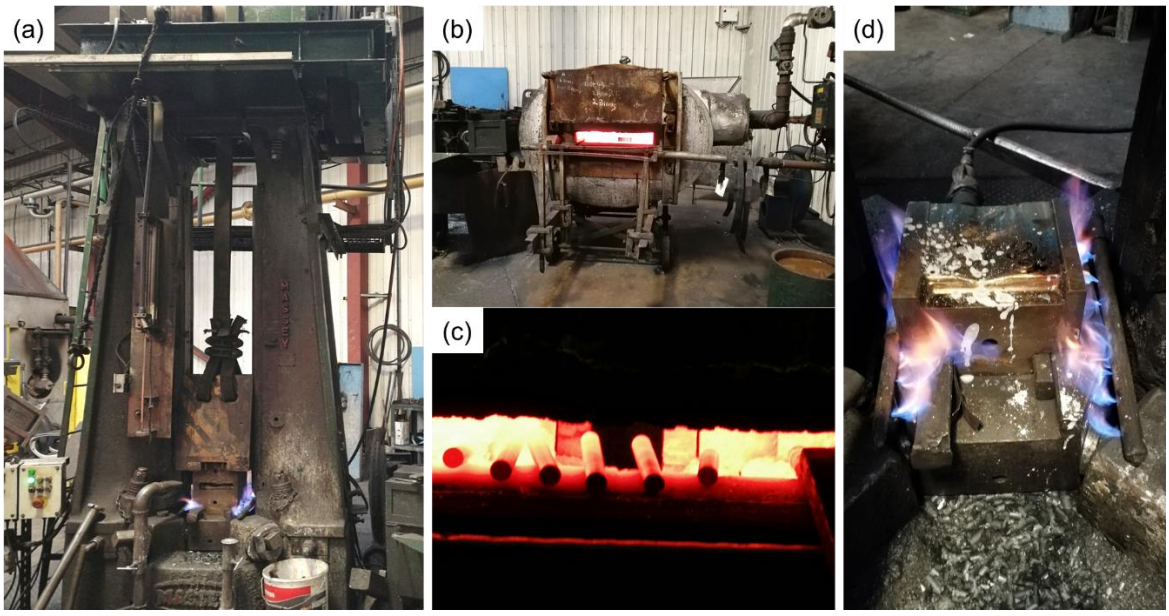


***Figure 3.7*** *– (a) Photograph of the industrially-used Massey 1.1 MSC drop hammer forge at W.H. Tildesley, (b) photograph of the gas furnace used to heat the preforms, (c) photographs of the preforms inside the gas furnace and (d) photograph of the dies used for the hot forging process.*

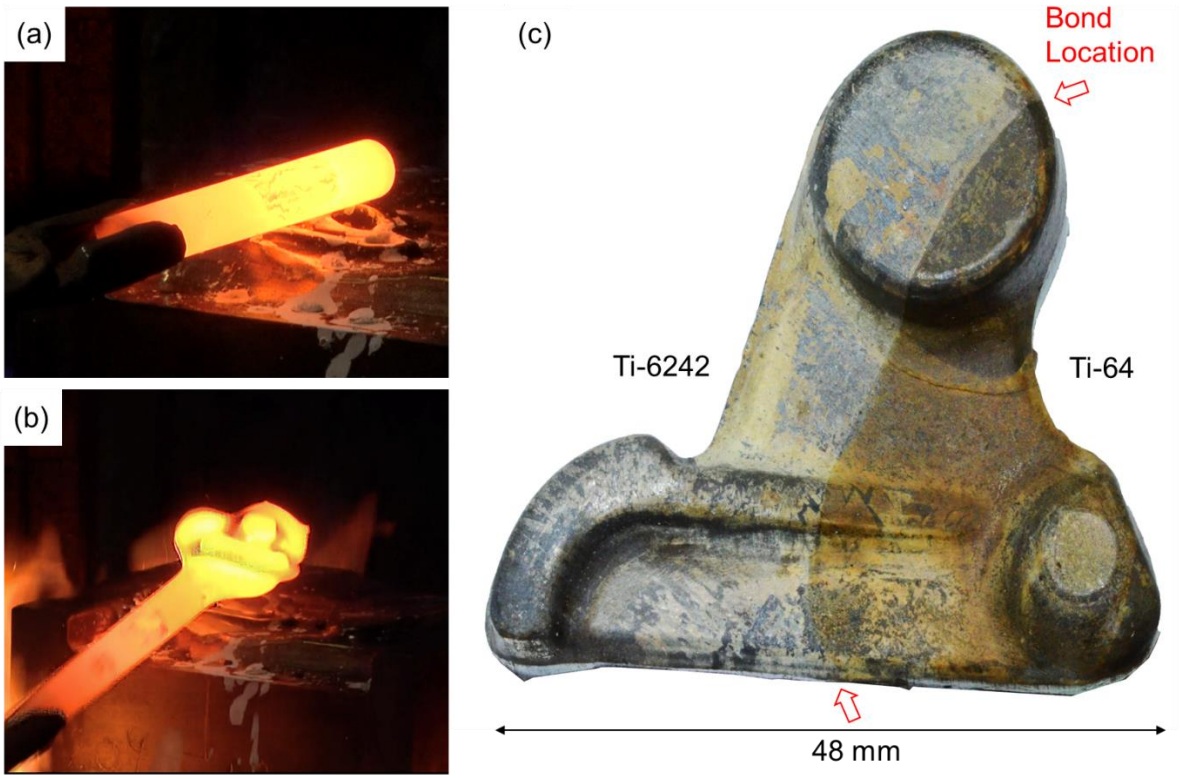


***Figure 3.8*** *– (a) Photograph of the preform before the first drop hammer blow, and (b) fractions of second after the first hammer blow. (c) A photograph of a final rocker arm near-net shaped component (adapted from* [153]*).*

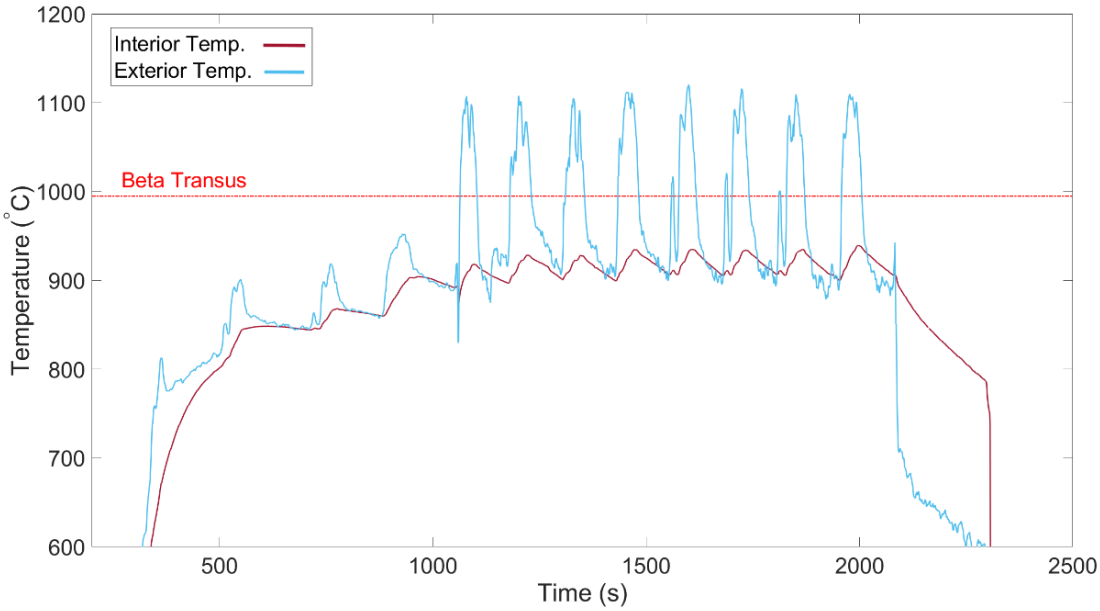


***Figure 3.9*** *– Graphs of the thermocouple measurements from the interior and exterior of the preform prior the forging process*

To monitor the temperature of the gas furnace, two thermocouples were fitted into the preform. The first thermocouple was located in one hole drilled in the surface of the preform and the second one was measuring the temperature of the surface. As shown in Figure 3.9, the temperature had a clear cycle and there was a significant difference between the measurement in the interior and at the exterior of the preform.

## *3.4. Mechanical Property Assessment*

### *3.4.1. Microhardness testing*

The hardness measurements across the bond were always conducted with at least 3 rows with 20 indentations in each and a dwell time for each indentation of 15 s, which is the ASTM E384 standard [161]. Each row crossed the bond diagonally, in order to evaluate more points in the proximity of the bond, as shown in Figure 3.10. The indents were spaced by 50 µm in the x-direction and 300 µm in the y-direction and the microhardness load was 9.81 kgf for all the samples with the exception of the bonds with CP-Ti which used a load of 1.962 kgf.

The distance from the indent to the bond was measured with the software ImageJ [162] from light micrograph mosaics obtained with a light microscope. However, this measurement was done manually for each point based on the microstructure observed in the micrographs. For dissimilar alloys with a significant change of chemistry, like the example in Figure 3.10 (a), this measurement was very consistent and the standard variation was less than 20 µm. However, for dissimilar alloys with finer microstructures, the measurement was more complicated because there was not a defined bond, like the example shown in Figure 3.10 (b). Therefore, in these cases, the standard variation was around 100 µm.

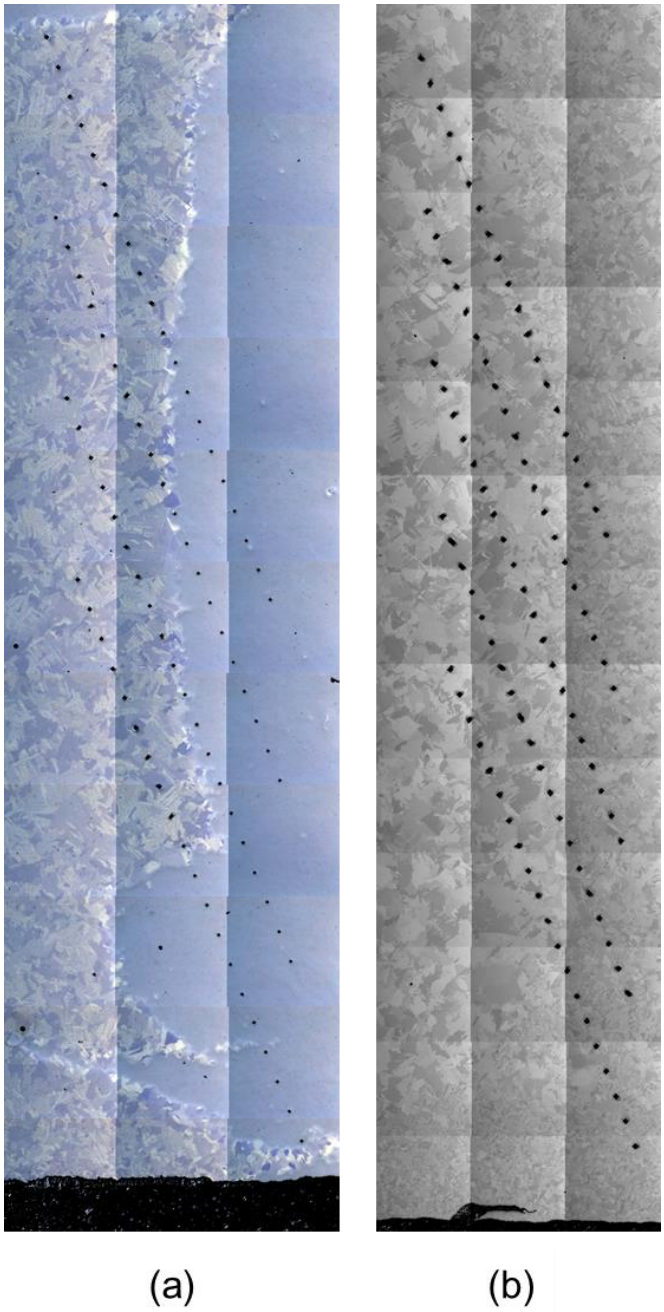


***Figure 3.10*** *– Light micrograph mosaics of the hardness indentations across the bond between (a) dissimilar titanium alloys and (b) similar titanium alloys.*

### *3.4.2. Tensile tests*

The tensile test specimens were machined to the final dimensions following the ASTM E8/E8M [163] specifications, which are shown in Figure 3.11. The initial FAST material for these samples were 250 mm diameters billets and the process to machine these samples was similar to that described in Figure 3.6. It was essential that the bond was located in the middle

of the sample and perpendicular to the tensile direction, to ensure equivalent tensile conditions for both alloys during the test. The tests were carried out at constant displacement and the strain was measured using an extensometer. Detailed information can be found in Section 5.2.3.

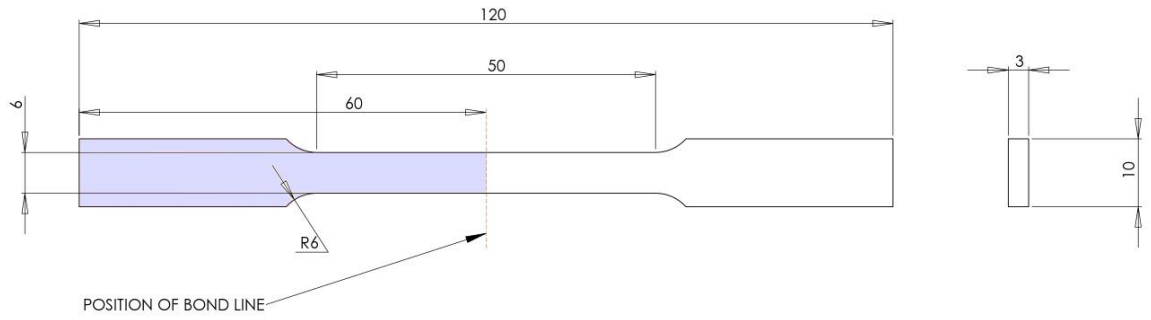


***Figure 3.11*** *– Technical drawing of the ASTM E8/E8M tensile specimen dimensions.*

### *3.4.3. Optical DIC test*

The optical digital image correlation (DIC) test consisted in using a light microscope to compare the initial microstructure of a bond, before and after applied strain. The microtester used for this test could not be positioned under the microscope, so the approach was to complete an interrupted test. The test started by using the light microscope to take micrographs of the sample, then, the sample was tested with the microtester up to a certain amount of strain. Finally, the sample would be unloaded and positioned in the optical microscope before starting the process described again. The samples had to be etched with hydrofluoric acid (HF) before testing, so features of the microstructure could be captured for the DIC analysis. A detailed description of the conditions and equipment used for this test can be found in Section 5.2.4.

The samples used for this test were machined with wire-EDM and machined to the dimensions shown in Figure 3.12. This design had a double gauge length in order to concentrate most of the strain in the bond region. To locate the bond and machine it in the correct position, it was required to follow the same process described in Figure 3.6.

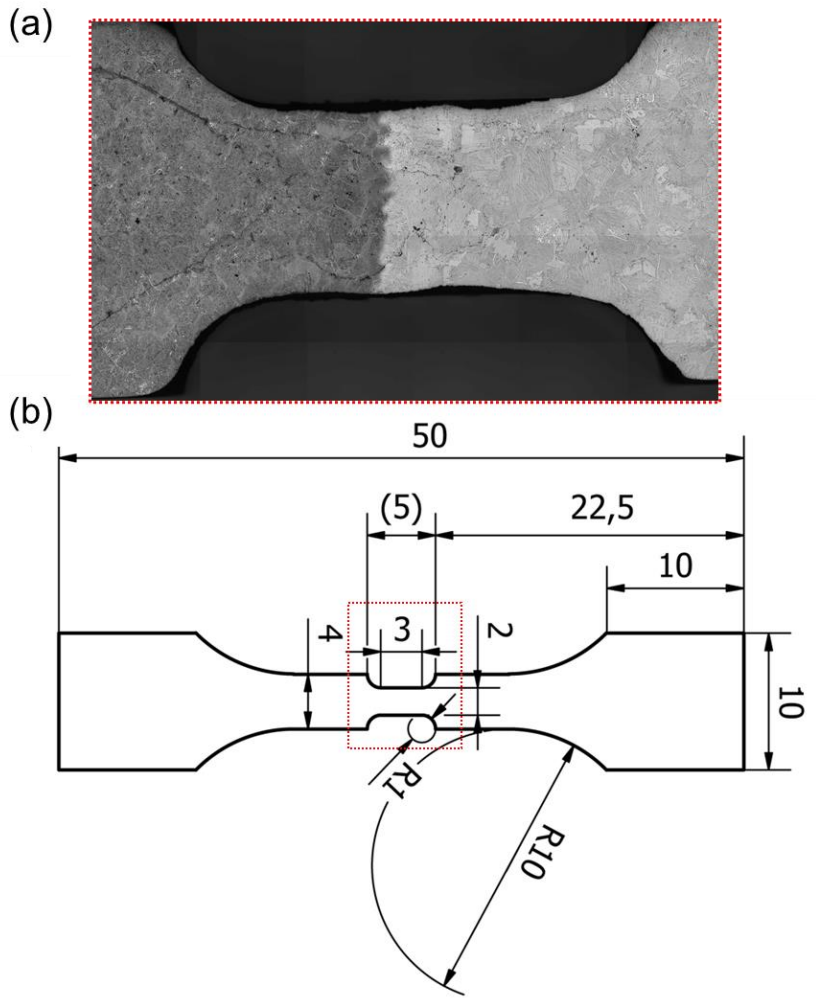


***Figure 3.12*** *– (a) Light micrograph of the bond in the DIC tensile specimen after etching it with HF. (b) Technical draw of the DIC tensile specimen dimensions.*

## *3.5. Material analysis*

### *3.5.1. Metallographic preparation*

The metallographic preparation of the samples analysed in this thesis was completed using the following procedure: -

First, most of the samples required sectioning before they could be hot mounted in Bakelite. There are two main machines used to section the samples: for long, rough cuts, a Buehler AbrasiMet benchtop was used, and for small, precise cuts, a Struers Secotom-20 was used. The samples were then hot mounted in conductive Bakelite with a Buehler SimpliMet and

ground with progressively finer grit SiC paper on a Struers Tegramin-25. Finally, the samples were polished with a solution made of 0.06 µm colloidal silica with 10% of hydrogen peroxide until the sample had a mirror finished surface.

### *3.5.2. Microstructural analysis*

To characterise the microstructure of the titanium alloys, light and scanning electron microscopes were employed. A Nikon Eclipse LV150 with cross polarized light was used to obtain microstructures of the titanium alloys. However, an Olympus Bx51 with the software Clemex Vision PE image analysis system was used to create mosaics. This microscope has an automated X,Y displacement table that reduced the amount of time required to obtain a mosaic. The FEI Inspect F50 SEM was used to obtain higher resolution micrographs.

The chemistry of the bond was measured with X-EDS point scans with a Philips XL30 SEM. The detector was first calibrated with a pure cobalt standard to obtain reliable quantitative data at each point. The points were linearly spaced perpendicular across the bond at a distance of 10-30 µm depending on the processing conditions of the sample. Each line scan had 15-20 points and a total of 3 scans in different locations were conducted for every sample. The dwell time for each point could vary between 1.5-2 minutes. This time was sufficient to obtain quality data without compromising processing time. The length of the scans was long enough to obtain the full diffusion profile for each bond. The data was then plotted using the MATLAB® software and the fitting of the points was obtained with the curve fitting app in the same software. Figure 3.13 shows an example of a typical point scan across the bond.

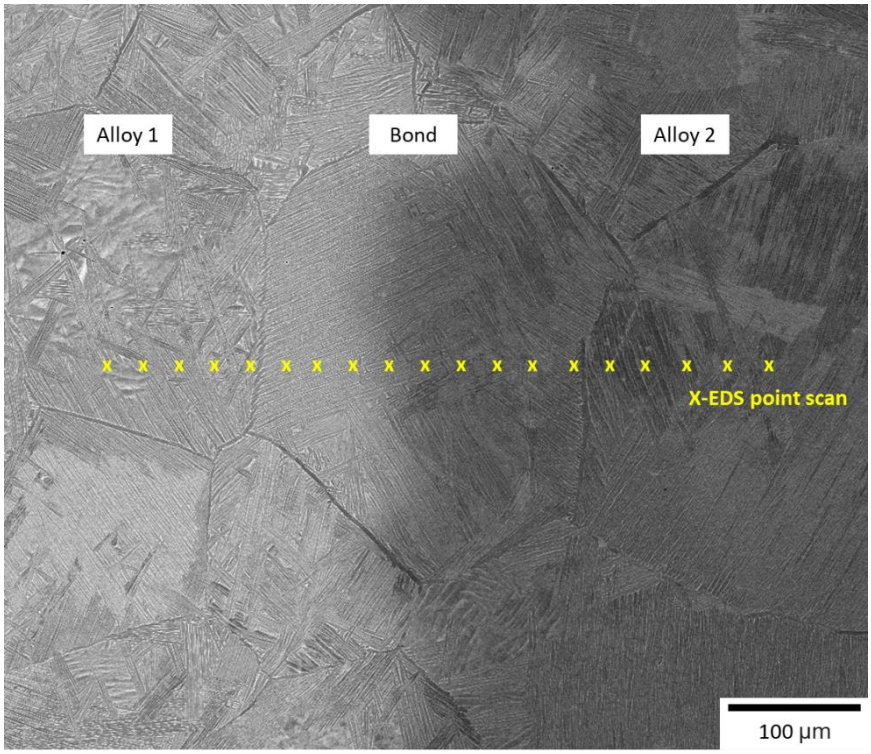


***Figure 3.13*** *– Backscattered micrograph of a FAST-DB bond with a X-EDS point scan across the bond.*

### *3.5.3. Powder analysis*

The powders used in this work were analysed with different methods. The particle size distribution (PSD) of the powder was measured with a Malvern Mastersizer 3000 laser diffraction particle size analyser with a wet dispersion method. Before starting the test, the equipment was flushed five times to avoid any potential contamination with powder of previous users. Then, a small amount of powder was added to a beaker with distilled water until the equipment had enough powder particles to make a measurement. A total of 20 measurements were performed and the final values for Dx10, Dx50 and Dx90 were the average of all these measurements.

The analysis of the external shape of the powder was done by sticking powder on carbon dots and taking micrographs in the SEM. It was important to blow compressed air over the carbon dot after sticking the powder to remove any loose powder and avoid damaging the microscope.

The study of the shape, microstructure and porosity of the powder was done by cold mounting the powder in epoxy resin. The process of cold mounting the powder consisted of

pouring the epoxy resin in a plastic measuring cup together with the titanium alloy powder and the resin hardener. Then, the mix was poured into a cold mounting mould and left under vacuum conditions for a few minutes until all the air bubbles were removed; finally, it was left to dry for at least 24h. Once the sample was ground and polished following the process described in Section 3.5.1, the sample was analysed under cross polarized light on the Nikon Eclipse LV150.

The shape and porosity measurements were performed with the Olympus Bx51 in combination with the software Clemex Vision PE image analysis system. This allowed the shape and porosity of the powder over large areas to be automatically measured. However, it had to be taken into account that a 2D surface of a 3D powder particle is being measured. Therefore, it was possible to have a similar situation to the one shown in Figure 3.14, where the measurements of three powder particles with the same diameter and shape are taken in different places. In addition to this, the automated software can have errors in the measurement, like the one shown in Figure 3.15, where after removing the particles from Figure 3.15 (b) that are at the edge of the micrograph, a region of 3 powder particles in Figure 3.15 (c) has also been removed. Consequently, those particles will have a lower aspect ratio and circularity than the real one.

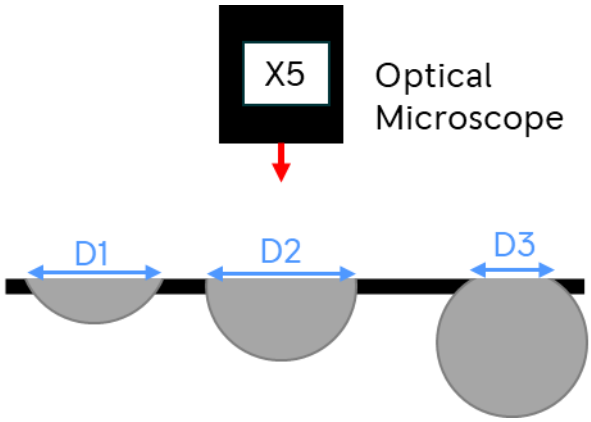


***Figure 3.14*** *– Illustration of the diameter measurements of the same powder particle with an optical microscope.*

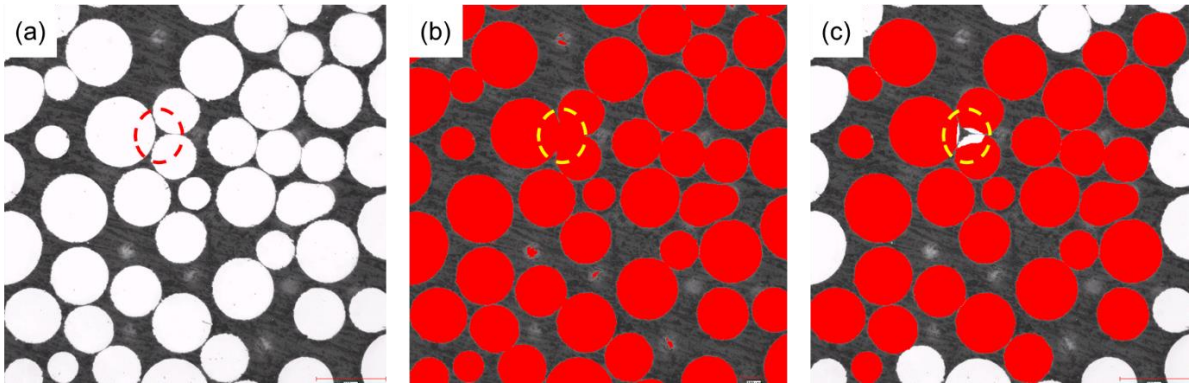


***Figure 3.15*** *– Images of the software Clemex Vision PE image analysis (a) before analysing the particles, (b) selecting all the particles in the images and (c) discarding the particles that are on the edge of the micrograph or have a smaller diameter than the threshold.*

## *3.6. Force Feedback*

The force feedback technique consists of measuring the reaction forces during a machining process to obtain the microstructural information of the sample being machined [164]. This is possible because the force produced in the interaction between the tool and the grain is dependent on the orientation of the grain, as shown in Figure 3.16. At the moment, this has only been achieved when machining flat surfaces; because machining none-flat surfaces would increase the difficulty to know the exact position of the tool.

For this work, the change of force during the machining process was measured with a dynamometer attached to the tool holder. Then, the force signal was processed through a code in MATLAB software (created by Daniel Suarez Fernandez and Oliver Levano Blanch) that positions the measurement of the force in the exact location measured.

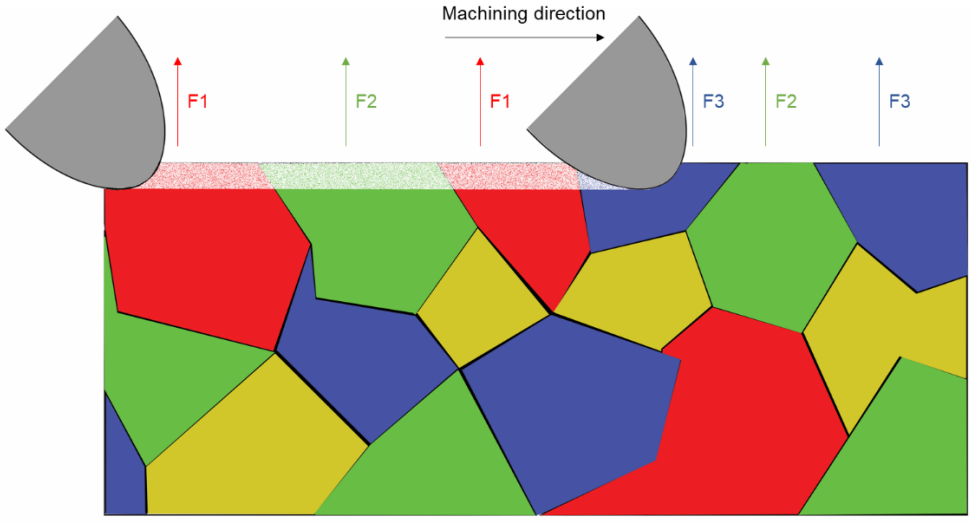


***Figure 3.16*** *– Schematic illustration of the force feedback technique showing how the force measured changes depending on the local orientation of the grain.*

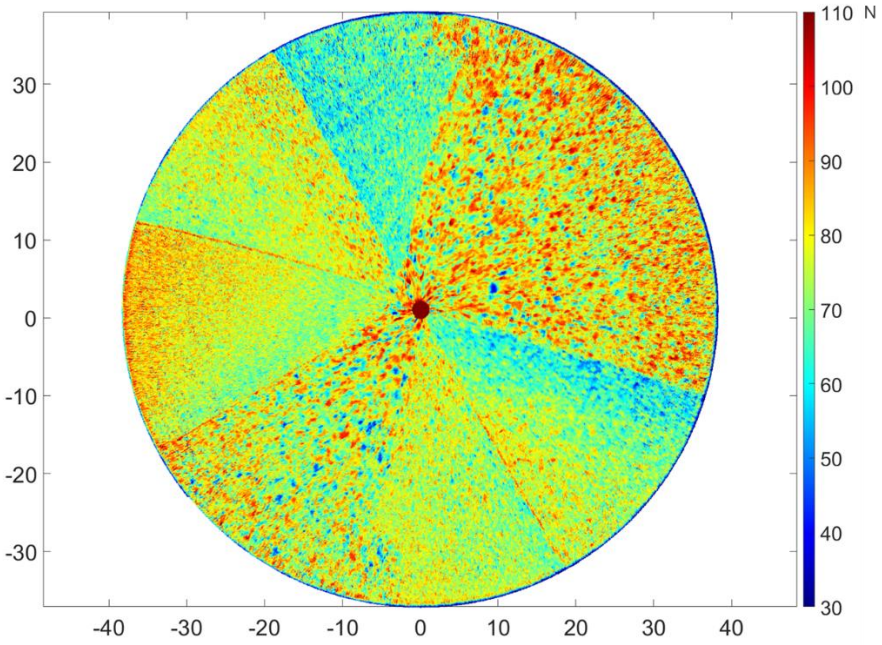


***Figure 3.17*** *– Force feedback plot of a multi-material component.*

The measurements of the cutting force across the bond were calculated by averaging the values of the forces parallel to the bond, as shown in Figure 3.18. From the microstructure 'fingerprint' map created in Figure 3.17, it is possible to extract a region containing only one bond with MATLAB. It is important to make sure the bond is parallel to our measurements, otherwise, the results could be affected. Once the bond is parallel to the axis, the average force was measured parallel to the bond in multiple location (N1, N2, N3, …., Nn) and plotted in a graph. The force points measured with the dynamometer were not distributed

homogeneously throughout the sample, so each Nn measurement is a bin of 100 µm thick that measures the average force of all the points inside that bin. The use of 100 µm bins had a good compromise between the resolution of the results and the noise generated.

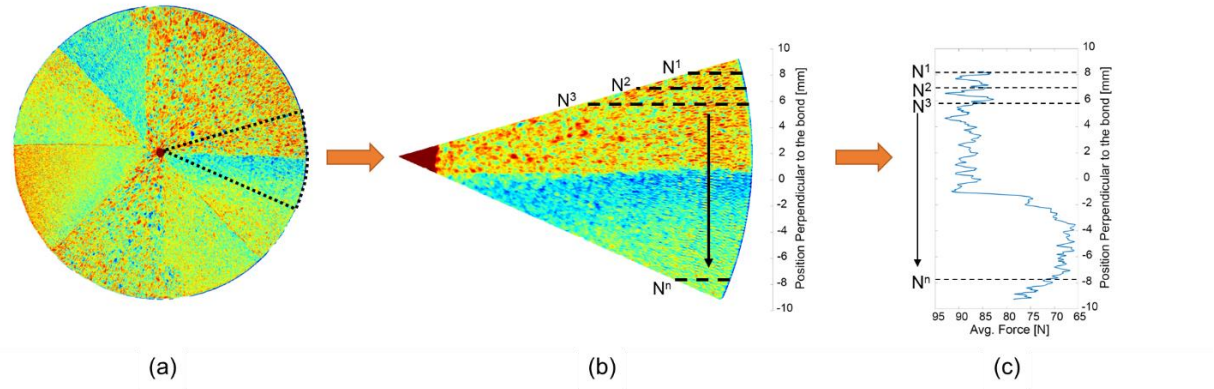


***Figure 3.18*** *– Image showing the process followed to measure the force across the bond. (a) Complete force feedback plot with a black dotted line selecting one region of the plot, (b) region extracted from the full plot with the corresponding measurements parallels to the bond and (c) is the final graph with the average forces measured from the extracted region.*

# 4. *Powder Characteristics*

## *4.1. Introduction*

This chapter introduces the different powders used in this thesis. It is important to understand the basic characteristics of the powder because they could affect the final microstructure and porosity of FAST material. It has been shown previously [165] that powder morphology is not critical during FAST consolidation: the effect of size and morphology can be nullified with a relative short dwell time above the beta transus. However, when the powder is processed below the beta transus, the powder morphology can influence the final microstructure of the material, as will be illustrated in Section 5.3.1.

In this thesis, a total of eight different titanium powders were used. This chapter presents the chemical composition of the powder, the particle size distribution (PSD), the morphology and the microstructure of the powders. Table 4.1 presents all the powders used in this thesis with the corresponding chapter in which they were used and their method of production.

## *4.2. Powder chemistry*

The chemistry of the powder used in this thesis is shown in Table 4.2. The table presents the elements in weight % and the chemical composition was measured by X-EDS, XRF (Bed Fusion) and LECO analysis. The chemical composition of this alloys can be compared with the ASTM B348/B348M – 19 [166]. Although this ASTM specification is used for solid components, it is a good approximation to the Rolls-Royce plc standards. The Ti-64 alloys used in the aerospace sector are considered Grade 23 because they should have a low wt. % of interstitial elements in order to improve the final ductility and the fracture toughness of the component. None of the Ti-64 powders comply with the ASTM B348/B348M – 19 [166] because only a maximum wt. % of 0.25 Fe and a maximum wt. % of 0.13 O are allowed. However, both alloys would comply with the specifications of standard Grade 5 Ti-64.

***Table 4.1*** *– Summary of the powders used in the thesis with their corresponding production method and featured chapter.*

| Powder | Type of Powder | Featured Chapter |
|---|---|---|
| **Ti-64_1** | PREP | Chapter 5 |
| **Ti-64_2** | PREP | Chapter 5, 6 and 7 |
| **Ti-6242_1** | EIGA | Chapter 5 |
| **Ti-6242_2** | EIGA | Chapter 6 and 7 |
| **CP-Ti** | HDH | Chapter 6 and 7 |
| **Ti-3-2.5** | HDH | Chapter 7 |
| **Ti-5553** | EIGA | Chapter 6 and 7 |
| **Beta C** | EIGA | Chapter 7 |

The titanium alloys CP-Ti, Ti-3-2.5 and Beta C comply with their corresponding Grade 1, Grade 9 and Grade 19 specifications [166]. The specifications for the Ti-6242 alloys are compared with the AMS 4919J standards [167]. The composition for Ti-6242_2 complies with the AMS 4919J standard but Ti-6242_1 does not comply with the standard because it has a Si content less than 0.06 wt. %. The Ti-5553 was compared with the Boeing Material Specification [168] and it was slightly out of specification because the O content was above 0.18 wt. %. This material was gas atomized from a landing gear section supplied by Safran landing Systems; hence, it is likely that the increase in oxygen occurred during the atomization stage [169].

Although some powders do not comply with the standards, it should not affect the results presented in this thesis. As mentioned in Section 1.2, the aims for this project are to further understand the diffusion bond between dissimilar titanium alloys. This has been successfully achieved with the powders named above.

## 4.3. Powder Particle Size Distribution (PSD)

The PSD was measured with a Malvern Mastersizer 3000 laser diffraction particle size analyser with a wet dispersion method as described in Section 3.5.3. The average statistical values are summarized in Table 4.3 and plotted with the volume density distribution in Figure 4.1.

***Table 4.2*** *– Chemical composition of titanium powder alloys used in this thesis.*

| Powder | Ti | Al | V | Sn | Zr | Mo | Cr | Fe | Si | C | S | O | N | H |
|---|---|---|---|---|---|---|---|---|---|---|---|---|---|---|
| **Ti-64_1** | Bal | 6.1 | 3.8 | - | - | - | - | 0.26 | - | 0.028 | 0.01 | 0.163 | 0.019 | 0.0029 |
| **Ti-64_2** | Bal | 6.0 | 3.6 | - | - | - | - | 0.16 | - | 0.023 | 0.01 | 0.181 | 0.003 | 0.0032 |
| **Ti-6242_1** | Bal | 5.7 | - | 2.2 | 4.3 | 2.2 | - | <0.05 | <0.05 | 0.04 | 0.01 | 0.118 | 0.008 | 0.0019 |
| **Ti-6242_2** | Bal | 5.6 | - | 1.8 | 4.4 | 1.9 | - | 0.05 | 0.09 | 0.07 | 0.01 | 0.148 | 0.002 | 0.0021 |
| **CP** | 99.7 | - | - | - | - | - | - | <0.05 | - | 0.005 | 0.001 | 0.143 | 0.003 | 0.0151 |
| **Ti-3-2.5** | Bal | 3.3 | 2.2 | - | - | - | - | <0.05 | - | 0.015 | 0.001 | 0.190 | 0.003 | 0.0105 |
| **Ti-5553** | Bal | 5.0 | 5.2 | - | - | 5.1 | 2.7 | 0.39 | - | 0.015 | 0.002 | 0.203 | 0.016 | 0.0033 |
| **Beta C** | Bal | 3.5 | 7.9 | - | 4.3 | 4.6 | 5.4 | <0.05 | - | 0.004 | 0.002 | 0.092 | 0.018 | 0.0022 |

Figure 4.1 shows the volumetric distribution for the titanium powder; it is clear that there are two different types of PSD distributions. The first type of powders shows a typical normal distribution like the ones produced by Ti-6242_1, Ti-6242_2, Ti-64_2 and CP-Ti powder in Figure 4.1 (b, c, d, e). The second type of distribution has a log normal distribution in which the volume density continues up to 650 µm due to a small amount of very large powder particles. This is the case for Ti-64_1, Ti-3-2.5, Ti-5553 and Beta C powders in Figure 4.1 (a, f, g, h).

***Table 4.3*** *– Average statistical PSD values of titanium powder alloys.*

| Powder | Dx (10) (µm) | Dx (50) (µm) | Dx (90) (µm) |
|---|---|---|---|
| **Ti-64_1** | 93.3 | 160 | 299 |
| **Ti-64_2** | 61.3 | 86.7 | 123 |
| **Ti-6242_1** | 93.5 | 113 | 137 |
| **Ti-6242_2** | 25.2 | 37.4 | 53.7 |
| **CP-Ti** | 50.5 | 99.4 | 181 |
| **Ti-325** | 39.8 | 115 | 246 |
| **Ti-5553** | 20.7 | 57.2 | 140 |
| **Beta C** | 42.3 | 124 | 292 |

## *4.4. Powder morphology*

The shape of the powder can influence its consolidation in the initial stages of the powder processing and the final microstructure [165,170]. The measurements of the aspect ratio and the circularity of the powder can be characterised using the software Clemex, as explained in Section 3.5.3.

The aspect ratio defines the general form of the powder. According to the ISO 9276-6 [171], the aspect ratio is the ratio between the shortest and the longest Feret's of the powder particle and can be calculated using Equation (4.1). The maximum and the minimum Feret's are defined as the furthest and shortest distances between two parallel tangents in the particle. The Feret's for three shapes are shown in Figure 4.2. The circularity represents the degree of similarity between the powder particle and a perfect circle; ISO9276-6 [171]defines the circularity with Equation (4.2).

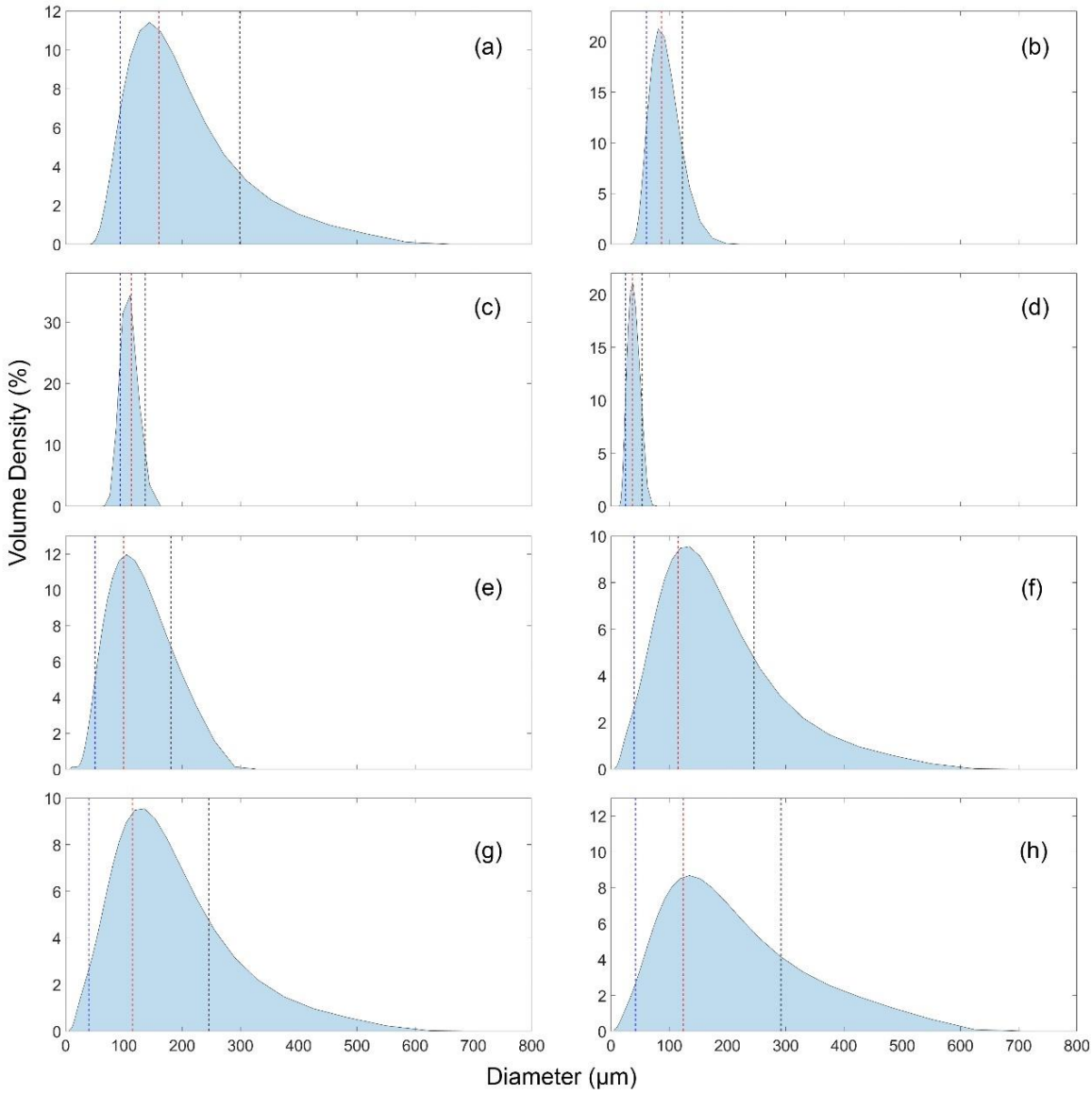


***Figure 4.1*** *– Volumetric distribution of titanium alloy powder. (a) Ti-64_1; (b) Ti-64_2; (c) Ti-6242_1; (d) Ti-6242_2; (e) CP-Ti; (f) Ti-3-2.5; (g) Ti-5553; (h) Beta C.*

$$Aspect\ Ratio = \frac{Fe_{min}}{Fe_{max}} \tag{4.1}$$

$$Circularity = \sqrt{\frac{4 * \pi * Area}{(P)^2}} \tag{4.2}$$

Where $Fe_{min}$ and $Fe_{max}$ represents the minimum and the maximum Feret's of each powder particle and $P$ represents the perimeter of the powder particle. Both parameters are

dimensionless and measure their values from 0 to 1, where 1 represents the highest value and 0 the lowest value. For the circularity, a value of 1 would mean that the particle is a perfect circle. This is shown in Figure 4.2, where the circular dashed line represents a perfect circle with the same area than the particle. For the aspect ratio, a value of 1 would mean that all the Feret's in the powder particle are the same and the particle is perfectly sphere. This is shown in Figure 4.2 where the minimum and maximum Feret's of the particles are plotted in blue and black, respectively. Overall, the aspect ratio effectively measures the elongation of the particle while the circularity quantifies the surface roughness of the particle.

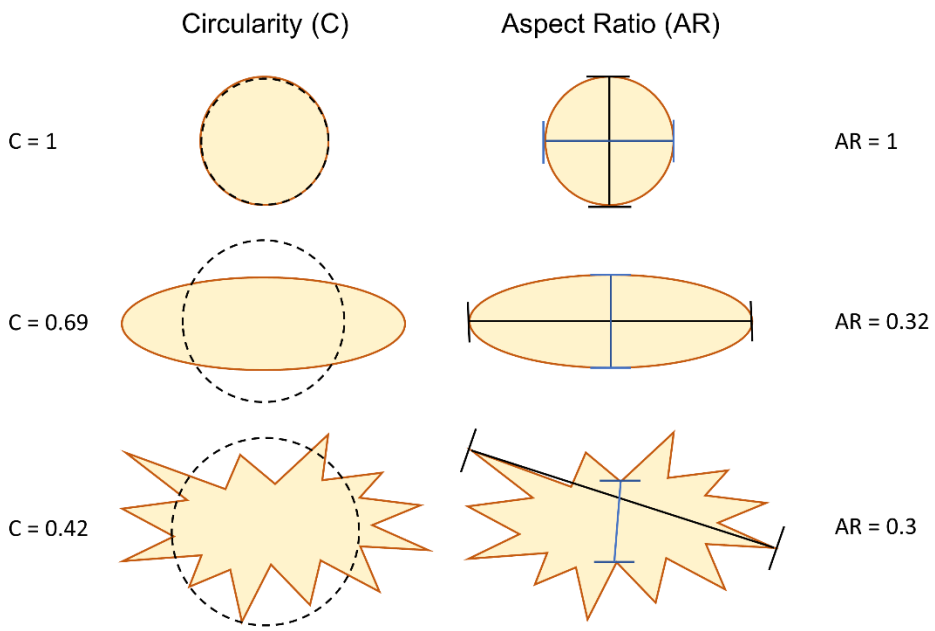


***Figure 4.2*** *– Illustration of three particles with their value numerical value of circularity and aspect ratio; the equivalent perfect circle in dashed lines and their longest and shortest Feret's line marked in black and blue respectively.*

Density maps of the circularity and the aspect ratio for the powders used in this thesis have been plotted in Figure 4.3. There are three main types of density distributions that correlate well with the three methods used to make these powders. The first type of distribution is formed by powder produced with the PREP process (Figure 4.3 (a, b)): both powders have concentrated density regions with values close to values of 1 for aspect ratio and circularity, which means that these powders are spherical powders with a smooth surface roughness. The second type of distribution is formed by powders produced with the EIGA process (Figure 4.3 (c, d, e, f)). These powders still have the highest density region with values close to 1 for the circularity and aspect ratio but the powder is more scattered compared to PREP powder;

there is a higher percentage of particles that have lower circularity and aspect ratio. Finally, the last type of distribution is formed by powder produced from the HDH process. These types of powder tend to have low circularity and aspect ratio as shown in Figure 4.3 (g, h), where the particles of these powders have a wide probability distribution.

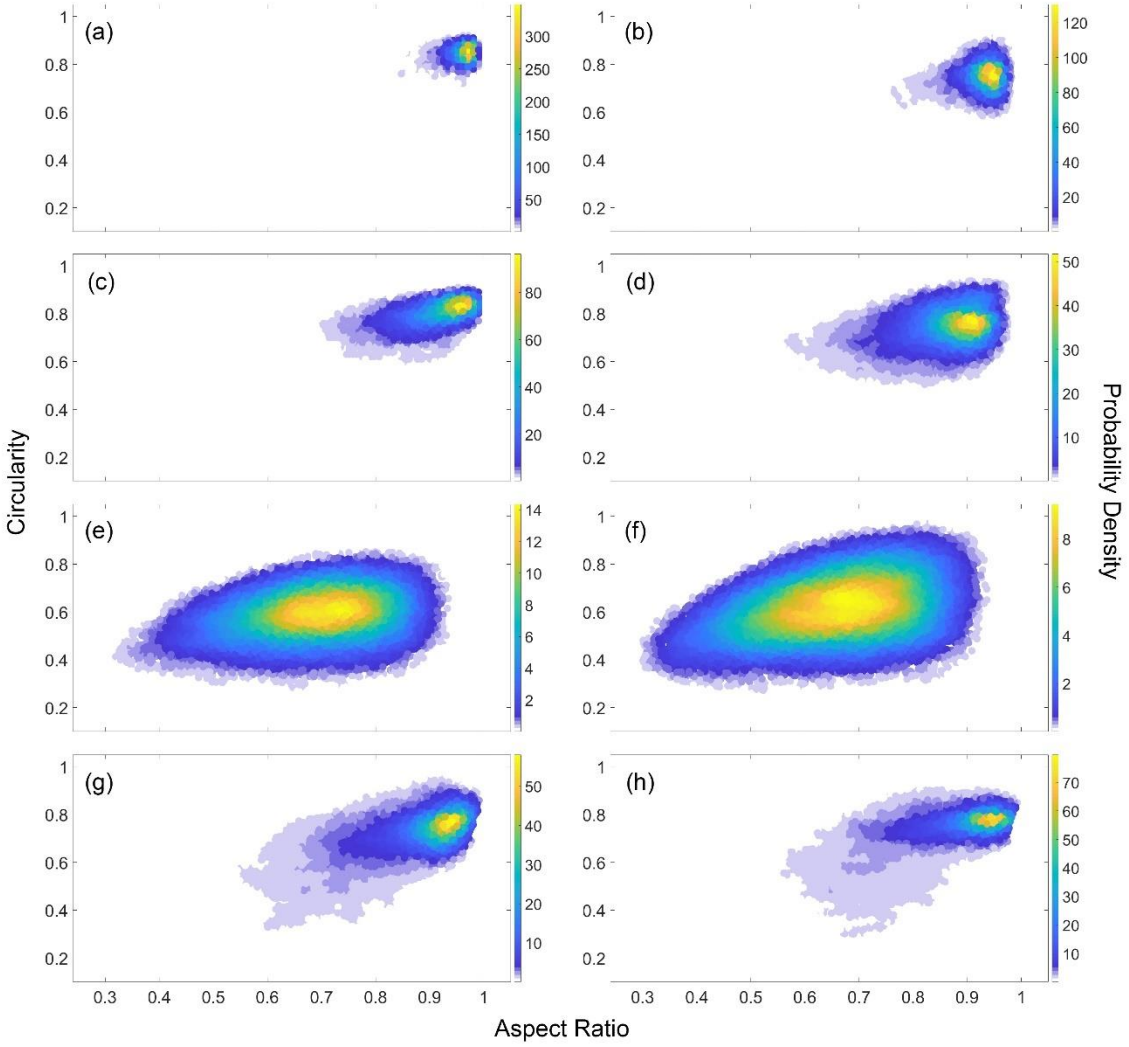


***Figure 4.3*** *– Probability density distribution of circularity and aspect ratio for titanium alloy powders. (a) Ti-64_1; (b) Ti-64_2; (c) Ti-6242_1; (d) Ti-6242_2; (e) CP-Ti; (f) Ti-3-2.5; (g) Ti-5553; (h) Beta C.*

The results presented in Figure 4.3 can be correlated with the SEM micrographs from Figure 4.4. The PREP powder shown in Figure 4.4 (a, b) have very spherical morphologies and the surface of the particles seems very smooth with very few satellite particles. In a similar way, the EIGA powder in Figure 4.4 (c, d, e, f) also has a spherical shape, but numerous particles with satellites fused to the surface are also observed. Finally, the HDH powder is completely different to the PREP and EIGA powder, it has an angular shape with a rough surface.

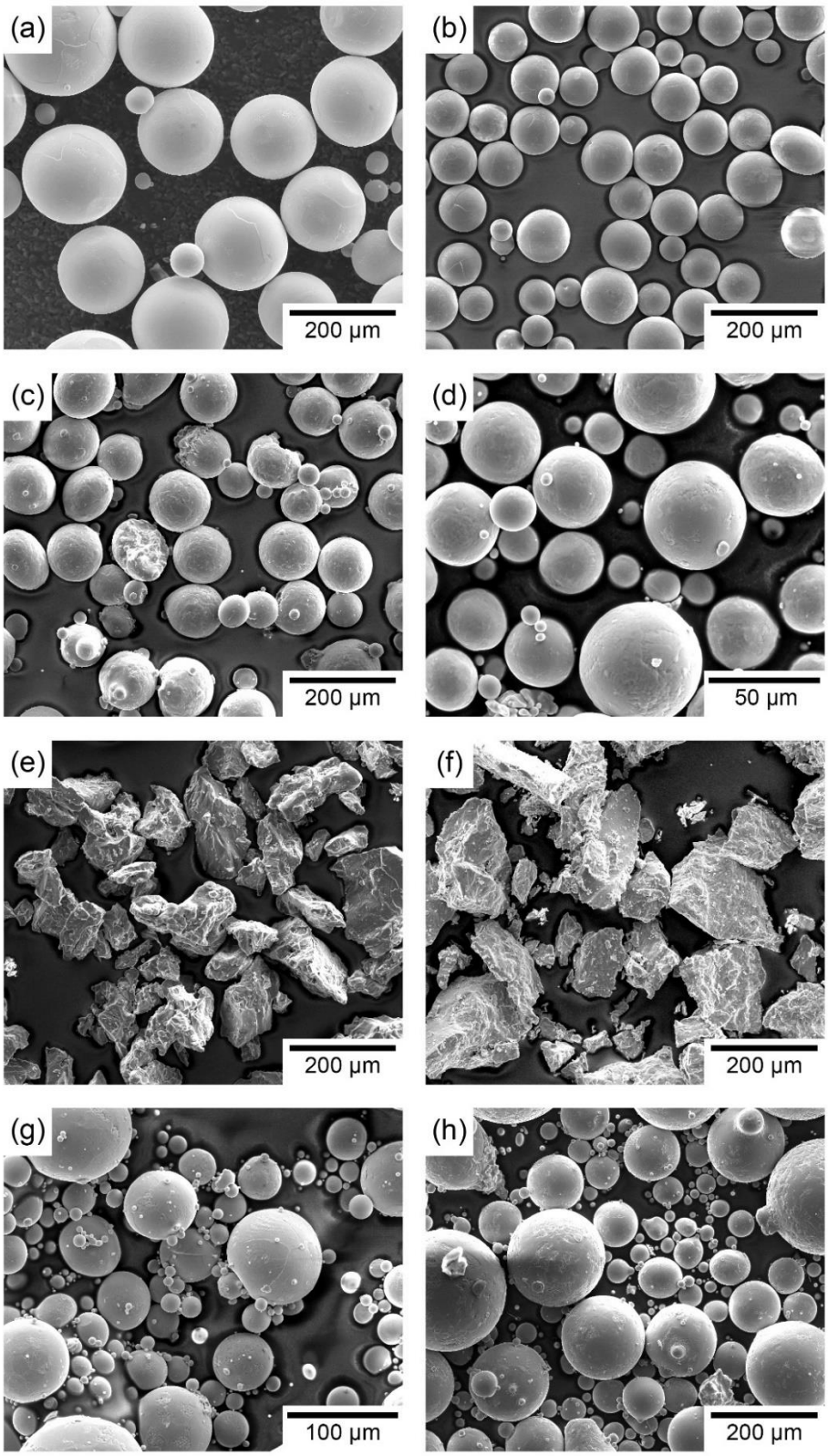


***Figure 4.4*** *– SEM micrographs of titanium alloy powders external surface. (a) Ti-64_1; (b) Ti-64_2; (c) Ti-6242_1; (d) Ti-6242_2; (e) CP-Ti; (f) Ti-3-2.5; (g) Ti-5553; (h) Beta C.*

It is important to mention that the Ti-6242_1 powder was recycled powder from the additive manufacturing (AM) process. Therefore, there were some defects in the powder introduced

during the AM process that were consolidated into the final FAST billets. A typical defect from AM is shown in Figure 4.5, which consists in the formation of fused powder that binds together to create a larger particle that can reach a few millimetres in size; like the particles shown in Figure 4.5 (a). Figure 4.5 (b) shows the same defect at higher magnifications and reveals that these large particles are formed of smaller powder particles fused together. Another common defect of recycled AM powder is that the O and C contents increase [172], which could reduce the mechanical properties of the final part [173]. However, this is not the case with this powder because the level of O and C are within the specification, as is shown in Table 4.1.

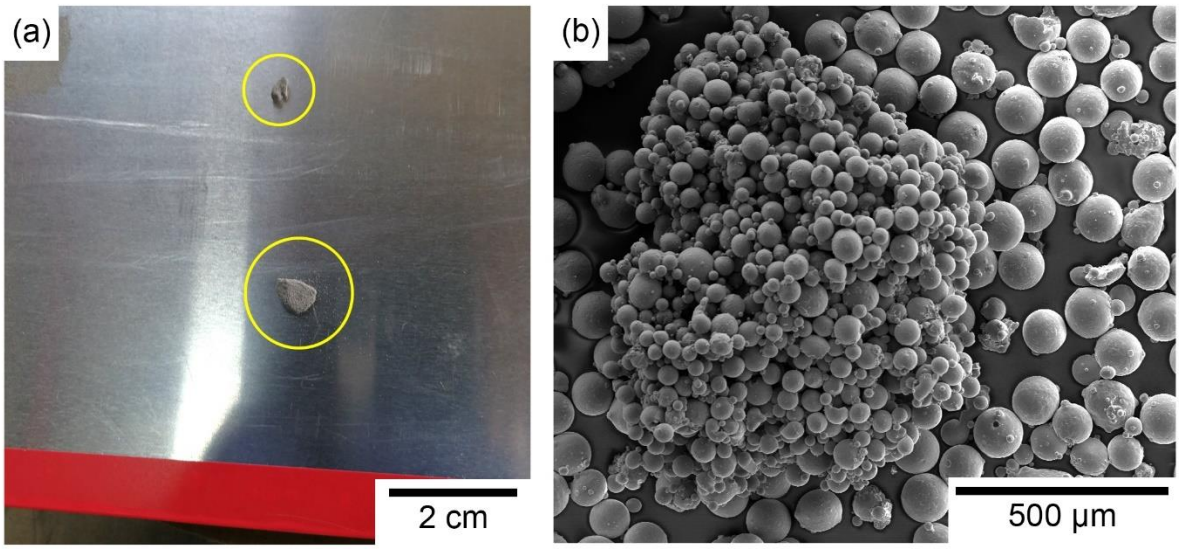


***Figure 4.5*** *– (a) Photo of typical defects produced by AM in Ti-6242_1 powder. (b) High resolution SEM micrograph of the defect in (a).*

## *4.5. Powder microstructure*

The microstructure of the powders is shown in Figure 4.6; the micrographs were taken using cross polarised light with the exception to the beta and near beta alloys in Figure 4.6 (g, h), which were taken under the SEM. The microstructure of the PREP and EIGA powder is a martensitic in nature, with a needle-like morphology in the powder in Figure 4.6 (a, b, c, d). This microstructure is produced because of the rapid cooling rate generated during the production of this powder. For EIGA process the cooling starts at 320 °C/s for large particles (>200°C/s) and can reach up to 11000°C/s for small powder particles (<38 µm) [174]. For PREP

process the cooling rate is quick but not as quick as EIGA process, it tends to be in order smaller than 100°C/s [175]. The CP-Ti and Ti-3-2.5 HDH powder has a microstructure formed of α equiaxial grains for both alloys as is shown in Figure 4.6 (e, f). The grains formed in CP-Ti are much larger than the ones formed in Ti-3-2.5. The beta alloys consist of retain β grains for both alloys, however, the grains in the Beta C alloy (Figure 4.6 (h)) are smaller than the Ti-5553 powder (Figure 4.6 (g)).

## *4.6. Powder porosity*

The porosity of the powders was also measured with the Clemex software and the results are presented in Table 4.4. In general, the porosity of the powders was relatively low with the highest value of porosity measured in the EIGA Ti-6242_1 powder with a total of 0.475% of area porosity; the lowest level was in the PREP Ti-64_1 powder with a total of 0.052% area porosity. Furthermore, the powder that had a major number of powder particles with pores was the HDH CP-Ti powder while the one with a smaller number of particles with pores was the Beta C powder.

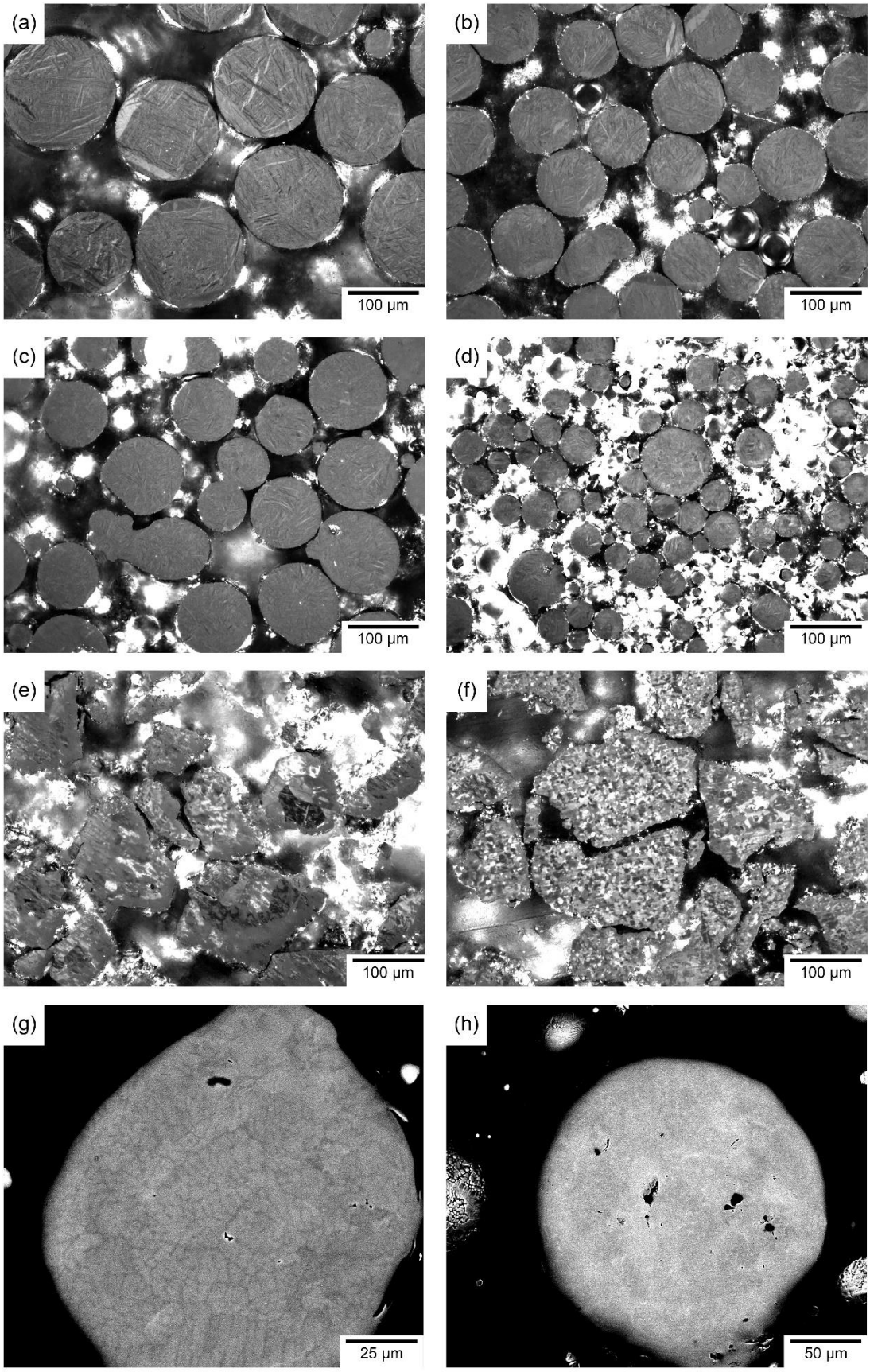


***Figure 4.6*** *– SEM micrographs of titanium alloy powders external surface. (a) Ti-64_1; (b) Ti-64_2; (c) Ti-6242_1; (d) Ti-6242_2; (e) CP-Ti; (f) Ti-3-2.5; (g) Ti-5553; (h) Beta C.*

***Table 4.4*** *– % of porosity measured in the titanium powders regarding the number of particles with pores and the % of area that represents the porosity.*

| Powder | % Particles with pores | % Porosity (Area) | Particles Measured |
|---|---|---|---|
| **Ti-6242_1** | 16.11 | 0.475 | 10,336 |
| **Ti-6242_2** | 12.18 | 0.328 | 20,664 |
| **Ti-6242_3** | 5.78 | 0.062 | 90,155 |
| **Ti-64_1** | 11.02 | 0.052 | 7,279 |
| **Ti-64_2** | 16.68 | 0.071 | 54,374 |
| **Ti-325** | 8.45 | 0.081 | 59,603 |
| **Ti-5553** | 5.85 | 0.152 | 46,207 |
| **CP-Ti** | 19.71 | 0.292 | 44,344 |
| **Beta C** | 4.59 | 0.256 | 23,884 |
| **Ti-6246** | 6.06 | 0.196 | 30,575 |

# 5. *Deformation Behaviour of a FAST Diffusion Bond Processed from Dissimilar Titanium Alloy Powders*



## *5.1. Introduction*

Titanium alloys are widely used in the aerospace sector due to their high strength-to-weight ratio, corrosion resistance and ability to operate at relatively high temperatures [4,12,16,20]. For example, 25-30% of the weight of a gas turbine aero-engine is made up of titanium alloys such as Ti-6Al-4V (Ti-64), Ti-6Al-2Sn-4Zr-2Mo (Ti-6242) and Ti-6Al-2Sn-4Zr-6Mo (Ti-6246) [4]. One of the issues with manufacturing in titanium, that restricts it largely to the aerospace sector is the high processing cost and the high Buy-to-Fly ratio (BTF), which can exceed 10:1 [5]. Aerospace titanium alloy components used in demanding environments require a good combination of creep and fatigue resistance, yet are designed and manufactured from a single titanium alloy with a similar microstructure and set of properties in different subcomponent regions. The performance of titanium components could be improved by using a tailored creep resistant or fatigue resistant titanium alloy in defined subcomponent regions. The ability to manufacture a component with dissimilar alloys in site-specific, subcomponent regions would enable designers to optimise the performance of titanium forged components. The greatest challenge for materials engineers is to determine the appropriate technology

(and whether it exists) to reliably join both alloys and to ensure that the bond does not compromise the structural integrity of the component. Additionally, there is a drive to move towards near-net shape manufacturing with low material wastage in order to reduce the excessive BTF of titanium aerospace parts.

An ideal candidate to create a near-net shape multi-titanium alloy component and reduce the BTF value is the solid-state powder consolidation technology known as spark plasma sintering (SPS) or field assisted sintering technology (FAST). FAST uses pulsed electrical current and mechanical pressure through graphite dies to fully consolidate powder into a shaped part. Dissimilar powders can be distributed into the mould with a degree of accuracy to obtain the multi-alloy components with alloys in site-specific regions. The advantages of FAST, in relation to conventional techniques, is that it can retain small grain sizes due to the high heating rates obtained with the Joule heating effect and it requires lower temperatures and dwell times to obtain a fully consolidated part [70,77,80,176]. There are three multi-physical parameters involved in the FAST process: electric current, voltage and pressure [176]. It has been observed that the electric current improves metal powder densification by the electromigration phenomenon, yet temperature still has the most dominant effect on densification [177]. Trzaska et al [178] also observed enhanced densification during the FAST of metal powders due to high dislocation densities and diffusion rates at interparticle contact regions. Additionally, previous studies have demonstrated an enhancement in diffusion when pulsed current is used [88,89]. In 2014, a short review by Kelly and Graeve [74], concluded that FAST/SPS was cheaper than conventional powder metallurgy processes such as hot pressing (HP). Since then, FAST has been shown to be capable of creating shaped parts in one step [114–116,179] or can be combined with hot forging to obtain near-net shaped parts with as-forged properties in two steps (and termed FAST-*forge*) [10,104,108,153]. Using FAST provides sustainable processing opportunities; titanium alloy powder and waste particulates (such as machining swarf) can be fully consolidated into pre-forging billets or final parts in one or two solid-state steps. This could lead to significant cost reductions in titanium alloy component manufacture compared to the conventional multi-step route [76].

To date, the diffusion bonds obtained using FAST produce a graded transition region between titanium alloys of the order of 300-500 μm [9] with the advantage that there is no resultant heat affected zone from the solid-state process. An example of a bond produced by FAST is

shown in Figure 5.1, where a chemically graded grain exists at the diffusion bond region. At higher magnification, there is a gentle transition from Ti-64 to Ti-6242 due to the change in Z contrast from the darker alpha laths in Ti-64 to brighter (more heavily stabilised) alpha laths in Ti-6242, but with the no noticeable difference morphology. There has been limited research focused on joining titanium alloys using FAST technology: He et al. [154] joined two solid blocks of Ti-64 with FAST and HP under several conditions and tested the strength of the bond with tensile tests. The failure points of the FAST joints occurred in the base material when processed at the highest temperatures. The FAST specimens achieved superior mechanical properties than the joints produced using HP for most of the conditions. Miriyev et al. [155] joined solid Ti-64 with AISI4330 steel achieving a tensile strength of 250 MPa in the joint. Kumar et al. [8] investigated similar flat bonds between commercially pure Ti (CP-Ti) and AISI304L using FAST, where an average strength of 260 MPa was recorded. However, when threads were incorporated into the bond, the average strength increased to 400 MPa. The main issue observed during the bonding of titanium to steel was the formation of intermetallic phases that produced a brittle failure in the bond region during mechanical testing. Pripanapong et al. [156,157] used FAST to join solid CP-Ti with magnesium alloys, achieving a tensile bond efficiency of 96% in relation to the bulk material. This efficiency was obtained when the Al content was increased, as it led to the precipitation of $Ti_3Al$, which locally increased the strength of the bond region. Zhao et al. [159] joined solid TiAl preforms using FAST and observed that the strength of the bond increased when the processing temperature increased due to the higher levels of diffusion. Nevertheless, the strength of the bond decreased when the pressure was increased due to recrystallization and grain growth.

Pope et al. [9] pioneered the use of FAST to diffusion bond dissimilar titanium alloy powders (termed FAST-DB), in combinations of Ti-64/Ti-5553 and Ti-64/CP-Ti into fully consolidated samples and demonstrated that the failure occurred in the lower strength alloy during uniaxial tensile loading. Although FAST has been well characterized as an effective process to bond dissimilar titanium alloys to form “architectural” microstructures [10,153,158,160], there has been limited research into the deformation mechanism and strain localization in the diffusion bond region during tensile loading, which is a key focus of this paper.

In the hexagonal close-packed (HCP) titanium alloys, the easiest slip modes occur along the <$11\bar{2}0$> direction for basal $\{0001\}$ and prismatic $\{10\bar{1}0\}$ planes. Additionally, $\vec{c} + \vec{a}$ slip occurs

on the $\{10\bar{1}1\}$ and $\{10\bar{2}2\}$ pyramidal planes [30,180,181]. This type of slip is more difficult than $\vec{a}$ slip at room temperature [12,16]. The activation of a slip system for a single crystal is dependent on the grain orientation relative to the loading direction, which is represented with the Schmid factor (m), and the critical resolved shear stress (CRSS) of the slip system [182]. For polycrystalline materials the interaction between neighboring grains has to be taken into account and it has been suggested that is necessary to add a hardening effect to the CRSS value [183]. The pyramidal CRSS for Ti-64 is often considered to be at least two times higher than the prismatic CRSS, and thought to be up to thirteen times higher for CP-Ti with a low oxygen content [29]. Furthermore, the CRSS for the prismatic and basal plane is thought to be ~ 1:1, but it has been observed in tensile and compressive tests for single grain and textured titanium alloys that the prismatic plane tend to have a lower value [26,30,31]. Although the global Schmid factor calculation does not take into account the local stress state, it has been found by Bridier et al [26] to be an adequate parameter for determining the active slip mode in Ti-64, i.e., with the activated slip systems corresponding to the those with the highest Schmid factor. However, recent high-resolution studies have shown that there is often more complex deformation occurring at the subgrain scale [27].

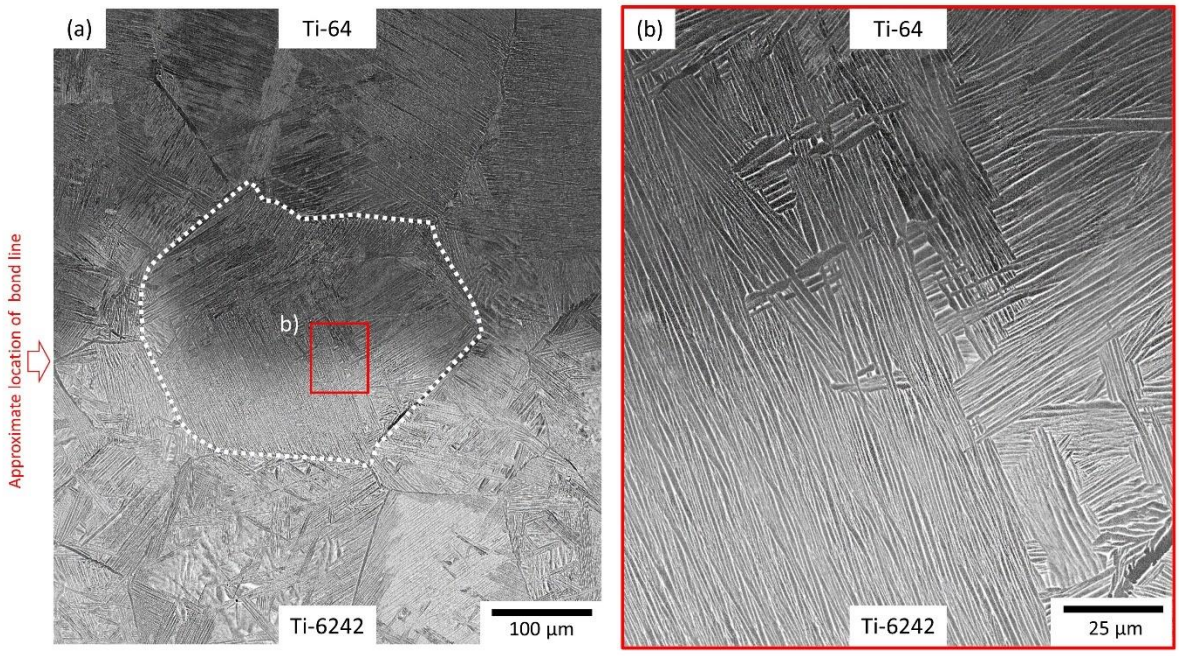


**Figure 5.1** — Backscattered electron micrographs of the FAST-DB bond between Ti-6242 and Ti-64; (a) Micrograph illustrating chemical grading across a grain at the diffusion bond region - the red arrow shows the approximate location of the bond. (b) Higher resolution micrograph of the diffusion bond and similar alpha colony morphology across the diffusion bond region.

In this study, optical Digital Image Correlation (DIC) is used to characterize the deformation of the diffusion bond region between Ti-64 and Ti-6242 under tensile loading at different length scales. DIC is a useful tool that can be used to map the local strain of a specimen through images [184–187]. The DIC technique works by tracking surface features while applying deformation and comparing the location of these features to their initial position. With optical DIC it is possible to quantify the strain localization at a mesoscale level. For example, Littlewood et al [188] and Lunt et al [189] used optical DIC in a forged Ti-64 specimen and a Ti-64 plasma wire deposition specimen to observe the effective strain of the grains and strain partitioning between neighboring grains of different crystallographic orientations.

The aim of this work is to assess the mechanical performance under uniaxial tensile strength of the FAST-DB joint between Ti-64 and Ti-6242 after subtransus and supertransus FAST processing.

## *5.2. Methodology*

This work presents two separate sets of experiments: one analyses the performance of the bond in a standard tensile test sample in both the subtransus and supertransus FAST processed condition. The second experiment uses optical DIC (higher resolution) to further understand the effect of the bond for supertransus conditions. The standard tensile test samples were machined from two separated FAST-DB discs of 250 mm diameter while the optical DIC samples were machined from one FAST-DB disc of 60 mm diameter.

### *5.2.1. Titanium alloy powders*

The titanium powder alloys used in this study were Ti-6Al-4V (Ti-64) and Ti-6Al-2Sn-4Zr-2Mo (Ti-6242). The morphology and microstructure of the powders are shown in Figure 5.2, where the nomenclature (S) and (D) has been added after the type of alloy to differentiate the powders used in the standard tensile test (S) and the optical DIC test (D). The top row of Figure 5.2 shows that Ti-6242 powder has a greater fraction of fine powder “satellites” and a higher frequency of particles partially melted compared to the Ti-64 powder. For Ti-6242 (S), it was observed the formation of fused powder joined together, which is typically observed in

recycled titanium powder that has been previously used in additive manufacturing processes. A martensitic microstructure is observed for all the powders in the middle row of Figure 5.2 due to the rapid cooling rates during powder production. The powder's aspect ratio, circularity and porosity were characterized using the optical microscope Olympus Bx51 with the software Clemex Vision PE image analysis system. The powder was cold mounted with epoxy-resin, followed by a short grinding and polishing. Then, the software Clemex Vision PE analyzed more than 20,000 powder particles for each powder type. The last row of Figure 5.2 shows the probability density of the powder as a function of the aspect ratio, circularity and the diameter of the powder. A perfect sphere will have value of aspect ratio and circularity of 1. Therefore, the Y axis represents the multiplication between the aspect ratio and the circularity because it shows how close to a perfect sphere the powder particle is. It is observed that the Ti-64 powder has more particles closer to a perfect sphere than the Ti-6242 powder, which correlates well with the SEM micrographs from the first row of Figure 5.2.

The particle size distribution (PSD) was measured using a Malvern Mastersizer 3000 laser diffraction particle size analyzer with a wet dispersion method. A total of 20 repetitions were conducted for each powder and the distributions can be found in Table 5.1. Additionally, Table 5.1 shows the porosity measured with the software Clemex for each powder type. The chemical composition of the elements were measured by X-EDS, XRF (Bed Fusion) and LECO analysis and the results are shown in Table 5.2.

### *5.2.2. FAST processing and test sample manufacture*

Two different tensile samples were made for different levels of mechanical assessment: one ASTM E8/E8M tensile specimen [163] was machined for a standard tensile test and a smaller bespoke tensile specimen was machined in order to study the deformation characteristics in the diffusion bond region. Table III shows the different tensile samples tested in this study and the FAST processing dwell temperature used for each one. The applied pressure of 32.5 MPa was used for all samples.

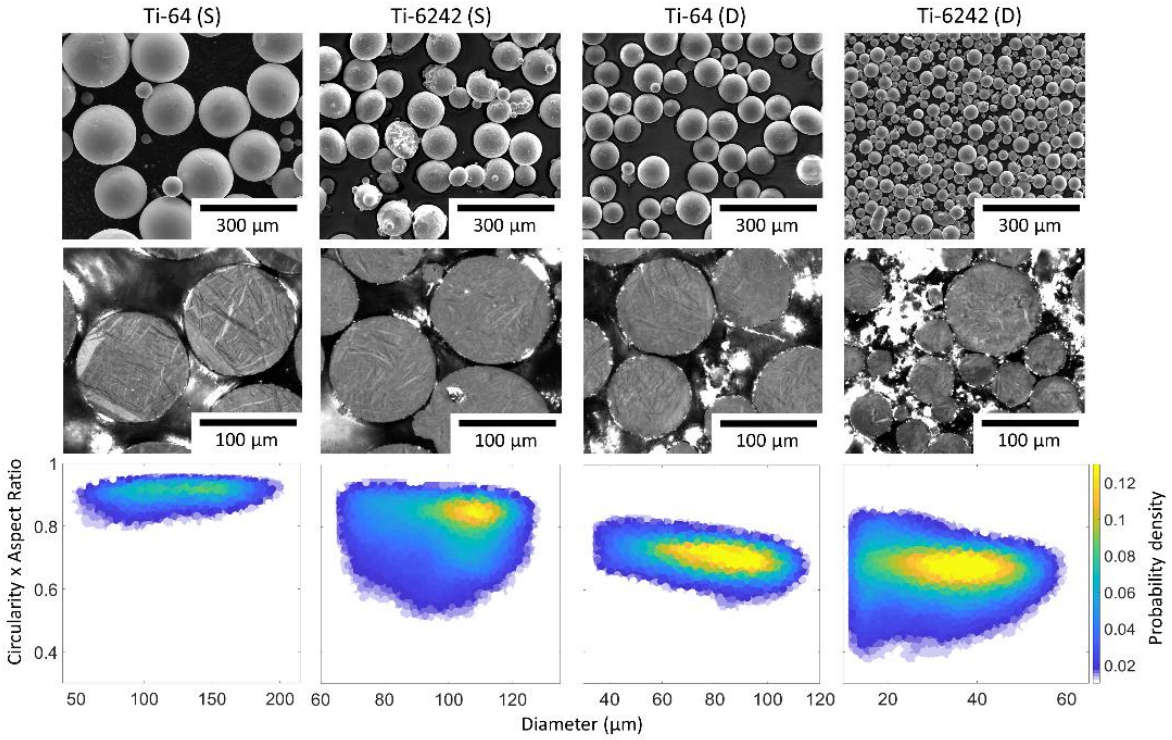


**Figure 5.2**—Micrographs and graphs showing the characteristics of the four powders used. The first row is made of secondary electron micrographs of the external appearance of the powder. The middle row are light micrographs of the powder microstructure under cross polarized light. The bottom row presents density plots of the aspect ratio and the circularity of the powder as a function of the diameter.

***Table 5.1 –*** *Particle size distribution and porosity of the titanium alloy powders.*

| Test | Disc | Powder | Dx (10) (µm) | Dx (50) (µm) | Dx (90) (µm) | Porosity (%) |
|---|---|---|---|---|---|---|
| **Standard tensile test** | Disc 1 and 2 | Ti-64 (S) | 93 | 160 | 299 | 0.05 |
| | | Ti-6242 (S) | 93.5 | 113 | 137 | 0.41 |
| **Optical DIC test** | Disc 3 | Ti-64 (D) | 61.3 | 86.7 | 123 | 0.07 |
| | | Ti-6242 (D) | 25.2 | 37.4 | 53.7 | 0.06 |

***Table 5.2*** *– Chemical composition of the four titanium alloy powders represented in* ***%.***

| Powder | Ti | Al | V | Sn | Zr | Mo | Fe | Si | C | S | O | N | H* |
|---|---|---|---|---|---|---|---|---|---|---|---|---|---|
| **Ti-64 (S)** | Bal. | 6.16 | 3.86 | - | - | - | 0.26 | - | 0.028 | 0.01 | 0.163 | 0.019 | 29 |
| **Ti-6242 (S)** | Bal. | 5.74 | - | 2.22 | 4.58 | 2.32 | <0.05 | <0.05 | 0.04 | 0.01 | 0.118 | 0.008 | 19 |
| **Ti-64 (D)** | Bal. | 6.02 | 3.66 | - | - | - | 0.16 | - | 0.023 | 0.01 | 0.181 | 0.003 | 32 |
| **Ti-6242 (D)** | Bal. | 5.69 | - | 1.89 | 4.41 | 1.93 | 0.05 | 0.09 | 0.07 | 0.01 | 0.148 | 0.002 | 21 |

H* is represented in parts per million (PPM)

Figure 5.3 presents the steps to manufacture the standard tensile test samples which were processed on an FCT System GmbH FAST Furnace Type H-HP D 250. The FAST furnace is capable of producing discs with a diameter of 250 mm and the temperature is measured with a pyrometer at the interface between the powder and the upper graphite ram. The powder was separated in the graphite ring by aluminum dividers, as shown in Figure 5.3 (a) and the two alloy powders were distribution as schematically illustrated in Figure 5.3 (c). Once the graphite ring was filled with the two powders, the dividers were carefully removed, leaving a straight interface between the two powders. The powder was fully consolidated in the FAST furnace to create a disc with a diameter of 250 mm and a thickness of 30 mm. To prevent oxidation of the titanium sample, the process was carried out under vacuum.

In this study, a total of two discs with the same alloy distribution were processed at two different temperatures with respect to the $\beta$ transus of both Ti-64 and Ti-6242, which is approximately 995°C: FAST processing was conducted at dwell temperatures of 970°C and 1030°C, which were respectively in the subtransus and supertransus phase regions for both alloys also. The surface of the FAST discs were then skimmed in order to accurately locate the bond line between the two alloys. The diffusion bonding was so effective that it was

challenging to visually locate the bond between these two alloys. A range of samples were machined, including tensile samples from the two FAST-DB discs, as shown in Figure 5.3 (c).

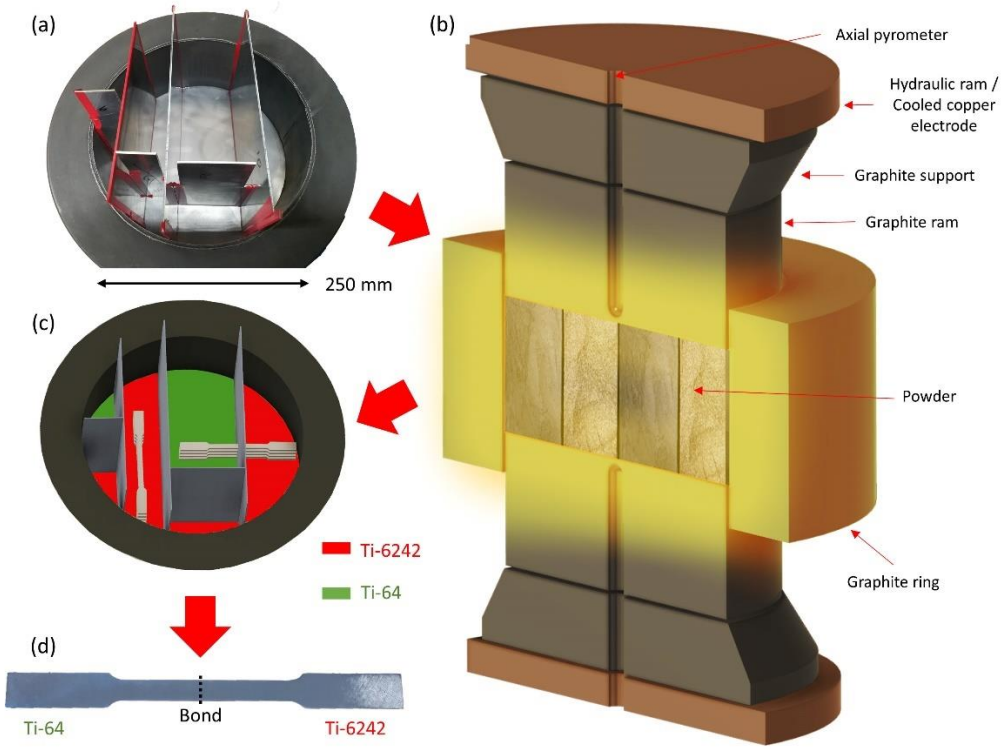


**Figure 5.3** — A schematic illustration of the FAST-DB process used to manufacture the tensile test samples. (a) A photograph of the graphite ring with the aluminum dividers, (b) a schematic representation of graphite ring layout during the FAST process, (c) a schematic illustration of how the FAST-DB billet was machined, (d) a photograph of a 120 mm long FAST-DB tensile sample.

The tensile samples for the optical Digital Image Correlation (DIC) test were produced on the smaller FCT System GmbH FAST Furnace Type HP D 25. Figure 5.4 shows the procedure followed to produce the samples for the optical DIC test. The temperature was also measured at the interface between the powder and the upper graphite ram with an axial pyrometer. The diameter of the graphite ring was 60 mm and the walls of the ring were covered with graphite foil to avoid the powder sticking in the graphite ring. A 3D printed polymer cross-shaped divider was used to separate the powders, as shown in Figure 5.4 (a). The divider maintained a straight interface between the two alloy powders when slowly removed from the graphite ring. For this sample, half of the graphite ring was filled with Ti-64 powder and the other half was filled with Ti-6242 powder. The powder was processed under vacuum conditions to avoid any oxidation and the process temperatures are shown in Table 5.3.

The tensile sample used was a double bone design and was 50 mm long, as shown in Figure 5.4 (c) - this design was used to constrain the location of the deformation. In order to locate the bond in the FAST disc, the surface was lightly ground using SiC paper until the bond was visible and the tensile samples were subsequently machined with the diffusion bond in the central region (Figure 5.4 (c)).

***Table 5.3*** *– Samples produced with FAST and the corresponding processing temperatures.*

| Test | Disc | Disc diameter (mm) | Processing conditions | Temperature (°C) | Name | Material |
|---|---|---|---|---|---|---|
| Standard tensile test | Disc 1 | 250 | Subtransus | 970 | T1 | Ti-6242 |
| | | | | | TDB1 | Ti-64/Ti-6242 |
| | Disc 2 | | Supertransus | 1030 | T2 | Ti-6242 |
| | | | | | TDB2 | Ti-64/Ti-6242 |
| Optical DIC analysis | Disc 3 | 60 | Supertransus | 1030 | TDIC | Ti-64/Ti-6242 |

### *5.2.3. Standard tensile testing*

As Table III shows, two discs were processed at the dwell temperatures of 970°C (subtransus) and 1030°C (supertransus). For each disc, samples were extracted using wire EDM and finish machined to ASTM E8/E8M [163] specifications. As Figure 5.3 (c) depicts, from each FAST disc, four tensile specimens were extracted entirely from the Ti-6242 region and four tensile samples were extracted across the bond region between Ti-64 and Ti-6242 (Figure 5.3 (d)). Before testing, one face of the tensile test samples was ground and polished to a mirror finish so the bond could be tracked during the tensile test. The tensile test was carried out using a Tinius Olsen 25 ST benchtop tester and LabView software was used to record the force and displacement of the sample. The force was read directly from the tester and the displacement was read from an Epsilon Axial Extensometer – Model 3542 with a gauge length of 50 mm.

The cross-head was set to a constant displacement of 0.01 mm/s and the test stopped when the sample failed.

For one TDB1 sample and one TDB2 sample, a GOM ARAMIS 3D system was used to measure the deformation of the sample with the DIC technique. The data obtained was post analyzed with the GOM Correlate software to extract the strain data of the x and y plane and MATLAB to plot the data in a 2D graph. It was necessary to create a pattern in the surface of the sample to obtain good measurements with the DIC technique. First, the sample was sprayed with white paint to create a homogenous layer in the sample. Then, the sample was sprayed with black paint to create an irregular pattern in the surface which allowed the local deformation in the specimen to be constantly tracked using the GOM system.

### *5.2.4. Optical digital image correlation and mechanical loading*

Microscale ex-situ DIC was carried out after tensile loading using a Kammrath-Weiss 5kN tensile/compression microtester, under displacement control at a rate of 0.02 mm/min, equipped with a control unit to provide displacement and load data. Subsequently, the crosshead displacements were transformed to engineering strain by using the initial gauge length. All measurements in the strain maps are determined in the unloaded state, as the sample had to be removed from the microtester after each deformation stage. It was not possible to image the sample whilst positioned within the tester, due to being unable to move the sample to the correct height. Images were acquired using a Zeiss Axio Imager 2 optical microscope, equipped with built-in mapping software enabling many images to be captured without any significant reduction in image quality. Focus interpolation was used by placing 36 points across the surface that were manually focused and then used as reference points during the image capture. The images were taken at a resolution of 1648 x 1436 pixels$^2$ with a 20% overlap and at a spatial resolution of 0.547 µm/pixel. Each matrix of images were stitched together using ImageJ image processing software [162,190] prior to the DIC analysis. Loading and subsequent imaging was repeated up to low plastic strains. For the complete series of images, ImageJ was also used for image manipulation in terms of shift and rotation correction to enable easy correlation. The displacements were computed using LaVision's DIC

software DaVis, version 8.4, using a standard fast Fourier transform (FFT) with an initial interrogation window size of 1024 x 1024 pixels$^2$ down to a final interrogation window size of 32 x 32 pixels$^2$ giving a spatial resolution of 17.51 x 17.51 µm$^2$. The strain analysis was performed using the in-house DefDAP 0.92 Python package [191], where the microscale DIC is typically presented as effective shear strain, $\gamma_{eff}$, as this takes into account all of the in-plane components [192,193]. This was calculated by the standard relationship given in Equation (5.1).

$$\gamma_{eff} = \sqrt{\left(\frac{(\varepsilon_{xx} - \varepsilon_{yy})}{2}\right)^2 + \left(\frac{(\varepsilon_{xy} + \varepsilon_{yx})}{2}\right)^2} \qquad (5.1)$$

where $\varepsilon_{xx}$ is the strain in the loading direction, $\varepsilon_{yy}$ is the strain normal to the loading direction and $\frac{(\varepsilon_{xy}+\varepsilon_{yx})}{2}$ is the in-plane shear component.

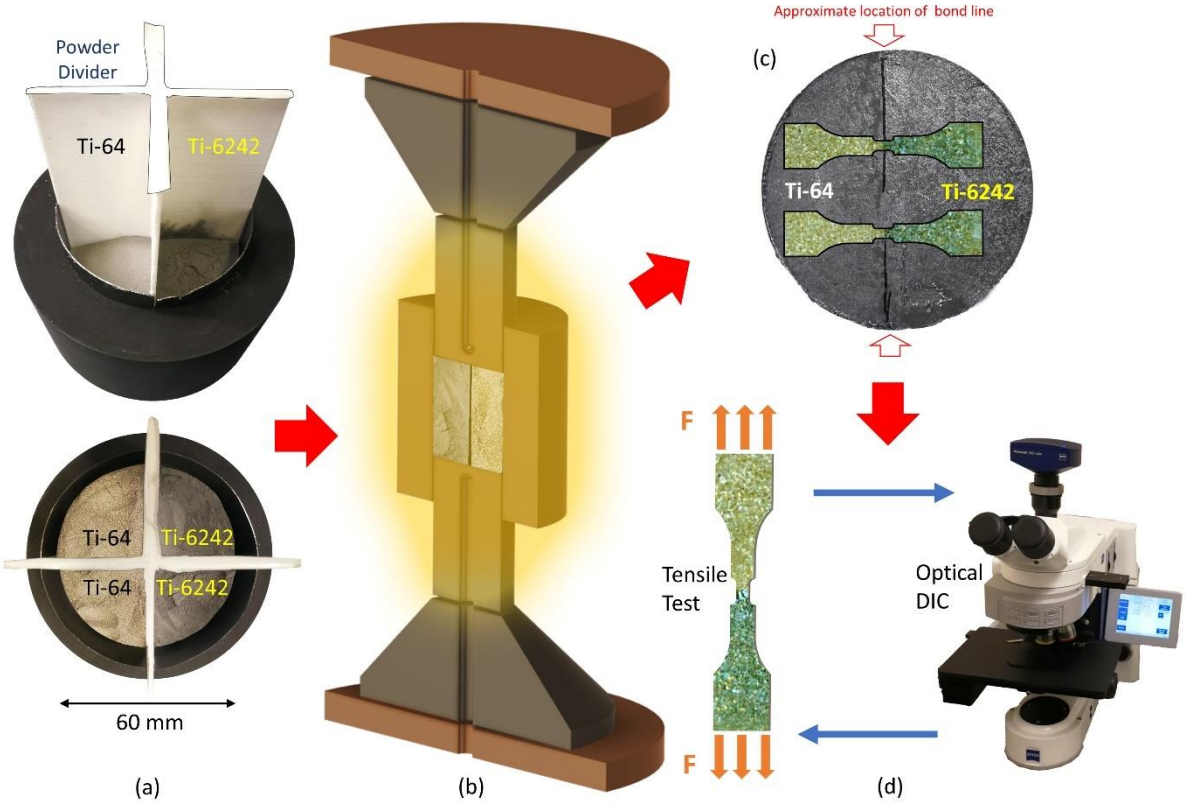


**Figure 5.4** – A schematic illustration of the process used to test the bond with optical Digital Image Correlation (DIC). (a) photographs of the graphite ring die with the cross-shaped polymer divider arrangement, (b) a schematic representation of graphite ring layout during the FAST process, (c) an image showing a 50 mm long tensile sample superimposed onto a photograph of the FAST-DB billet and (d) a representation of the optical DIC procedure.

### 5.2.5. Grain texture measurements using electron backscatter diffraction (EBSD)

After mechanical loading, post-deformation EBSD was performed in the region of interest to enable the strain localization to be correlated to the underlying microstructure. Orientation mapping was performed in a Field Emission Gun (FEG) (FEI Sirion) Scanning Electron Microscope (SEM) equipped with an Aztec EBSD system and a Nordlys II detector, at an accelerating voltage of 20 kV. An area of 3 x 1 $mm^2$ was covered with a step size of 2.3 µm, to give sufficiently detailed grain orientation information for comparison with the 2D strain measurements.

### 5.2.6. Analysis techniques

The tensile samples had to be sectioned before they could be metallographically prepared. A Struers Secotom-20 was used to section the materials. The specimens were then hot mounted with conductive Bakelite and ground with progressively finer grit SiC paper on a Struers Tegramin-25. A solution made of 0.06 µm colloidal silica with 10% of hydrogen peroxide was used to obtain a mirror finish in the surface of the specimen after the grinding stages. The micrographs were obtained with a FEI Inspect F50 SEM.

The local chemistry adjacent to the bond was measured with X-EDS point scans with a Philips XL30 SEM. The detector was calibrated with a pure cobalt standard at the beginning of each session. The chemical scanning was conducted perpendicular to the diffusion bond line, with a total of 15-20 points linearly spaced between them and a dwell time of 2 min per point. The data was plotted with the software MATLAB and the fitting curve were obtained with the curve fitting app in the same software using the complimentary error function given in Equation (5.2).

The hardness profile of the material was measured with a Struers Durascan 70 G5. A total of 100 indentations, distributed in 5 rows, was perform across the bond. The 5 rows were parallel and diagonally crossed the bond in order to provide higher density of data points in the proximity of the bond, thus increasing the resolution of the hardness profile across bond.

Each indentation had a dwell time of 15 s, in accordance with the ASTM E384 standard [161]. The load used for the indentation was 9.81 kgf for all the samples. The distance from each indentation to the bond was measured manually with the software ImageJ from light micrographs and plotted with MATLAB.

## 5.3. Results

### 5.3.1. Microstructure of FAST-DB consolidated preforms

The microstructure obtained for the subtransus (TDB1) and the supertransus (TDB2) FAST-DB samples are shown in Figure 5.5 (a, b). The primary observations are that (1) both conditions have achieved full consolidation and no porosity is evident and (2) processing in the subtransus region produces a much finer microstructure compared to when processing in the single-phase beta region (supertransus condition). In both cases the bond region thickness is of the order of 300 μm which agrees with the X-EDS measurements in Figure 5.6.

The subtransus microstructure consists of equiaxed primary alpha (~ 20 μm) which formed as recrystallized clusters at the original sites of particle-particle boundaries during processing. A more lath-type morphology evolves between these equiaxed alpha clusters, which is transformed secondary alpha from the beta that existed at 970°C. This FAST microstructure is very similar to what would be observed in the as-HIP'ed condition [194]. This bimodal structure is far less apparent in the Ti-6242 compared to Ti-64: this is due to the finer Ti-6242 powder particle size which leads to a finer dispersion (and more homogeneous appearance) of equiaxed alpha, deriving from the particle-particle interfaces during consolidation. Although the secondary alpha laths are much less defined in Ti-6242 compared to Ti-64, there is a smooth chemical and microstructural transition across the bond. The only noticeable variation under backscattered electron imaging is the increase in Z contrast in both the alpha and residual beta phase of Ti-6242: this is due to the increased alloy additions with higher atomic weights, such as Zr and Sn in more creep resistant alloy.

The resultant microstructure in the supertransus FAST processed billet is a fully transformed large equiaxed grain structure with continuous grain boundary alpha due to the slow cooling

(9°C/min) after the 1030°C and 1 hr dwell. The grain boundary alpha would have formed first during cooling and then the secondary alpha within the grains transformed from the beta phase. The grains in the mid-section of Figure 5.5 (b) show evidence of chemical grading as the darker Ti-64 alpha laths morph into the brighter, more heavily stabilized Ti-6242 alpha without any noticeable change in secondary alpha size or morphology.

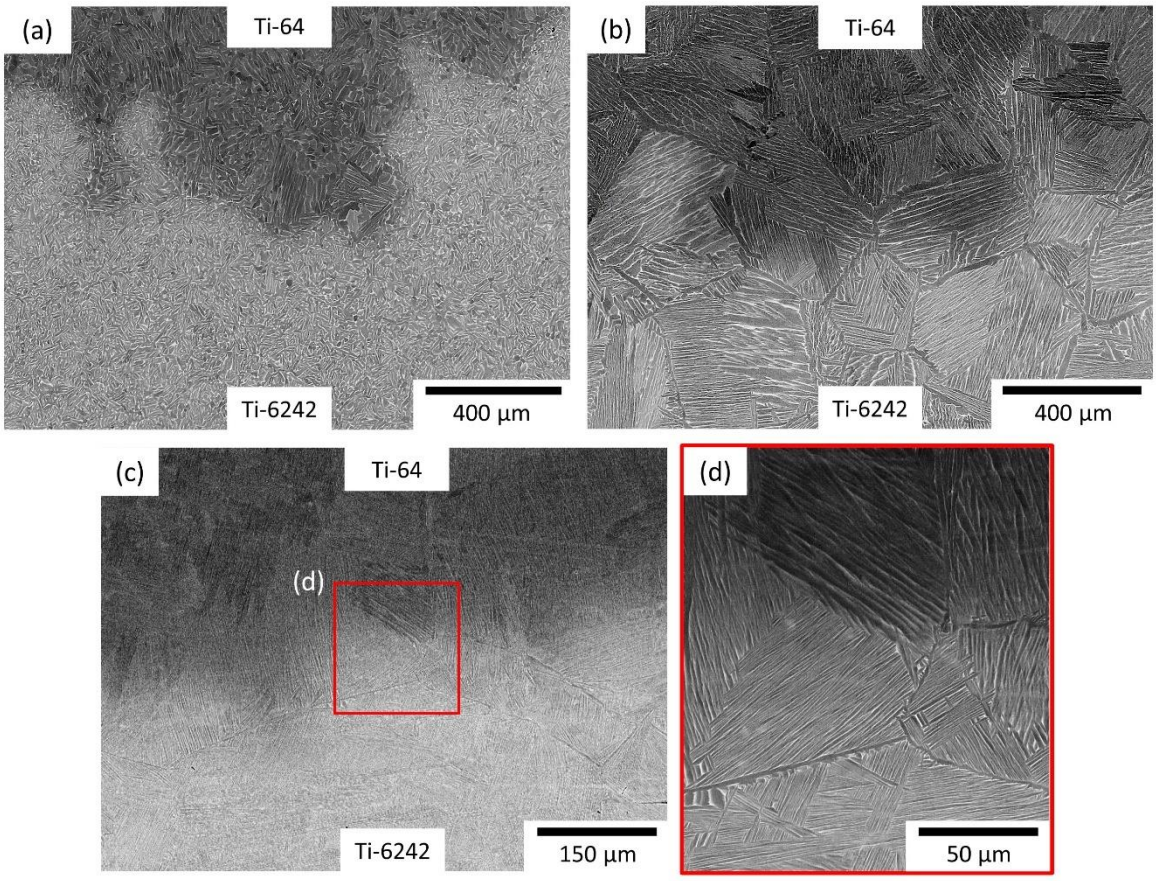


**Figure 5.5** — Backscatter electron images of the FAST-DB sample processed under (a) subtransus conditions (TDB1), (b) supertransus conditions (TDB2), (c) supertransus conditions (TDIC), (d) supertransus conditions (TDIC) at higher magnification.

In the case of the supertransus condition, there is no noticeable change in grain size in the two alloys, and therefore the effects of the original powder sizes are nullified through the FAST processing after 1 hr dwell in the single-phase beta. This elimination of the effect of the original powder size is also observed with the TDIC sample in Figure 5.5 (c, d), which used a smaller PSD powder than the powder used for TDB2 but obtained a similar grain size distribution.

The 60 mm diameter sample produced at the University of Sheffield had a higher cooling rate (63°C/min) which resulted in a finer alpha lath colony size and more colony variant as shown in Figure 5.5 (c, d). The powder was fully consolidated by achieving a density of 99.98%.

### *5.3.2. Hardness and diffusion profile of the FAST-DB bond*

Figure 5.6 (a–e) shows the gradual change of the elements across the diffusion bond in subtransus and supertransus processing conditions measured by X-EDS. It is important to measure the distance of the bond, as it will determine if the strain measured in certain areas is due to the diffusion bond or the base material. The variation of the chemical composition of the elements was curve fitted with the complimentary error function in Equation (5.2) [24].

$$c = \frac{A_0}{2} erfc\left(\frac{x - J1}{2\sqrt{J2}}\right) \quad \textbf{(5.2)}$$

*C* is the chemical composition of an element at a certain distance, $A_0$ is the initial element concentration, $erfc$ is the complementary error function and $x$ is the distance to the bond. The coefficients $J1$ and $J2$ were calculated by the curve fitting app in MATLAB to ensure the curves fit well with the data.

As expected, the diffusion gradient of the elements when FAST processed in the supertransus region is higher than when FAST processed under subtransus conditions. The variation between the supertransus and subtransus conditions tends to be around 100 µm. For supertransus processing conditions, the fastest interdiffusing element is Zr with a diffusion distance of 180 µm from the Ti-6242 into the Ti-64 alloy; the diffusion distances for Mo, Sn and V are very similar (~100 µm) at supertransus conditions. In the lower temperature, subtransus conditions, the diffusion distances are shorter, with Zr being the fastest diffuser at the bond interface. The maximum length of the diffusion bond in subtransus conditions is 150 µm, while for supertransus conditions the maximum distance is 350 µm. The diffusion profile of Al (Figure 6e) is complicated to measure for both conditions because both titanium alloys have a very similar Al composition. Furthermore, the X-EDS measurements of Al have a high variation between them, which makes the curve fitting of the diffusion profile less accurate. Therefore, the diffusion of Al can be interpreted as constant through the diffusion bond.

Figure 6f shows the variation of Al and Mo equivalent across the diffusion bond for the supertransus conditions calculated with Equations (5.3) and (5.4) [37].

$$Al\ eq\ (wt\%) = Al + 10(O + N + C) + {}^{1}/_{3}\,Sn + {}^{1}/_{6}\,Zr \qquad \textbf{(5.3)}$$

$$Mo\ eq\ (wt\%) = Mo + 2.5Fe + {}^{2}/_{3}\,V + 1.25(Cr + Ni + Cu) + {}^{1}/_{3}\,Nb \qquad \textbf{(5.4)}$$

The curves show a higher value of Al and Mo equivalent for Ti-6242 than for Ti-64. The Al equivalent curve has a smooth transition between both alloys, but the Mo equivalent reaches the minimum value just after crossing the bond. This is because V is a faster diffuser in β-Ti compared to Mo. The data used to build these curves is based in the X-EDS data plotted in Figure 5.6 (a-e). Therefore, it has to be taken into account that there are could be small variation to the actual Al and Mo equivalent.

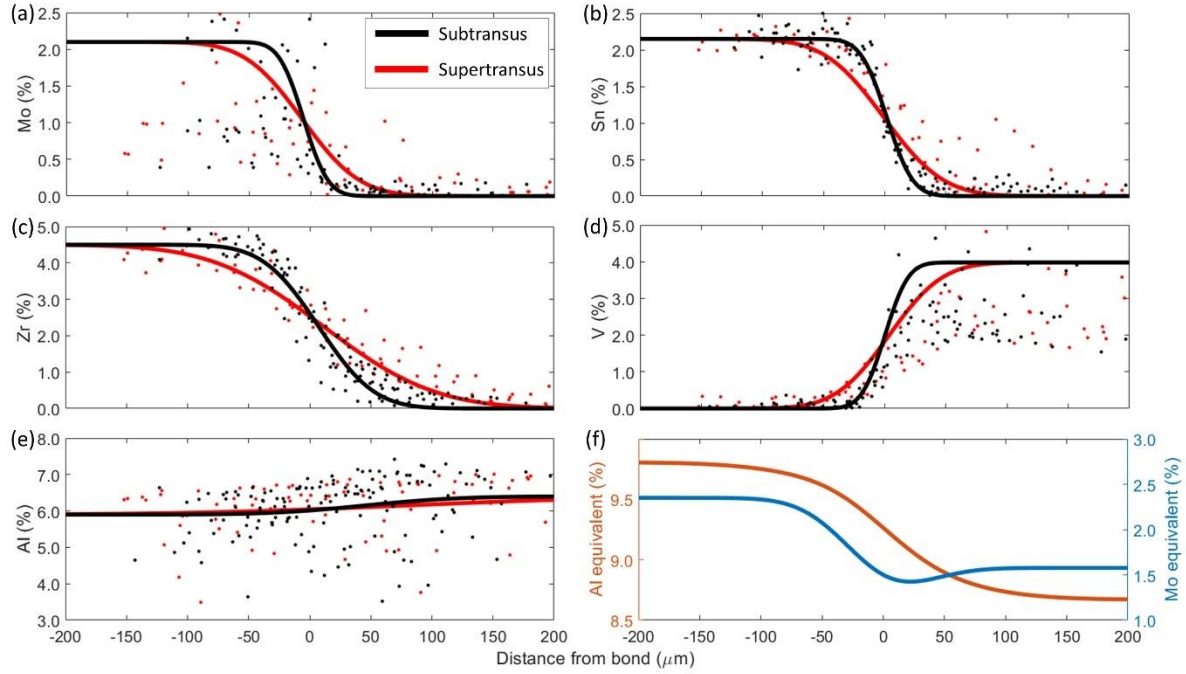


**Figure 5.6** – Plots showing the element composition across a Ti-64 and a Ti-6242 bond when processed under subtransus and supertransus FAST conditions for: (a) Mo, (b) V, (c) Zr, (d) Sn and (e) Al. (f) Plot of the Al and Mo equivalent across the diffusion bond.

The hardness of the bond is shown in Figure 5.7 for the subtransus and supertransus FAST processing conditions. The hardness has a similar value for both alloys and it does not show any variation when moving across the diffusion bond. There is scatter in the hardness data, especially for the TDB2, given that the hardness varies depending on the tested region and the grain orientation. On average, the hardness for the subtransus material is slightly higher

than the supertransus material which is expected due to the finer grain structure (see Figure 5.5).

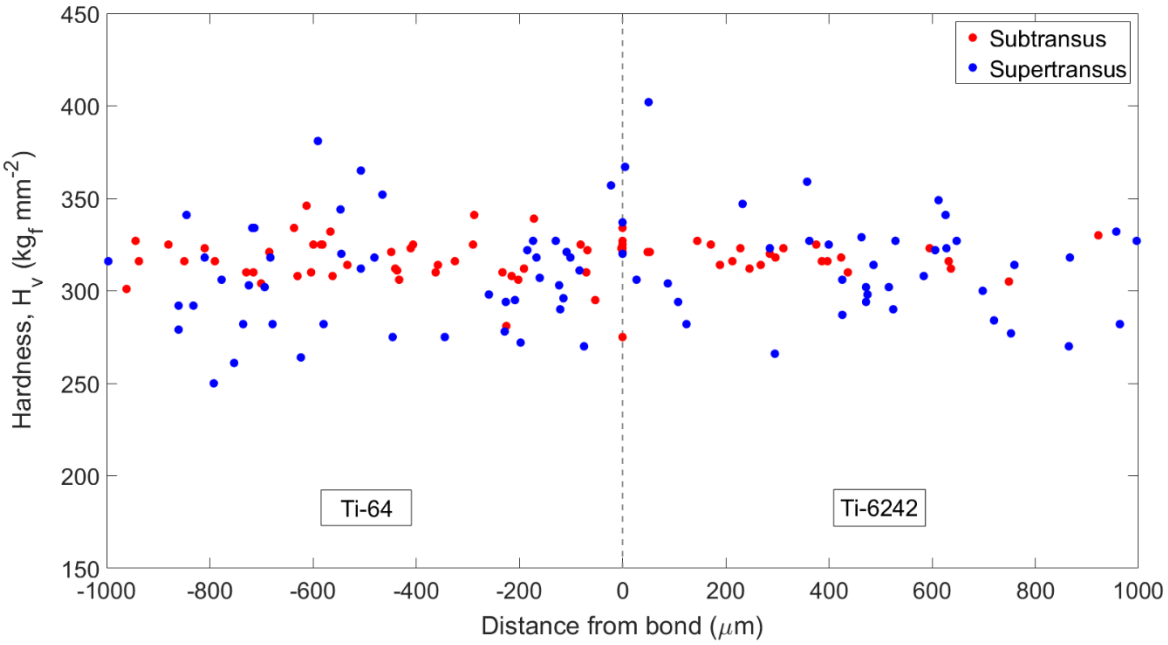


**Figure 5.7** – Vickers microhardness profiles across the FAST-DB bonds processed under subtransus and supertransus conditions.

### *5.3.3. Tensile behavior*

Tensile tests were carried out on the FAST-DB dissimilar alloy material (TDB1, TDB2) and the alloy Ti-6242 (T1, T2). As repeats for each condition were very consistent, Figure 5.8 displays one stress-strain plot for each material condition. Figure 5.8 shows the curves for the FAST-DB material (Ti-64/Ti6242) overlaid on the results for a sample made of one alloy (Ti-6242). The FAST-DB and Ti-6242 (monolithic) material have very similar yield characteristics in both subtransus and supertransus conditions: the only difference being that the FAST-DB material failed at a slightly lower strain with more localized deformation prior to failure compared to the equivalent Ti-6242 monolithic condition.

In both cases, when the specimen was processed under subtransus FAST conditions, a higher yield stress point and a higher ultimate tensile strength was obtained for both materials. Additionally, for the FAST-DB material, a decrease in the strain to failure was observed for TDB2 in relation to TDB1.

Overall, the values obtained in the tensile test are very similar to that obtained from material processed from the conventional processing route. However, it is also worth noting that the microstructure of the FAST-DB material has not been optimized to achieve the highest ultimate tensile strength (UTS). FAST has a number of parameters that can be changed to modify the final microstructure. For that reason, there can be other combinations of these parameters that result in higher UTS for the material.

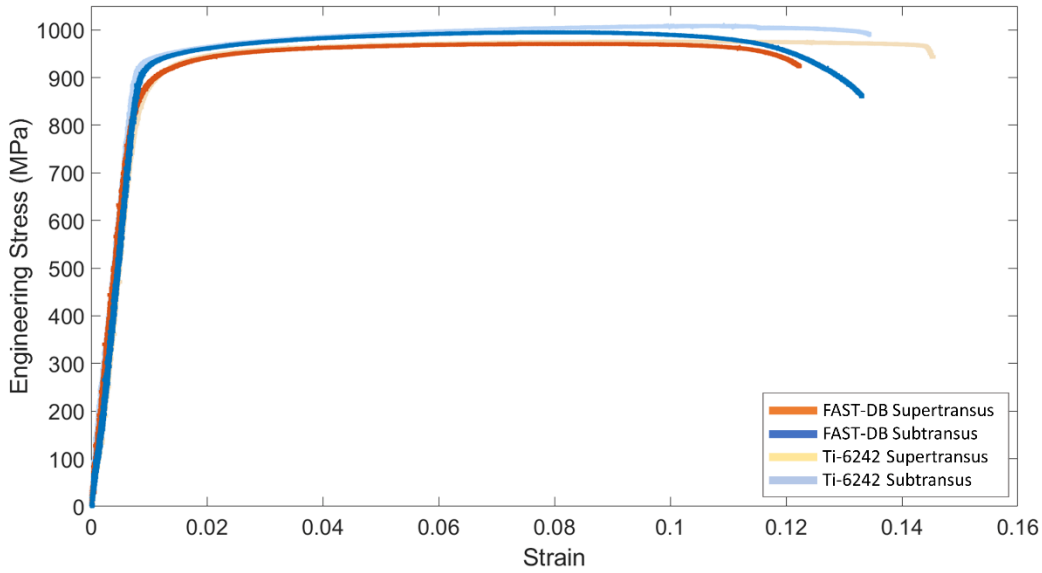


**Figure 5.8** – Stress strain curves of ASTM E8/E8M specimens for the FAST-DB Ti-64/Ti-6242 dissimilar alloy material and Ti-6242 material, processed under subtransus and supertransus conditions.

One sample of TDB1 and TDB2 was analyzed using DIC to characterize the strain localization during a tensile testing, for a FAST-DB sample when processed at sub- and supertransus temperatures. Figure 5.9 (a) shows the local deformation of two specimens at a strain of 0.07 and it is apparent that the subtransus sample has three distinct regions with different levels of strain. The bulk Ti-6242 region accommodates the lowest strain, then there is a smooth transition of strain accumulation across the relatively small diffusion bond region into the bulk Ti-64 region - which accommodates the highest levels of strain. These three regions are clearly differentiated in the subtransus specimen.

In the supertransus FAST processed specimen, the grain size and transformed beta structure is very similar for both alloys, with large grains that cross the diffusion bond region (as shown in Figure 1 and 5). Due to the large grain structure these three regions are less distinct in the

DIC strain map of the supertransus specimen and the strain is distributed more homogeneously over the specimen.

In Figure 5.9 (b) the average strain in the x direction is plotted against the y direction of the samples. From Figure 5.9 (b), it is clear that for both processing conditions, the Ti-64 regions accommodate higher levels of strain than the Ti-6242 regions. Furthermore, in both cases, there is a smooth transition of strain across the diffusion bond from Ti-64 to Ti-6242. In the subtransus samples, the local difference in the strain between the two alloys is higher than the supertransus conditions as the strain is more homogenously distributed in the latter case. In fact, twice as much strain is accommodated in the Ti-64 region compared to the higher strength Ti-6242 alloy region when processed in the subtransus region.

All the FAST-DB samples fractured in the bulk Ti-64 region, which has a lower strength than alloy Ti-6242; as clearly shown in Figure 5.10 (a). The two alloys for the subtransus material can be differentiated very well due to the surface cold deformation in Ti-64 at the high strain levels. For the supertransus material both alloys deformed in a similar manner (as observed in the DIC homogeneous strain profile in Figure 5.9 (b) and therefore it is more difficult to locate the bond line between the two alloys in Figure 5.10 (b). From the data in Figure 5.9 (b), the Ti-64 bulk material accommodated higher strains when FAST processed under subtransus conditions compared to the supertransus processed material. The subtransus failure is normal to the tensile axis, whereas the supertransus samples failed at a shear angle to the tensile axis, which indicates the fracture of the specimen is controlled by a combination of normal and shear stress failure.

The fracture surface of the subtransus specimens were much smoother compared to the supertransus specimens where rough fracture features were observed. Both types of materials suffered from a ductile fracture, as dimpled features were observed in the fractographs in Figure 5.10 (c-f). The fracture surface for the subtransus processed material exhibited voids and an equiaxed dimple pattern that confirms a normal mode fracture. The supertransus processed material exhibited a transgranular failure due to the observation of cracks along the colonies of alpha laths. Additionally, parabolic shaped dimples were also observed indicating a shear mode stress component in the bottom region of the sample (Figure 5.10 (f)).

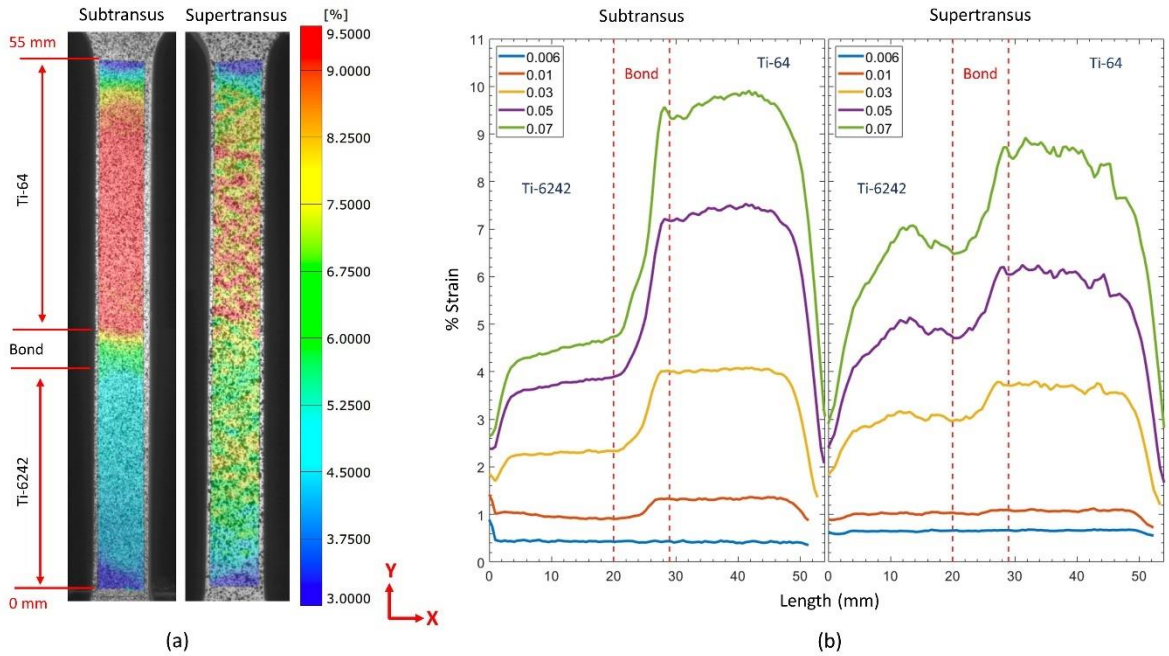


**Figure 5.9** – Results obtained with the DIC performed to the standardize samples. An image of the strain in different parts of the sample is shown in (a) for a subtransus specimen and a supertransus specimen. (b) The two graphs show the average strain at each part of the subtransus and supertransus specimens at incremental stages of the tensile test.

### *5.3.4. Optical Strain Map*

The deformation for the subtransus material was shown clearly in Figure 5.9 where there is a smooth transition across the bond. Nevertheless, the DIC technique used previously had insufficient spatial resolution to show the deformation for the supertransus material. Thus, mesoscale optical DIC technique was used during an interrupted tensile test of a FAST-DB specimen to characterize the evolution of local plastic strain across the bond - for a specimen processed under supertransus conditions. Although the higher resolution optical DIC is unable to resolve individual slip bands, it can detect local differences in strain between individual prior beta grains. The strain maps obtained from the optical DIC were complemented with information of the α phase prismatic and basal Schmid factor. The Schmid factor was calculated from EBSD orientation maps using the software MTEX following the conventional approach where the global stress condition is used. With this approach, it is assumed that the nominal applied stress can be directly related to the stress state in the individual α grains [26]. This is a simplistic approach that ignores other factors but previous studies have found a

strong agreement between the predicted Schmid factor and the actual active slip system in HCP metals [195].

The specimens tested in Figure 5.9 have a similar diffusion and hardness profile as the material plotted in Figure 5.6 and Figure 5.7 and the microstructures of such specimens are shown in Figure 5.5 (c, d).

Figure 5.11 (a) shows IPF maps of the diffusion bond between Ti-64 and Ti-6242. It can be observed that there is no clear indication that the two dissimilar alloys are joined from the crystal orientation map. There is no clear mismatch between the two alloys, and some grains contain a chemical grading from Ti-64 to Ti-6242 across the diffusion bond. However, from the band contrast map in Figure 5.11 (b), the location of the bond can be roughly estimated due to the gradual change in contrast from one region to the other, where the Ti-6242 side is slightly darker than the right, Ti-64 side. For a more quantitative comparison of the orientations of the grains for each alloy, normalized frequency distributions of the Schmid factor have been plotted in Figure 5.11 (c), for both basal and prismatic slip in each side of the bond, where the Schmid factor provides an assessment of the relative ease of slip. The results show that the highest Schmid factor frequency in the specimen is in the Ti-6242 side for the values between 0.4 and 0.5 in the prismatic plane. The Schmid factor for Ti-64 is similar for the basal and prismatic planes and the frequency shows a small increase for values between 0.4 and 0.5. Furthermore, the prediction of plastic strain in the two alloys was based purely on the Schmid factor information, it would be expected to see more concentrated deformation in Ti-6242 due to the higher number of grains with Schmid factor values of 0.4 and above [26].

The Schmid factor maps for the prismatic and basal planes across the FAST-DB bond are plotted in Figure 5.12 (a, b). Figure 5.12 (c) shows a micrograph of the etched microstructure of the tensile specimen in the diffusion bond region. This micrograph can be correlated with the optical effective shear strain map shown in Figure 5.12 (d). It has to be taken into account that Figure 5.12 (d) has a horizontal line going across the specimen that does not represent the real strain value. These artefacts are a result of slight misalignments between individual frames that cannot be corrected during the stitching process, but they do not mask the underlying deformation of the material. It is clear that all the deformation has occurred in the

Ti-64 region with just a little deformation happening on the diffusion bond on the bottom of the sample.

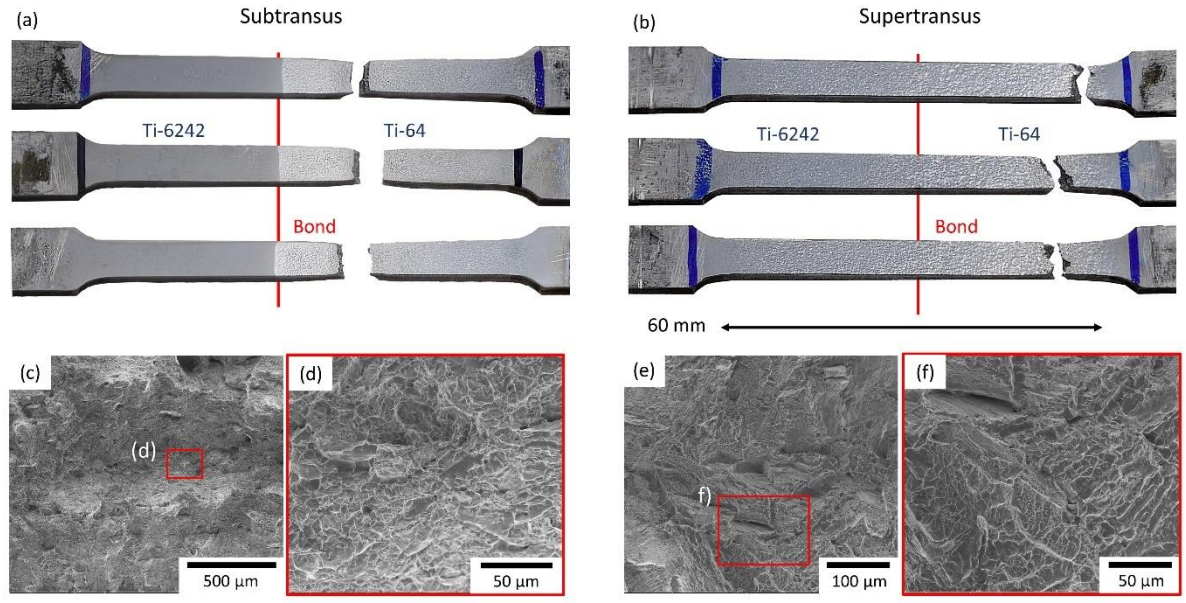


**Figure 5.10** – Images of the failure location in the standard tensile test for the (a) subtransus specimens and (b) supertransus specimens. SEM fractographs of the fracture surface of the subtransus tensile specimens (c) at low and (d) high magnification, and for supertransus tensile specimens at (e) low and (f) high magnifications.

This is evident in Figure 5.13 where the effective shear strain for all the specimen is mapped and plotted. It should be noted that the two horizonal lines showing strain across the samples in Figure 5.13 (a) are the same stitching artefacts as observed in Figure 5.12 (d). The plot in Figure 5.13 (b, c) show the average shear strain and the 95th percentile values are plotted against the distance, in a similar way to Figure 5.9 (b). These values were calculated from each vertical column of pixel data in the width direction of the sample. The 95th percentile value is used to highlight the comparative maximum level of strain in each column. Additionally, the 95th percentile value was used instead of the maximum value to avoid excessive noise from the data.

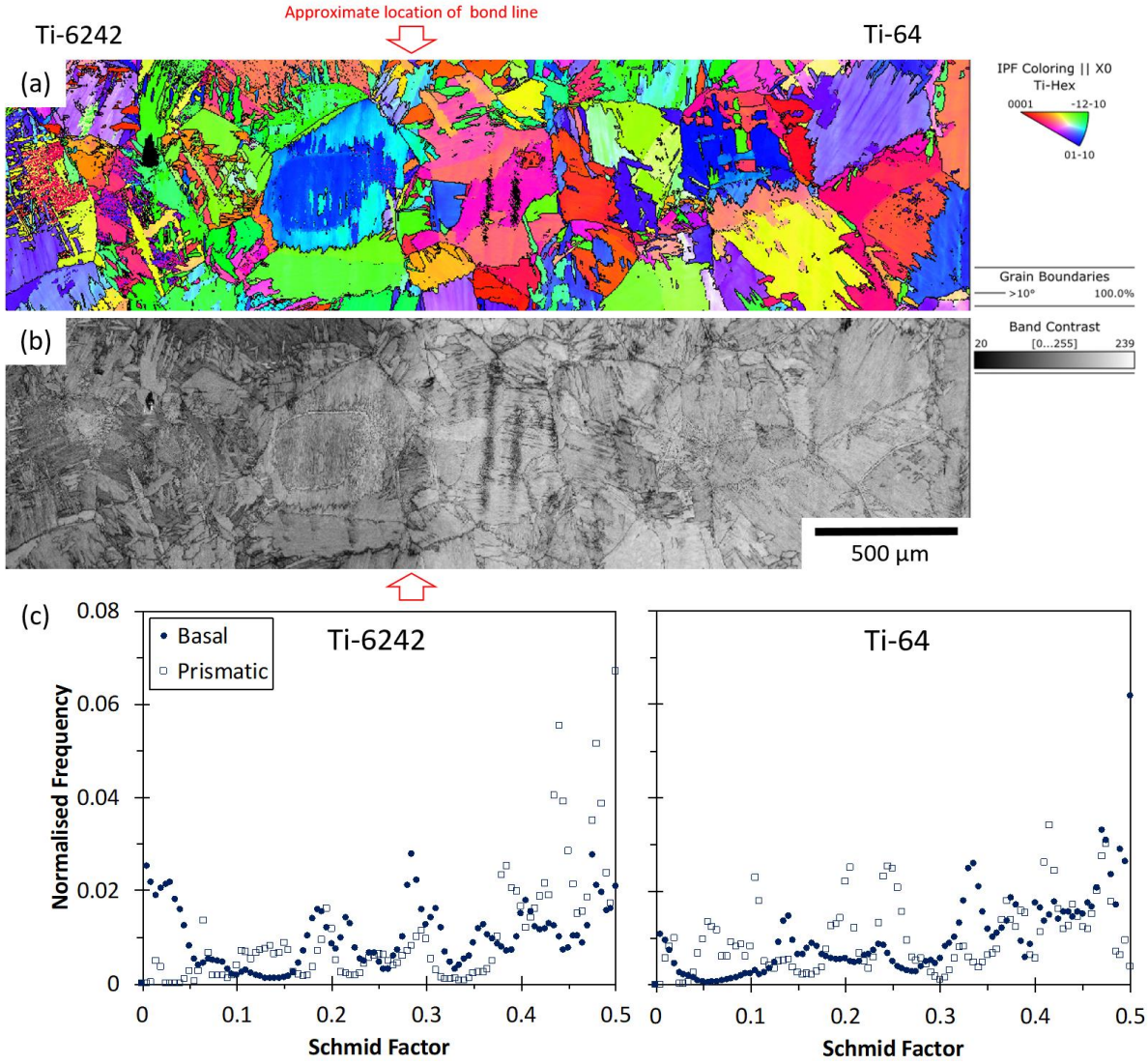


**Figure 5.11** – (a) EBSD map of the FAST-DB bond with the IPF for titanium hexagonal and cubic. (b) Band contrast micrograph showing the location of the bond and the slip band located in the Ti-64 region. (c) Graphs plotting the normalized frequency against the Schmid Factor for the basal and prismatic plane in the Ti-6242 and the Ti-64 regions.

The graph in Figure 5.13 (b) shows three defined regions. First, the strain is constant in Ti-6242 until a sharp increase of strain occurs at the start of the diffusion zone. Then, the strain remains constant across the diffusion bond region and increases when the composition is entirely Ti-64, which correlates with the observations in the standard tensile test. Furthermore, there are two main peaks in the Ti-64 region and the closest one to the bond is located at around 800 µm. The maximum effective shear strain between the two alloys is about four times higher in Ti-64 compared to Ti-6242. For the chemically graded, diffusion bond region, the maximum effective shear strain is approximately three times lower than the bulk Ti-64 and approximately two times higher than that measured in the Ti-6242 bulk. Lunt

et al. [189,196] observed similar levels of maximum shear strain in the grain boundaries of a Ti-64 produced by plasma wire deposition.

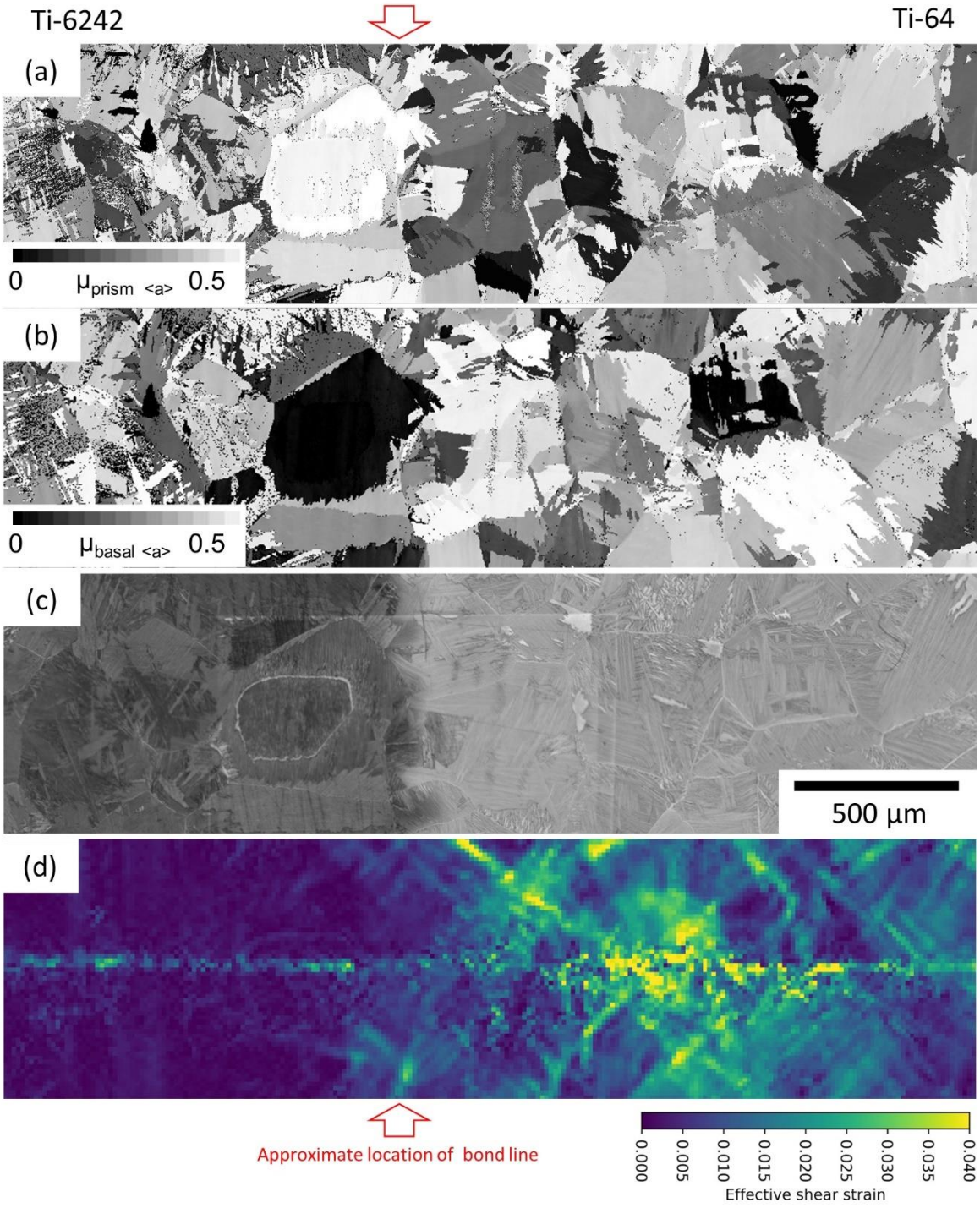


**Figure 5.12** – Mapping of the Schmid factor for the (a) prismatic and (b) basal planes. (c) Optical micrograph of the FAST-DB bond after etching with HF. (d) Mapping of the effective shear stresses in the FAST-DB sample after applying tensile strength.

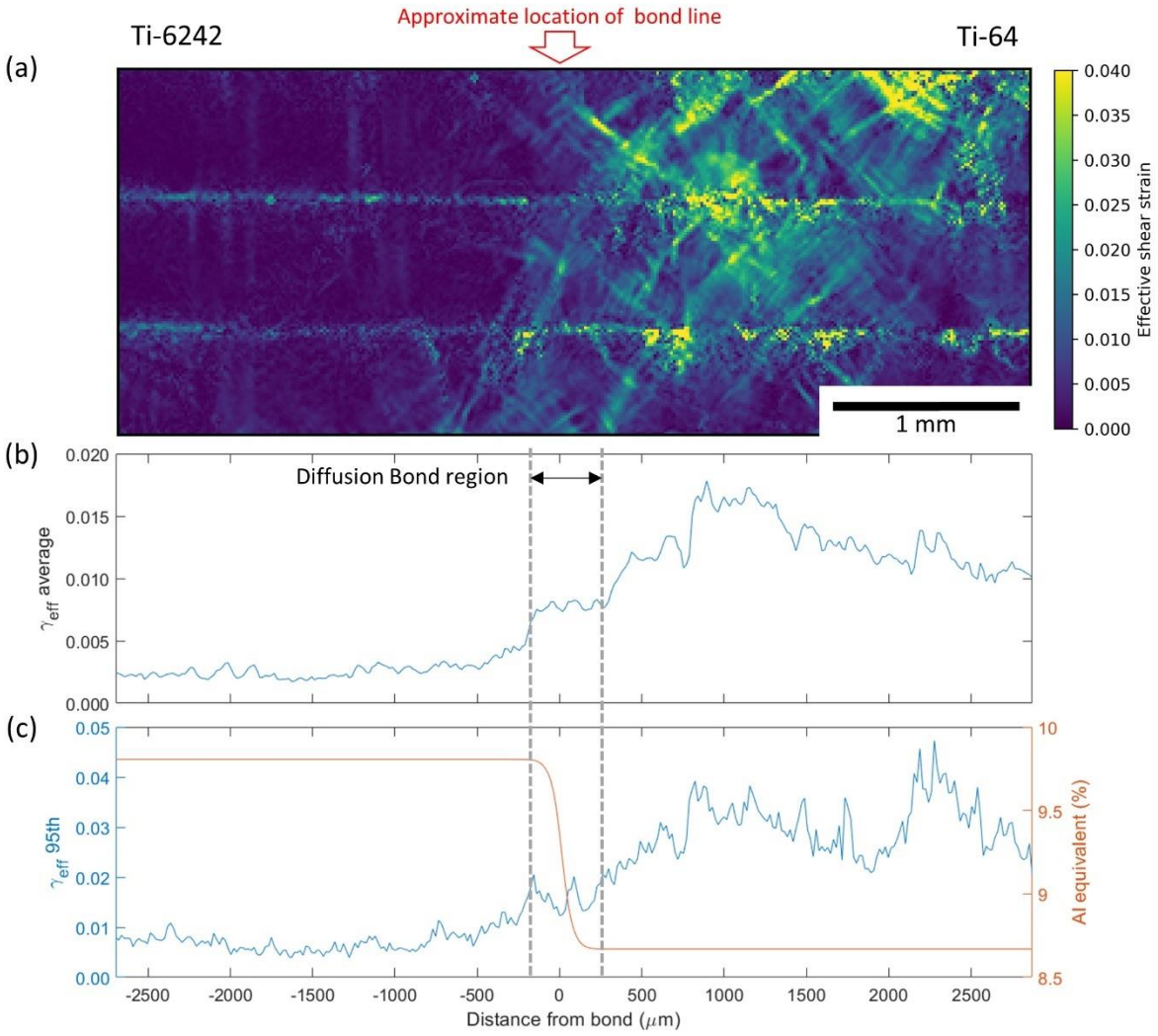


**Figure 5.13** – (a) Mapping of the effective shear stresses in the FAST-DB specimen after applying tensile strength. Development of the effective shear strain profiles across the FAST-DB bond for b) the average effective shear strain and c) the 95$^{th}$ percentile of effective shear strain.

## *5.4. Discussion*

### *5.4.1. Bond characterization*

The results presented in Figure 5.6 show a higher diffusion of elements for the samples processed at supertransus temperatures compared to those at subtransus conditions. There are two main reasons for this difference; first, the diffusion coefficients follow an Arrhenius law, that increases as temperature increases [89,197]. Secondly, titanium is an allotropic material with a dominant HCP crystal structure when processing below the beta transus and

a BCC crystal structure above the beta transus. It has been proven that the BCC beta phase has three orders of magnitude greater diffusion than the HCP alpha phase, which correlates well with the results obtained in this study. Furthermore, the diffusion in the HCP alpha phase is anisotropic and is dependent on the orientation of the c-axis [198].

The change in diffusion kinetics when the sample is processed above and below the beta transus has no effect on the average hardness value across the bond, as shown in Figure 5.7. Nevertheless, it is possible to appreciate that throughout the sample, the supertransus hardness measurements are more scattered compared to the subtransus condition. This variation is due to the different microstructures developed after FAST processing (Figure 5.5). The supertransus processed microstructure consists of large grains while the subtransus samples consists of much finer grains. Hence, in the case of the supertransus sample, the hardness indenter tends to apply the load in one large grain, whereas in the subtransus sample, multiple finer grains are tested. The HCP crystal structure has different hardness values depending on the orientation tested [199]. Therefore, testing individual grains - as in the supertransus condition - results in higher variability in the hardness measurements than the average hardness value generated from testing multiple grains – in the subtransus condition. Furthermore, the hardness of the alpha and beta phases are different and the hardness measurements depend on the volume fraction of each phase [200]. Consequently, for the supertransus microstructure, the volume fraction of alpha and beta measured will vary depending if the measurement is taken at the center of the grain or at the alpha-rich grain boundary. Meanwhile, the amount of alpha and beta phase tested for the subtransus material is more homogenous due to the finer microstructure distributed throughout the sample.

### *5.4.2. Deformation behavior of the bond*

The use of DIC provides a more in-depth understanding of the deformation behavior of FAST-DB material processed at sub- and supertransus temperatures, as shown in Figure 5.9 (a). However, the technique has some limitations in terms of resolution because it calculates the strain of a region by averaging several pixels together. Thus, the subtransus specimen shows three well defined strain regions, as the fine grained microstructure for the subtransus specimen results in the DIC averaging multiple grains. The supertransus specimen shows a

graded, less defined variation of strain across the specimen as the DIC is averaging a smaller number of grains due to the larger grain size.

The dissimilar deformation observed in Figure 5.9 is due to the differences in mechanical properties between the two alloys: Ti-6242 has a yield strength ~70MPa higher than Ti-64, hence, the Ti-64 region plastically deforms before the Ti-6242 region. This is shown very clearly in Figure 5.9 (b), where after a total strain of 0.01, the degree of plastic deformation partitioned in the Ti-64 region is much higher than in the Ti-6242.

Another observation is that the microstructural condition of these FAST-DB samples impacts on the differential strain observed between Ti-64 and Ti-6242 regions when processed at sub- and supertransus temperatures. As shown in Figure 5.5 (a), the Ti-6242 region in the subtransus specimen has a finer microstructure than the Ti-64 region, leading to higher tensile properties due to the shorter slip length. Meanwhile, the supertransus sample has a very similar microstructure in both alloys, for this reason the difference in strain between the two alloys in this sample is dominated by the differential alloy chemistry. The finer Ti-6242 microstructure in the subtransus FAST-DB sample (leading to defined strain regions in the DIC analysis) explains the higher ductility to failure compared to the supertransus specimen in Figure 5.8, even though the strain was distributed more homogeneously in the latter. Furthermore, it is shown in Figure 5.9 (b) that Ti-64 subtransus can withstand more plastic deformation than the supertransus microstructure, which is demonstrated by the stress strain curves (Figure 5.8) and the fracture location in Figure 5.10.

The use of optical DIC has provided a better understanding of the local deformation across the chemically graded diffusion bond for supertransus specimens. In Figure 5.12, the results in the Ti-64 region are similar to the ones observed by Littlewood et al [188] for forged Ti-64, in which grains with higher Schmid factor had 3 times more strain than grains with lower Schmid factors. From Figure 5.12 (a), it was expected to see some strain in the soft grain next to the bond because it had a high Schmid factor: the same grain is a hard oriented grain in the basal plane, but it has been reported that slip in prismatic plane has lower CRSS than the basal plane [8,30,180,201]. However, there is no effective shear strain in that region. For the basal plane, there is a soft grain next to the bond but again, very little strain is observed in that region. Figure 5.12 (d) has a similar evolution of the strain than the subtransus specimen

observed in Figure 5.9 (a). In both figures, there is high strain in the Ti-64 region, then, there is a decrease of strain in the bond and it finishes with very low strain in Ti-6242.

The transition region measured in the optical DIC test is more accurate than the one calculated from the standard tensile test (Figure 5.9 (b)): this region has been highlighted with grey dotted lines in Figure 5.13 (b, c) and it shows a region with a constant value of effective shear strain. The distance of that region is approximately 410 µm and the total diffusion length for Zr in the bond is around 360 µm as shown in Figure 5.6 (b). Although the region in Figure 5.13 (b, c) is larger than the measured diffusion in Figure 5.6 (b), it has to be taken into account that this measurement was taken after applying strain to the specimen. Therefore, it is possible that the diffusion distance across the bond is slightly greater than the original measurement. It is clear that the bond acts as a transition zone between the two alloys and that high shear strains and deformation will partition to the lowest strength alloy, i.e. – Ti-64: interestingly, even when a soft oriented grain for easy prismatic slip is present in the bond.

The distinct change in shear stress across the bond correlates with the chemical grading and variation in Al and Mo equivalents from Ti-64 to Ti-6242 as shown in Figure 5.13 (c) for Al equivalent. The Al and Mo equivalent are calculated from equations (3) and (4) and the information in Table II.

For Ti-6242, the Al equivalent is 9.44% and the Mo equivalent is 2.05%; for Ti-64, the Al equivalent is 8.09% and the Mo equivalent is 2.84%. There is a difference of 1.35% in the Al equivalent and 0.79% in the Mo equivalent between the alloys. In the bond region, the Al equivalent is always higher than in the bulk Ti-64, as shown in Figure 5.6 (f). Previous studies [202,203] observed an increment in the strength of the alloy with the increase of the Al or Mo equivalent in titanium alloys. The results also showed that the effect of Al equivalent was more significant than Mo equivalent in the strength of the alloy. Additionally, Williams et al [30] observed that the CRSS increased in a TiAl alloy when the Al content increased. This could explain the fact that there is no effective shear in the soft grain for the prismatic plane that is crossing the bond in Figure 5.12.

The higher Al equivalent content will increase the strength of the alloy due to a higher solid solution strengthening effect [37]. This agrees with the observed deformation within the diffusion bond when there is gradual change in the alloy chemistry from Ti-64 to Ti-6242. The Al equivalent profile across the diffusion bond, shown in Figure 5.13 (c), has a smooth

transition between the alloys and it reaches its lowest value in the bulk Ti-64. Therefore, the diffusion bond region has a local higher strength due to the higher solid solution strengthening effect compared to the bulk Ti-64. However, it is important to consider that the microstructural variables can affect the performance of the bond and not all titanium alloy combinations have a smooth transition across the bond. For example, Pope et al [9] observed a fine secondary alpha in the diffusion bond region between Ti-5553 with CP-Ti or Ti-64, which created a hardness peak at the bond. The tensile samples still failed in the lower strength alloy, but the unexpected microstructure in the bond could have reduced the mechanical integrity of the bond.

# 6. *Residual Stresses*

## *6.1. Introduction*

The ability to accurately bond dissimilar materials without degrading the structural integrity of critical components would enable designers to optimise key components and systems. However, a joint between two materials can potentially create chemical, thermal or plastic deformation induced mismatching, that could introduce residual stresses in the bond [39,204].

Residual stresses are remaining stresses inside a component when no external stress is applied. These stresses can have a direct impact on the mechanical properties and service performance of a component. Under fatigue loading, a component with high tensile residual stresses will fail at lower cycles to failure than the same component with low inherent residual stresses from the manufacturing process [4,205]. However, there is an improvement in the fatigue life of the component when there are compressive residual stresses, as such stresses oppose the initiation and opening of surface cracks [4,206–210]. Fairfax et al [211] showed that from 147 residual stresses failure cases analysed, 55 of these involved some type of joint or bond. Therefore, it is essential to understand the formation of residual stresses when developing new joining and diffusion bonding processes.

Two of the most common techniques in the aerospace sector are electron beam welding (EBW) and inertia friction welding (IFW). Nevertheless, there is an increase of residual stresses in the joint when joining titanium alloys with EBW [123,212,213] and LFW [6]. Most of the residual stress investigations carried out on EBW and LFW have focussed on joining the same titanium alloy, but there are a few investigations that focus on joining dissimilar titanium alloys. Xie et al [214] investigated the residual stresses of a LFW joint between a $\beta$ processed Ti17 and an $\alpha + \beta$ processed Ti17 using both the (1) contour and (2) X-ray diffraction (XRD) method. The results showed an initial asymmetric tensile peak in the join with a 440 MPa peak on the $\beta$ Ti17 side, a 350 MPa peak on the $\alpha + \beta$ Ti17 side and a stress of 200 MPa at the

centre of the weld. Bandyopadhyay et al [215] joined Ti-64 to Ti-5553 using LFW and used the energy-dispersive XRD method to characterise the residual strain in the bond. Again, a peak was observed across the bond with a higher strain in the Ti-5553 region. However, this residual stress peak was reduced after further heat treatment at 704ºC for 2h with a subsequent air cooling stage.

There are a limited number of investigations measuring the residual stresses produced during the consolidation of powder using FAST or HIP routes. The residual stress measurements carried out on the more established HIP process can be used as a benchmark for FAST processed material, as the cooling and unloading stages are very similar. Li et al [33, 34] predicted potential residual stresses in HIP caused by thermal stresses due to non-uniform densification of the powder. The heat source in HIP is surrounding the canned powder, this heat can lead to quicker densification of the external powder layers. This external layer, termed “densification wave”, can support the load that creates this non uniform densification. It was observed that the unloading of the sample is the critical stage for the formation of the residual stresses. An approach to reduce the residual stresses in the unloading stage was to closely control the pressure and temperature. These observations agree with the predictions calculated by Bahei-El-Din et al [216] whereby the cooling rate has the greatest influence on the residual stress profile in HIP processed material. Nevertheless, the effect of the pressure was only significant when the cooling rate was higher than 1ºC/s. In addition, the prediction showed that the HIP dwell time had little effect on residual stresses. Parker et al [217] measured the residual stresses of Inconel 718 joined to tungsten through HIP with an XRD method. It was observed that the residual stresses in the axial and hoop directions were relatively low (190 and 160 MPa, respectively). There have been a couple of investigations on the residual stresses generated through FAST during the consolidation of tantalum and ruthenium. Angerer et al [218] compared the residual stresses between FAST and hot pressing (HP) of a sample made of tantalum. They showed that there was no difference in the RS profiles between the two processing routes, with both samples showing a compressive stress normal to the component and tensile parallel to the component. The exact same approach was applied to ruthenium [219] where in this case, FAST reduced the residual stresses in relation to HP, which according to the authors, was due to the more rapid grain growth in the FAST material.

As yet, there has been no investigation into the development of residual stresses when applying FAST for the consolidation of titanium alloy powders or to diffusion bond two different titanium alloy powders.

This chapter investigates the residual stresses produced during the bonding of two dissimilar titanium alloy powders through the FAST process. Furthermore, the study shows the residual stress evolution in bonds of near-net shape components that have been subsequently hot forged using the FAST-*forge* route [104].

## *6.2. Methodology*

In this study a total of four different 60 mm diameter disks (Figure 6.1) were made using the FAST method. The alloys used were Ti-64, Ti-6242, Ti-5553 and CP-Ti. Furthermore, two near-net shaped components from a previous study [16] were used (Figure 6.2), one made of Ti-5553/Ti-64 and the other one made of Ti-64/Ti-6242.

### *6.2.1. Materials*

A total of four titanium alloy powders were used in this study to make the 60 mm diameter disks and the Ti-64/Ti-6242 near-net shaped component: Ti-6Al-4V (Ti-64_2), Ti-6Al-2Sn-4Zr-2Mo (Ti-6242_2), CP-Ti and Ti-5Al-5V-5Mo-3Cr (Ti-5553). The detailed information of these powders can be found in Chapter 4. The information of the material used for the Ti-5553/Ti-64 near-net shaped component can be found in Pope et al [10].

### *6.2.2. Experimental procedure*

The 60 mm as FAST disks were made at the University of Sheffield using an FCT Systeme GmbH SPS Furnace Type HP D 25. Table 6.1 shows all the as FAST disk produced at the University of Sheffield with the corresponding processing conditions and the nomenclature that will be used in this chapter. A general description of the procedure followed to make samples using FAST can be found in Section 3.2.

To make the samples FDB1, FDB2 and FDB3 it was necessary to introduce a 3D printed polymer divider with a shape of a cross into the graphite ring, like the one in Figure 3.3. Then, half of the graphite ring was filled with one titanium alloy powder and the other half with a different titanium alloy powder. Figure 6.1 (a) shows the state of the sample lay up when the plastic divider is removed from the graphite ring. Then, after following the steps described in Section 3.2.1, the sample was processed using FAST.

A total of four different processing parameters were used to produce the as-FAST material, see Table 6.1 . The dwell temperature used to process the samples was 30°C higher than the highest beta transus of the alloys processed, with the only exception of FDB3. At the end of the dwell stage, the sample was left to cool inside the vacuum chamber and the pressure decreased from 35 MPa to 1 MPa during the first minute of the cooling cycle.

For the residual stress characterization, a total of two samples were made for each of the FAST processing parameters: one sample was analysed using XRD and the other using the contour method [220]. For FDB3 conditions, only one sample was made, and it was analysed with XRD. Figure 6.1 illustrates the three processing steps carried out for each sample; furthermore, Figure 6.1 (c) shows the locations in the samples where the RS analysis was undertaken using the XRD and the contour methods.

The near-net shaped components were processed using the FAST-*forge* manufacturing route. More details about how FF1 and FF2 were made can be found in Pope et al [10] and Section 3.3 respectively.

### *6.2.3. Residual stresses*

The residual stress measurements were carried out across the bond using X-Ray Diffraction (XRD) and the contour method. The hole-drilling based on ESPI method was discarded as it can only process the stresses in a single alloy. The method required 3 strain gausses distributed around the hole to measure the changes of strain. Then, the measurement of each strain gausses is combined with the properties of the materials to calculate the final residual stresses. If this method is used for more than one alloy, the final residual stresses would be wrong because the method requires the three measurements made in the same alloy and

that would not be possible in a bond. Therefore, it was determined that the technique would not show effective results across the bond between the two alloys.

***Table 6.1*** *– Summary of the FAST processing parameters for each sample.*

| | | | | FAST processing parameters | | | | |
|---|---|---|---|---|---|---|---|---|
| | **Name** | **Diameter (mm)** | **Alloys** | **Heating Rate (°C/min)** | **Pressure (MPa)** | **Dwell Temperature (°C)** | **Dwell Time (mins)** | **Cooling Rate (°C/min)** |
| **As FAST** | F1 | 60 | Ti-64 | 100 | 35 | 1030 | 20 | 63 |
| | FDB1 | 60 | Ti-64 / Ti-6242 | 100 | 35 | 1030 | 20 | 63 |
| | FDB2 | 60 | CP-Ti / Ti-5553 | 100 | 35 | 930 | 20 | 63 |
| | FDB3 | 60 | CP-Ti / Ti-5553 | 100 | 35 | 1000 | 20 | 63 |
| **FAST-forge** | FF1 | 250 | Ti-64 / Ti-5553 | 25 | 35 | 1200 | 60 | 6.5 |
| | FF2 | 250 | Ti-64 / Ti-6242 | 25 | 32.5 | 1030 | 60 | 6.5 |

#### *6.2.3.1.* X-Ray Diffraction

The equipment and method used to measure the residual stresses with XRD was the Proto LXRD Stress Diffractometer and the $\sin^2\psi$ method [221]. The measurements were done under the standardised method using the NPL Good Practice Guide ISO 17025. The XRD measured surface residual stress in-plane, 2D and shear stress to a depth of 10-50 μm. To obtain the diffraction peaks from the crystallographic planes, two anode targets were used. For α and α+β type titanium alloys, a copper anode target with a wavelength of 1.54 nm was selected to measure the diffraction peak for the {2 1 3} crystallographic plane. For the metastable β

titanium alloy, a vanadium anode target with a wavelength of 2.50 nm was selected to measure the diffraction peaks for the {2 1 1} crystallographic plane. A nickel filter was used for all the alloys. The XRD scan for FDB2, FDB3 and FF2 was carried out across the bond with one anode, and then repeated with the second anode. The data was combined together with the bond as the reference. The strains in {2 1 1} and {2 1 3} produced by the Bragg reflections were used to calculate the stresses. The Bragg's angle varied for each alloy, for CP-Ti and Ti-6242 it was 139.69°, for Ti-64 it was 142° and for Ti-5553 it was 145°. The Young's modulus and the Poisson's ratio used to calculate the residual stresses are shown in Table 6.2. A total of 10 profiles were characterized for each measurement with an exposure time of 4 seconds per profile. The beta angle varied between 0-30° for axial measurements and 0-25° for radial measurements. The oscillation of the beta angle was $\pm$ 3˚ and the round collimator used had an aperture size of 1 mm diameter. A measurement of the background noise was done before and after the samples measurements to clean the final signal. To measure the XRD in the as FAST material, they were first sectioned in half with a Secotom-20 and then electropolished with a Struers Lectropol-5 electrolytic polisher to ensure that there was minimal residual stress generated from the mechanical cut. The measurements of the as FAST material were conducted across the bond, as shown in Figure 6.1 (c). Contrary to that, the measurements for the FAST-*forge* components were made in the surface as shown in Figure 6.2.

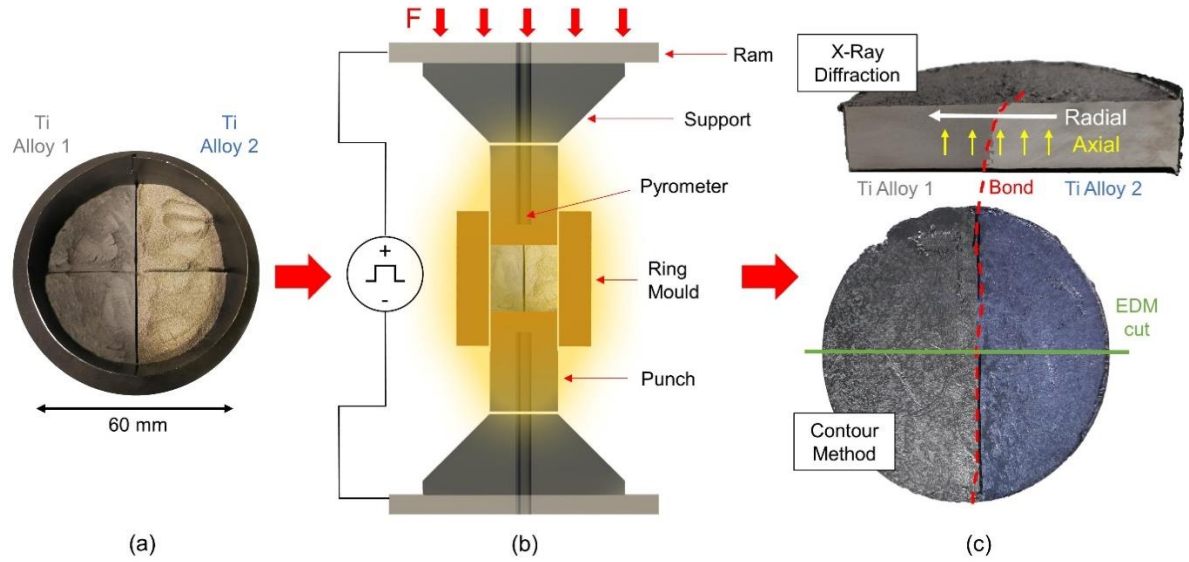


***Figure 6.1*** *– Photograph of the two titanium alloys powders in the graphite ring mould after removing the dividers. b) Cross section schematic of a FAST machine. c) Photograph of the samples after being process with FAST. The sample sectioned in half shows the location were the XRD measured the residual stresses and the bottom samples shows the location of the EDM cut.*

***Table 6.2*** *– Summary of the mechanical properties used for the calculation of the residual stresses.*

| | CP-Ti | Ti-6242 | Ti-64 | Ti-5553 |
|---|---|---|---|---|
| **Young's modulus (GPa)** | 105 | 111.5 | 114 | 110 |
| **Poisson's ratio** | 0.37 | 0.32 | 0.342 | 0.285 |

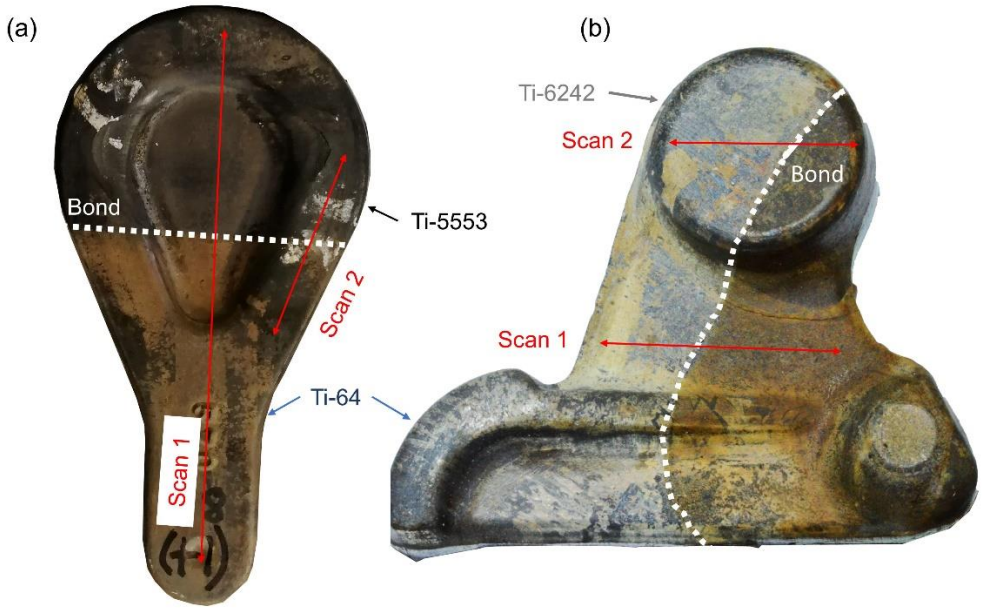


***Figure 6.2*** *– Photograph showing the XRD scanning paths for (a) eyebolt (FF1) and (b) rocker arm (FF2).*

### *6.2.3.2.* Contour method

The contour method developed by Prime [220] was used to measure the stresses across the plane of several bonds. First, the samples were sectioned with wire electrical discharge machine (EDM) to ensure a "stress-free" cut. The equipment used to section the sample was the Agie Charmilles CUT 400 Sp Electrical. The sample was cut with a 0.25 mm brass wire using a steady rate and the samples were clamped at both sides to ensure a stable cut. The two sectioned planes were then scanned with an Alicona Infinite Focus IFM G4 to obtain the 2D surface profile. The Alicona scans were conducted at 5x magnification using a 1 μm vertical resolution and 10 μm lateral resolution. Then, the data obtained with the 2D scan was cleaned by removing all the outline points and noise. The data from each half was aligned and it was calculated the average value of residual stress. This process was done using the software

MATLAB®. Some of the samples could not be averaged because there were significant differences between both halves due to poor clamping. However, the data from those samples is presented for each halve individually.

To evaluate the residual stresses, it was necessary to build a 3D finite element (FE) model with Abaqus™ using the data obtained from the scans and the mechanical properties in Table 6.2. A GOM ATOS TripleScan III was used to create the 3D models for the FE model. Then, the bond between the two alloys with its respective mechanical properties was defined in the 3D models. The measurement of the residual stress through the FEM software was evaluated by calculating the necessary stresses in the material to obtain a surface like the one scanned after sectioning the sample with EDM. The location of the EDM cut for the as-FAST material is shown in Figure 6.1 (c), while the EDM cut for the FAST-*forge* material is shown in Figure 6.3.

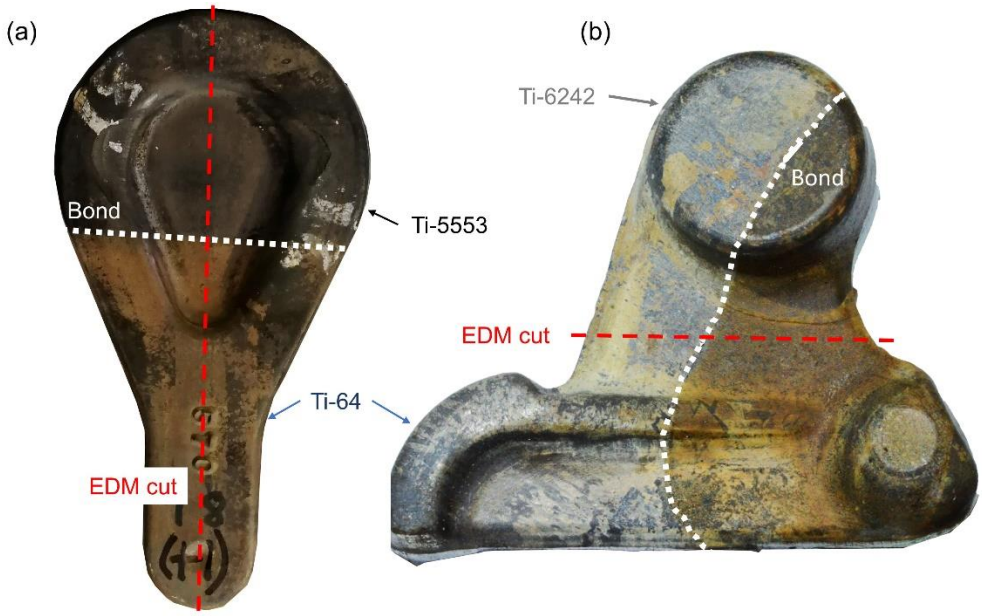


***Figure 6.3*** *– Photograph of the two final FAST-DB near net shape components with the location of the EDM cut for(a) eyebolt (FF1) and (b) rocker arm (FF2).*

### *6.2.4. Analysis techniques*

Prior to analysis, samples were metallographically prepared using progressively finer grit SiC grinding paper. The final polishing stage was conducted with 0.06 µm colloidal silica combined with 10% concentration hydrogen peroxide with an MD-Chem pad cloth. All the metallographic procedure was carried out with a Struers Tegramin-25. The microstructure of

the titanium alloys was viewed with the optical microscope Nikon Eclipse LV150 and with the FEI Inspect F50 SEM. The final density of the samples was measured with the Clemex software following the procedure explained in Section 3.5.3.

The X-EDS point scans were measured using the Philips XL30 SEM, more details can be found in Section 3.5.2. The hardness profile was obtained with a Struers Durascan 70 G5 and a detailed procedure can be found in Section 3.4.1.

## 6.3. Results and Discussion

### 6.3.1. Characterization of as FAST material

The microstructure of the samples produced using FAST for this study are shown in Figure 6.4. The primary observations are that F1 and FDB1 have reached a densification of 99.98% and no porosity is visible in Figure 6.4 (a, b). However, the FAST-DB samples FDB2 and FDB3 have some visible porosity, especially in the Ti-5553 region, as shown in Figure 6.4 (c, d). The final density for Ti-5553 in FDB2 and FDB3 is 99.82% and 99.40%, respectively. Yet, the final density in CP-Ti for FDB2 and FDB3 is 99.92% in both cases. It is possible to obtain a higher densification for these alloys, as shown by Pope et al. [9], however, the temperature and dwell time used in this work was not high enough to fully consolidate these powders. Nevertheless, this small amount of porosity should not affect the residual stress measurements of the FAST material.

The F1 sample has a classic fully transformed, large equiaxed grain structure (300-500 µm). The sample was cooled from 1030°C with an average cooling rate of 63°C/min, which created a relatively fine α lamellas with an average width of 2 µm. The same microstructure was also achieved for FDB1 sample in the Ti-64 region, as the processing conditions were the same. The Ti-6242 side in FDB1 also has a classic fully transformed, large equiaxed grain structure but the size of the grains is slightly smaller (200-300 µm) and the α lamellas average width is 1.5 µm. The bond between the two alloys has a smooth transition from the darker Ti-64 alpha colonies to the brighter ones in Ti-6242. Furthermore, there is not a noticeable change in the secondary alpha size or morphology, as shown in Figure 6.4 (b). The change of brightness between the two alloys in the micrographs is due to the higher atomic weights of the elements in the Ti-6242 alloy, such as Zr and Sn.

The microstructure in FDB2 and FDB3 in Figure 6.4 (c, d) is very similar and the main difference between them is the temperature at which they were processed. The CP-Ti microstructure consists in large grain size with plate like substructures while the microstructure of Ti-5553 consists of large prior β grains in both samples (100 - 300 µm). The bond between the two

alloys transitions from an α alloy to a β alloy, which creates a microstructure with the formation of lamellas and fine secondary alpha [9].

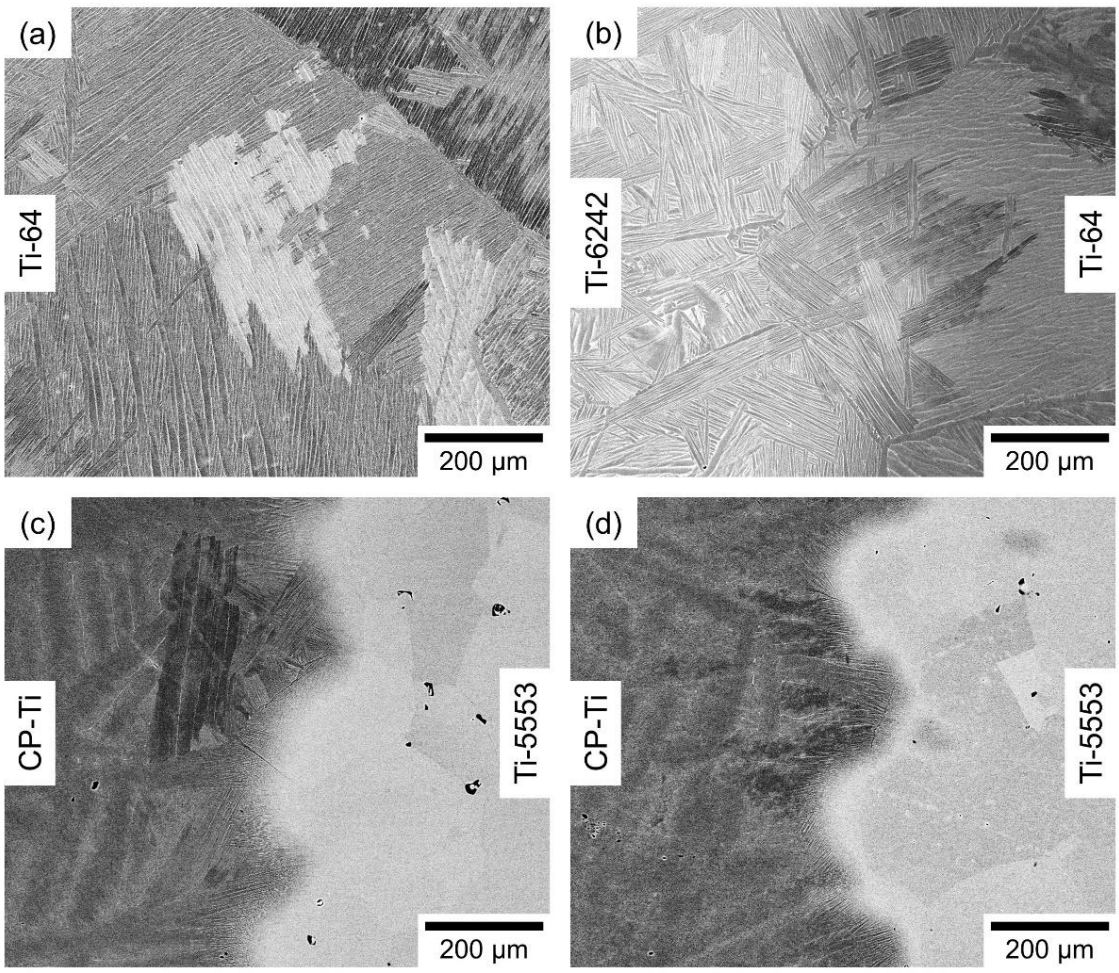


***Figure 6.4*** *– Backscatter electron micrographs of the as FAST samples for (a) Ti-64 (F1), (b) Ti-6242 / Ti-64 (FDB1), (c) Ti-5553 / CP-Ti (FDB2) and (d) Ti-5553 / CP-Ti (FDB3).*

The diffusion profiles for the three bonds (FDB1, FDB2 and FDB3) are shown in Figure 6.5 and they were measured with X-EDS. The diffusion of the elements across the bond for all the samples is relatively small, if compared to standard joining conditions where the HAZ can reach a few millimeters. The length of the diffusion zone across the bond was used to determine if the residual stresses measured were due to a possible chemical misfit across the bond.

For FDB1, the element with higher diffusion is V with an approximate diffusion of 220 µm. Meanwhile, for FDB2 and FDB3 the element with higher diffusion is Al with an approximate diffusion of 270 µm. FDB3 has significant higher diffusion of the elements compared to FDB2

due to their respective processing temperatures. Overall, it is safe to assume that for the three FAST-DB samples, the diffusion zone across the bond will probably be less than 300 µm.

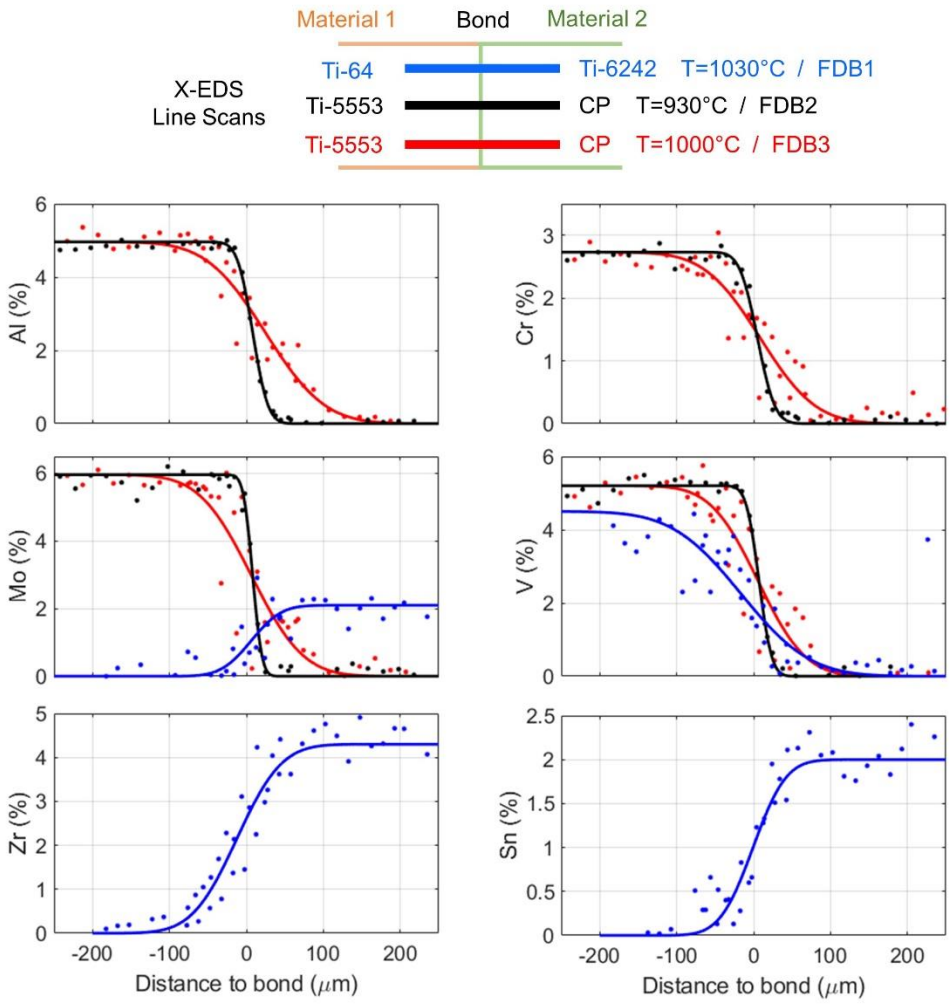


***Figure 6.5*** *– Diffusion profiles of the six elements that comprise of the titanium alloys Ti-64, Ti-5553 and Ti-6242. Each graph represents the diffusion profile across the bond of one FAST-DB sample.*

The microhardness variation across the bond for the three samples is plotted in Figure 6.6. The plots have been divided between FDB1, that has a bond made of two similar titanium alloys, and FDB2 and FDB3, that have a bond made of contrasting types of titanium alloys; these two plots present different hardness behaviours. On the one hand, the hardness across the bond FDB1 does not present any noticeable changes because both alloys have a similar hardness value. On the other hand, the hardness across the bond for FDB2 and FDB3 present a clear transition of hardness between CP-Ti and Ti-5553. CP-Ti bulk material has an average hardness of 160 Hv while Ti-5553 has an average value of 300 Hv. Therefore, the hardness increases in a steady state from the alloy with lower hardness to the one with highest

hardness. The difference in the diffusion profiles between FDB2 and FDB3 observed in Figure 6.5 seems to have little effect in the behaviour of the hardness across the bond. In comparison with the results obtained by Pope et al [9], a peak of hardness in the bond region has not been observed. This will be discussed in more detail in Section 6.3.2.3.

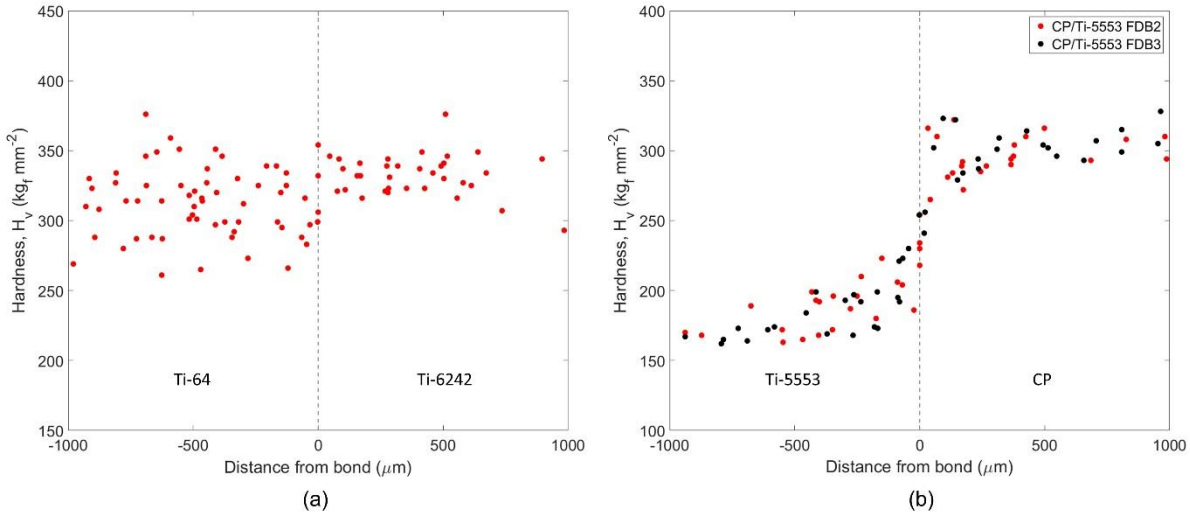


***Figure 6.6*** *– Graphs plotting the hardness profile across the bond for (a) FDB2 and FDB3, (b) FDB1.*

## *6.3.2. Residual Stress measurements of as FAST material*

The residual stress measurements were conducted with the contour method for a general measurement of the sample and with the XRD method for a more precise measurement across the bond.

### *6.3.2.1. Ti-64 (F1)*

In Figure 6.7 is shown the displacement field of the sample and the residual stresses measured for the monolithic Ti-64 (F1). The Alicona scan on the EDM face obtained a high precision profile that revealed small displacements. However, there was a mismatch of the two halves due to cutting artefacts that were intensified because of the low stresses measured. Figure 6.7 (a) shows a negative displacement of the core of the disc with a positive displacement in the outer layer.

The residual stresses measured with the contour method show compressive stresses in the core of the disc and tensile stresses in the outer layer, see Figure 6.7 (b). The intense blue areas in the core of the disc are due to the EDM artefacts. Furthermore, the stresses

measured in the far left of the samples are due to the hole made in the disc to cut the sample with wire-EDM, as explained in Section 6.2.3.2. Overall, the stresses measured in the sample are very low, which is expected from a relatively slow cooled sample.

Figure 6.8 presents more precise measurements done in F1 with the XRD method. The residual stresses and the shear stresses measured across F1 are in agreement with the contour method results. The stresses are very low throughout the sample with the maximum values measured around 100 MPa.

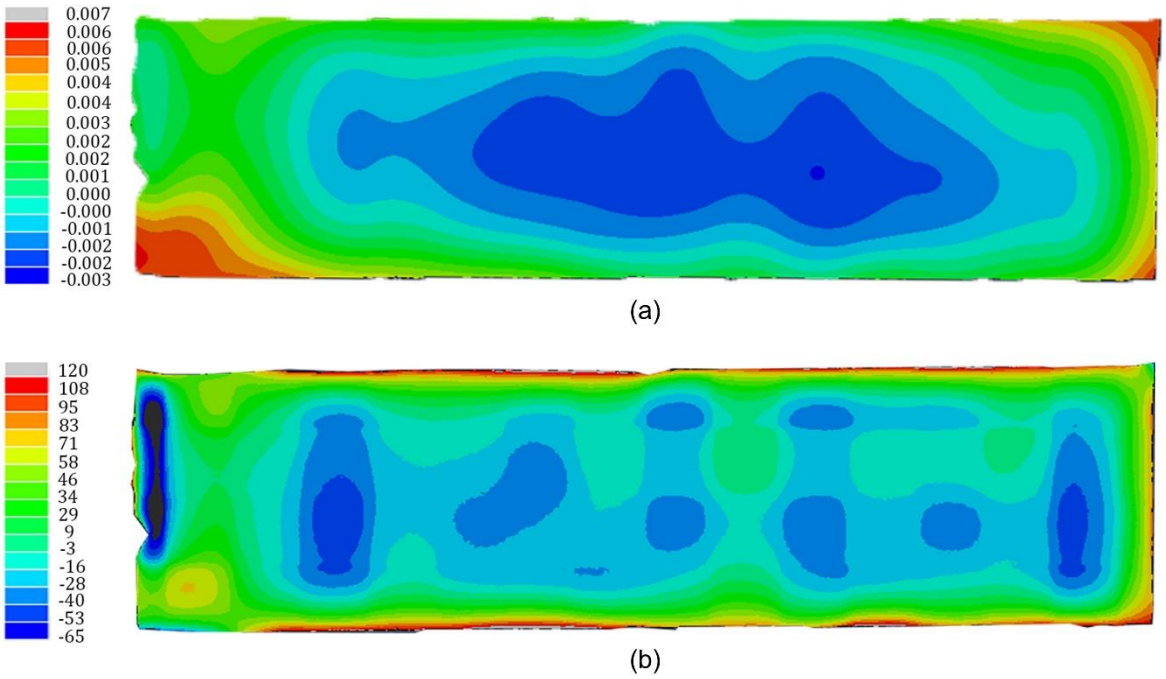


***Figure 6.7*** *– (a) Average value of displacement for the wire-EDM faces of F1; (b) residual stresses of F1 sample in the cross section of the disc.*

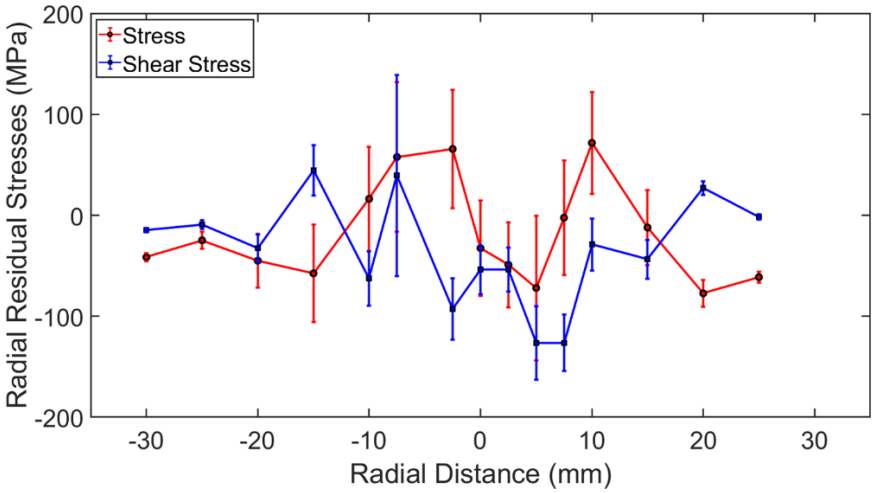


***Figure 6.8*** *–Plot of the radial residual stresses of the F1 sample measured with XRD.*

#### *6.3.2.2. Ti-64 / Ti-6242 (FDB1)*

In Figure 6.9 is shown the displacement field and the stresses measured with the contour method for the FDB1 sample. The surface scan carried out with the Alicona obtained a high-resolution surface profile with no clear indication of the bond location. The results also showed non-matching halves due to low stresses in the material, which highlighted the cutting artefacts produced by the wire-EDM in the sample.

Figure 6.9 (a) presents the averaging displacements of both halves, that led to identify two different displacement behaviours in the centre of the sample. However, this difference in the displacement has little effect on the residual stresses measured in the region of the bond, as shown in Figure 6.9 (b). Additionally, there seems to be an increase of the stresses near the edge of the Ti-64 region, but this is caused due to the hole made in the sample, in order to section it through wire-EDM. Overall, the stresses in this component are very low and the general trend observed is the formation of a compressive core and a tensile outer skin, similar to F1 in Figure 6.7 (b). However, with this result it is difficult to determine the stresses in the bond.

There are various factors that can affect the lack of accuracy of contour method in the bond. The diffusion in the bond is very small, in the order of 200 µm for FDB1 and 50 µm for FDB2, as shown in Figure 6.5. Additionally, the joined materials have similar elastic parameters, which are used to calculate the stresses in the contour method model, as explained in Section

6.2.3.2. Furthermore, the contour method lacks the lateral resolution of other techniques due to roughness from the wire-EDM cut.

Some of these issues can be solved by using higher resolution technique such as the XRD. Nevertheless, to measure the residual stresses across the bond, an alternative approach had to be used. Laboratory ("soft") X-rays cannot provide the required resolution due to larger apertures for the given beam intensity. Larger apertures provide a surface area averaged measurement while smaller apertures require extremely high collection times. Furthermore, titanium alloys require high collection times compared to other metals such as steel or nickel alloys. The alternative approach was to use a sequential, overlapping scan across the interface.

The measurements of the XRD technique are shown in Figure 6.10. The residual stress in the Ti-6242 region tend to have a slight increase towards the bond, before decreasing again in the Ti-64 region. The stresses measured through the sample are low, which matches with the results obtained with the contour method. The shear stress measured for this sample has a similar trend to the residual stress measurements.

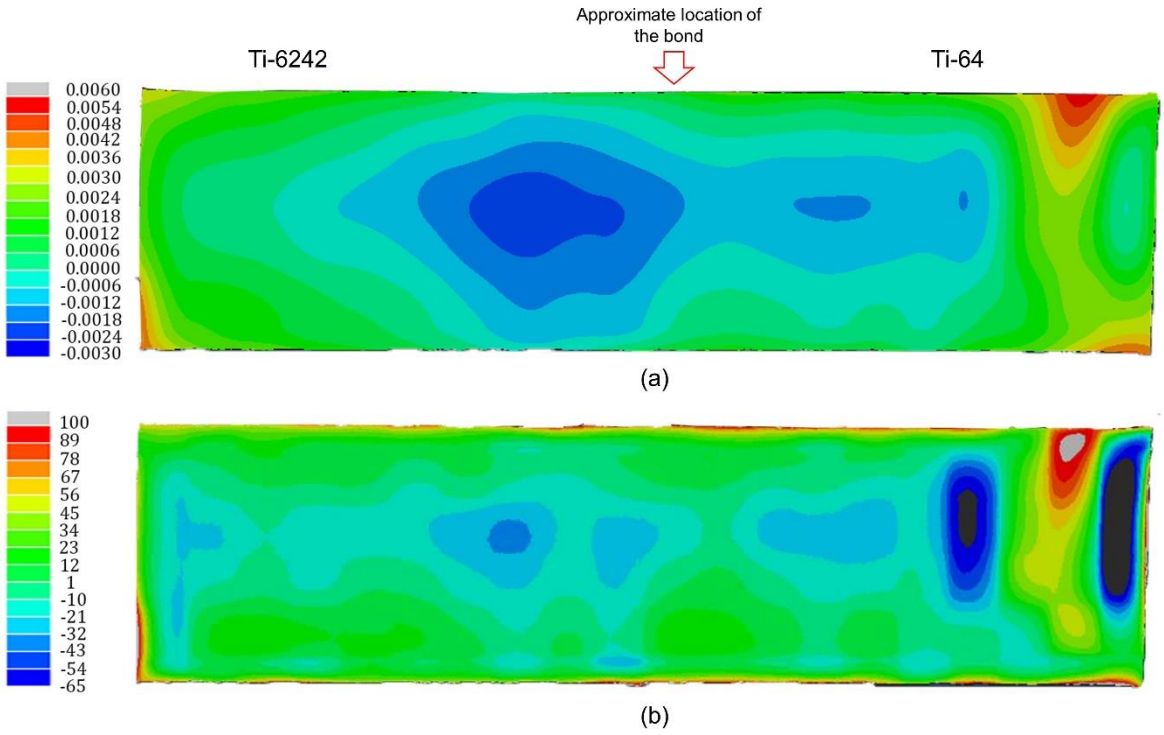


***Figure 6.9*** *– (a) Average value of displacement for the wire-EDM faces of FDB1; (b) residual stresses of FDB1 sample in the cross section of the disc.*

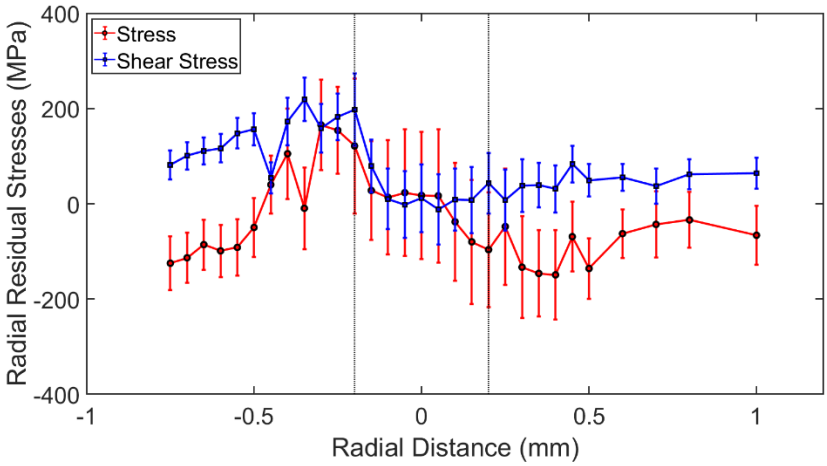


***Figure 6.10*** *– Radial residual stresses plot of the FDB1 sample measured with XRD.*

### *6.3.2.3.* CP-Ti / Ti-5553 (FDB2, FDB3)

Figure 6.11 shows the displacement field and the residual stress profile calculated with the contour method for FDB2. The Alicona scan obtained a high-resolution surface profile of the EDM face. However, there was a mismatch between the two halves due to cutting artefacts that were intensified by the low stresses in the sample. Nevertheless, the averaging of both halves led to a possible distinction of the bond region, as shown in Figure 6.11 (a). These variations in the displacement can be observed in the residual stress profile in Figure 6.11 (b). The value of the stresses between CP-Ti and Ti-5553 are very similar but there seems to be a larger region of compressive stress in CP-Ti compared to Ti-5553. The stresses on the sample are very low and the general trend observed in the sample is the formation of a compressive core and a tensile skin. The stresses across the bond seem to have a smooth transition from one alloy to the other. Nevertheless, the contour method does not have the resolution to provide any conclusive results for the reasons explained in Section 6.3.2.2.

Figure 6.12 shows the results obtained with XRD scans across the bond for the samples FDB2 and FDB3. As explained in Section 6.2.3.1, the alpha and the metastable beta type alloys had to be measured with different sources, hence, why there are four measurements plotted for the radial residual stresses in Figure 6.12 (a, b). The radial stresses and shear stresses measured across the bond differ significantly between the two samples. FDB2 has very low residual stresses across the bond for both phases while FDB3 has moderate to high compressive radial stresses and tensile shear stresses towards the interface. Despite the values of the residual stresses, both samples have a similar profile, showing an increase of

residual stresses towards the interface from the alpha phase. A similar trend is observed for the axial stresses in the alpha region, where there is an increase of the stresses towards the bond. The values of the axial residual stress are higher than the radial residual stress for both samples. Furthermore, the axial residual stress shows a compressive behaviour towards the bond for FDB2 and a tensile behaviour towards the bond for FDB3.

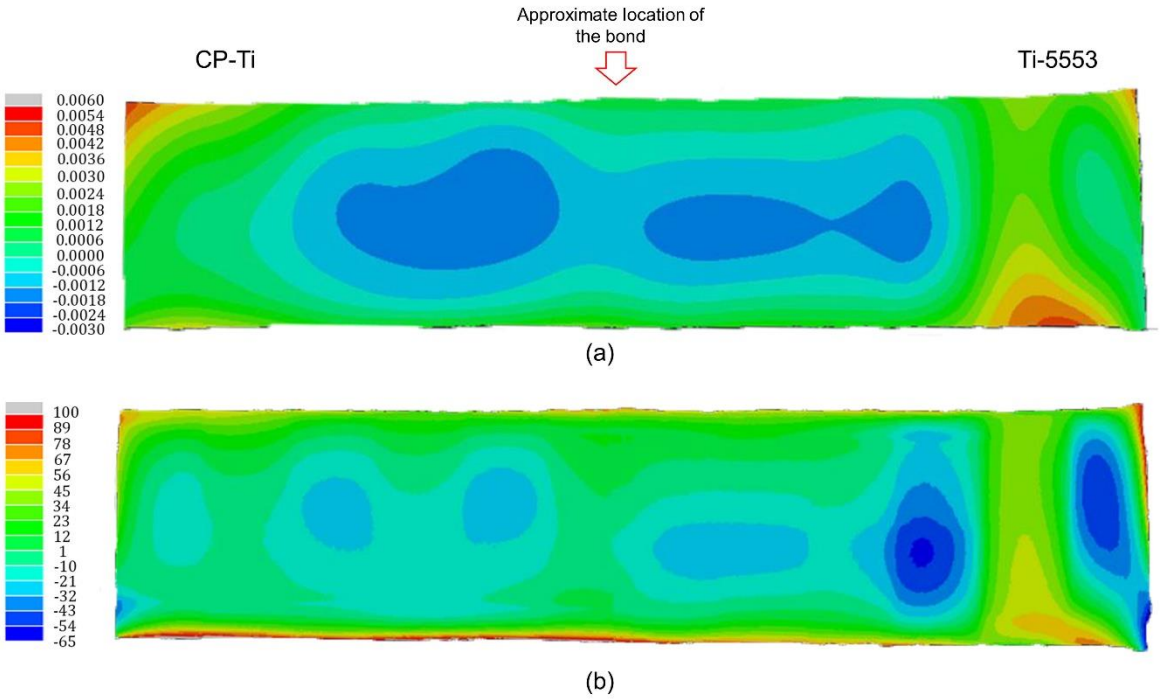


***Figure 6.11*** *– (a) Average value of displacement for the wire-EDM faces of FDB2; (b) residual stresses of FDB2 sample in the cross section of the disc.*

The significant change of radial residual stresses measured between FDB2 and FDB3 could be due to the technique used. It is possible to obtain an increase in stress across the bond due to multiple reasons such as dissimilar thermal, plastic deformation or chemical mismatch [39,204]. It is likely that the increases of strain in the bond is a consequence of a chemical mismatch due to the change of microstructure between a CP-Ti and Ti-5553.

One of the microstructures that can form in a bond between these two alloys is a fine secondary alpha that increases the hardness at the bond, as observed by Pope et al [9]. The formation of these fine secondary alpha in conventional Ti-5553 are due to an ageing heat treatment with a temperature ranging within 400-650°C. The size and volume fractions of the alpha phase increase when increasing the aging temperatures [222]. It has been observed that the alpha phase forms within 90-120 s after reaching the aging temperature for Ti-5553

quenched and aged 570°C [223]. Furthermore, when Ti-5553 is aged at 600°C, the formation of alpha can occur after 0 s [224]. FDB2 and FDB3 did not have an ageing heat treatment but the cooling rate was relatively slow (66°C/min), which could be equivalent to a very short aging process. Only fine secondary alpha was observed in the bond location; however, this could also be due to the local chemistry produced in the bond. For example, Manda et al [225] observed that the alpha phase precipitation was easier for chemistries with lower formation energy/atom values. The precipitation of the alpha in the beta matrix can produce residual strains in the microstructure, as pointed out by Zheng et al [224]. These residual strains can be produced because a short aging heat treatment will not produce a thermodynamic equilibrium microstructure. Therefore, it is likely that the interface between the two phases will not be fully coherent.

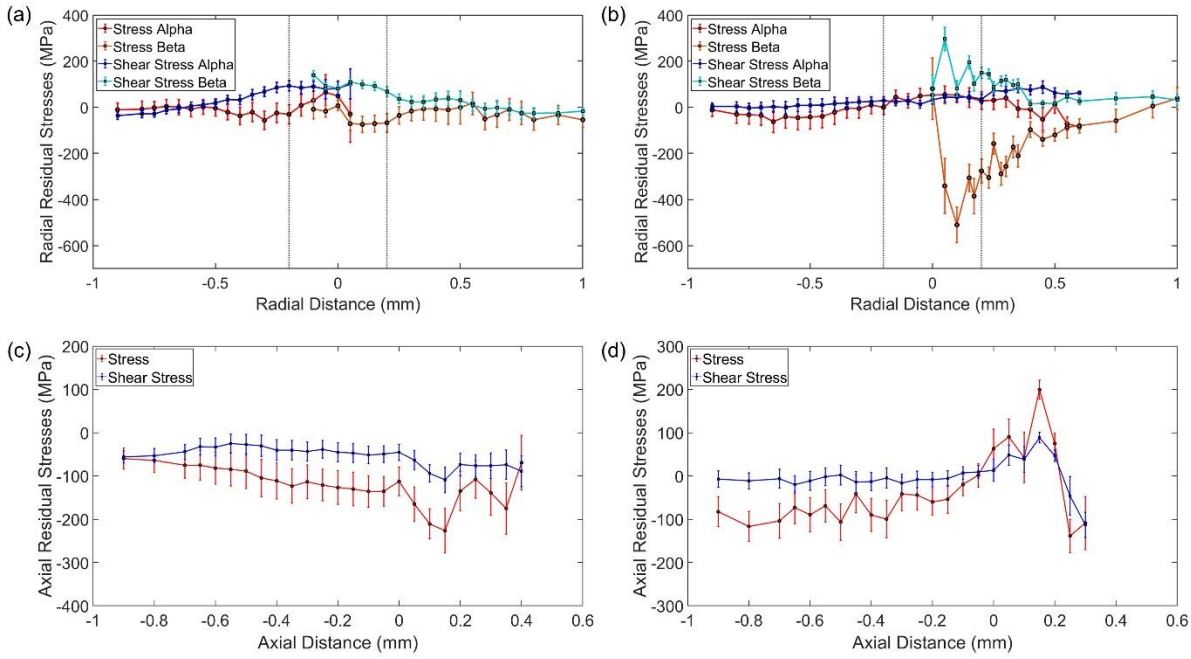


***Figure 6.12*** *– Plot measured with XRD of radial residual stresses (a) FDB2, (b) FDB3; and axial residual stresses (c) FDB2 and (d) FDB3.*

The samples that Pope et al [9] tested were processed at 1200°C, which is 200-270°C higher than the temperature used to process the samples in this chapter. Although the hardness profile in Figure 6.5 does not show a peak of hardness in the bond for any of the samples, fine secondary alpha has been observed in the bond for FDB2 and FDB3, as shown in Figure 6.13 (a, b) respectively. One possible reason why the hardness does not show a peak is because the region with fine secondary alpha is only 10 µm for FDB3 (Figure 6.13 (d)) and less for FDB2 (Figure 6.13 (c)). Hence, it is very difficult to caption this with a micro indentation.

The XRD method used to measure the residual stresses across the bond consisted of overlapping the different scans analysed in the sample, as explained in Section 6.2.3.1. One of the issues with measuring the stresses in this manner, is that the final values have to be averaged between the multiple overlapping measurements. Therefore, it is possible that certain stresses in very small areas have been removed when averaging the values. The diffusion profile for FDB2 is only 50 µm while for FDB3 is 200 µm, as shown in Figure 6.5. For this reason, it is a possibility that the peak of residual stresses observed in FDB3 it also happens in FDB2.

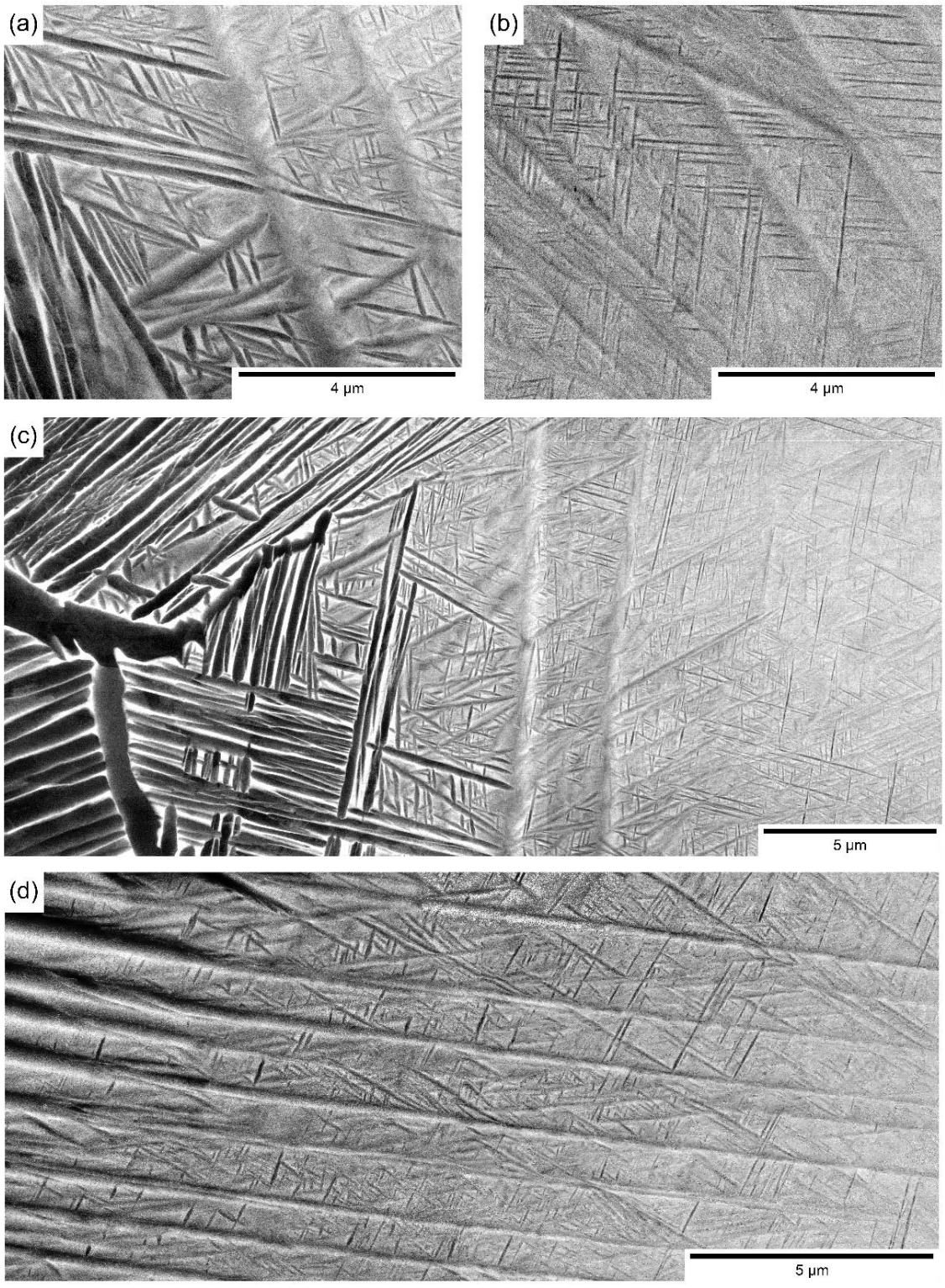


***Figure 6.13*** *– Backscatter electron micrograph and mosaics at high resolution of the bond between CP-Ti and Ti-5553 for (a, c) FDB2 and (b, d) FDB3.*

### 6.3.3. FAST-forge

The residual stresses were also measured from FAST-*forge* material produced from dissimilar titanium alloys. In Section 6.3.2., it has been shown that the residual stresses produced across the bond of as-FAST material are relatively low. In this section, the residual stresses are measured from two different near-net shaped components; one component is made of Ti-6242/Ti-64 (FF1) and the other component is made of Ti-5553/Ti-64 (FF2).

#### 6.3.3.1. Characterization Ti-5553/Ti-64 (FF1)

The near-net shaped component FF1 is shown in Figure 6.14 with micrographs of the bond and a 2D hardness map of the region in the bond. The bond of the forged component can be divided in two different types of bonds; one bond that is perpendicular to the forging direction (BT1) (Figure 6.14 (a, b)) and one bond that is parallel to the forging direction (BT2)(Figure 6.14 (c, d)). All the micrographs show a clear region and a darker region that corresponds to Ti-5553 and Ti-64, respectively.

The BT1 shows the grain limits for Ti-5553 slightly deformed due to the high strain produced during the forging. Furthermore, it is observed an absence of any clear microstructural features as a result of heating the material above the β transus and quenching it at the end of the process. The Ti-64 alloy in BT1 has an equiaxial microstructure due to dynamic globularisation mechanism cause by the high strain suffered during the forging process [226]. It is also observed that the microstructure in the bond has a very sharp transition.

The BT2 has the same microstructure for Ti-5553 observed in Figure 6.14 (a) but in this case the Ti-64 has a deformed Widmanstätten microstructure. Contrary to BT1, in BT2 there is a transition of the microstructure across the bond as shown in Figure 6.14 (d). The darker lamellas in Ti-64 start to get brighter across the bond until they reach the Ti-5553 microstructure. More information about the microstructure and the strain across the sample can be found in Pope et al [10] publication.

The hardness of the bond is shown as a 2D hardness map in Figure 6.14 (h). The bulk material shows a hardness around 500 Hv for Ti-5553 and 350 Hv for Ti-64, which is an increase from the as FAST material in Figure 6.6. The hardness across the bond has a smooth transition between both alloys. However, the change of hardness between the two alloys is longer for

BT2 compared to BT1. This cannot be fully appreciated from the 2D map because of the limited number of points that could be tested across the bond and the hardness data was interpolated to create this map.

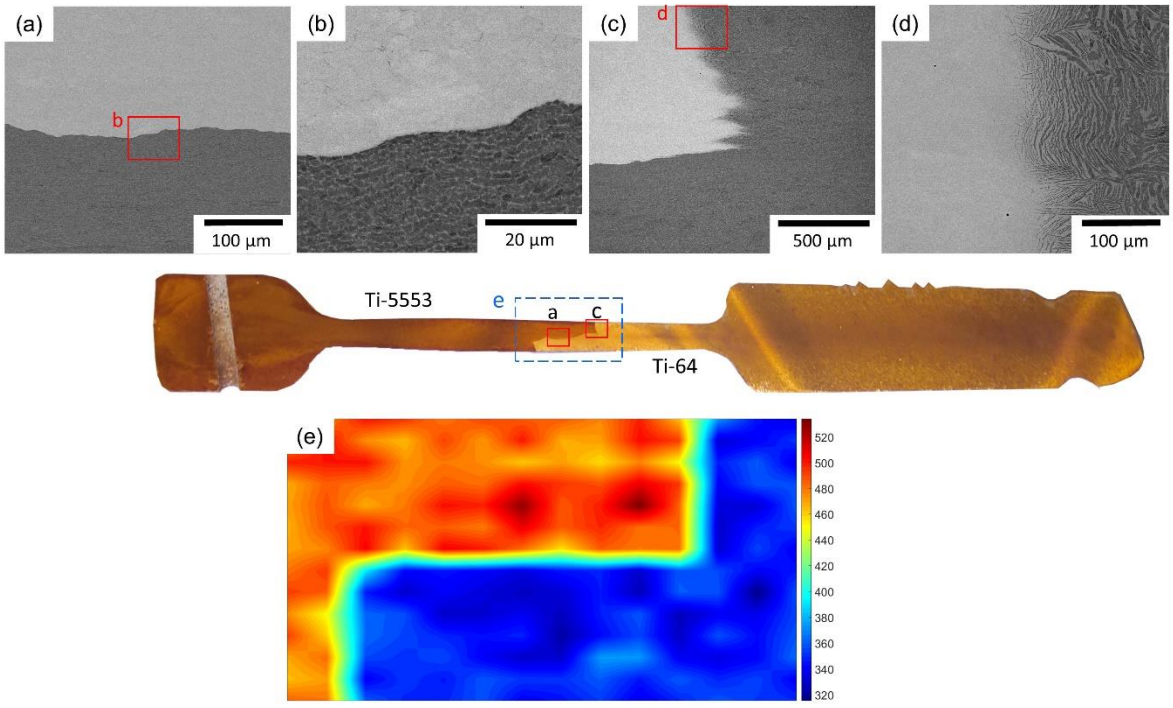


***Figure 6.14*** *– Cross section of FF1 after heat tinting the EDM face with backscatter electron micrographs for (a, b) BT1, (c, d) BT2 and (e) 2D microhardness map of the bond region.*

The diffusion of the two distinctive bond types, BT1 and BT2, is shown in Figure 6.15. For all the elements the diffusion is higher in BT2 than in BT1, with an average diffusion distance of 150 µm and 50 µm, respectively. This correlates well with the results and micrographs presented in Figure 6.14.

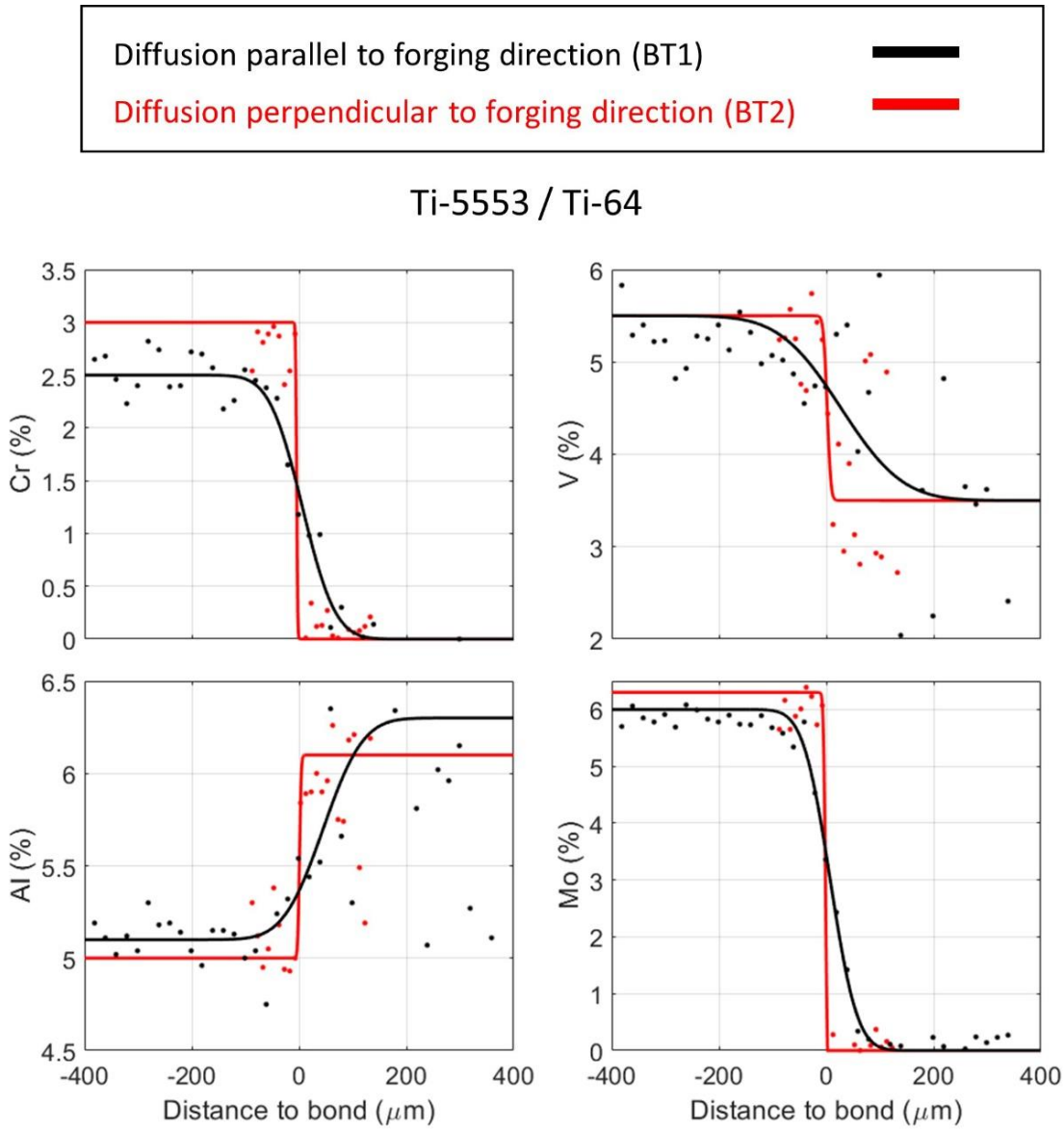


***Figure 6.15*** *– Diffusion profiles of the four elements that componse the titanium alloys Ti-64 and Ti-5553. Each graph represents the diffusion profile across the bond of one FAST-DB sample for BT1 and BT2.*

### *6.3.3.2. Characterization Ti-6242/Ti-64 (FF2)*

The near-net shaped FAST-DB forged component made of Ti-64 and Ti-6242 is shown in Figure 6.16 along with the corresponding electron micrographs and the 2D hardness map. In Figure 6.16 (a, b, c), under the Z contrast of the backscatter electron mode, the brightest alloy represents Ti-6242 alloy, while the darker one is Ti-64. In this case, the location of the bond is in the top right corner of the forged component and the two bond regions are not as well defined as in FF1. The component has a similar microstructure for both alloys, which consists of a martensitic structure with large parent beta grains. These types of microstructures are

typical after supertransus forging followed by water quenching. In some areas close to the bond, darker elongated alpha regions have formed, similar to that shown in Figure 6.16 (b), this is probably caused by partial recrystallization near to the bond.

The microhardness results in Figure 6.16 (d) shows that the hardness of FF2 is higher than FDB1. The hardness of the two alloys is very similar but Ti-6242 has higher hardness overall. Furthermore, there is a smooth transition across the bond with no significant increase or decrease of hardness inn the adjacent region. More details of how this sample was produced can be found in Section 3.3.

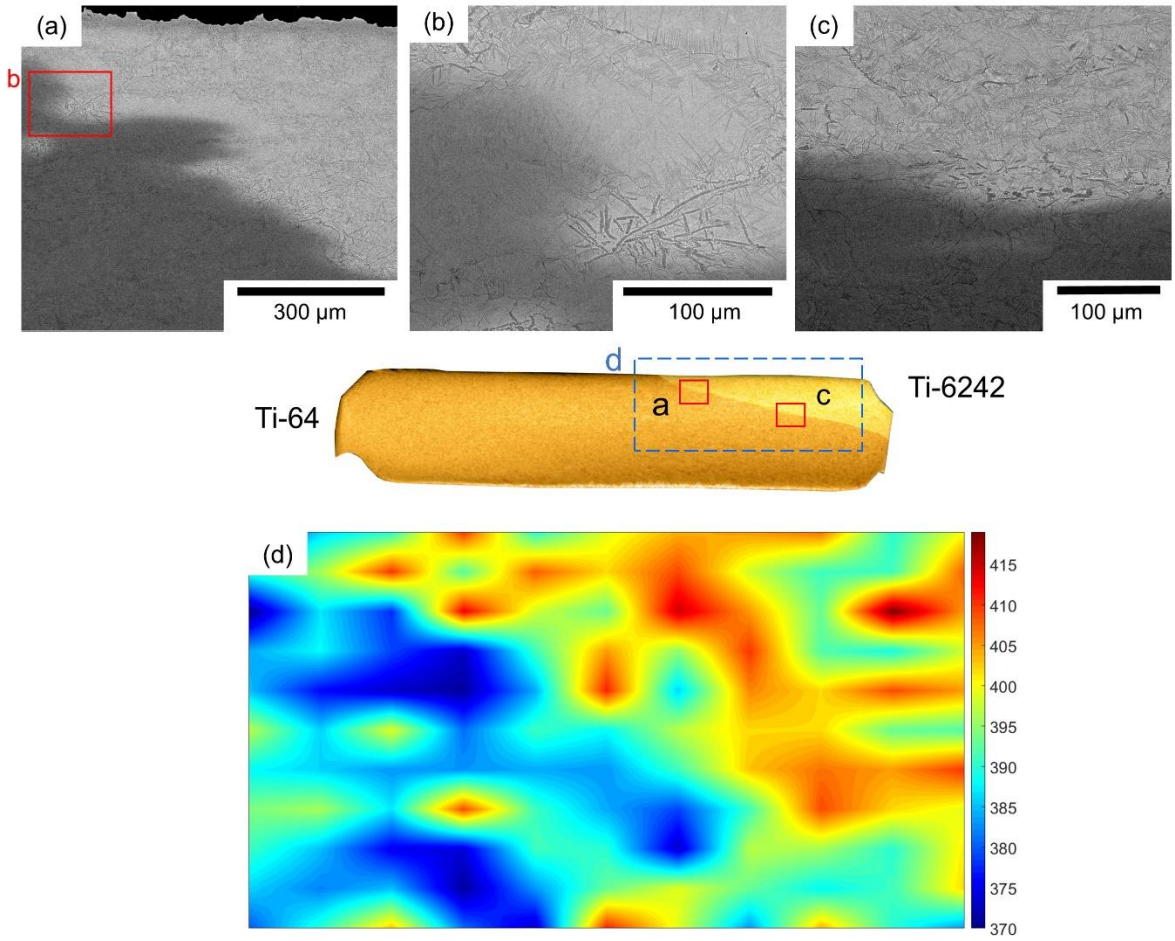


***Figure 6.16*** *– Cross section of FF2 after heat tinting the EDM face with SEM micrograph for (a, b) BT1, (c) BT2 and (d) 2D microhardness map of the bond region.*

The diffusion of the elements in this sample was measured perpendicular (BT1') and parallel (BT2') to the forging direction, in the same manner it was measured for FF1 in Figure 6.15. The diffusion of BT2' was measured in the region shown in Figure 6.15 (a) and the diffusion of BT1' was measured in the region shown in Figure 6.15 (c). The results show a similar trend

to the ones observed in FF1. For all the elements, the diffusion of the BT2' is larger than the one measured for BT1', as shown in Figure 6.17.

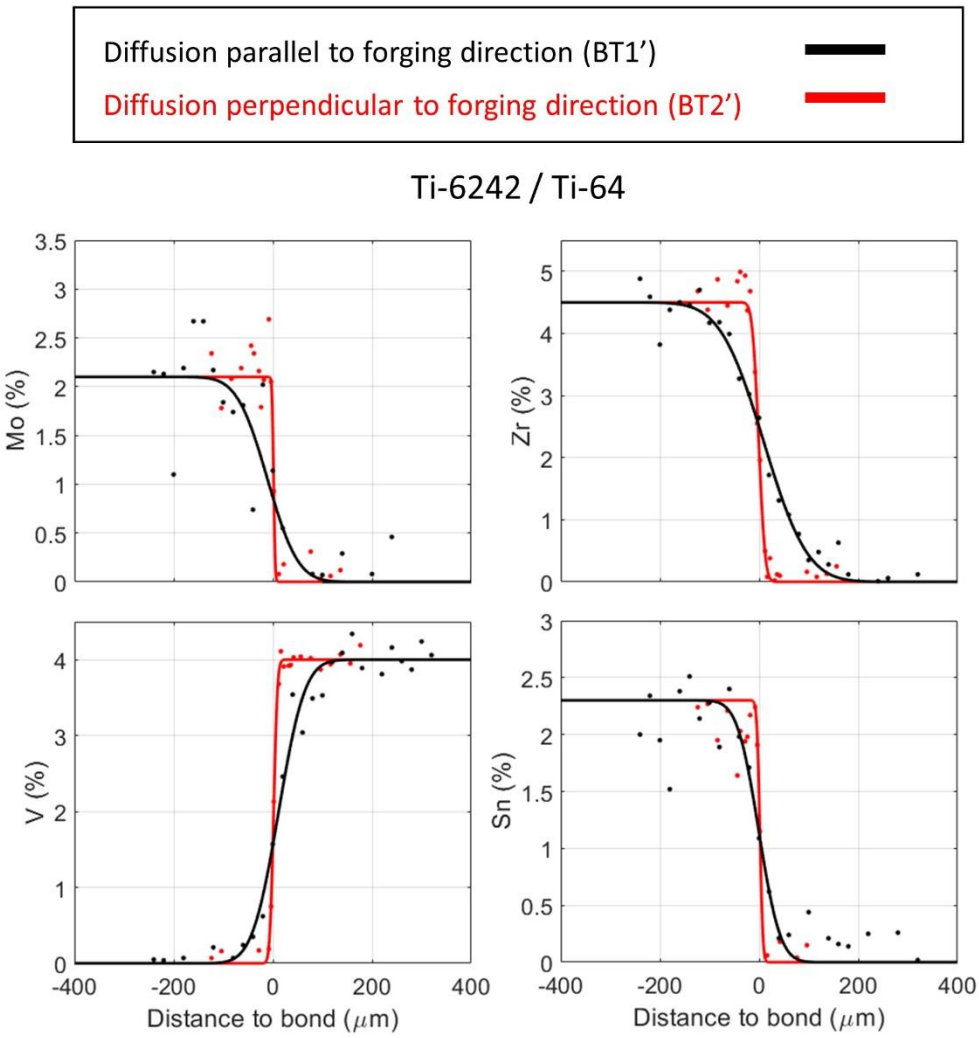


***Figure 6.17*** *– Diffusion profiles of the four elements that componse the titanium alloys Ti-64 and Ti-6242. Each graph represents the diffusion profile across the bond of one FAST-DB sample for BT1' and BT2'.*

## *6.3.4. Residual Stresses* FAST-*forge*

### *6.3.4.1.* Ti-5553 / Ti-64 (FF1)

The residual stresses for FF1 are expected to be higher than the ones in the as-FAST material because it has been hot forged and water quenched. For this sample, a high quality EDM cut was achieved, which reduced the number of errors in the measurement. Figure 6.18 (a) shows the Alicona scan of the EDM face in the region of the bond. From the displacement data, it is not possible to distinguish both alloys, which indicates there must be a smooth transition

between the two alloys. When this data is used to measure the stresses of the original component (Figure 6.18 (b)), there is a stress region inside the red box that can be related to position of the bond shown in Figure 6.14. The residual stresses generated in the bond are relatively low and there seems to be a smooth transition between both alloys. Overall, the stresses in the component can be considered low to moderate. The Ti-64 region has compressive residual stresses at the surface, while the bulk region has tensile residual stresses. On the left-hand side of the sample, the Ti-5553 shows a compression zone but this could be due to a change in geometry. Furthermore, the higher tensile stresses in that same region are due to the hole made in the component as part of the cutting process, as explained in Section 6.2.3.2.

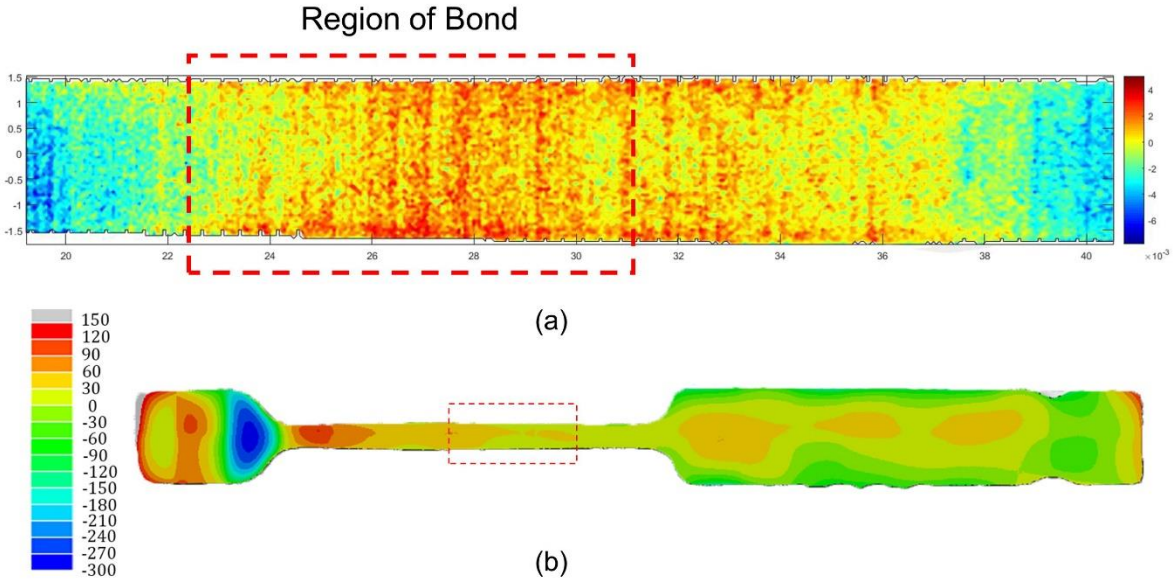


***Figure 6.18*** *– (a) Displacement map from the Alicona scan of the bond of FF1. (b) Residual stresses map of the FF1 made with the contour method.*

### *6.3.4.2.* Ti-64 / Ti-6242 (FF2)

The measurements of the residual stresses in the bond between Ti-64 and Ti-6242 for the forged material were conducted at the highest strain region, as shown in Figure 6.3. Figure 6.19 shows the profile measured from the Alicona scan of the EDM and the 3D representation of the EDM face measured with the Alicona. There is a clear mismatch between the profile of the two halves; the profile in (a) has an S-shape while the profile in (c) has a U-shape. However, the differences between the two halves could be due to the geometry of the component and the clamping method used during the EDM cutting process. Additionally, the

sample is relatively small so it was not possible to use the same cutting method used in the other components, in which a hole was drilled to fit the EDM cable. The displacements and the residual stresses measured for each half of the sample are shown in Figure 6.20. Figure 6.20 (a, b) shows higher displacement and stresses in the right-hand side of the samples. However, by looking at Figure 6.20 (b) it can be observed that the higher stresses occurred only in the bottom right region. This distribution of stresses happened because the bottom left part of the sample is made of Ti-64 while the top part is made of Ti-6242, as shown in Figure 6.16. For the other half, the displacement in Figure 6.20 (b) is distributed more homogeneously. The stresses presented in Figure 6.20 (d) are also distributed more homogeneously throughout the sample. Nevertheless, the top right corner continues to exhibit the lower stresses due to the dissimilar titanium alloy in that region. Overall, there are high residual stresses with a compressive outer layer and a tensile core. Additionally, there is a smooth transition of the residual stresses across the bond.

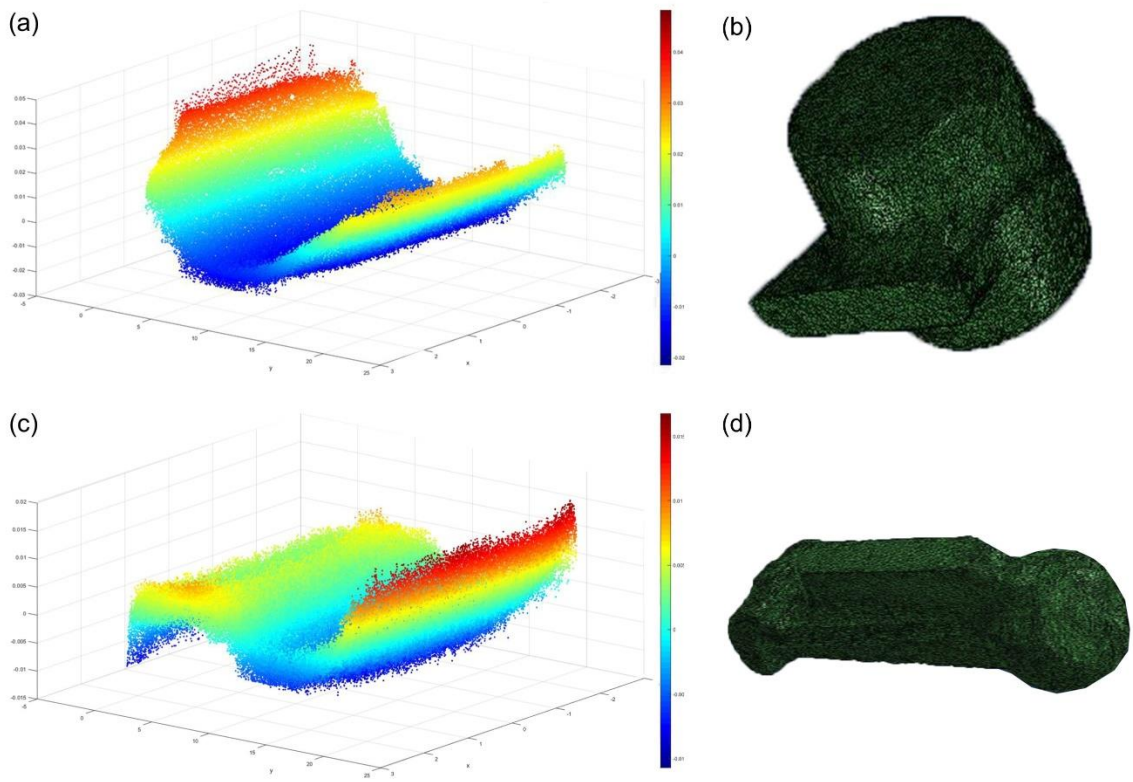


***Figure 6.19*** *– (a, c) Displacement map from the Alicona scan of the bond for each halve of FF2. (b, d) Digital model of the FF2 sample.*

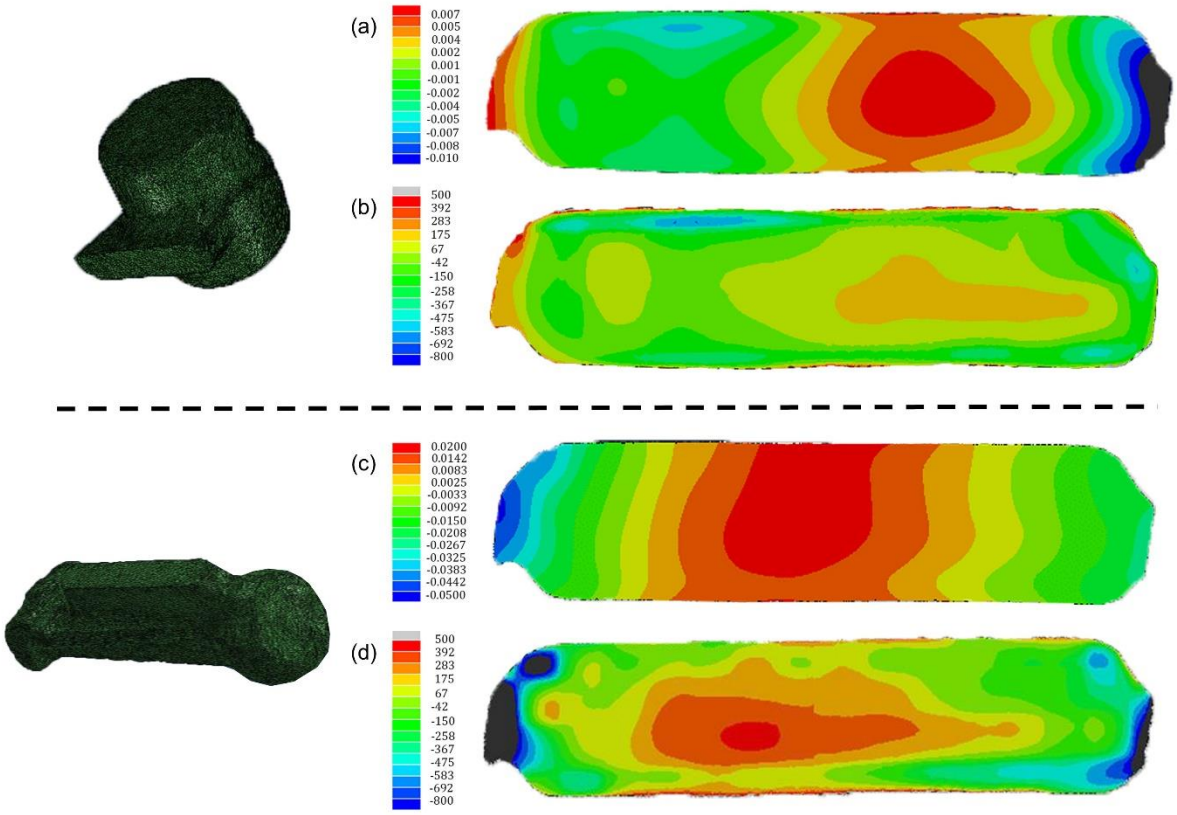


***Figure 6.20*** *– (a, c) Displacement map of FF2 made with the contour method. (b, d) Residual stresses map of the FF2 calculated with the contour method.*

### *6.3.4.3.* XRD of FAST-forge (FF1, FF2)

The residual stresses measured with the contour method for FF1 and FF2 show a general idea of the stresses expected in the sample. However, the contour method cannot resolve with significant resolution the stresses across the bond, as observed in Section 6.3.2. with the as-FAST material. Therefore, the XRD method was used to measure stresses across the bond with more precision.

The XRD measurements were done before sectioning the sample with wire-EDM to avoid modifying the initial residual stresses in the material. Hence, the measurements had to be done on the surface of the sample. However, it was not possible to determine a clear peak in the measurement because there was alpha case at the surface of the forged component. Figure 6.21 (a) shows how the measurement should look in order to define the position of the peak and Figure 6.21 (b) shows how the actual measurement looked. Therefore, it was not possible to measure the residual stress for the forged components with the XRD technique.

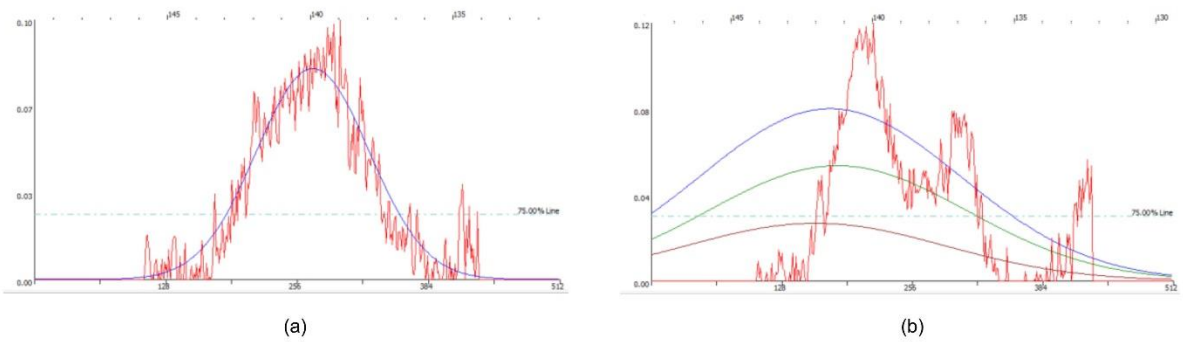


***Figure 6.21*** *– XRD signal of a (a) good measurement and (b) an alpha case measurement.*

# 7. *Machining of FAST-DB components*

## *7.1. Introduction*

It has been demonstrated that dissimilar titanium alloys can be diffusion bonded successfully with the solid-state processing technology - FAST. In Section 2.13.3 all the previous work done with FAST to join dissimilar titanium alloys was reviewed. Then, in Chapter 5 it has been shown that the failure of a FAST-DB component occurs in the lowest strength titanium alloy, as opposed to the bond region, even if the orientation of grains at the bond are more favourably orientated to resist dislocation slip compared to the bulk material. Furthermore, Chapter 6 shows that joining dissimilar alloys with FAST induces low residual stresses, this is a major advantage compared to other joining techniques such as fusion and friction welding. Therefore, the use of FAST to create multi-material components has great potential in the aerospace sector. However, the finishing production steps for most titanium components involves significant machining operations to create final shape tolerances and ensure a good surface finish, and multi materials components will be no exception to this.

Most of the studies concentrating on the machining of multi-material components are focussed on drilling multi-material stacks: there has been minimal research on the effects of turning operations on multi-material components, and no research has certainly been published on multi-materials components made up of dissimilar titanium alloys. Matusi [227] and Ullah [228] studied the forces of three bonds: Al (A1070) with CP-Ti, Al (A5052) with ductile cast iron and stainless steel (SUS304) with mild steel (S15CK). These studies used a turning operation with a strain gage-based data acquisition system to measure the forces. Overall, different forces across the bond were observed and a directionality effect of machining was identified. Although the study included force data, no information of the surface or subsurface damage in the bond or parent material was included. In another study, Ullah [229] observed a directionality effect in the surface roughness of a machined sample consisting of Al (A1070) with CP-Ti. Again, this study only included a map of the surface

roughness as the paper focused on the characterization technique itself, rather than the actual surface finish.

There have been other studies investigating the machinability of a bimetallic pistons made of Al and cast iron produced by die casting [230–233]. These studies showed a difference in forces between both materials and higher tool wear when machining multi-material components. Additionally, Malakizadi et al [234] concluded that thermal cracking was the main wear mechanism of CBN inserts when milling bimetallic engine blocks.

All the previous studies have analysed the force signal measured directly from the data recorded during the test. However, this has limitations because they cannot locate the actual position of the bond. Hence, it is difficult to really understand the effect of the bond during the machining operation. The novel machining technique termed force feedback, enables the microstructure to be created directly from the machining operation - creating digital fingerprints [164]. The use of force feedback in multi-material components creates a map with the actual location of the bond and the corresponding force for specific location on the workpiece surface. An example is shown in Figure 7.1, where (a) shows a mosaic constructed from optical micrographs of an etched FAST-DB sample made with six dissimilar titanium alloys, and (b) shows the force feedback plot of the same sample.

Another important aspect to take into consideration from the previous research of machining multi-material components is that the different materials were joined with inertia friction welding (IFW) technology. IFW produces heat affected zones (HAZ) in the union as well as high residual stresses [6]. These joints have to be interpreted as three material regions instead of two because they are made of the two bulk parent materials and the plastically affected zone, which has a length greater than a millimetre. The issues in the bond can be avoided when FAST is used to create the components. As shown in Chapter 5, the diffusion in the bond is very small and it is possible to observe grains that contain both microchemistries.

It is important to notice that none of the studies, mentioned above, have taken into account the subsurface damage or the actual surface finish of the sample. The damage in the bond can have a significant influence on the mechanical properties of the component, especially when they are subject to fatigue loading [235]. An understanding of the actual damage produced in the bond and adjacent regions from machining operations will be key to determining the success and uptake of multi-materials components in industry.

The focus of the work in this chapter is to understand the effect of the directionality when machining multi-material components, so that companies such as Rolls-Royce plc know how to obtain the best surface finish, if and when they decide to use this technology in a future. In this study, several coupons made of multiple dissimilar alloys were machined and characterized. The results include the analysis of forces as well as the characterization of the surface finish and the subsurface damage in multiple titanium bond combinations.

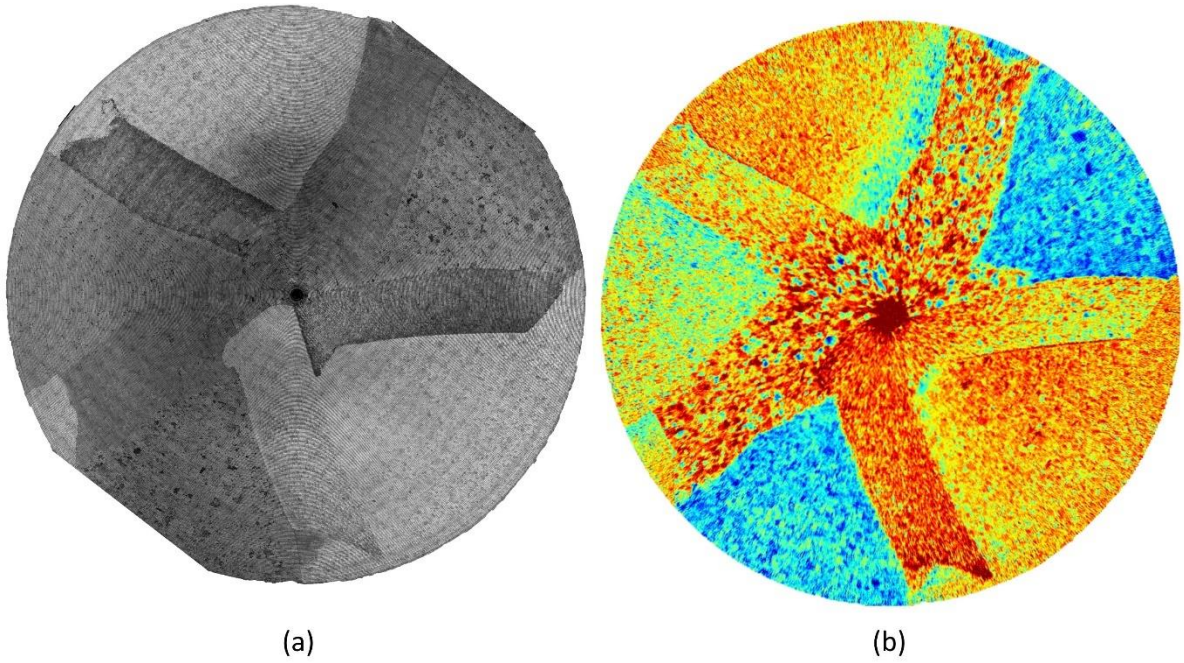


***Figure 7.1*** *– Machined surface of a FAST-DB sample made of 6 dissimilar titanium alloys in the shape of the Sheffield Titanium Alloy Research (STAR) logo. (a) Optical micrograph mosaic made with the Clemex software after etching the surface of the sample. (b) Force feedback data recorded directly from the machining trials.*

## *7.2. Methodology*

A total of three 80 mm FAST-DB discs were made using different processing conditions. One of the discs had both faces machined in order to assess the directionality effect while the other two samples had only one face machined.

### 7.2.1. Powder

The powder used to make the FAST-DB samples are: Ti-6Al-2Sn-4Zr-2Mo_2 (Ti-6242), Ti-6Al-4V_2 (Ti-64), Ti-5Al-5V-5Mo-3Cr (Ti-5553), Ti-3Al-8V-6Cr-4Mo-4Zr (Beta C) and Ti-3Al-2.5V (Ti-3-2.5). More detailed information of the powder can be found in Chapter 4.

### 7.2.2. FAST

The 80 mm FAST-DB billets were processed at the University of Sheffield using an FCT Systeme GmbH SPS Furnace Type HP D 25. The detailed procedure explaining how samples in FAST are made can be found in Section 3.2.

Each billet produced for this work was made of five dissimilar titanium alloys. A 3D printed polymer divider was used to separate the powders while they were being poured in the graphite ring. Figure 7.2 (a) shows the distribution inside the graphite ring of the different powders used to make the discs after the 3D printed divider had been removed. The distribution of the powders was planned in a way that ensured that the alloys Ti-64 and Ti-6242 had a bond with each of the remaining alloys. In addition to this, there is a region of Ti-64 that is twice as large as the rest of the powders with the purpose to use it as an identifier for the force feedback analysis. The powder was processed at a constant pressure of 25 MPa, under vacuum and with the conditions shown in Table 7.1. Table 7.1 also lists the diffusion bonds studied in this chapter with their corresponding disc. Figure 7.2 presents a schematic of the process used to make and test the samples.

### 7.2.3. Machining

The machining operation selected for these trials was face turning for two main reasons: firstly, there was a larger area to machine in the front and back faces of the disc than at the outer wall of the disk. Furthermore, the tools machined the same bond multiple times before completing the face turning operation, which allowed to study consistent bond effects in the machining forces. Secondly, it was more stable to clamp a cylindrical sample through the outer walls than through the flat faces. High stability is a critical requirement when measuring

the feedback forces, otherwise there is too much noise within the raw data. For these tests, a set of soft jaws (specifically manufactured for this study) ensured a rigid a stable system (Figure 7.2 (c)).

***Table 7.1*** *– Processing conditions and bond of the FAST-DB discs.*

| Sample | Temperature [°C] | Time [min] | Alloy 1 | Alloy 2 |
|---|---|---|---|---|
| **Disc 1** | 970 | 25 | Ti-5553 | Ti-64 |
| | | | Ti-5553 | Ti-6242 |
| | | | BetaC | Ti-64 |
| | | | BetaC | Ti-6242 |
| | | | Ti-6242 | Ti-64 |
| **Disc 2** | 1100 | 60 | Ti-5553 | Ti-6242 |
| | | | BetaC | Ti-6242 |
| **Disc 3** | 1100 | 25 | BetaC | Ti-6242 |

The machining operation was conducted in a WFL M100 MillTurn CNC machining centre at the Advanced Manufacturing Research Centre (AMRC) located in Rotherham. To record the forces during the machining trials, a Kystler 9129AA dynamometer plate was used. The dynamometer contained eight piezoelectric sensors that measured the forces in three spatial axes. The voltage signal was collected through the multichannel charge amplifier (Kistler Type 5070) in combination with the Data Acquisition system (Kistler DAQ Type 5697A1) and it was finally saved through Kistler's Dynoware software. The dynamometer was connected directly to the machine arm and supported the tool holder to obtain a direct measurement of the machining forces. Figure 7.3 shows the setup of the dynamometer and the tool holder in the CNC machine for these trials.

The tool insert selected for this study was a CNMG 12 04 08 SM 1115 manufactured by Sandvik Coromant.

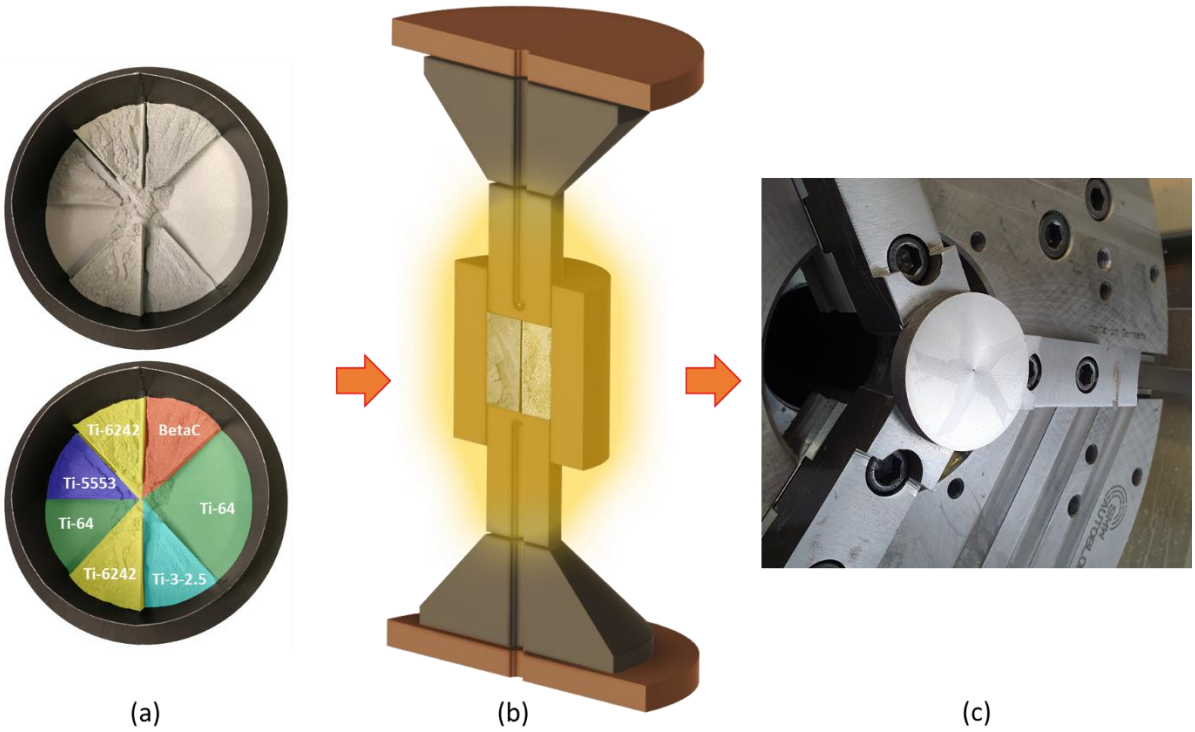


***Figure 7.2*** *– A schematic of the experimental workflow used in this chapter, were (a) is the distribution of the powders inside the graphite ring, (b) represents processing the powder with FAST and (c) is a photograph of the face turning operation.*

The face turning operation was conducted at constant RPM (G97) instead of a standard constant cutting speed operation (G96). One of the reasons for this is that with a G97 operation, the cutting speed decreases as the tool moves to the centre of the sample, hence, the machining forces can be analysed at different cutting speeds. The other reason is that the code used to analyse the force feedback response required constant RPM. More details on the force feedback technique can be found in Section 3.6.

The acquisition rate of the data was 30 kHz and the machining parameters for these tests were 0.15 mm depth of cut (ap), feed of 15 mm/rev ($f_{rev}$) and a constant value of 137 RPM. The minimum number of points recorded with the dynamometer was 52.3 pts/mm, although this amount increased when the tool moved towards the centre of the sample.

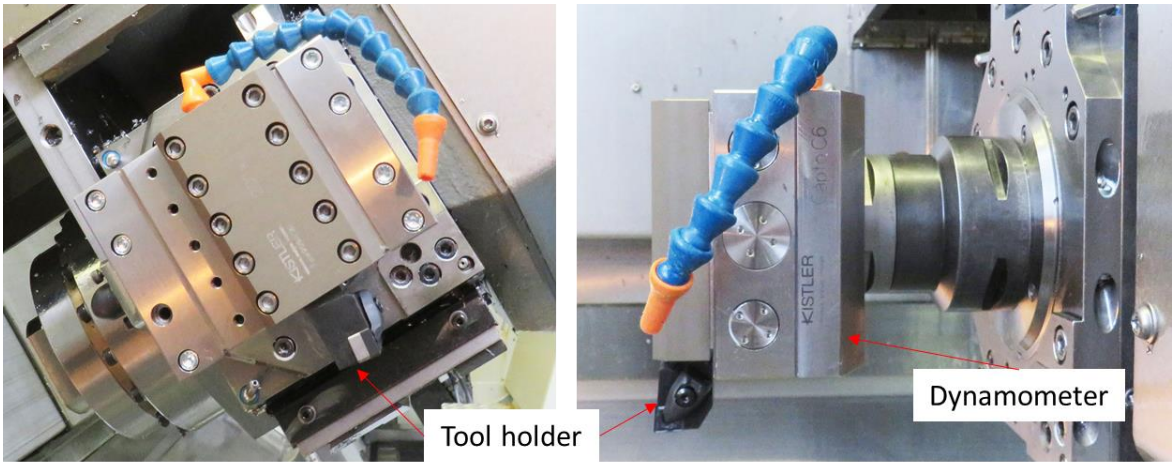


***Figure 7.3*** *– Photograph of Kistler Type 5070 dynamometer plate installed in the WFL M100 MillTurn machining centre with the tool holder and insert in place prior to the machining operation. (a) Front and (b) lateral view of the dynamometer and the tool holder.*

### *7.2.4. Analysis Techniques*

The analysis of the forces across the bond was done with MATLAB software, more details can be found in Section 3.6. The surface roughness was measured with an Alicona microscope and the data was postprocessed with the Alicona software to create a 2D map of the bond surface. Moreover, the data in the scanned plane had to be corrected to ensure it represented a flat surface. This correction is necessary because the Alicona has a vertical resolution of 100 nm and it is very difficult to ensure the scanned surface is completely parallel to the lens.

To characterise the machining surface, the discs were first sectioned in eight parts with a Struers Secotom. Each part had one bond in the middle of the sample. Then, the samples were cleaned with soap and isopropanol and then the machined surface was analysed using scanning electron microscopy using both secondary and backscattered electron imaging modes. These samples were then sectioned perpendicular to the bond, hot mounted and metallographic prepared to characterise the subsurface damage. More information of the analysis techniques can be found in Section 3.5.

## 7.3. Results

The results of the machining trials are presented in this section. The results are focused on the alloys Ti-64 and Ti-6242, hence, all the bonds contain at least one of these alloys. Although the discs contained Ti-3-2.5, as mentioned in Figure 7.2 (a), the analysis of this bond will not be presented in this section because one of the samples did not have a straight bond and the results measured are not conclusive. However, the remaining five bonds were straight and are presented in this section.

### 7.3.1. Materials characterization

The microstructure of the majority of the alloys is very similar because the five bonds are made of alloys that are α + β or β alloy type. Figure 7.4 shows the force feedback plot of disc one with the corresponding backscattered micrographs at the bond locations. The micrographs in (c) and (d) correspond to Ti-6242 with the β alloys Ti-5553 and BetaC, while (e) and (f) correspond to Ti-64 bonded with the same β alloys. Finally, (b) shows the bond produced between Ti-64 and Ti-6242.

The microstructure of Ti-64 and Ti-6242 is very similar: both alloys consists of a typical equiaxial primary alpha grains (~20 µm) with residual beta phase in between the alpha grains. It is also possible to observe a more lath-type morphology between the equiaxial grains; this is clearer in Ti-64. The microstructure of these samples is similar to the ones tested in Chapter 5. The beta alloys have a similar microstructure that consists of large prior β grains with a size of 200-300 µm. It is also noticeable that the grains size of the Beta C are larger than the ones inTi-5553.

The microstructures of the bonds between an α + β with a β alloy are similar. All the bonds formed a lamellar structure with a progressive reduction in lamellar width from the α + β alloys to the β alloys. Furthermore, the bonds involving Ti-5553 formed a fine secondary alpha, like the one generated in Chapter 6. However, this cannot be resolved in these comparative micrographs because it requires higher magnification micrographs. It is also possible to observe some porosity in the β alloys.

The bond between Ti-64 and Ti-6242 shows the formation of lamellar alpha, typical microstructure expected for a supertransus processed material. It is possible that the microstructure in the bond region is a result of the bond local chemistry being more heavily beta stabilised and thus, resulting in supertransus processing in this region.

The diffusion of elements in the bond can be estimated from analysis of the microstructure across the bonds. From the micrographs, the changes in the microstructure seem to be between 50 – 150 µm, which would correlate well with the diffusion measured in Sections 6.3.1 and 5.3.1. It is not expected to have diffusion distances greater than 400 µm because previous authors [9] have observed this diffusional distance when processing the samples at temperatures 250°C higher with a dwell time 35 min longer. Therefore, it was considered not necessary to measure the diffusion bond distance as a variation of 100 µm was thought not to affect the results of the machining tests.

The hardness of the bonds was measured and plotted in Figure 7.5. The plots (a) and (b) show that the hardness profiles between the α + β alloys with Ti-5553 are very similar. Additionally, Ti-64 and Ti-6242 have a lower value of hardness than Ti-5553 and there is a peak of hardness in the bond. This result compares well with the work of Pope et al [10], whom observed the formation of fine secondary alpha that increased the hardness in the bond. However, this peak is not observed when Ti-64 and Ti-6242 are bonded with BetaC. Instead, there is a smooth transition between both alloys. Finally, no major variation is observed in the hardness profile between Ti-6242 and Ti-64.

### *7.3.2. Effect of forces in the machining direction.*

The analysis of the forces in disc 1 is novel because this is the first time that force feedback has been used before to assess dissimilar titanium alloy components. Figure 7.6 shows the top and bottom faces of disc 1, with its corresponding machining direction. The maps demonstrate that the force feedback plots are very accurate and can detect any irregularities in the bond. In addition to this, the plots show a change of the forces on the bond when machining different faces. This is very clear for the bonds that contain Ti-5553, because there is a higher force when the tool goes into Ti-5553 and a reduction of force when the tool moves out into the neighbouring alloy. This effect is clearer when the forces across the bond are

averaged from the force feedback plots, as shown with Figure 7.7, Figure 7.8 and Figure 7.9. More details on how the average force was calculated can be found in Section 3.6.

The forces show a clear directionality effect when machining a bond involving Ti-5553 and an α + β alloy (Ti-64 or Ti-6242), as shown in Figure 7.7. When machining from an α + β alloy to Ti-5553, there is an increase of forces in the bond. Nevertheless, there is a smooth transition when machining from Ti-5553 to the α+β alloys. The forces in the bond when machining from Ti-5553 and Ti-64 shows a flat section close to value 0, this will be explained in more details in Section 7.3.4.

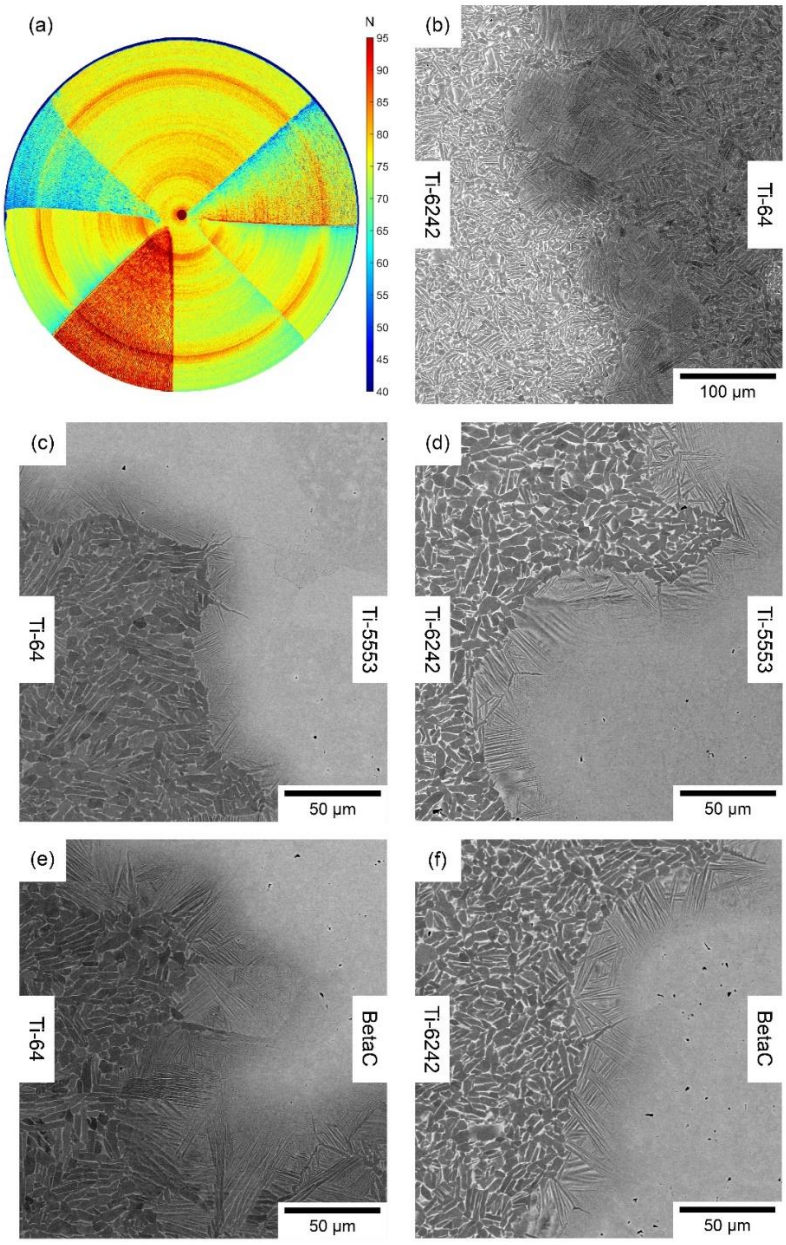


***Figure 7.4*** *– Backscattered electron micrographs of the microstructure in the bonds for Disc 1.*

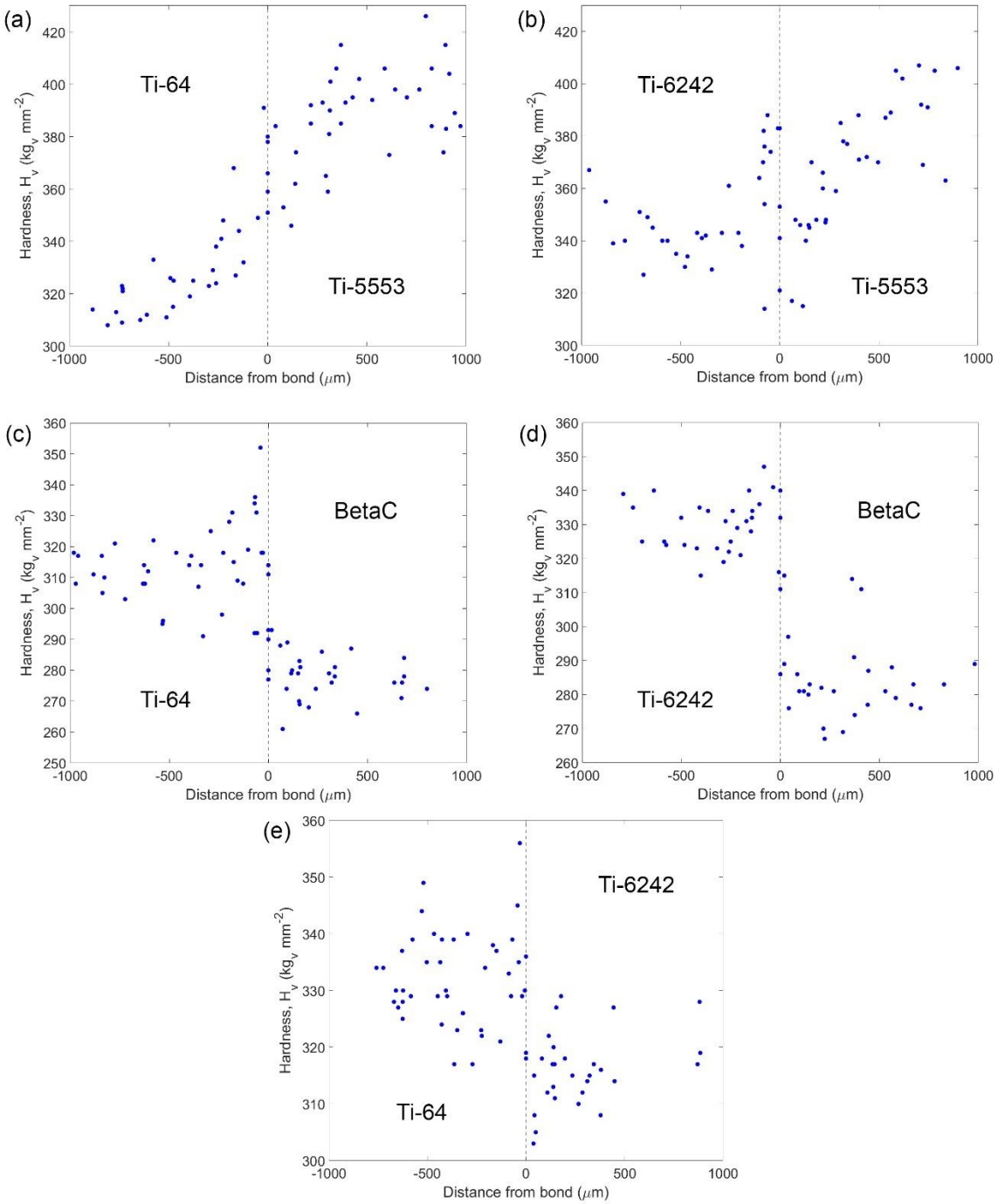


***Figure 7.5*** *– Hardness profiles of the bonds in Disc 1*

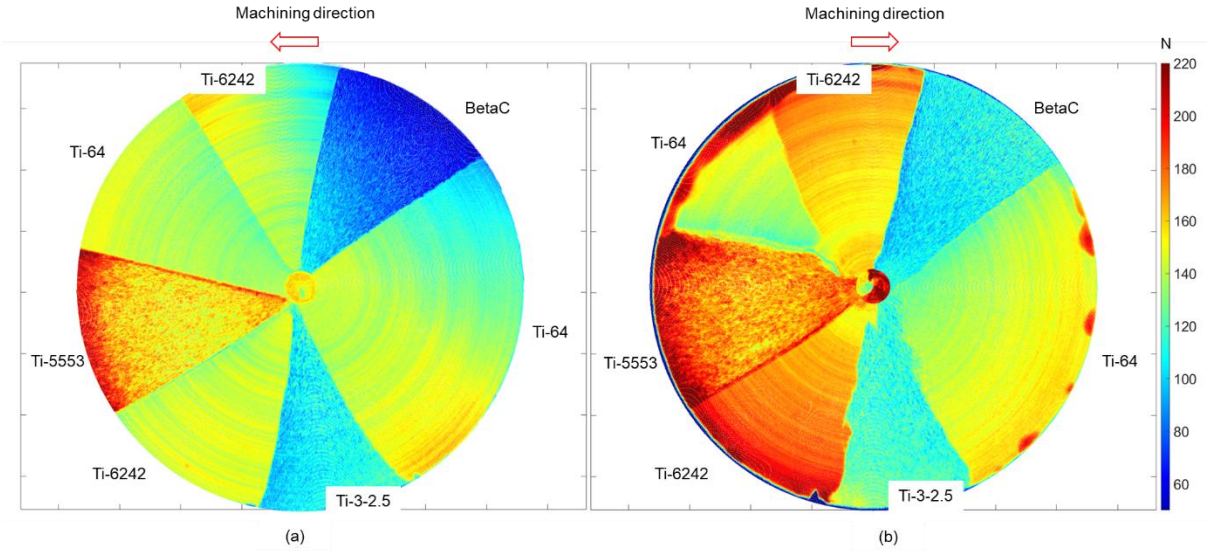


***Figure 7.6*** *– Force feedback maps of the (a) top and (b) bottom face of Disc 1.*

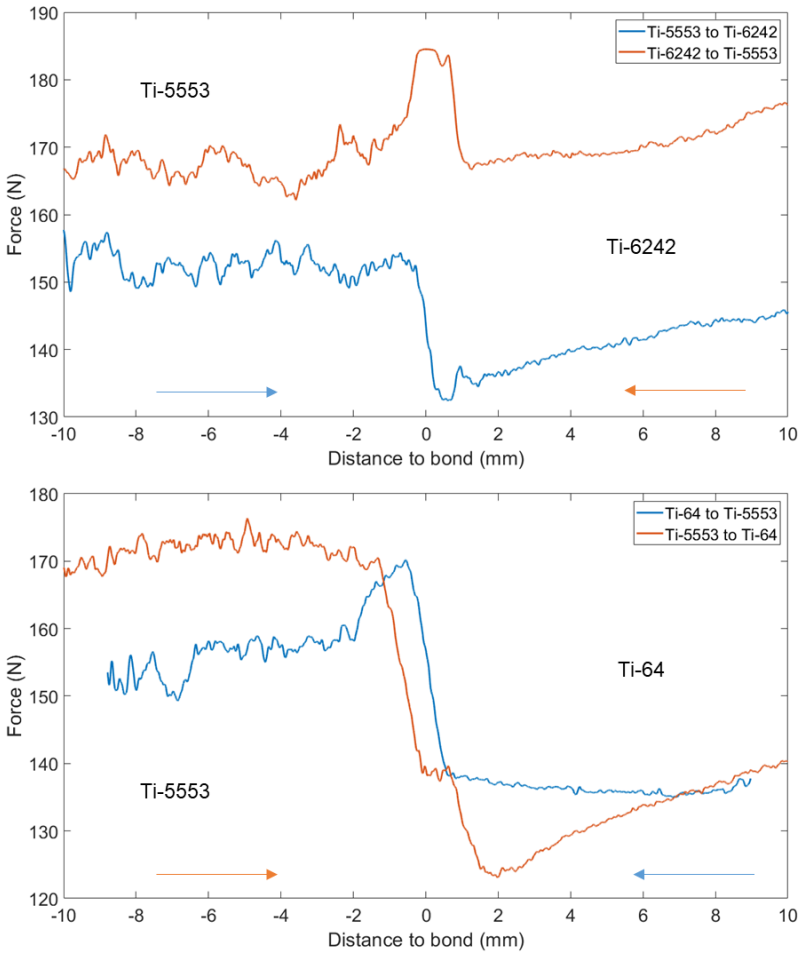


***Figure 7.7*** *– Plots of the force response affected by the machining direction for Ti-5553 with Ti-6242 and Ti-64 bonds respectively.*

Figure 7.8 presents the average forces of the bonds made of BetaC with the α + β alloys. The graphs show that the forces of BetaC are lower than those for the α + β alloys. In addition to this, there is a similar trend of forces when machining in different directions. However, it can be appreciated a small increase of forces when machining from Ti-6242 to BetaC. This increase in force is not observed when BetaC is machined with Ti-64.

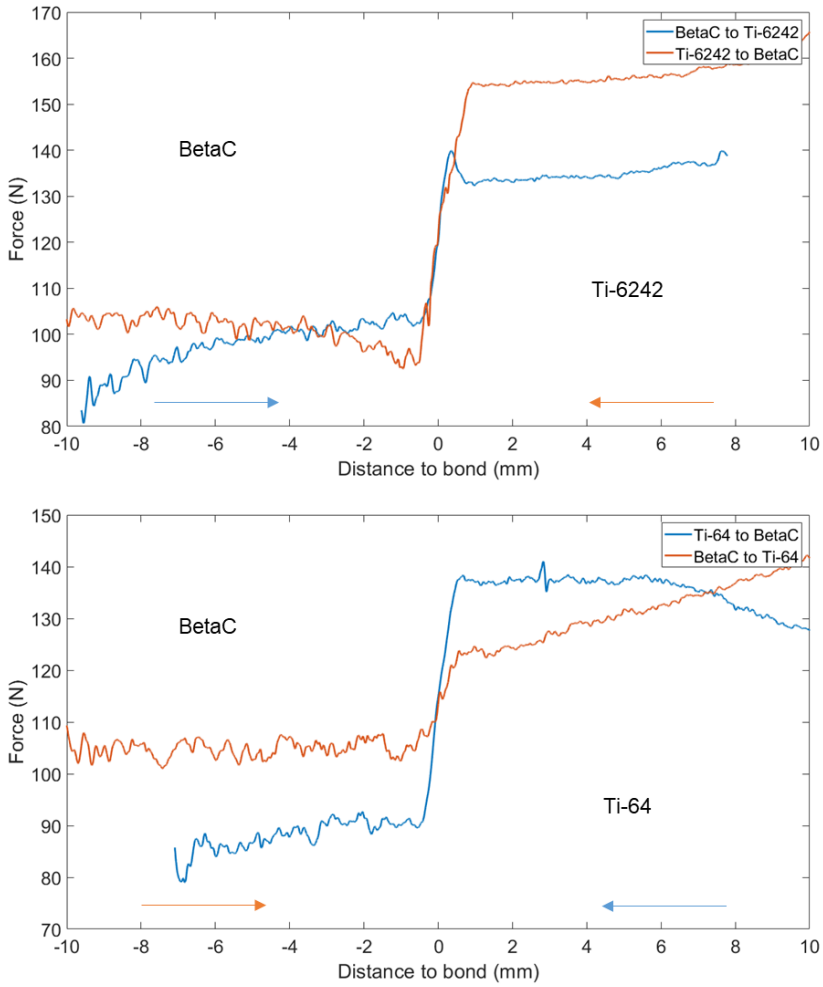


***Figure 7.8*** *– Force response affected by the machining direction for BetaC with Ti-6242 and Ti-64 bonds respectively.*

Figure 7.9 presents the average forces across the bond made of Ti-6242 and Ti-64. The results show a minor variation of forces in the bond depending on the machining direction. There seems to be a small peak in the force response when machining from Ti-64 to Ti-6242 and the transition of the forces is also smaller for this bond. This peak is similar to the one observed in Figure 7.8 when machining from BetaC to Ti-6242. Unlike the peaks of forces produced in Figure 7.7, this peak is very narrow, and it appears to occur at the start of the Ti-6242 region.

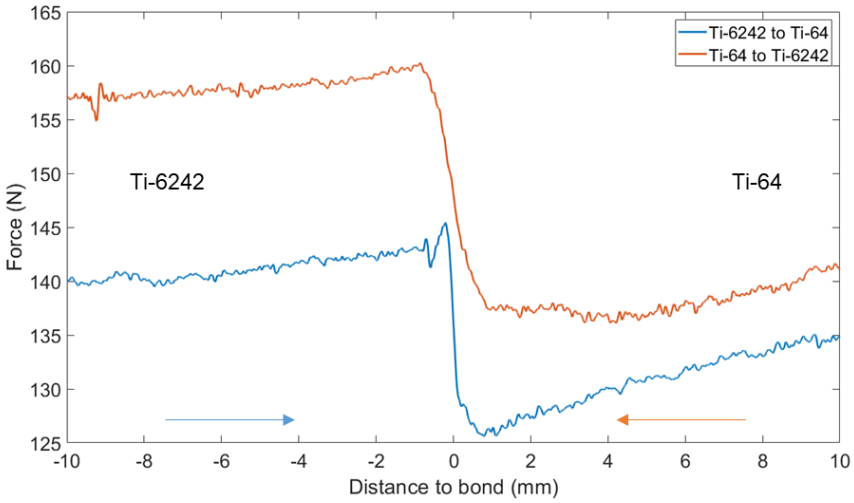


***Figure 7.9*** *– Force response affected by the machining direction for Ti-64 with Ti-6242 bond.*

### *7.3.3. Effect of surface finish in the machining direction.*

It is clear from Section 7.3.2 that the specific alloys joined and the machining direction directly effects the force response. Furthermore, the Alicona microscope was used to map the surface roughness and then compared with the corresponding force feedback maps.

Figure 7.10 shows the surface roughness and the force feedback maps of Ti-5553 joined with the α+β alloys. The results reveal a correlation between the forces and the surface roughness in the bond. When machining from Ti-5553 to one of the α+β alloys, the forces decrease in the bond, which correlates well with a small valley produced in the surface of the bond. However, when machining from α+β alloys to Ti-5553, the forces increase in the bond, which correlates well with a formation of a peak in the bond region. It is noticed that when machining from Ti-5553, there is a small peak in the surface just before reaching the small valley. Nevertheless, when machining in the direction from the α+β alloys through to Ti-5553, a small valley in the surface is observed ahead of the subsequent elevation in the surface.

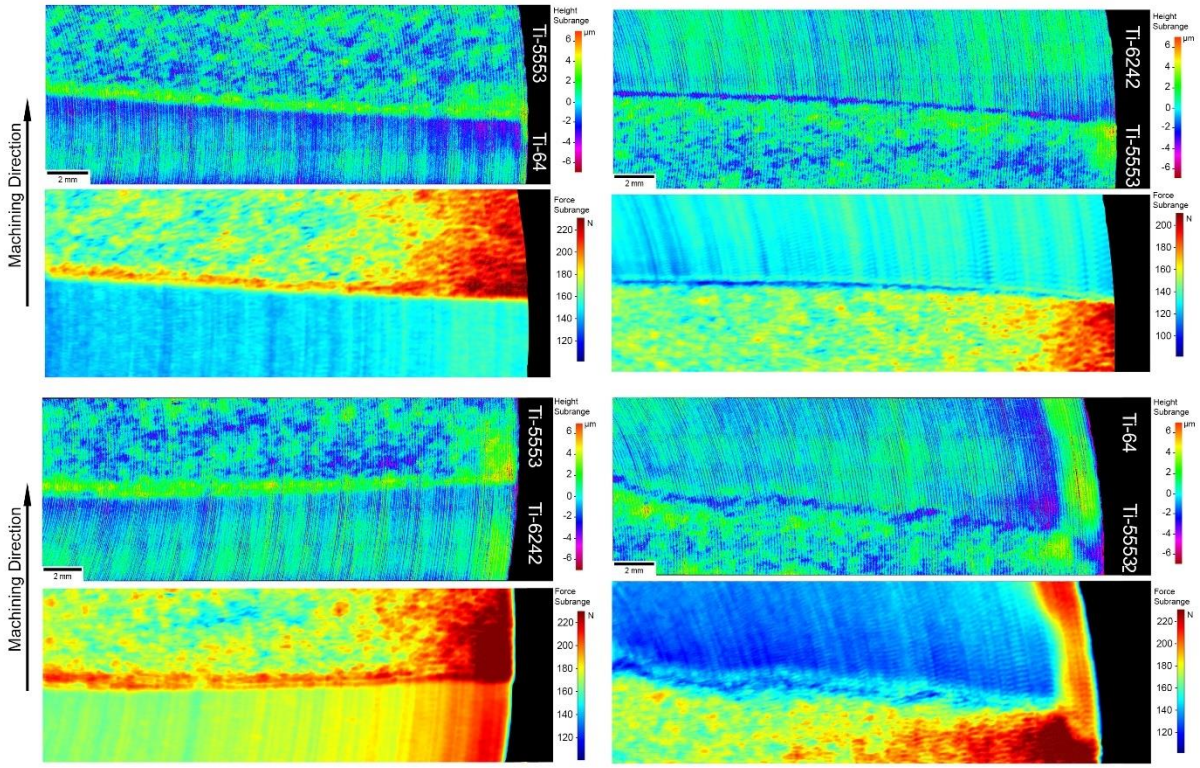


***Figure 7.10*** *– Map of the surface roughness and force feedback for bonds made of Ti-5553 with Ti-6242 and Ti-64 respectively.*

Figure 7.11 shows the scanning electron micrographs of the surface finish for the bonds between Ti-5553 and the α+β alloys. The micrographs in (a), (b), (e) and (f) were imaged using the secondary electron mode to obtain a better detail of the topography of the regions. The micrographs in (c), (d), (g) and (h) were imaged using backscattered electron mode to reveal the exact location of the bond.

The surface finish, when machining from Ti-5553 to α+β alloys, presents clear damage at the location of the bond. These results compare well with Figure 7.10 where a valley of the surface was observed when machining in this direction. However, when machining from an α+β alloy to Ti-5553, there is no evident surface damage caused by the bond, apart from pick-up located randomly on the surface. This result does not correlate well with Figure 7.10 where a peak at the surface was observed in the bond. The challenge with the topographical map and the force feedback data is that it is difficult to determine the exact location of the bond. The increase in the surface finish does not occur in the bond, it occurs at approximately 200 - 300 µm away from the bond line, as depicted by the yellow boxes in Figure 7.12.

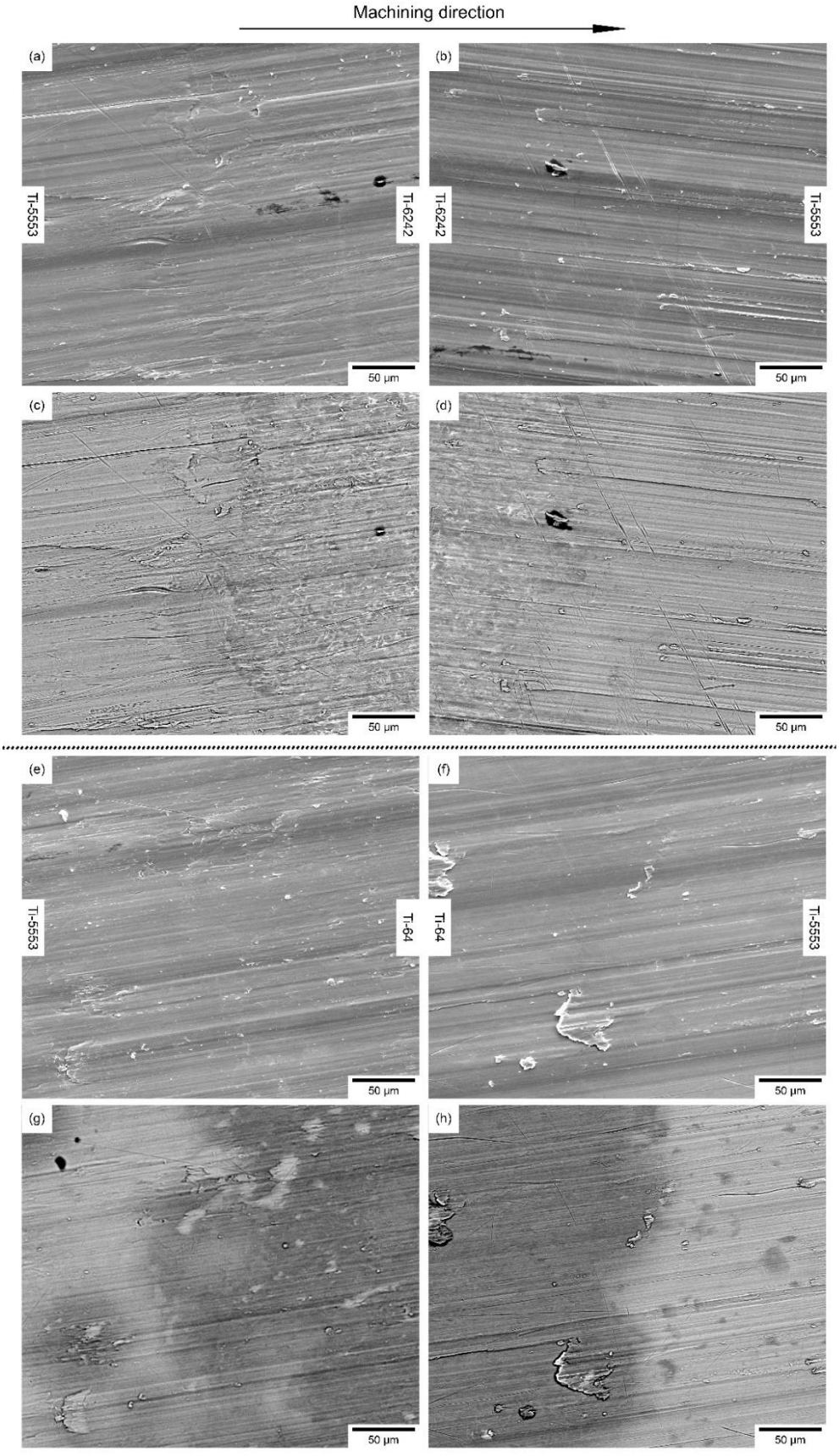


***Figure 7.11*** *– (a), (b), (e), (f) Secondary electron and (c), (d), (g), (h) backscattered electron micrographs of the machined surface in the bonds made of Ti-5553 with Ti-6242 and Ti-64.*

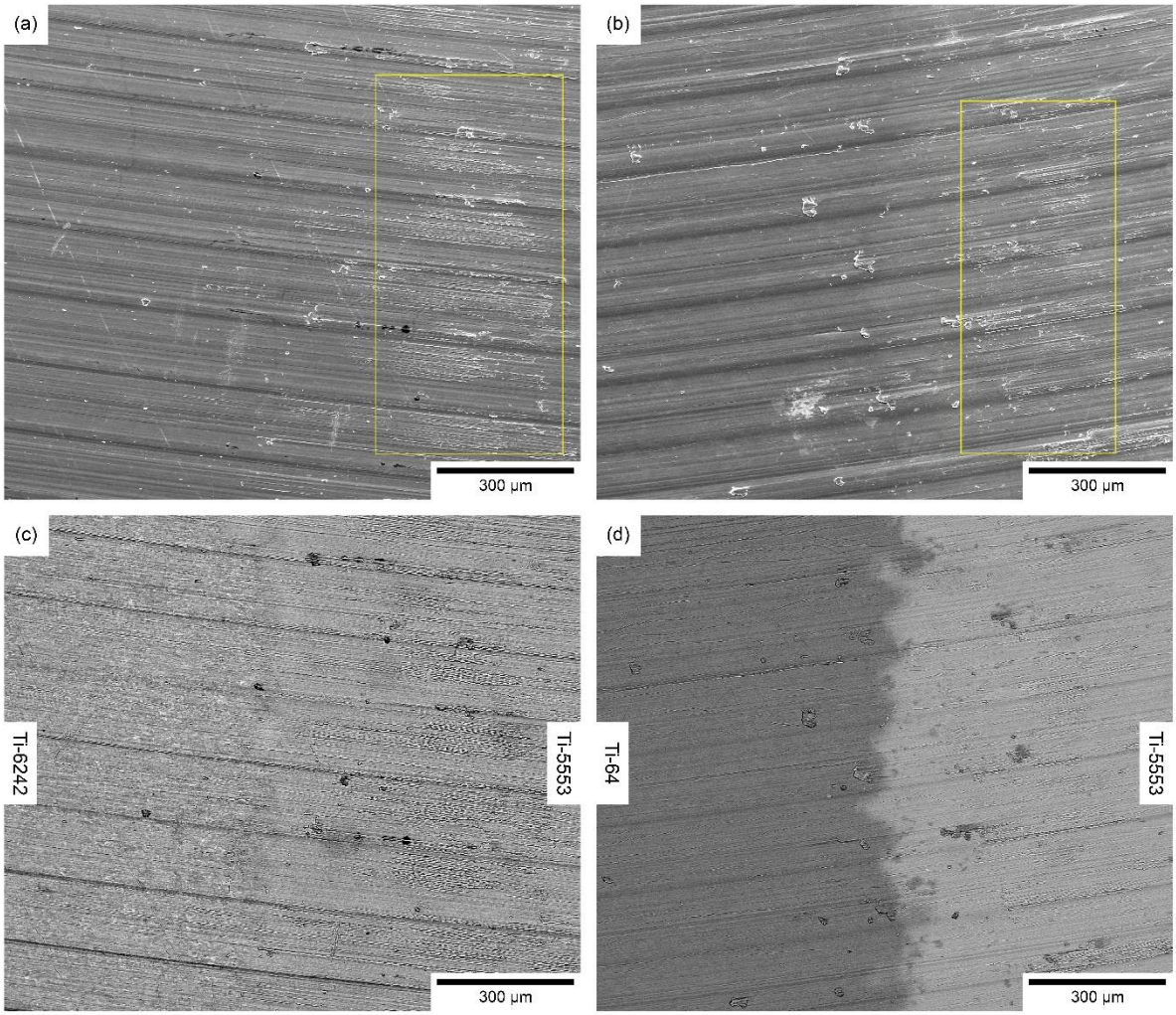


***Figure 7.12*** *– (a), (b) Secondary electron and (c), (d) backscattered electron micrographs of the bonds made with Ti-5553 showing the location of the pick-up close to the bond.*

Figure 7.13 shows the surface roughness and the force feedback maps of BetaC joined with the α+β alloys. As shown in Figure 7.8, there are no apparent peaks of forces for any machining direction, there is only a small peak when machining from BetaC to Ti-6242. Therefore, the surface roughness characteristics are very similar for the four bonds. The general trend is the formation of a valley in the BetaC region and the formation of a peak in the α+β alloys region. This behaviour is more obvious for the bond consisting of BetaC and Ti-6242, which are at the extreme ends of the beta stability alloy range.

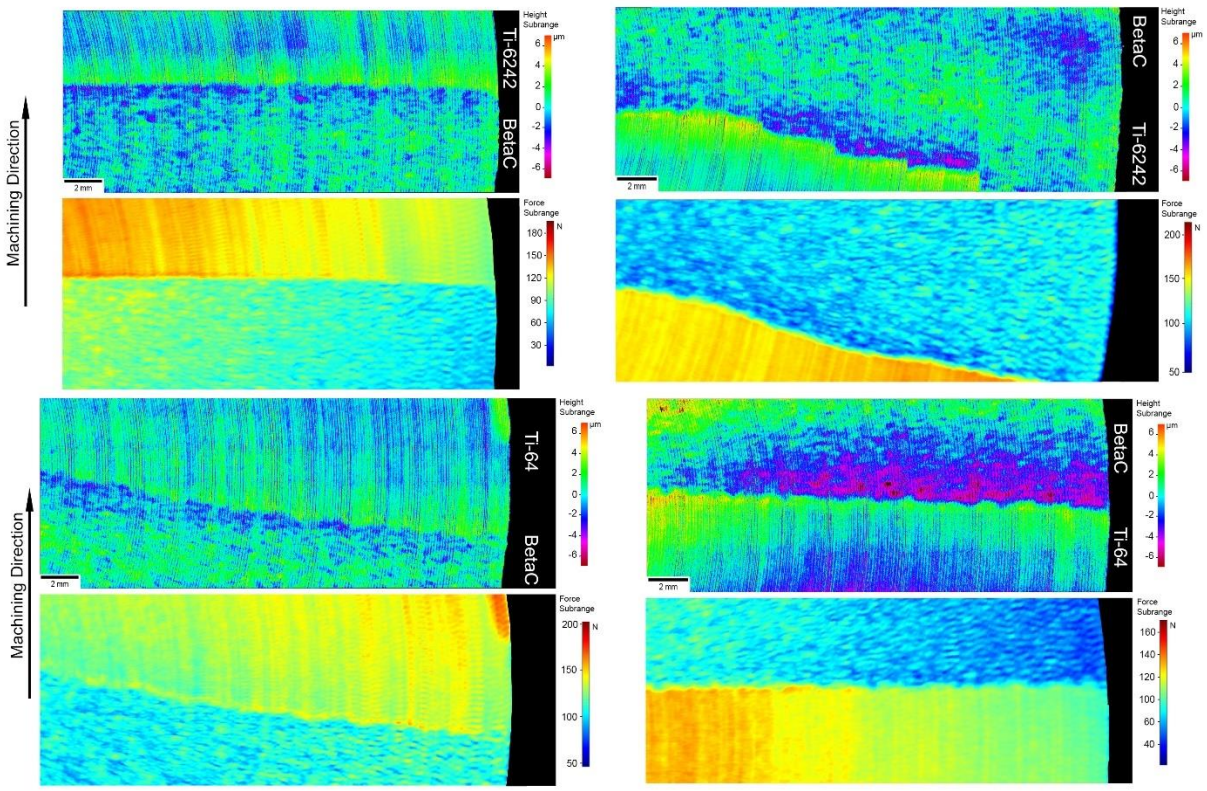


***Figure 7.13*** *– Map of the surface roughness and force feedback for bonds made of Ti-5553 with Ti-6242 and Ti-64 respectively.*

The micrographs of the surface finish for the bonds consisting of the alloy BetaC are shown in Figure 7.14. The characteristics of the surface finish are very similar to the ones observed for the bonds with Ti-5553. There is clear damage when machining from BetaC to an α+β alloy but not in the other machining direction. The relation of the bonds with the surface roughness maps and the surface finish is more complicated for the BetaC bonds than for the Ti-5553 bonds. The surface finish in the BetaC region is very poor, probably because the machining conditions were outside the optimum parameters for this particular alloy. Therefore, it is very difficult to determine a single zone of pick-up, similar to Ti-5553.

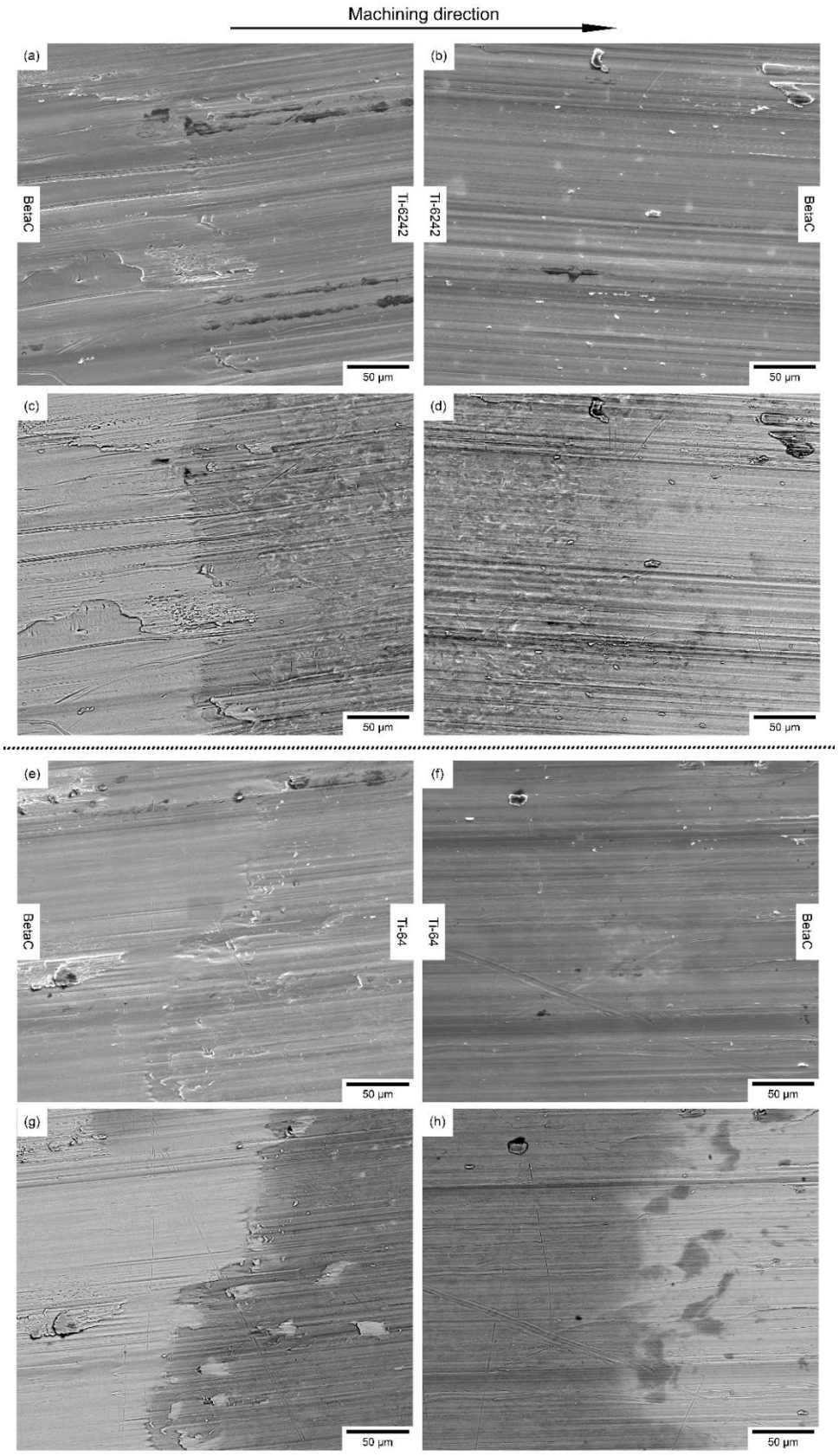


***Figure 7.14*** *– (a), (b), (e), (f) Secondary electron and (c), (d), (g), (h) backscattered electron micrographs of the machined surface in the bonds made of BetaC with Ti-6242 and Ti-64.*

Figure 7.15 shows the surface roughness and the force feedback maps of Ti-6242 bonded to Ti-64. The surface roughness exhibits no significant change in height across the bond irrespective of the machining direction. Nevertheless, it is observed that in the Ti-64 region, close to the bond, there is a small region with a valley in the surface finish of the material. The force plot shows the force required to machine Ti-6242 is higher than Ti-64, similar to the results observed in Figure 7.10.

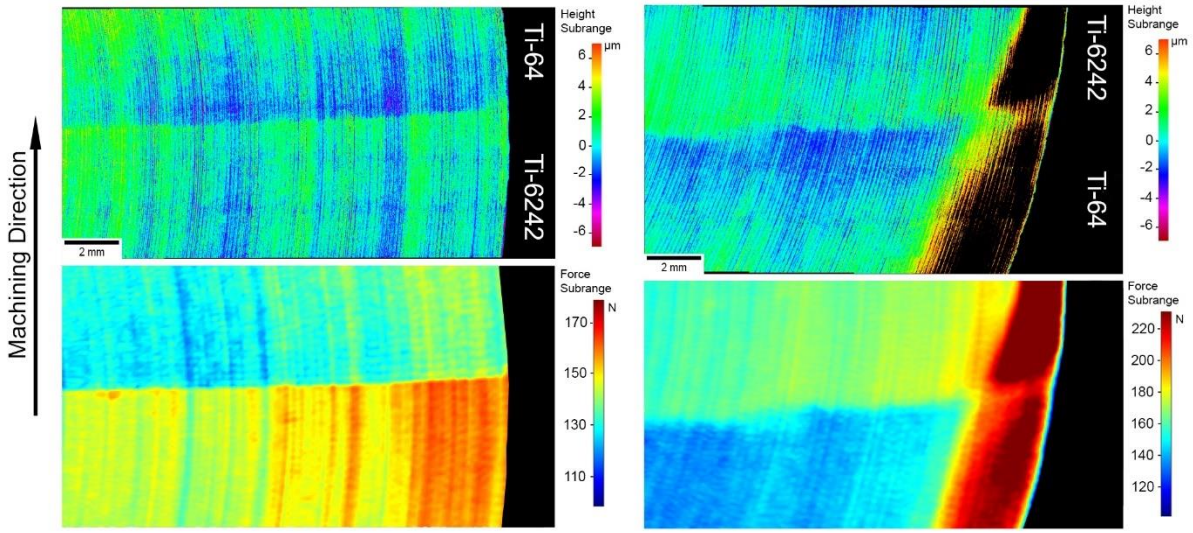


***Figure 7.15 – Map of the surface roughness and force feedback for bonds of Ti-6242 with Ti-64.***

The micrographs of the surface finish for the bond consisting of Ti-64 and Ti-6242 are shown in Figure 7.16. The results shows that there is no surface damage created in the bond irrespective of the machining direction. This is a significant difference in comparison with the bonds with a β alloy.

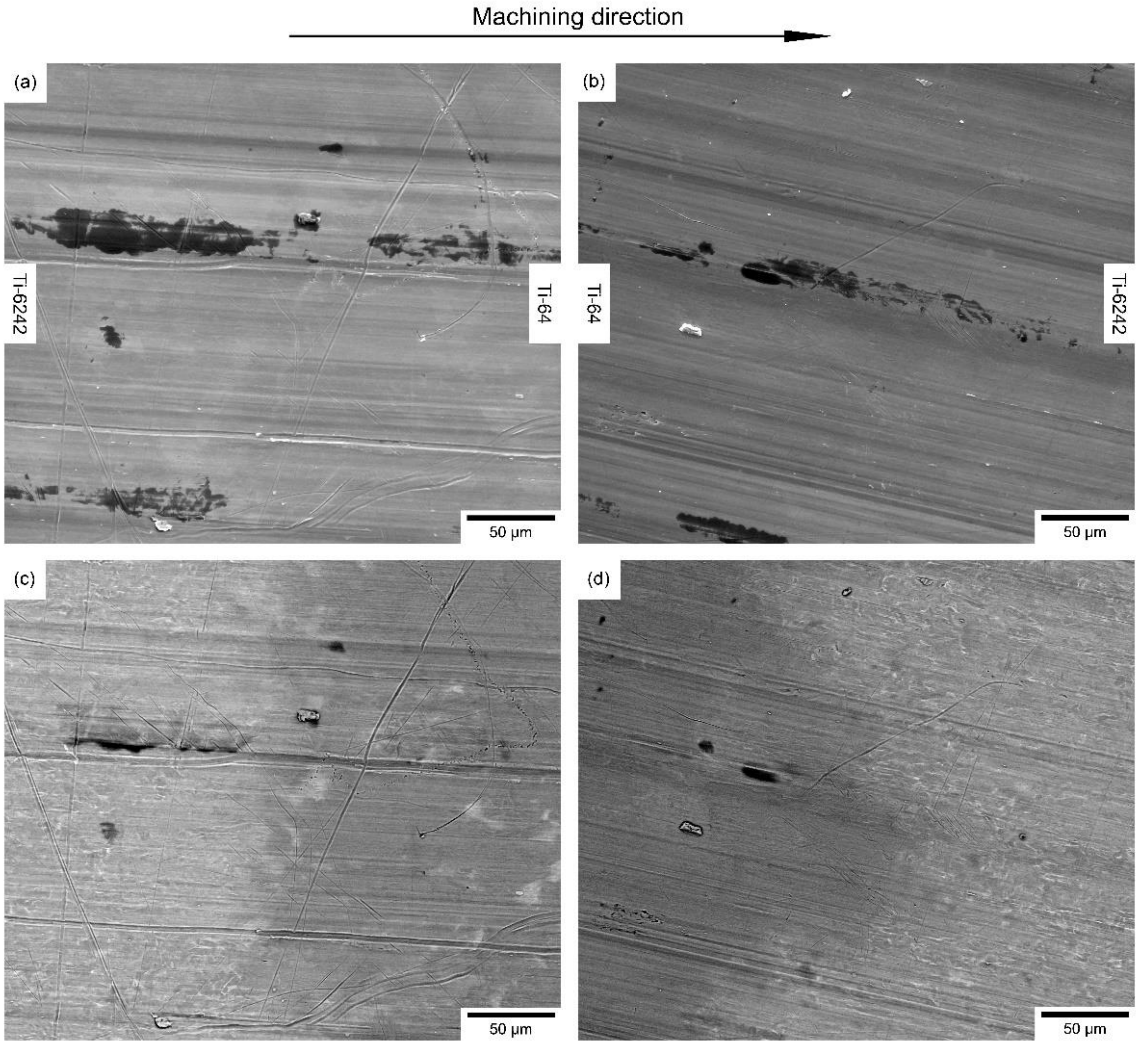


***Figure 7.16*** *– (a), (b) Secondary electron and (c), (d) backscattered electron micrographs of the machined surface in the bonds made of Ti-64 with Ti-6242.*

The results found for the bonds containing a β alloy are consistent with other machining trials carried out on FAST material processed in different conditions. An example of the bond made of BetaC and Ti-6242 in discs 2 and 3 are shown in Figure 7.17. The bond in disc 2 shows a high amount of pick-up generated in BetaC, however, all this pick-up accumulates in the exact location of the bond. The bond in disc 3 has less pick-up generated than in disc 2, however, there is evident damage in the bond, similar to the that observed in Figure 7.14. Although the machining parameters were the same for both discs, the workpiece microstructure is different. Therefore, the results show that changing the machining parameters for specific β alloys can reduce the damage generated in the bond, although it may not be enough to avoid damage altogether.

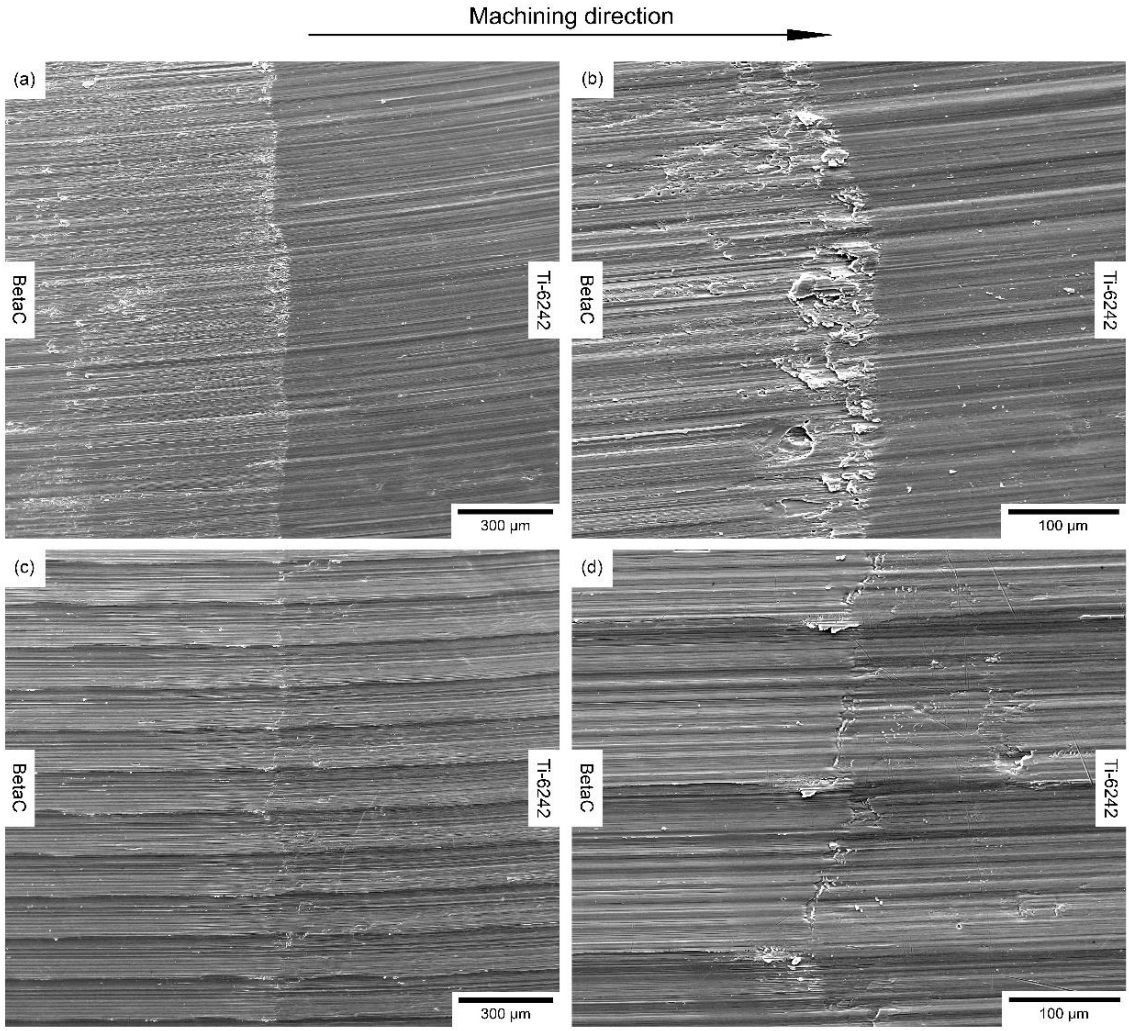


***Figure 7.17*** *– Secondary electrons micrographs of the machined surface in the bond made between BetaC and Ti-6242 for (a), (b) Disc 2 and (c), (d) Disc 3.*

### *7.3.4. Subsurface damage of the bond.*

The machining process can generate subsurface damage in the material, which can cause the failure of the component during in service [235,236]. In this section, the subsurface damage generated in the bond due to the machining process is assessed.

The micrographs of the bond's cross section made between Ti-5553 and the α+β alloys are shown in Figure 7.18. As mentioned in Section 7.3.1., the microstructure for Ti-64 and Ti-6242 bonds is very similar: fine scale secondary alpha forms at the bond region and significantly increases the local hardness levels.

There is no distinct difference in the subsurface damage across the bonds, regardless of the machining direction. When machining from Ti-5553 to α+β alloys, the deformation of the microstructure is lower than when machining in the opposite direction. The bond between Ti-5553 and Ti-6242 presents a small dip in the surface just at the beginning of the Ti-6242 microstructure in (a). Furthermore, there is a subtle increase of the surface level - in front of the dip - that compares well with the results observed in Figure 7.10. The bond between Ti-5553 and Ti-64 only shows a small amount of damage in (g), with the formation of a crack initiation points in the surface. In addition to this, in Figure 7.7 one of the graphs shows a constant value of force in the middle of the bond. That constant value is related with the micrographs in (e) because it shows the formation of multiple bonds in that location and the tool had to cross both alloys twice.

The subsurface damage of BetaC with the α+β alloys is shown in Figure 7.19. For these bonds, there is a smooth transition of hardness across the bond, as shown in Section 7.3.1. The subsurface damage in the bond between BetaC and Ti-6242 is similar to the one observed between Ti-5553 and Ti-6242, with a higher subsurface damage when machining from Ti-6242 into Ti-5553. Furthermore, when machining in direction from BetaC to Ti-6242, it is possible to observe an increase in the surface level in the location of the bond. This relates well with the surface damage observed when machining in this direction. There is also some damage in the bond when machining from Ti-6242 to BetaC, caused by the deformation of the finer laths near the beta region. The bond made of BetaC with Ti-64 contains less damage compared with the Ti-6242 bond. However, it has to be taken into account that these micrographs only show a 2D cross the section of the bond, so there may be microstructural information that has not been captured.

Finally, the subsurface of the bond made of Ti-64 with Ti-6242 is shown in Figure 7.20. The deformation of the microstructure is very small and unaffected by the machining directionality. Moreover, the surface across the bond has a constant surface roughness and no damage is observed in it. Nevertheless, it is possible to observe some particles above the surface that could be surface contamination in the sample because in Figure 7.16 there is no obvious pick-up generated in the bond.

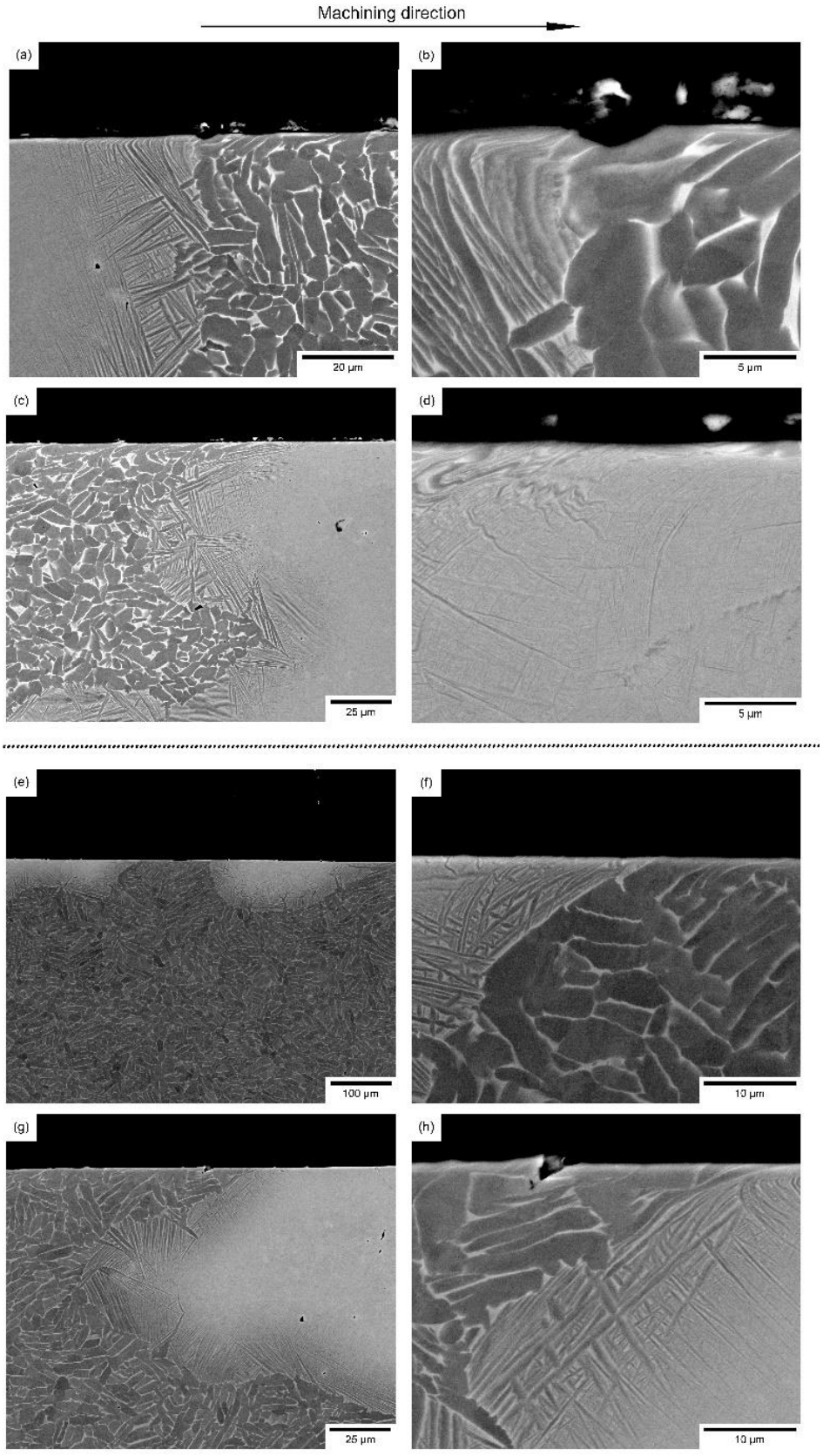


***Figure 7.18*** *– Backscattered electron micrographs of the subsurface damage for the bonds made of Ti-5553 with (a), (b), (c), (d) Ti-6242 and (e), (f), (g), (h) Ti-64.*

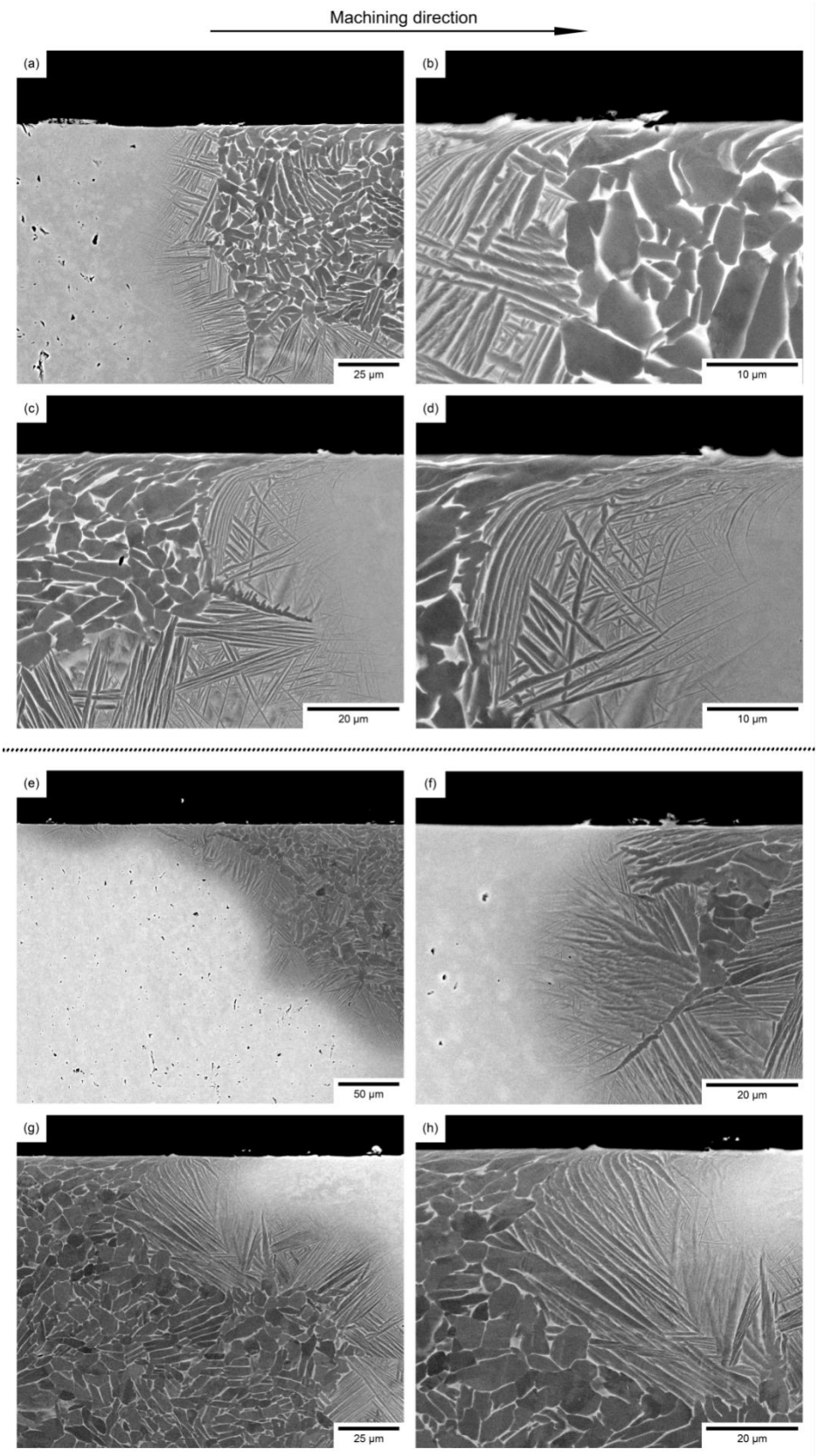


***Figure 7.19*** *– Backscattered electron micrographs of the subsurface damage for the bonds made of BetaC with (a), (b), (c), (d) Ti-6242 and (e), (f), (g), (h) Ti-64.*

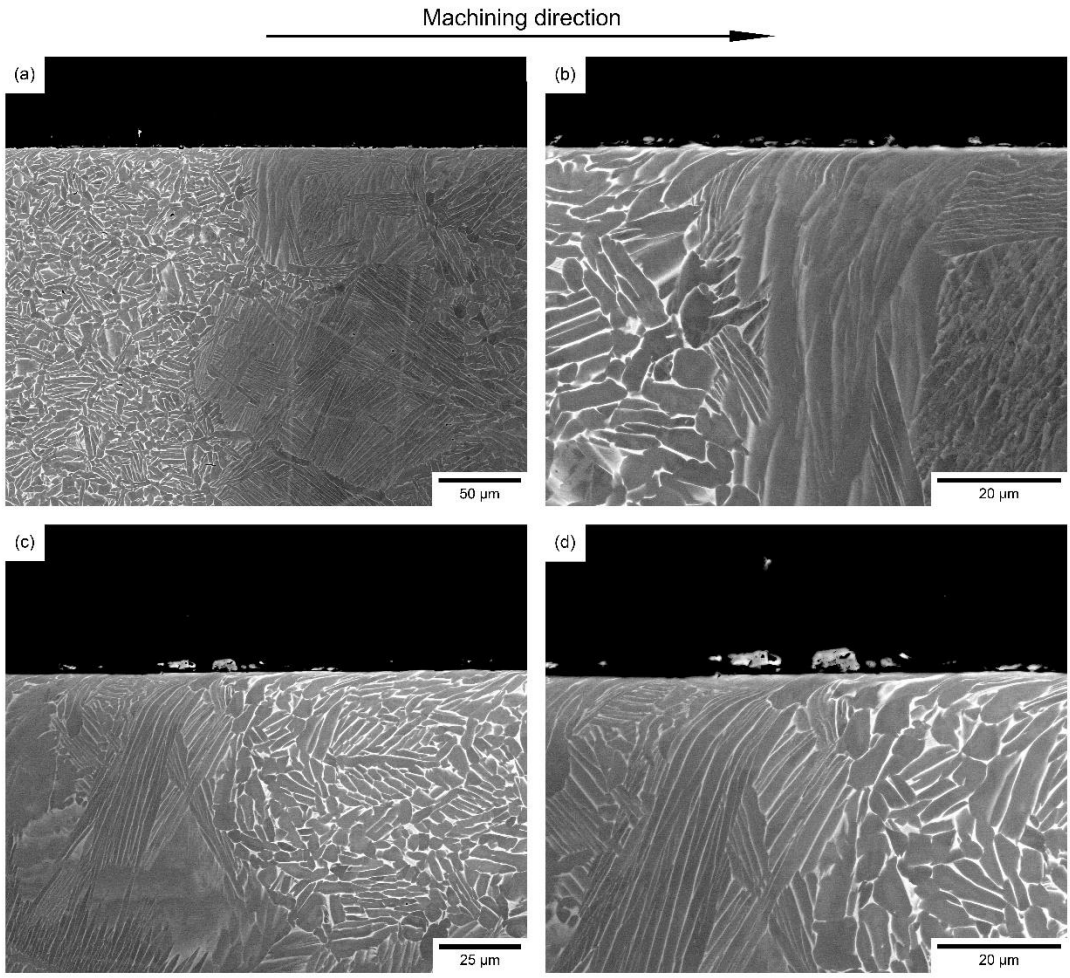


***Figure 7.20*** *– Backscattered electron micrographs of the subsurface damage for the bonds made of Ti-64 with Ti-6242.*

Figure 7.21 shows the bond between Ti-5553 and Ti-6242 in disc 2. The microstructure of Ti-6242 in disc 2 is a classic fully transformed, large equiaxed grain structure and the bond has the formation of fine secondary alpha, as shown in (d). The machining direction was from Ti-5553 to Ti-6242 and as appreciated in (a) and (b), there is a high amount of pick up in the bond. The cross section of the sample revealed that the formation of this pick up occurred in the middle of the bond, in the region where the fine secondary alpha is formed. This example demonstrates that even if the processing conditions of the material are different, the machinability of the bond is similar to the results presented in this chapter.

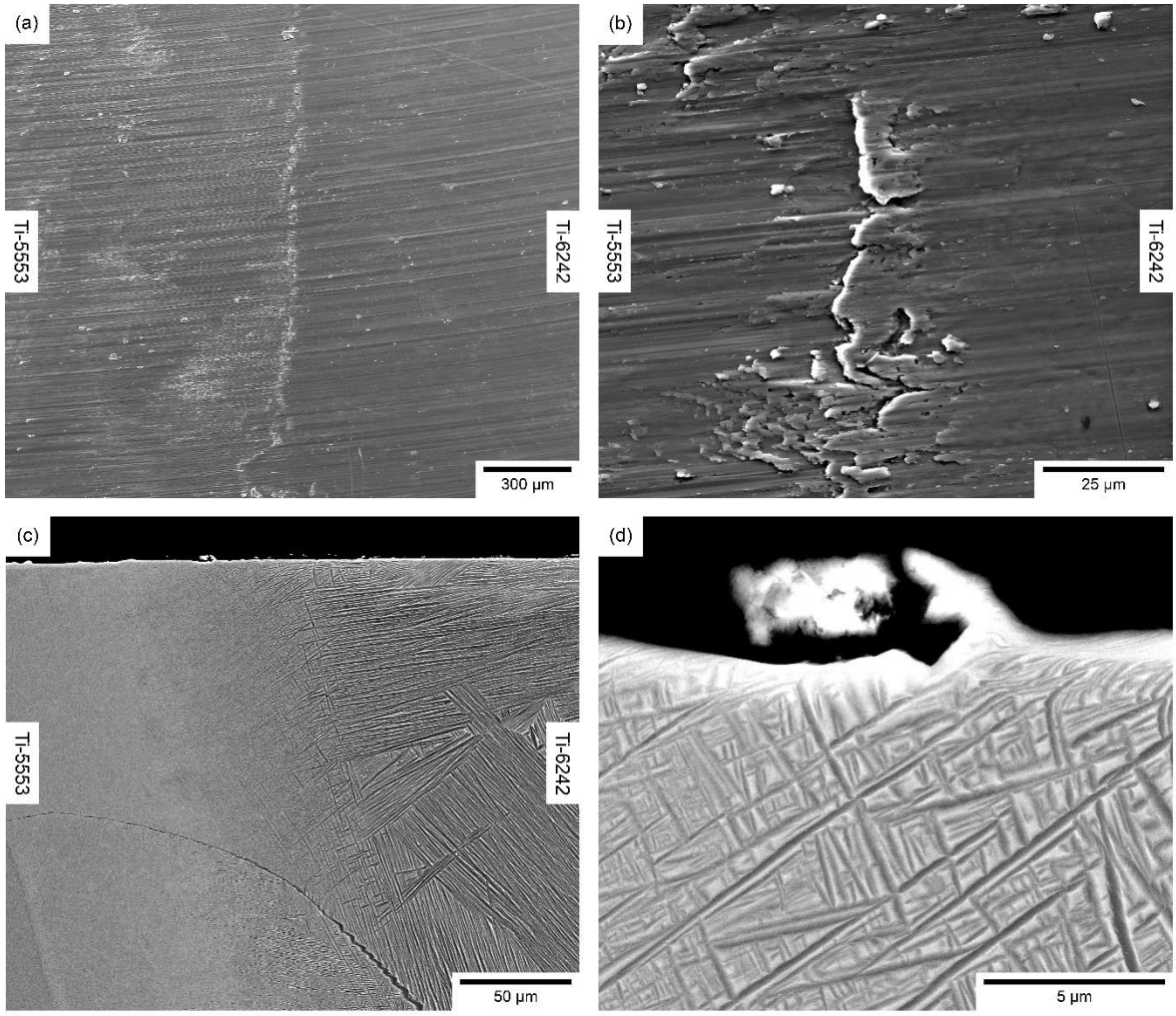


***Figure 7.21*** *–(a), (b) Secondary electron and (c), (d) backscattered electron micrographs of the machined surface and the cross section for the bond between Ti-5553 and Ti-6242 in Disc 2.*

## *7.4. Discussion*

The microstructural characterisation shown in this work, presents clear evidence of a small amount of porosity in BetaC and Ti-5553, this is caused for three different reasons.

(1) The processing conditions were not ideal for these alloys, which require higher temperatures or pressure to fully consolidate.

(2) The tap density of the β alloys is lower than the α + β powders. However, the powders were filled to the same height, as shown in Figure 7.2. This means that the α + β powder fully consolidated before the β powders, which prevented its full consolidation.

(3) The beta powder had a higher amount of internal porosity, as shown in Section 4.6. This type of porosity is very difficult to eliminate through sintering or HIP'ing routes.

Table 7.2 effectively summarises the results presented in Section 7.3 and shows information about the bonds presented in discs 1,2 and 3 such as, if there was a peak in the forces; if the surface level decreased; and if there was damage in the surface. Notice that the table does not include the Ti-64 / Ti-6242 bond because there is no noticeable damage regardless of the machining direction.

Table 7.2 shows that there is not a clear relationship between the peak of forces measured in the Z axis and the damage found in the bond for discs 1 and 2. Furthermore, the surface roughness maps correlate well with the damage found in the bond region that are made with Ti-5553, but there is not a direct relationship for the bonds containing the BetaC alloy. The only parameter that seems to correlate well with the surface damage is the direction of the machining operation across the bond. Damage in the bond always occurs when machining from a β alloy through to an α+β alloy.

Although the microstructure resultant of the processing conditions influences the amount of pick-up generated and the severity of the damage, it does not change the damage characteristics in the bond when machining from a β to an α+β alloy. This is demonstrated by two supertransus bonds with different dwell times in Figure 7.17 or a subtransus bond in Figure 7.14.

The location of the bond does not exhibit damage when machining from an α+β to β alloy. However, the surface roughness (in Figure 7.10) reveals a very clear peak in the surface level, which is correlates with an increase of forces in that region. This pick-up region is located at approximately 200 - 300 μm from the bond, which is greater than the expected diffusion distance in the bond for a subtransus microstructure, as discussed in Chapter 5. The Z-contrast brightness of the pick-up in the backscattered electron micrographs in Figure 7.12 shows that the pick-up is not exclusively from the α+β alloy, and there is some blended pick-up from the β alloy also.

***Table 7.2*** *– Summary of bond characterization presenting the relation between the directionality of the machining, the microstructure, the force in Z, the surface roughness and the pickup in the bond.*

| Sample | Bonds (direction) | Peak force in Z | Decrease of surface | Damage in the bond |
|---|---|---|---|---|
| **Disc 1** | Ti-5553/Ti-6242 | No | Yes | Yes (low) |
| **Disc 2** | Ti-5553/Ti-6242 | Yes | - | Yes (high) |
| **Disc 3** | Ti-5553/Ti-6242 | Yes | - | Yes (low) |
| **Disc 1** | Ti-6242/Ti-5553 | Yes | No | No |
| **Disc 1** | Ti-64/Ti-5553 | Yes | No | No |
| **Disc 2** | Ti-64/Ti-5553 | Yes | - | No |
| **Disc 3** | Ti-64/Ti-5553 | Yes | - | - |
| **Disc 1** | Ti-5553/Ti-64 | No | Yes | Yes |
| **Disc 1** | BetaC/Ti-6242 | No | Yes | Yes (low) |
| **Disc 2** | BetaC/Ti-6242 | Yes | - | Yes (low) |
| **Disc 3** | BetaC/Ti-6242 | Yes | - | Yes (high) |
| **Disc 1** | Ti-6242/BetaC | Yes | Yes | No |
| **Disc 1** | Ti-64/BetaC | No | Yes | No |
| **Disc 2** | Ti-64/BetaC | No | - | No |
| **Disc 3** | Ti-64/BetaC | No | - | No |
| **Disc 1** | BetaC/Ti-64 | No | Yes | Yes |

The direction of machining has little impact on the subsurface damage. The subsurface damage for all the bonds is shown in Figure 7.18 - 7.20 and the micrographs reveal similar

damage in the bulk material and the bonds. Although there seems to be a higher subsurface damage when machining from a β to an α+β alloy, the difference is only a few microns. Therefore, it is possible to conclude that the machining directionality does not play a significant role regarding the machining induced damage, at least for the testing programme conditions presented in this chapter.

There has been previous research comparing the machinability between a β alloys and α+β alloy. The machining of Ti-5553 tends to create higher forces compared to Ti-64 [237–239]. This is caused because the thermal conductivity of Ti-5553 (22 W/mK) is 30% higher than that of Ti-64 (15 W/mK) at 700°C [239]. Lower thermal conductivities promote the formation of chip segmentation, which reduces the reaction force. However, higher thermal conductivity transfers the heat from the material to the chip, which reduces the degree of softening occurring in the material during machined [239]. In addition to this, several studies have shown that beta alloys, such as Ti-5553 and BetaC, tend to adhere more to the cutting face of the tool compared to conventional Ti-64, which creates larger built-up edge chip thickness [239–241]. This correlates well with Figure 7.17 and 7.21, where there is a large amount of pick-up in the bond when machining from a β to an α+β alloy. Furthermore, Rashid et al [242] observed the formation of built-up edge (BUE) in beta alloys is higher for more ductile workpieces. In Figure 7.17, the sample processed at a higher temperature had a larger amount of pick-up. There is no information about the tensile properties for both materials, but it is expected that the disc processed at higher temperature will have larger grains, therefore, the ductility between both alloys is expected to be different. From the stress-strain curves in Chapter 5 (Figure 5.8), it is expected a higher ductility from the sample processed at a higher temperature.

From all this information, it is clear that the effects observed when machining multi-materials are influenced by the workpiece microstructure and or, the CNC machine. Some of the faces were machined in two different CNC machines, in order to check that the trends in the forces were consistent in different equipment. Although the same machining conditions, samples and tools were used for both machines, the forces produced were larger for one of the machines, as shown in Figure 7.22. The difference in force between the two machines is likely to be caused by a calibration of the dynamometer because the same samples were used for both tests. The tests occurred in separated machining trials and the dynamometer had to be

calibrated for each trial. There is not a consistent method to calibrate the dynamometer, for this reason it is likely that there was a difference of forces on that day. Nevertheless, the same force trends were observed for all of the bonds tested, meaning that the directionality effects are not linked to the CNC machine used for most of the tests.

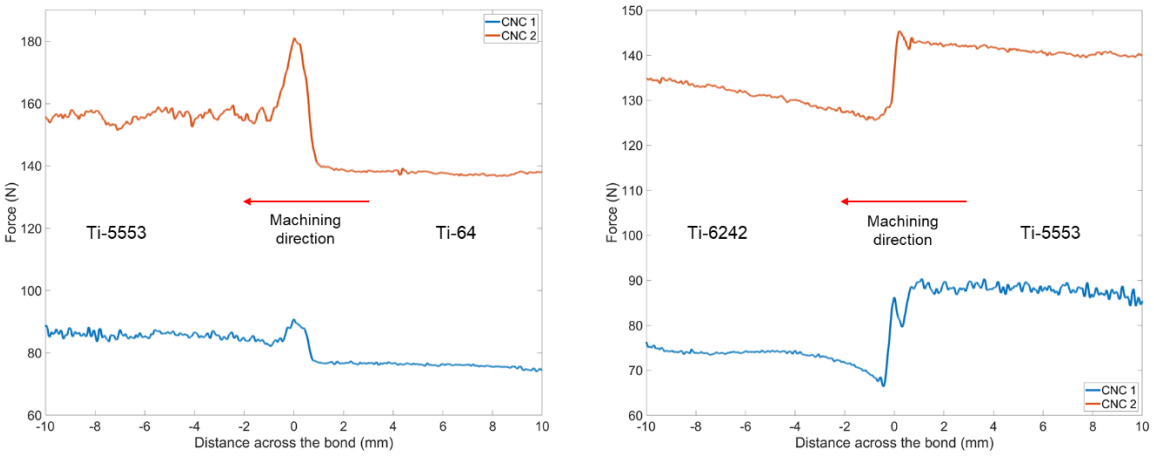


***Figure 7.22*** *– Plot of the forces produced in two different CNC machines when machining the same bonds with the same machining conditions and tool.*

In previous investigations, it has been observed that there are multiple factors affecting the surface roughness of titanium components in machining operations, such as; tool shape, geometry and tool wear, temperature, tool coating, feed rate, cutting speed, depth of cut and BUE formation [243]. Some of the parameters such as tool geometry, tool coating and tool wear can be discarded as a factor, because the two alloys were machined with the same tool during the same machining operation. The rest of the parameters cannot be discarded because there is not enough data or the data is difficult to measure while processing. For example, the feed rate, cutting speed and depth of cut should be the same for both alloys, but the machinability of α+β alloy and β alloys is different, so it is possible that the Numerical Control (NC) of the equipment used, had to adjust the settings to maintain the same parameters. If the tool decreases the speed during the initial stages of β alloy machining, it could take a fraction of a second for the machine to increase the power to maintain the same speed. In that fraction of second, as the machine is adjusting the settings, the speed decreases and both the pick-up and reaction forces increases. All this relates well with the observations from the Alicona and force feedback maps, as well as the pickup generated in Figure 7.12.

However, this will not be possible to demonstrate without being able to obtain the data of the actual speed of the machine.

# 8. Conclusions and Further Work

## 8.1. Conclusions

This thesis exploits that the use of FAST to diffusion bond dissimilar titanium alloys from powder has the potential to become a disruptive technology in the aerospace sector, when multi-material components are required. Furthermore, the work has demonstrated the key advantages of the solid-state process and highlighted the best ways to work with these materials.

Three main areas have been investigated in this thesis; (1) the deformation of a diffusion bond between two similar alloys, (2) the residual stresses generated in FAST-DB material and (3) the machinability of a FAST-DB component. The conclusions of this work will be presented in this section.

### 8.1.1. Integrity of the bond

- The bonds made with dissimilar titanium alloys have shown excellent mechanical integrity. The diffusion of alloying elements across the bond varied depending on the processing conditions, but the dwell time and hold temperature were particularly dominant on the bond characteristics.
- The level of diffusion measured in the bonds ranged from 50 to 350 µm. However, the major difference was observed when the powder was processed above or below the beta transus temperature. For subtransus conditions, the diffusion observed ranged from 50 to 150 µm, while for supertransus conditions the diffusion ranged from 150 to 350 µm. This is caused by the allotropic phase change from an HCP to a BCC crystal structure when processed below and above the beta transus, respectively.
- The bonds generated in the thesis show no evidence of defects or cracks in the diffusion bond region.

- In chapter 7 it is possible to see some porosity in the bulk material of the β alloys. The porosity is a consequence of the initial compaction of the powder because the β alloys used in this work had less efficient tap density compared to the α+β alloy powders. This means that, for the same volume, powders that compact better will have less initial porosity between the particles and more mass will be used. Therefore, the displacement of the ram stopped when the α+β alloy powder(s) were fully consolidated without allowing time for the β alloys powder to fully consolidate.

### *8.1.2. Mechanical properties and deformation of the bond*

The first experimental chapter of the thesis studied the deformation behaviour of a FAST-DB bond between the alloys Ti-64 and Ti-6242.

- The work showed consistently that the failure of FAST-DB bonds, with these two alloys, occurs in the lowest strength alloy (i.e. Ti-64), far away from the bond location. This observation occurred regardless of whether the sample was processed above or below the beta transus.
- The distribution of the strain in the samples during the tensile test varied for different processing conditions. The subtransus sample had a smooth transition across the bond, with a higher strain in the Ti-64 region. Meanwhile, the supertransus sample had a more homogeneous distribution across the sample, but there was still a difference of strain between the two alloys.
- The work proved that the strength of the FAST-DB samples is similar to a conventionally processed monolithic titanium sample. This will give further confidence to those designers who are looking to exploit FAST-DB technology for parts.
- For a bond made of two similar alloys, the crystal orientation from the EBSD maps does not show any significant changes in microtexture across the bond. Therefore, it is difficult to determine the exact location of the bond line just by observing the EBSD maps, it is necessary to also use band contrast or backscattered electron imaging maps.

- The results at a mesoscale level showed that the deformation occurs in the Ti-64 region, even if the bond has more favourable oriented grains for the prismatic slip. This is caused by the local microchemistry and an increase of the solid strengthening across the bond when transitioning from the Ti-64 to the Ti-6242 chemistry. Consequently, it is very clear that most of the strain occurs outside of the diffusion transition zone.

### *8.1.3. Residual Stresses in FAST-DB and FAST-forge material*

The thesis also studied the residual stress profiles of FAST material, FAST-DB and forged multi-material component.

- From the X-ray diffraction and the contour method results, it can be concluded that the FAST material has very low residual stress. The low residual stress is thought to be caused by the homogeneous heating of the sample in the graphite dies and a relatively slow cooling rate.
- The addition of a diffusion bond made with similar titanium alloys, such as Ti-64 and Ti-6242, does not show significant changes in the residual stress profile of the material. It was possible to observe a small increase in the stresses close to the bond location, but the overall stresses are still very low.
- There can be chemical misfit when bonding two extreme dissimilar titanium powders such as CP-Ti and Ti-5553. These alloys generate a new microstructure in the bond region: The fine secondary alpha laths generated increases in the residual stresses in the bond due to the stresses that the alpha lath produces in the matrix.
- The residual stresses measured with the contour method of closed-die forged FAST-DB material showed similar stresses to conventional forged titanium in the bulk material. Additionally, there was a smooth transition of the stresses across the bond, which means that there are not deleterious changes in the residual stresses close to the bond.
- The conform method struggles to resolve the stresses in the exact location of the bond. Therefore, further work is required to fully understand the stresses generated in the bond for forged materials.

### *8.1.4. Machineability of FAST-DB components*

In this work, the machineability of FAST-DB material with dissimilar titanium alloys have been investigated. The force feedback [164] technique showed the changes of force when machining these samples: this was correlated with the surface roughness maps made with a microscope. Furthermore, the surface and subsurface damage was investigated using optical and scanning electron microscopy.

- When machining $\alpha$+$\beta$ alloys bonded to $\beta$ alloys, the direction of the machining operation affected the generation of damage in the bond. The force measured in the bond was affected by the directionality, however, there was not a clear link to the damage.
- Surface damage always occurred when machining from the $\beta$ through to the $\alpha$+$\beta$ alloys, and the severity of the damage was determined by the machining parameters used or the microstructure of the workpiece.
- The most common damage generated in the machining surface of the bond was smeared titanium from one of the alloys, which is caused by titanium sticking in the tool and then being deposited in the surface while machining the sample. This is also known as “pick-up”, and it was always detected in the exact location of the bond.
- No subsurface microstructural damage was observed in the bond, regardless of the machining direction and the microstructure of the workpiece.
- It is believed that the damage observed in the surface occurred due to two main reasons: the first one is related to the machinability of each alloy and the second reason is linked to how the CNC machine responds to the sudden change of alloy chemistry.
- The diffusion bond of titanium alloys with similar mechanical properties and machinability do not cause issues in the bond during machining operations, regardless of the machining direction.

## 8.2. Future work

The recommended future work can be divided in three main sections, each one related to one experimental chapter.

### 8.2.1. Mechanical properties and deformation of the bond

This work has characterised the deformation mechanisms in the bond between two dissimilar titanium alloys with similar mechanical properties. However, there is still further research to be done to fully understand the mechanical properties of the bond.

The change of microstructure across the bond between some titanium alloys could potentially affect the deformation behaviour of the bond, showing a different performance to the one observed between Ti-64 and Ti-6242. For example, when joining Ti-6242 with Ti-6246, only the amount of Mo is the primary difference in the alloy chemistry, but the microstructure is transformed from a fully lamellar to a Widmanstätten as FAST-DB material transitions from Ti-6242 to Ti-6246. In addition to this, the optical DIC technique has helped to elucidate the deformation at a mesoscale level, however, this technique was not able to fully resolve individual slip bands inside the grains. The study of the diffusion bond deformation with HR-DIC techniques [192] would help to fully understand the deformation slip behaviour close or at the bond. It would be of great interest to study an area that has a single grain (and parent beta orientation) containing both alloy chemistries, similar to the one shown in Figure 5.1. This would provide interesting data about the effect of Mo on the propensity for slip. This would have a wider impact for new titanium alloys in addition to the upscaling of the FAST-DB technology.

All the mechanical properties presented in this thesis and previous work done by other researchers have used as FAST material [9]. Although the use of a FAST-*forge* [104] route has the potential to be used for industrial applications, there has been very little research that looks into the mechanical properties of FAST-*forge* material. Further research should be done in order to fully understand the potential advantages or issues of forging a bond with the mechanical properties.

All the tests conducted on FAST material have been at room temperature. Yet, most of the titanium components inside the jet engine operate at medium to high temperatures. Before FAST-DB material can be used inside a jet engine, it is important to see if the results observed at room temperature are the same at the expected operational temperatures. The creep response of the bond region could be worse than the bulk material and there is also a risk on the formation of different phases in the bond caused by the increase of temperatures. Furthermore, it would be important to study the corrosion behaviour and ballistic behaviour of the FAST-DB material because the components could operate in maritime and defence environments.

### *8.2.2. Residual stresses of FAST-DB and* FAST*-forge material*

This thesis has presented the residual stresses generated in FAST and FAST-DB of several titanium alloys combinations. Nevertheless, there is still some parts that require further research.

The stresses generated in a forged FAST-DB component were only studied with the contour method, which showed a smooth transition between both alloys. However, it has been demonstrated that the XRD method has better resolution in the bond. For that reason, it would be necessary to further study the forged components using the XRD method.

The results presented in this thesis also showed differences in the stresses generated in the bond processed from CP-Ti and Ti-5553 with different conditions. To further understand if the differences are caused by the processing conditions or it is linked to a limitation of the technique, a comparison of the mean angular deviation (MAD) value could be done between both values. The MAD will not show the exact value of residual stresses because it measures the averaged angular misfit between the measured and expected Kikuchi bands. However, a similar trend in both samples would increase the likelihood that the difference in results is caused by the limitation of the technique. Furthermore, the use of transmission electron microscopy (TEM) could reveal in detail if the secondary alpha phase generated in the bond causes stress in the matrix, which, could be linked to the high residual stresses measured with the XRD method.

To fully exploit the FAST process, it will be required to produce larger samples than the 60 mm discs used in this study. There is a risk of heating heterogeneities when producing larger samples using FAST, which could cause higher residual stresses than the ones presented in this study. Therefore, the residual stresses of larger samples should be studied before using this material for industrial applications.

### *8.2.3. Machining of FAST-DB material*

The machining of multi-material components has been studied in this thesis. The results have presented a clear machining directionality effect, but further work is required to fully understand the causes of this directionality. The following further work recommendations will help to better understand the machinability of multi-material components.

One of the greatest unknowns in this work, is the response of the control unit when machining two dissimilar alloys. In theory, the control units are designed so the response is always constant and immediate. However, this has not been studied when machining two dissimilar alloys. Therefore, it is possible that there is a reaction time across the bond that causes some of the damage observed in this work.

In addition to this, the work has presented the results of forces for multiple microstructures machined under the same machining conditions. Changing the machining conditions could affect the forces generated in the bond, as well as the damage generated. Further work is required to understand this relationship. Then, the next step would be to develop an adaptative machining code that changes to the optimal machining conditions in each part of the component, in order to minimise the amount of damage generated in the bond. Given the difficulty of testing and analysing the forces and the damage generated in the bond, the use of machining simulations could help to identify the optimal machining conditions before doing the (relatively expensive) machining trials. This study would be similar to the study Dredge et al [244] carried out for single titanium alloy components.

# 9. *References*


[1] European Aviation Environmental Report 2019, Eur. Union Aviat. Saf. Agency. (2019) 1–112. https://ec.europa.eu/transport/sites/default/files/2019-aviation-environmental-report.pdf (accessed July 11, 2021).

[2] EPA Finalizes Airplane Greenhouse Gas Emission Standards, United States Engiromental Prot. Agency. (2020). https://nepis.epa.gov/Exe/ZyPDF.cgi?Dockey=P1010TFZ.pdf (accessed July 7, 2021).

[3] Destination 2050 - A route to net zero European aviation, Eur. Aviat. Trade Assoc. (2021) 1–191. https://www.destination2050.eu/wp-content/uploads/2021/03/Destination2050_Report.pdf (accessed July 11, 2021).

[4] A.P. Mouritz, Introduction to aerospace materials, Woodhead Publishing, Cambridge, England, 2012. doi:10.1533/9780857095152.

[5] S. Babu, W. Peter, R. Dehoff, L.J. Love, Report on Additive Manufacturing for Large-Scale Metals Workshop, Oak Ridge Natl. Lab. (2016). https://info.ornl.gov/sites/publications/files/Pub62831.pdf (accessed November 19, 2020).

[6] A.R. McAndrew, P.A. Colegrove, C. Bühr, B.C.D. Flipo, A. Vairis, A literature review of Ti-6Al-4V linear friction welding, Prog. Mater. Sci. (2018). doi:10.1016/j.pmatsci.2017.10.003.

[7] M. Yakout, M. Elbestawi, S.C. Veldhuis, A Review of Metal Additive Manufacturing Technologies, Trans Tech Publ. 278 (2018) 1–14. doi:10.4028/www.scientific.net/SSP.278.1.

[8] N. Naveen Kumar, G.D. Janaki Ram, S.S. Bhattacharya, H.C. Dey, S.K. Albert, Spark Plasma Welding of Austenitic Stainless Steel AISI 304L to Commercially Pure Titanium, Trans. Indian Inst. Met. 213 (2015) 287–297. doi:10.1007/s12666-015-0589-6.

[9] J.J. Pope, E.L. Calvert, N.S. Weston, M. Jackson, FAST-DB: A novel solid-state approach

for diffusion bonding dissimilar titanium alloy powders for next generation critical components, J. Mater. Process. Technol. 269 (2019) 200–207. doi:10.1016/j.jmatprotec.2019.02.011.

[10] J. Pope, M. Jackson, Fast-forge of diffusion bonded dissimilar titanium alloys: A novel hybrid processing approach for next generation near-net shape components, Metals (Basel). 9 (2019) 654. doi:10.3390/met9060654.

[11] O. Levano Blanch, D. Lunt, G.J. Baxter, M. Jackson, Deformation Behaviour of a FAST Diffusion Bond Processed from Dissimilar Titanium Alloy Powders, Metall. Mater. Trans. A Phys. Metall. Mater. Sci. 52 (2021) 3064–3082. doi:10.1007/s11661-021-06301-w.

[12] G. Lutjering, C.W. James, Titanium, 2nd ed., Springer, Berlin, Germany, 2007.

[13] A. Russell, The Rev. William Gregor (1761-1817), discoverer of titanium., Mineral. Mag. J. Mineral. Soc. 30 (1955) 617–624. doi:10.1180/minmag.1955.030.229.01.

[14] M.A. Hunter, Metallic titanium, J. Am. Chem. Soc. 32 (1910) 330–336. doi:10.1021/ja01921a006.

[15] W. Kroll, Method for manufacturing titanium and alloys thereof, 217,773, 1938.

[16] C. Leyens, M. Peters, Titanium and Titanium Alloys: Fundamentals and Applications, Wiley-VCH, Weinheim, Germany, 2003. doi:10.1002/3527602119.

[17] Mineral commodity summaries 2018, 2018. doi:10.3133/70194932.

[18] M. Jackson, R.R. Boyer, Titanium and its Alloys : Processing , Fabrication and Mechanical Performance, in: Encycl. Aerosp. Eng., John Wiley & Sons, Ltd, New Jersay, USA, 2010: pp. 1–16.

[19] W. Kroll, The Production of Ductile Titanium, Trans. Electrochem. Soc. 78 (1940) 35. doi:10.1149/1.3071290.

[20] V.A. Joshi, Titanium alloys: An atlas of structures and fracture features, Taylor & Francis, New York, USA, 2006.

[21] Z.Z. Fang, J.D. Paramore, P. Sun, K.S.R. Chandran, Y. Zhang, Y. Xia, F. Cao, M. Koopman, M. Free, Powder metallurgy of titanium–past, present, and future, Int.

Mater. Rev. 63 (2018) 407–459. doi:10.1080/09506608.2017.1366003.

[22] R. V. Mises, Mechanik der plastischen Formänderung von Kristallen, J. Appl. Math. Mech. 8 (1928) 161–185.

[23] P.G. Partridge, The crystallography and deformation modes of hexagonal close-packed metals, Metall. Rev. 12 (1967) 169–194. doi:10.1179/mtlr.1967.12.1.169.

[24] C. Núñez, A. Roca, J. Jorba, Comportamiento mecanico de los materiales. Volumen I. Conceptos fundamentales, 2nd ed., Publicacions i edicions Universitat de Barcelona, 2002.

[25] M.F. Ashby, D.R.H. Jones, Engineering materials 1: an intorduction to properties, applications and design, Volume 1, Elsevier, 2012.

[26] F. Bridier, P. Villechaise, J. Mendez, Analysis of the different slip systems activated by tension in a α/β titanium alloy in relation with local crystallographic orientation, Acta Mater. 53 (2005) 555–567. doi:10.1016/j.actamat.2004.09.040.

[27] D. Lunt, T. Busolo, X. Xu, J. Quinta da Fonseca, M. Preuss, Effect of nanoscale α2 precipitation on strain localisation in a two-phase Ti-alloy, Acta Mater. 129 (2017) 72–82. doi:10.1016/j.actamat.2017.02.068.

[28] University of Cambridge, (n.d.). https://www.doitpoms.ac.uk/tlplib/slip/slip_geometry.php (accessed July 4, 2021).

[29] S. Zaefferer, A study of active deformation systems in titanium alloys: Dependence on, Mater. Sci. Eng. A. 344 (2003) 20–30. doi:10.1016/S0921-5093(02)00421-5.

[30] J.C. Williams, R.G. Baggerly, N.E. Paton, Deformation behavior of HCP Ti-Al alloy single crystals, Metall. Mater. Trans. A Phys. Metall. Mater. Sci. 33 (2002) 837–850. doi:10.1007/s11661-002-0153-y.

[31] I.P. Jones, W.B. Hutchinson, Stress-state dependence of slip in Titanium-6Al-4V and other H.C.P. metals, Acta Metall. 63 (1981) 951–968. doi:10.1016/0001-6160(81)90049-3.

[32] H.M. Flower, Microstructural development in relation to hot working of titanium alloys, Mater. Sci. Technol. 6 (1990) 1082–1092. doi:10.1179/mst.1990.6.11.1082.

[33] W.G. Burgers, Cubic-Body-Centered Modification Into The Hexagonal-Close-Packed Modification Of Zirconium, Physica. (1933) 561–586. doi:https://doi.org/10.1016/S0031-8914(34)80244-3.

[34] D.A. Porter, K. Easterling, Phase Transformations in Metals and Alloys, 2nd ed., CRC Press, Florida, USA, 1992.

[35] A. Flick, Ueber Diffusion, Ann. Phys. 170 (1855) 59–86. doi:doi:10.1002/andp.18551700105.

[36] B. Bolkstein, M. Mendelev, D. Srolovitz, Thermodynamics and kinetics in materials science: a short course, Oxford University Press, Oxford, UK, 2005.

[37] I. Weiss, S.L. Semiatin, Thermomechanical processing of alpha titanium alloys - An overview, Mater. Sci. Eng. A. (1999). doi:10.1016/s0921-5093(98)01155-1.

[38] I. Weiss, S.L. Semiatin, Thermo-mechanical processing of beta titanium alloys an overview, Mater. Sci. Eng. A. 243 (1998) 46–65.

[39] G.E. Dieter, Mechanical metallurgy, 3rd ed., McGraw-Hill Education, New York, USA, 1989.

[40] G.E. Dieter, H.A. Kuhn, S.L. Semiatin, Handbook of Workability and Process Design, ASM International, Ohio, USA, 2003.

[41] V.A. Duz, V.S. Moxson, O.M. Ivasishin, Recent Developments in Titanium Powder Metallurgy, Ti-2007 Sci. Technol. (2007) 1067–1070.

[42] P. Sun, Z.Z. Fang, Y. Zhang, Y. Xia, Review of the Methods for Production of Spherical Ti and Ti Alloy Powder, Jom. 69 (2017) 1853–1860. doi:10.1007/s11837-017-2513-5.

[43] J.J. Dunkley, Metal Powder Atomisation Methods for Modern Manufacturing manufacturing techniques, Johnson Matthey Technol Rev. 63 (2019) 226–232. doi:10.1595/205651319X15583434137356.

[44] B.J. Dawes, R. Bowerman, R. Trepleton, Introduction to the Additive Manufacturing Powder Metallurgy Supply Chain Exploring the production and supply of metal powders for AM processes, Johnson Matthey Technol Rev. 59 (2015) 243–256. doi:10.1595/205651315X688686.

[45] S.A. Miller, P.R. Roberts, ASM Handbook Volume 7: Powder Metal Technologies and Applications, ASM International, Ohio, USA, 1990.

[46] O.M. Ivasishin, D. Eylon, V.I. Bondarchuk, D.G. Savvakin, Diffusion during Powder Metallurgy Synthesis of Titanium Alloys, Defect Diffus. Forum. 277 (2008) 177–185. doi:10.4028/www.scientific.net/DDF.277.177.

[47] M. Steytler, R. Knutsen, Identifying challenges to the commercial viability of direct powder rolled titanium: A systematic review and market analysis, Materials (Basel). 13 (2020). doi:10.3390/ma13092124.

[48] Malvern Instruments, Optimizing metal powders for additive manufaturing, (2017) 1–18. https://www.materials-talks.com/wp-content/uploads/2020/10/WP170823MetalPowdersAdditiveManufacture-EN-1.pdf?utm_source=MaterialsTalks&utm_medium=blog&utm_campaign=Additive-Manufacturing-Campaign&utm_term=54919&utm_content=entryContentLink (accessed July 20, 2021).

[49] ISO / ASTM52900-15, Standard Terminology for Additive Manufacturing – General Principles – Terminology, ASTM International, West Conshohocken, USA, 2015. doi:10.1520/ISOASTM52900-15.

[50] Z. Liu, B.E.I. He, T. Lyu, Y.U. Zou, A Review on Additive Manufacturing of Titanium Alloys for Aerospace Applications : Directed Energy Deposition and Beyond Ti-6Al-4V A Review on Additive Manufacturing of Titanium Alloys for Aerospace Applications : Directed Energy Deposition and Beyond Ti-, JOM. (2021) 1–15. doi:10.1007/s11837-021-04670-6.

[51] L. Zhang, Y. Liu, S. Li, Y. Hao, Additive Manufacturing of Titanium Alloys by Electron Beam Melting : A Review, Adv. Eng. Mater. 20 (2018) 1700842. doi:10.1002/adem.201700842.

[52] P.A. Kobryn, E.H. Moore, S.L. Semiatin, The effect of laser power and traverse speed on microstructure, porosity, and build height in laser-deposited Ti-6Al-4V, Scr. Mater. 43 (2000) 299–305. doi:10.1016/S1359-6462(00)00408-5.

[53] L. Zhao, J. Guillermo, S. Macías, A. Dolimont, A. Simar, E. Rivière-lorphèvre,

Comparison of residual stresses obtained by the crack compliance method for parts produced by different metal additive manufacturing techniques and after friction stir processing, Addit. Manuf. 36 (2020) 101499. doi:10.1016/j.addma.2020.101499.

[54] Y.F. Yang, S.D. Luo, G.B. Schaffer, M. Qian, Sintering of Ti–10V–2Fe–3Al and mechanical properties, Mater. Sci. Eng. A. 528 (2011) 6719–6726. doi:10.1016/j.msea.2011.05.041.

[55] C.F. Yolton, F.H. Sam Froes, Conventional titanium powder production, in: Titan. Powder Metall. Sci. Technol. Appl., Butterworth-Heinemann, Oxford, UK, 2015: pp. 21–32.

[56] A.G.K. Jinka, A finite-element prediction of densification kinetics during the hot isostatic pressing of metal powder compacts, Mater. Process. Technol. 57 (1996) 382–392. doi:10.1016/0924-0136(95)02069-1.

[57] A. V. Muley, S. Aravindan, I.P. Singh, Nano and hybrid aluminum based metal matrix composites: An overview, Manuf. Rev. 2 (2015) 1–13. doi:10.1051/mfreview/2015018.

[58] S. Abkowitz, S. Abkowitz, H. Fisher, Titanium alloy components manufacture from blended elemental powder and the qualification process, in: Titan. Powder Metall. Sci. Technol. Appl., Butterworth-Heinemann, Oxford, UK, 2015: pp. 299–312.

[59] Z.Z. Fang, P. Sun, Pathways to Optimize Performance / Cost Ratio of Powder Metallurgy Titanium Pathways to Optimize Performance / Cost Ratio of Powder Metallurgy Titanium – A Perspective, Key Eng. Mater. 520 (2012) 15–23. doi:10.4028/www.scientific.net/KEM.520.15.

[60] J. Duszczyk, L.Z. Zhauang, L. Buekenhout, Densification of a rapidly solidified nickel aluminide powder-I application of hot-isostatic pressing diagrams, J. Mater. Sci. 33 (1998) 2735–2743. doi:10.1023/A:1017561114365.

[61] N. Town, S. Lawler, Construction methods for small modular reactors (SMRs), in: Handb. Small Modul. Nucl. React., Woodhead Publishing, Cambridge, UK, 2014: pp. 299–322.

[62] W.B. Li, K.E. Easterling, Cause and effect of non-uniform densification during hot

isostatic pressing, Powder Metall. 35 (1992) 47–52. doi:10.1179/pom.1992.35.1.47.

[63] W.B. Li, K.E. Easterling, M.F. Ashby, Instantaneous and residual stresses developed in hot isostatic pressing of metals and ceramics, Metall. Trans. A. 22 (1991) 1071–1078. doi:10.1007/BF02661100.

[64] P. Guyot, G. Antou, N. Pradeilles, A. Weibel, M. Vandenhende, A. Maı, Hot pressing and spark plasma sintering of alumina : Discussion about an analytical modelling used for sintering mechanism determination, Scr. Mater. 85 (2014) 35–38. doi:10.1016/j.scriptamat.2014.04.013.

[65] Z. Shen, M. Johnsson, Z. Zhao, M. Nygren, Spark Plasma Sintering of Alumina, J. Am. Ceram. Soc. 85 (2002) 1921–1927. doi:10.1111/j.1151-2916.2002.tb00381.x.

[66] R. Yamanoglu, I. Daoud, E.A. Olevsky, Spark plasma sintering versus hot pressing – densification , bending strength , microstructure , and tribological properties of Ti5Al2 . 5Fe alloys, Powder Metall. 62 (2018) 178–186. doi:10.1080/00325899.2018.1441777.

[67] J.P. Kelly, O.A. Graeve, Spark Plasma Sintering as an Approach to Manufacture Bulk Materials: Feasibility and Cost Savings, JOM. 67 (2015) 29–33. doi:10.1007/s11837-014-1202-x.

[68] K. Inoue, Electro-Discharged Sintering, 319,821, 1966. https://patentimages.storage.googleapis.com/0a/68/bb/162df6a9b6b160/US3241956.pdf.

[69] Z.A. Munir, D. V. Quach, M. Ohyanagi, Electric current activation of sintering: A review of the pulsed electric current sintering process, J. Am. Ceram. Soc. 94 (2011) 1–19. doi:10.1111/j.1551-2916.2010.04210.x.

[70] M. Suárez, A. Fernández, J.L. Menéndez, R. Torrecillas, H.U. Kessel, J. Hennicke, R. Kirchner, T. Kessel, Challenges and Opportunities for Spark Plasma Sintering : A Key Technology for a New Generation of Materials, Sinter. Appl. 13 (2013) 319–342. doi:10.5772/53706.

[71] D.M. Hulbert, A. Anders, D. V. Dudina, J. Andersson, D. Jiang, C. Unuvar, U. Anselmi-Tamburini, E.J. Lavernia, A.K. Mukherjee, The absence of plasma in “spark plasma

sintering," J. Appl. Phys. 104 (2008). doi:10.1063/1.2963701.

[72] U. Anselmi-Tamburini, J.R. Groza, Critical assessment: electrical field/current application–a revolution in materials processing/sintering?, Mater. Sci. Technol. 33 (2017) 1855–1862. doi:10.1080/02670836.2017.1341692.

[73] R. Orru, R. Licheri, A. Mario, A. Cincotti, G. Cao, Consolidation / synthesis of materials by electric current activated / assisted sintering, Mater. Sci. Eng. R. 63 (2009) 127–287. doi:10.1016/j.mser.2008.09.003.

[74] J.P. Kelly, O.A. Graeve, Spark Plasma Sintering as an Approach to Manufacture Bulk Materials: Feasibility and Cost Savings, Jom. 67 (2015) 29–33. doi:10.1007/s11837-014-1202-x.

[75] N.S. Weston, F. Derguti, A. Tudball, M. Jackson, Spark plasma sintering of commercial and development titanium alloy powders, J. Mater. Sci. 50 (2015) 4860–4878. doi:10.1007/s10853-015-9029-6.

[76] N.S. Weston, M. Jackson, FAST-forge of titanium alloy swarf: A solid-state closed-loop recycling approach for aerospace machining waste, Metals (Basel). 10 (2020) 296. doi:10.3390/met10020296.

[77] O. Guillon, J. Gonzalez-Julian, B. Dargatz, T. Kessel, G. Schierning, J. Räthel, M. Herrmann, Field-assisted sintering technology/spark plasma sintering: Mechanisms, materials, and technology developments, Adv. Eng. Mater. 16 (2014) 830–849. doi:10.1002/adem.201300409.

[78] D. Giuntini, J. Raethel, M. Herrmann, A. Michaelis, E.A. Olevsky, Advancement of Tooling for Spark Plasma Sintering, J. Am. Ceram. Soc. 98 (2015) 3529–3537. doi:10.1111/jace.13528.

[79] T. Vanherck, G. Jean, M. Gonon, J. Lobry, F. Cambier, Spark plasma sintering: Homogenization of the compact temperature field for non conductive materials, Int. J. Appl. Ceram. Technol. 12 (2015) E1–E12. doi:10.1111/ijac.12187.

[80] N.S. Weston, B. Thomas, M. Jackson, Processing metal powders via field assisted sintering technology (FAST): a critical review, Mater. Sci. Technol. 35 (2019) 1306–1328. doi:10.1080/02670836.2019.1620538.

[81] T.B. Holland, U. Anselmi-Tamburini, A.K. Mukherjee, Electric fields and the future of scalability in spark plasma sintering, Scr. Mater. 69 (2013) 117–121. doi:10.1016/j.scriptamat.2013.02.047.

[82] R.M. German, Sintering Theory and Practice, Wiley, Hoboken, USA, 1996.

[83] J.E. Garay, Current-Activated, Pressure-Assisted Densification of Materials, Annu. Rev. Mater. Res. 40 (2010) 445–468. doi:10.1146/annurev-matsci-070909-104433.

[84] W. Tang, L. Zhang, J. Zhu, Y. Chen, W. Tian, T. Liu, Effect of direct current patterns on densi fi cation and mechanical properties of binderless tungsten carbides fabricated by the spark plasma sintering system, Int. J. Refract. Met. Hard Mater. 64 (2017) 90–97. doi:10.1016/j.ijrmhm.2017.01.010.

[85] T. Nagae, M. Yokota, M. Nose, S. Tomida, T. Kamiya, S. Saji, Effects of Pulse Current on an Aluminum Powder Oxide Layer During Pulse Current Pressure Sintering, Mater. Trans. 43 (2002) 1390–1397.

[86] X.P. Li, M. Yan, H. Imai, K. Kondoh, G.B. Schaffer, M. Qian, The critical role of heating rate in enabling the removal of surface oxide fi lms during spark plasma sintering of Al-based bulk metallic glass powder, J. Non_Crystalline Solids. 375 (2013) 95–98. doi:10.1016/j.jnoncrysol.2013.05.001.

[87] C. Yang, D.G. Mo, H.Z. Lu, X.Q. Li, W.W. Zhang, Z.Q. Fu, L.C. Zhang, E.J. Lavernia, Reaction diffusion rate coef fi cient derivation by isothermal heat treatment in spark plasma sintering system, Scr. Mater. 134 (2017) 91–94. doi:10.1016/j.scriptamat.2017.03.005.

[88] R. Li, P. Niu, S. Deng, T. Yuan, G. Liu, Diffusivity of Ti-Ni Diffusion Couple Enhanced by Pulse Current During Spark Plasma Sintering, Metall. Mater. Trans. B Process Metall. Mater. Process. Sci. 51 (2020) 6–10. doi:10.1007/s11663-019-01725-7.

[89] R. Li, T. Yuan, X. Liu, K. Zhou, Enhanced atomic diffusion of Fe-Al diffusion couple during spark plasma sintering, Scr. Mater. 110 (2016) 105–108. doi:10.1016/j.scriptamat.2015.08.012.

[90] O.A. Troitskii, Electromechanical effect in metals, JETP Lett. 10 (1969) 11–13.

[91] H. Conrad, Effects of electric current on solid state phase transformations in metals,

Mater. Sci. Eng. A. 287 (2000) 227–237. doi:10.1016/S0921-5093(00)00780-2.

[92] J. Jeong, J. Han, D. Kim, Effect of Electric Field on the Migration of Grain Boundaries in Alumina, J. Am. Ceram. Soc. 18 (2000) 915–918. doi:10.1111/j.1151-2916.2000.tb01294.x.

[93] S. Starnes, H. Conrad, Grain size distribution in ultrafine-grained yttria-stabilized zirconia deformed without and with an electric field, Scr. Mater. 59 (2008) 1115–1118. doi:10.1016/j.scriptamat.2008.07.025.

[94] H. Conrad, D. Yang, Effect of the strength of an AC electric field compared to DC on the sintering rate and related grain size of zirconia ( 3Y-TZP ), Mater. Sci. Eng. A. 559 (2013) 591–594. doi:10.1016/j.msea.2012.08.146.

[95] Y. Kim, D. Lee, J. Hwang, H. Jin, S. Hyung, Fabrication and characterization of powder metallurgy tantalum components prepared by high compaction pressure technique, Mater. Charact. 114 (2016) 225–233. doi:10.1016/j.matchar.2016.03.005.

[96] Y. Lee, J. Hwoan, D. Shin, H. Lee, T. Nishimura, B. Jang, W. Kwon, Y. Kim, S. Kim, Y. Han, Phase transformation on spark plasma sintered dense polycarbosilane-derived SiC without additive, Scr. Mater. 143 (2018) 188–190. doi:10.1016/j.scriptamat.2017.02.031.

[97] C. Maniere, L. Durand, A. Weibel, C. Estourn, Spark-plasma-sintering and finite element method: From the identification of the sintering parameters of a submicronic a - alumina powder to the development of complex shapes, Acta Mater. 102 (2016) 169–175. doi:10.1016/j.actamat.2015.09.003.

[98] M. Zadra, F. Casari, L. Girardini, A. Molinari, Microstructure and mechanical properties of cp-titanium produced by spark plasma sintering, Powder Metall. 51 (2008) 59–65. doi:10.1179/174329008x277000.

[99] R. Chaudhari, R. Bauri, Microstructure and Mechanical Properties of Titanium Processed by Spark Plasma Sintering ( SPS ), Met. Microstrut. Anal. 3 (2014) 30–35. doi:10.1007/s13632-013-0112-6.

[100] C.I. Pascu, O. Gingu, P. Rotaru, I. Vida-Simiti, A. Harabor, N. Lupu, Bulk titanium for structural and biomedical applications obtaining by spark plasma sintering ( SPS )

from titanium hydride powder, J. Therm Anal Calorim. 113 (2013) 849–857. doi:10.1007/s10973-012-2824-2.

[101] B. Sharma, S.K. Vajpai, K. Ameyama, Preparation of strong and ductile pure titanium via two-step rapid sintering of TiH2 powder, J. Alloys Compd. 683 (2016) 51–55. doi:10.1016/j.jallcom.2016.05.020.

[102] D. Garbiec, P. Siwak, A. Mróz, Effect of compaction pressure and heating rate on microstructure and mechanical properties of spark plasma sintered Ti6Al4V alloy, Arch. Civ. Mech. Eng. 16 (2016) 702–707.

[103] C. Menapace, N. Vicente, A. Molinari, C. Menapace, N.V. Jr, A. Molinari, Hot forging of Ti – 6Al – 4V alloy preforms produced by spark plasma sintering of powders Hot forging of Ti – 6Al – 4V alloy preforms produced by spark plasma sintering of powders, Powder Metall. 56 (2013) 102–110. doi:10.1179/1743290112Y.0000000003.

[104] N.S. Weston, M. Jackson, FAST-forge − A new cost-effective hybrid processing route for consolidating titanium powder into near net shape forged components, J. Mater. Process. Technol. 243 (2017) 335–346. doi:10.1016/j.jmatprotec.2016.12.013.

[105] Y.F. Yang, H. Imai, K. Kondoh, M. Qian, Comparison of spark plasma sintering of elemental and master alloy powder mixes and prealloyed Ti-6Al-4V powder, Int. J. Powder Metall. 50 (2014) 41–47.

[106] Y. Long, T. Wang, H.Y. Zhang, X.L. Huang, Enhanced ductility in a bimodal ultra fi ne-grained Ti – 6Al – 4V alloy fabricated by high energy ball milling and spark plasma sintering, Mater. Sci. Eng. A. 608 (2014) 82–89. doi:10.1016/j.msea.2014.04.057.

[107] S.K. Vajpai, M. Ota, T. Watanabe, R. Maeda, T. Sekiguchi, T. Kusaka, K. Ameyama, The Development of High Performance Ti-6Al-4V Alloy via a Unique Microstructural Design with Bimodal Grain Size Distribution, Metall. Mater. Trans. A. 46 (2015) 903–914. doi:10.1007/s11661-014-2649-7.

[108] E. Calvert, B. Wynne, N. Weston, A. Tudball, M. Jackson, Thermomechanical processing of a high strength metastable beta titanium alloy powder, consolidated using the low-cost FAST-forge process, J. Mater. Process. Technol. 254 (2018) 158–

170. doi:10.1016/j.jmatprotec.2017.11.035.

[109] Y.F. Yang, H. Imai, K. Kondoh, M. Qian, Enhanced Homogenization of Vanadium in Spark Plasma Sintering of Ti-10V-2Fe-3Al Alloy from Titanium and V-Fe-Al Master Alloy Powder Blends, JOM. 69 (2017) 663–668. doi:10.1007/s11837-017-2271-4.

[110] T. Voisin, J. Monchoux, M. Hantcherli, S. Mayer, H. Clemens, A. Couret, Microstructures and mechanical properties of a multi-phase b -solidifying TiAl alloy densified by spark plasma sintering, Acta Mater. 73 (2014) 107–115. doi:10.1016/j.actamat.2014.03.058.

[111] T. Voisin, J. Monchoux, M. Perrut, A. Couret, Obtaining of a fi ne near-lamellar microstructure in TiAl alloys by Spark Plasma Sintering, Intermetallics. 71 (2016) 88–97. doi:10.1016/j.intermet.2016.01.003.

[112] H. Jabbar, J. Monchoux, M. Thomas, A. Couret, Microstructures and deformation mechanisms of a G4 TiAl alloy produced by spark plasma sintering, Acta Mater. 59 (2011) 7574–7585. doi:10.1016/j.actamat.2011.09.001.

[113] T. Voisin, J. Monchoux, M. Thomas, C. Deshayes, A. Couret, Mechanical Properties of the TiAl IRIS Alloy, Metall. Mater. Trans. A. 47 (2016) 6097–6108. doi:10.1007/s11661-016-3801-3.

[114] T. Voisin, J.-P. Monchoux, L. Durand, N. Karnatak, M. Thomas, A. Couret, An Innovative Way to Produce γ-TiAl Blades: Spark Plasma Sintering, Adv. Eng. Mater. 17 (2015) 1408–1413. doi:10.1002/adem.201500019.

[115] C. Manière, L. Durand, A. Weibel, G. Chevallier, C. Estournès, A sacrificial material approach for spark plasma sintering of complex shapes, Scr. Mater. 124 (2016) 126–128. doi:10.1016/j.scriptamat.2016.07.006.

[116] C. Manière, E. Torresani, E.A. Olevsky, Simultaneous spark plasma sintering of multiple complex shapes, Materials (Basel). 12 (2019) 1–14. doi:10.3390/ma12040557.

[117] F. Zhang, M. Reich, O. Kessler, E. Burkel, The potential of rapid cooling spark plasma sintering for metallic materials, Mater. Today. 16 (2013) 192–197. doi:10.1016/j.mattod.2013.05.005.

[118] A.B. Short, Gas tungsten arc welding of α + β titanium alloys : a review Gas tungsten arc welding of a z b titanium alloys : a review, Mater. Sci. Technol. 25 (2013) 309–324. doi:10.1179/174328408X389463.

[119] A. Squillace, U. Prisco, S. Ciliberto, A. Astarita, Effect of welding parameters on morphology and mechanical properties of Ti – 6Al – 4V laser beam welded butt joints, J. Mater. Eng. Technol. 212 (2012) 427–436. doi:10.1016/j.jmatprotec.2011.10.005.

[120] J.L. Huang, N. Warnken, J. Gebelin, M. Strangwood, R.C. Reed, On the mechanism of porosity formation during welding of titanium alloys, Acta Mater. 60 (2012) 3215–3225. doi:10.1016/j.actamat.2012.02.035.

[121] M.S. Sai, V. Dhinakaran, K.P.M. Kumar, V. Rajkumar, B. Stalin, T. Sathish, A systematic review of effect of different welding process on mechanical properties of grade 5 titanium alloy, Mater. Today Proc. 21 (2020) 948–953. doi:10.1016/j.matpr.2019.09.027.

[122] I.T. Watkins, H.M. Davies, O.G. Stanners, S. Marchisio, Powder interlayer bonding of geometrically complex Ti-6Al-4V parts, Int. J. Adv. Manuf. Technol. 106 (2020) 3629–3639. doi:10.1007/s00170-019-04685-z.

[123] W. Rae, Z. Lomas, M. Jackson, S. Rahimi, Measurements of residual stress and microstructural evolution in electron beam welded Ti-6Al-4V using multiple techniques, Mater. Charact. 132 (2017) 10–19. doi:10.1016/j.matchar.2017.07.042.

[124] S.Q. Wang, W.Y. Li, K. Jing, X.Y. Zhang, D.L. Chen, Microstructural evolution and mechanical properties of electron beam welded dissimilar titanium alloy joints, Mater. Sci. Eng. A. 697 (2017) 224–232. doi:10.1016/j.msea.2017.05.028.

[125] L. Tan, Z. Yao, W. Zhou, H. Guo, Y. Zhao, Microstructure and properties of electron beam welded joint of Ti – 22Al – 25Nb / TC11, Aerosp. Sci. Technol. 14 (2010) 302–306. doi:10.1016/j.ast.2010.02.002.

[126] H. Zhang, P. He, J. Feng, H. Wu, Interfacial microstructure and strength of the dissimilar joint Ti 3 Al / TC4 welded by the electron beam process, Mater. Sci. Eng. A. 425 (2006) 255–259. doi:10.1016/j.msea.2006.03.048.

[127] G. Turichin, I. Tsibulsky, V. Somonov, M. Kuznetsov, A. Akhmetov, Laser-TIG Welding

of Titanium Alloys Laser-TIG Welding of Titanium Alloys, IOP Conf. Ser. Mater. Sci. Eng. 142 (2016) 012009. doi:10.1088/1757-899X/142/1/012009.

[128] K. Zhang, Z. Lei, Y. Chen, M. Liu, Y. Liu, Microstructure characteristics and mechanical properties of laser-TIG hybrid welded dissimilar joints of Ti – 22Al – 27Nb and TA15, Opt. Laser Technol. 73 (2015) 139–145. doi:10.1016/j.optlastec.2015.04.028.

[129] J. Li, J. Shen, S. Hu, H. Zhang, X. Bu, Microstructure and mechanical properties of Ti-22Al-25Nb / TA15 dissimilar joint fabricated by dual-beam laser welding, Opt. Laser Technol. 109 (2019) 123–130. doi:10.1016/j.optlastec.2018.07.077.

[130] F. Fomin, M. Froend, V. Ventzke, P. Alvarez, S. Bauer, N. Kashaev, Metallurgical aspects of joining commercially pure titanium to Ti-6Al-4V alloy in a T-joint configuration by laser beam welding, Int. J. Adv. Manuf. Technol. 97 (2018) 2019–2031. doi:10.1007/s00170-018-1968-z.

[131] Y. Liu, C. Liu, W. Liu, Y. Ma, C. Zhang, Q. Cai, B. Liu, Microstructure and properties of Ti / Al lightweight graded material by direct laser deposition, Mater. Sci. Technol. 34 (2018) 945–951. doi:10.1080/02670836.2017.1412042.

[132] L.E.I. Yan, X. Chen, Y. Zhang, J.W. Newkirk, F. Liou, Fabrication of Functionally Graded Ti and γ -TiAl by Laser Metal Deposition, JOM. 69 (2017) 2756–2761. doi:10.1007/s11837-017-2582-5.

[133] C. Schneider-Maunoury, L. Weiss, P. Acquier, D. Boisselier, P. Laheurte, Functionally graded Ti6Al4V-Mo alloy manufactured with DED-CLAD process, Addit. Manuf. 17 (2017) 55–66. doi:10.1016/j.addma.2017.07.008.

[134] Y. Liang, D. Liu, H. Wang, Microstructure and mechanical behavior of commercial purity Ti / Ti – 6Al – 2Zr – 1Mo – 1V structurally graded material fabricated by laser additive manufacturing, Scr. Mater. 74 (2014) 80–83. doi:10.1016/j.scriptamat.2013.11.002.

[135] Y. Liang, X. Tian, Y. Zhu, J. Li, H. Wang, Compositional variation and microstructural evolution in laser additive manufactured Ti / Ti – 6Al – 2Zr – 1Mo – 1V graded structural material, Mater. Sci. Eng. A. 599 (2014) 242–246. doi:10.1016/j.msea.2014.01.092.

[136] T. Qian, D. Liu, X. Tian, C. Liu, H. Wang, Microstructure of TA2 / TA15 graded structural material by laser additive manufacturing process, Transations Nonferrous Met. Soc. Chine. 24 (2014) 2729–2736. doi:10.1016/S1003-6326(14)63404-X.

[137] H.S. Ren, D. Liu, H.B. Tang, X.J. Tian, Y.Y. Zhu, H.M. Wang, Microstructure and mechanical properties of a graded structural material, Mater. Sci. Eng. A. 611 (2014) 362–369. doi:10.1016/j.msea.2014.06.016.

[138] B. Thomas, F. Derguti, M. Jackson, Continuous Extrusion of Titanium Particulates, Proc. 13th World Conf. Titan. (2016) 107–115. doi:10.1002/9781119296126.ch16.

[139] K. Gangwar, M. Ramulu, A. Cantrell, D. Sanders, Microstructure and Mechanical Properties of Friction Stir Welded Dissimilar Titanium Alloys: TIMET-54M and ATI-425, Metals (Basel). 6 (2016) 252. doi:10.3390/met6100252.

[140] Y. Guo, Y. Chiu, M.M. Attallah, H. Li, S. Bray, P. Bowen, Characterization of Dissimilar Linear Friction Welds of a - b Titanium Alloys, J. Mater. Eng. Perform. 21 (2012) 770–776. doi:10.1007/s11665-012-0129-z.

[141] Y. Ji, S. Wu, D. Zhao, Microstructure and Mechanical Properties of Friction Welding Joints with Dissimilar Titanium Alloys, Metals (Basel). 6 (2016) 108. doi:10.3390/met6050108.

[142] S. Rajan, P. Wanjara, J. Gholipour, A.S. Kabir, Fatigue Behavior of Linear Friction Welded Ti-6Al-4V and Ti-6Al-2Sn-4Zr-2Mo-0.1Si Dissimilar Welds, Materials (Basel). 14 (2021) 3136. doi:10.3390/ma14113136.

[143] S. Rajan, P. Wanjara, J. Gholipour, A.S.K. Kabir, Joining of Dissimilar Alloys Ti-6Al-4V and Ti-6Al-2Sn-4Zr-2Mo-0.1Si Using Linear Friction Welding, Materials (Basel). 13 (2020) 3664. doi:10.3390/ma13173664.

[144] G.D. Wen, W.Y. Li, S.Q. Wang, H.Z. Guo, D.L. Chen, Strain-controlled fatigue properties of linear friction welded dissimilar joints between Ti – 6Al – 4V and Ti – 6.5A – 3 . 5Mo – 1 . 5Zr – 0 . 3Si alloys, Mater. Sci. Eng. A. 612 (2014) 80–88. doi:10.1016/j.msea.2014.06.010.

[145] J. Yang, J. Li, J. Xiong, J. Liao, F. Jin, Effect of welding parameters on microstructure characteristics and fatigue properties of dissimilar joints prepared by linear friction

welding on TC11 and TC17 titanium alloys, Weld. World. 64 (2020) 683–695. doi:10.1007/s40194-019-00817-x.

[146] P. Zhao, L. Fu, H. Chen, Low cycle fatigue properties of linear friction welded joint of TC11 and TC17 titanium alloys, J. Alloys Compd. 675 (2016) 248–256. doi:10.1016/j.jallcom.2016.03.113.

[147] C. Pleydell-Pearce, Resistance Bonding of Dissimilar Alloys Using a Powder Interlayer: A Feasibility Study, 2008.

[148] P. Davies, H. Davies, S. Marchisio, The Bonding of Additive Manufactured Ti-6Al-4V via the Powder Interlayer Bonding (PIB) Process, MATEC Web Conf. 321 (2020) 04041. doi:10.1051/matecconf/202032104041.

[149] P.D. Davies, H.M. Davies, I. Watkins, D.A. Britton, The joining of gamma titanium aluminides via the powder interlayer bonding method, Int. J. Adv. Manuf. Technol. 109 (2020) 2049–2054. doi:10.1007/s00170-020-05725-9.

[150] P. Davies, A. Johal, H. Davies, S. Marchisio, The fatigue performance of titanium alloys joined via the powder interlayer bonding method, Int. J. Adv. Manuf. Technol. 109 (2020) 1553–1561. doi:10.1007/s00170-020-05737-5.

[151] P. Davies, A. Johal, H. Davies, S. Marchisio, Powder interlayer bonding of titanium alloys: Ti-6Al-2Sn-4Zr-6Mo and Ti-6Al-4V, Int. J. Adv. Manuf. Technol. 103 (2019) 441–452. doi:10.1007/s00170-019-03445-3.

[152] O. Stanners, J. Russell, S. John, H.M. Davies, S. Marchisio, Powder interlayer bonding of nickel-based superalloys with dissimilar chemistries, Materials (Basel). 14 (2021) 2029. doi:10.3390/ma14082029.

[153] O. Levano, N. Weston, J. Pope, A. Tudball, D. Lunn, G. Baxter, M. Jackson, FAST- forge of novel Ti-6Al-4V/Ti-6Al-2Sn-4Zr-2Mo bonded, near net shape forgings from surplus AM powder, MATEC Web Conf. 321 (2020) 03010. doi:10.1051/matecconf/202032103010.

[154] D. He, Z. Fu, W. Wang, J. Zhang, Z.A. Munir, P. Liu, Temperature-gradient joining of Ti-6Al-4V alloys by pulsed electric current sintering, Mater. Sci. Eng. A. 535 (2012) 182–188. doi:10.1016/j.msea.2011.12.061.

[155] A. Miriyev, A. Stern, E. Tuval, S. Kalabukhov, Z. Hooper, N. Frage, Titanium to steel joining by spark plasma sintering (SPS) technology, J. Mater. Process. Technol. 213 (2013) 161–166. doi:10.1016/j.jmatprotec.2012.09.017.

[156] P. Pripanapong, S. Kariya, T. Luangvaranunt, J. Umeda, S. Tsutsumi, M. Takahashi, K. Kondoh, Corrosion behavior and strength of dissimilar bonding material between Ti and Mg alloys fabricated by spark plasma sintering, Materials (Basel). 9 (2016) 665. doi:10.3390/ma9080665.

[157] P. Pripanapong, J. Umeda, H. Imai, M. Takahashi, K. Kondoh, Tensile Strength of Ti/Mg Alloys Dissimilar Bonding Material Fabricated by Spark Plasma Sintering, Int. J. Eng. Innov. Res. 5 (2016) 253–259.

[158] N. Vicente, A. Fedrizzi, N. Bazzanella, F. Casari, F. Buccioti, A. Molinari, Microstructure of interface of SPS co-sintered and sinter bonded cp2-Ti and Co – 28Cr – 6Mo, Powder Metall. 56 (2013) 143–148. doi:http://dx.doi.org/10.1179/1743290112Y.0000000040.

[159] K. Zhao, Y. Liu, L. Huang, B. Liu, Y. He, Diffusion bonding of Ti-45Al-7Nb-0.3W alloy by spark plasma sintering, J. Mater. Process. Technol. 230 (2016) 272–279. doi:10.1016/j.jmatprotec.2015.11.030.

[160] G. Martin, D. Fabrègue, F. Mercier, J.A. Chafino-Aixa, R. Dendievel, J.J. Blandin, Coupling electron beam melting and spark plasma sintering: A new processing route for achieving titanium architectured microstructures, Scr. Mater. 122 (2016) 5–9. doi:10.1016/j.scriptamat.2016.05.001.

[161] ASTM Standard, Standard Test Method for Microindentation Hardness of Materials, ASTM Int. (2017). doi:10.1520/E0384-17.

[162] J. Schindelin, I. Arganda-Carreras, E. Frise, V. Kaynig, M. Longair, T. Pietzsch, S. Preibisch, C. Rueden, S. Saalfeld, B. Schmid, J.Y. Tinevez, D.J. White, V. Hartenstein, K. Eliceiri, P. Tomancak, A. Cardona, Fiji: An open-source platform for biological-image analysis, Nat. Methods. 9 (2012) 676–682. doi:10.1038/nmeth.2019.

[163] ASTM E8, ASTM E8/E8M standard test methods for tension testing of metallic materials 1, Annu. B. ASTM Stand. 4. (2010). doi:10.1520/E0008.

[164] D. Suárez, M. Jackson, P. Crawforth, K. Fox, B.P. Wynne, Using machining force feedback to quantify grain size in beta titanium, Materialia. 13 (2020) 100856. doi:10.1016/j.mtla.2020.100856.

[165] N.S. Weston, A novel solid-state processing route to generate cost-effective titanium alloy components, University of Sheffield, 2017.

[166] ASTM B348 / B348M-19, Standard Specification for Titanium and Titanium Alloy Bars and Billets, 2015. doi:10.1520/B0348_B0348M-19.

[167] SAE, Titanium Alloy Sheet, Strip, and Plate, 6Al - 2Sn - 4Zr - 2Mo - 0.08Si, Duplex Annealed, USA, 2019. doi:https://doi.org/10.4271/AMS4919J.

[168] S.D. Bartus, Evaluation of Titanium-5Al-5Mo-5V-3Cr (Ti-5553 ) Alloy Against Fragment and Armor-Piercing Projectiles (No. ARL-TR-4886), 2009.

[169] G. Chen, P. Tan, S.Y. Zhao, W.W. He, H.P. Tang, Spherical Ti-6Al-4V powders produced by gas atomization, Key Eng. Mater. 704 (2016) 287–292. doi:10.4028/www.scientific.net/KEM.704.287.

[170] J.J. Pope, The Diffusion Bonding of Dissimilar Titanium Alloy Powders using Field Assisted Sintering Technology, University of Sheffield, 2019.

[171] ISO 9276-9 Representation of results of particle size analysis — Part 6: Descriptive and quantitative representation of particle shape and morphology, 2008.

[172] Y. Sun, M. Aindow, R.J. Hebert, The effect of recycling on the oxygen distribution in Ti-6Al-4V powder for additive manufacturing, Mater. High Temp. 35 (2018) 217–224. doi:10.1080/09603409.2017.1389133.

[173] V. V. Popov, A. Katz-Demyanetz, A. Garkun, M. Bamberger, The effect of powder recycling on the mechanical properties and microstructure of electron beam melted Ti-6Al-4 V specimens, Addit. Manuf. 22 (2018) 834–843. doi:10.1016/j.addma.2018.06.003.

[174] A.M. Mullis, L. Farrell, R.F. Cochrane, N.J. Adkins, Estimation of cooling rates during close-coupled gas atomization using secondary dendrite arm spacing measurement, Metall. Mater. Trans. B Process Metall. Mater. Process. Sci. 44 (2013) 992–999. doi:10.1007/s11663-013-9856-2.

[175] A. Lawley, Atomization, Encycl. Mater. Sci. Technol. (2001) 387–392. doi:10.1016/b0-08-043152-6/00077-2.

[176] Z.Y. Hu, Z.H. Zhang, X.W. Cheng, F.C. Wang, Y.F. Zhang, S.L. Li, A review of multi-physical fields induced phenomena and effects in spark plasma sintering: Fundamentals and applications, Mater. Des. 191 (2020) 108662. doi:10.1016/j.matdes.2020.108662.

[177] S. Deng, R. Li, T. Yuan, P. Cao, S. Xie, Electromigration-Enhanced Densification Kinetics During Spark Plasma Sintering of Tungsten Powder, Metall. Mater. Trans. A. 50 (2019) 2886–2897. doi:10.1007/s11661-019-05201-4.

[178] Z. Trzaska, R. Cours, J. Monchoux, Densification of Ni and TiAl by SPS : Kinetics and Microscopic Mechanisms, Metall. Mater. Trans. A. 49 (2018) 4849–4859. doi:10.1007/s11661-018-4775-0.

[179] C. Manière, E. Nigito, L. Durand, A. Weibel, Y. Beynet, C. Estournès, Spark plasma sintering and complex shapes: The deformed interfaces approach, Powder Technol. 320 (2017) 340–345. doi:10.1016/j.powtec.2017.07.048.

[180] H. Numakura, Y. Minonishi, M. Koiwa, 〈1123〉{1011} slip in titanium polycrystals at room temperature, Scr. Metall. 20 (1986) 1581–1586. doi:10.1016/0036-9748(86)90399-6.

[181] Y. Minonishi, S. Morozumi, H. Yoshinaga, {1122} <1123> slip in titanium, Scr. Metall. 16 (1982) 427–430. doi:10.1016/0036-9748(82)90166-1.

[182] I. Bantounas, D. Dye, T.C. Lindley, The effect of grain orientation on fracture morphology during high-cycle fatigue of Ti-6Al-4V, Acta Mater. 57 (2009) 3584–3595. doi:10.1016/j.actamat.2009.04.018.

[183] W.B. Hutchinson, M.R. Barnett, Effective values of critical resolved shear stress for slip in polycrystalline magnesium and other hcp metals, Scr. Mater. 63 (2010) 737–740. doi:10.1016/j.scriptamat.2010.05.047.

[184] F. Hild, S. Roux, Comparison of Local and Global Approaches to Digital Image Correlation, Exp. Mech. 52 (2012) 1503–1519. doi:10.1007/s11340-012-9603-7.

[185] F. Hild, S. Roux, Digital image correlation: From displacement measurement to

identification of elastic properties - A review, Strain. 42 (2006) 69–80. doi:10.1111/j.1475-1305.2006.00258.x.

[186] J.Q. Da Fonseca, P.M. Mummery, P.J. Withers, Full-field strain mapping by optical correlation of micrographs acquired during deformation, J. Microsc. 218 (2005) 9–21. doi:10.1111/j.1365-2818.2005.01461.x.

[187] B. Pan, K. Qian, H. Xie, A. Asundi, Two-dimensional digital image correlation for in-plane displacement and strain measurement: A review, Meas. Sci. Technol. 20 (2009) 105002. doi:10.1088/0957-0233/20/6/062001.

[188] P.D. Littlewood, A.J. Wilkinson, Local deformation patterns in Ti-6Al-4V under tensile, fatigue and dwell fatigue loading, Int. J. Fatigue. 43 (2012) 111–119. doi:10.1016/j.ijfatigue.2012.03.001.

[189] D. Lunt, A. Ho, A. Davis, A. Harte, F. Martina, J. Quinta da Fonseca, P. Prangnell, The effect of loading direction on strain localisation in wire arc additively manufactured Ti–6Al–4V, Mater. Sci. Eng. A. 788 (2020) 139608. doi:10.1016/j.msea.2020.139608.

[190] C.A. Schneider, W.S. Rasband, K.W. Eliceiri, NIH Image to ImageJ: 25 years of image analysis, Nat. Methods. (2012). doi:10.1038/nmeth.2089.

[191] M.D. Atkinson, R. Thomas, A. Harte, P. Crowther, J. Quinta da Fonseca, DefDAP: Deformation Data Analysis in Python, (2020). doi:https://doi.org/10.5281/zenodo.3688097.

[192] F. Gioacchino, J. Quinta da Fonseca, Plastic Strain Mapping with Sub-micron Resolution Using Digital Image Correlation, Exp. Mech. 53 (2013) 743–754. doi:10.1007/s11340-012-9685-2.

[193] D. Lunt, J.Q. da Fonseca, D. Rugg, M. Preuss, Microscopic strain localisation in Ti-6Al-4V during uniaxial tensile loading, Mater. Sci. Eng. A. 680 (2017) 444–453. doi:10.1016/j.msea.2016.10.099.

[194] K. Zhang, The Microstructure and Properties of Hipped Powder Ti alloys, The University of Birmingham, 2009.

[195] X. Xu, D. Lunt, R. Thomas, R.P. Babu, A. Harte, M. Atkinson, J.Q. Fonseca, M. Preuss, Identification of active slip mode in a hexagonal material by correlative scanning

electron microscopy, Acta Mater. 175 (2019) 376–393.

[196] D. Lunt, A. Ho, A. Davis, F. Martina, J. Hönnige, J. Quinta, P. Prangnell, Microscopic strain localisation in WAAM Ti-6Al-4V during uniaxial tensile loading, MATEC Web Conf. 321 (2020) 03008.

[197] Y. Mishin, C. Herzig, Diffusion in the Ti-Al system, Acta Mater. 48 (2000) 589–623. doi:10.1016/S1359-6454(99)00400-0.

[198] M. Köppers, C. Herzig, M. Friesel, Y. Mishin, Intrinsic self-diffusion and substitutional Al diffusion in α-Ti, Acta Mater. 45 (1997) 4181–4191. doi:10.1016/S1359-6454(97)00078-5.

[199] F.K. Mante, G.R. Baran, B. Lucas, Nanoindentation studies of titanium single crystals, Biomaterials. 20 (1999) 1051–1055. doi:10.1016/S0142-9612(98)00257-9.

[200] M. Shahedi Asl, A. Sabahi Namini, A. Motallebzadeh, M. Azadbeh, Effects of sintering temperature on microstructure and mechanical properties of spark plasma sintered titanium, Mater. Chem. Phys. 203 (2018) 266–273. doi:10.1016/j.matchemphys.2017.09.069.

[201] G. Lütjering, J.C. Williams, Titanium : Engineering Materials and Processes, Ed. SPRINGER. second edi (2007) 1–442. doi:10.1007/978-3-540-73036-1.

[202] Y. Yulan, W. Weiqi, L. Fengli, L. Weiqing, Z. Yongqiang, The effect of aluminum equivalent and molybdenum equivalent on the mechanical properties of high strength and high toughness titanium alloys, Mater. Sci. Forum. 618 (2009) 169–172. doi:10.4028/www.scientific.net/MSF.618-619.169.

[203] S. Sneddon, D.M. Mulvihill, E. Wielewski, M. Dixon, D. Rugg, P. Li, Deformation and failure behaviour of a titanium alloy Ti-407 with reduced aluminium content: A comparison with Ti-6Al-4V in tension and compression, Mater. Charact. 172 (2021) 110901. doi:10.1016/j.matchar.2021.110901.

[204] P.J. Withers, H.K.D.H. Bhadeshia, Residual stress part 2 - Nature and origins, Mater. Sci. Technol. 17 (2001) 366–375. doi:10.1179/026708301101510087.

[205] W. Elber, Technical Memorandum Nasa Tm X-71943 the Effects of Shot-Peening Residual Stresses on the Fracture and Crack Growth Properties of D6Ac Steel, Nasa

Tech. Memo. (1973).

[206] J.D. Almer, J.B. Cohen, B. Moran, The effects of residual macrostresses and microstresses on fatigue crack initiation, Mater. Sci. Eng. A. 284 (2000) 268–279. doi:10.1016/S0921-5093(99)00779-0.

[207] D. Busse, Extending fatigue life of aircraft fuselage structures using laser-peening, Cranfield University, 2017.

[208] G.S. Schajer, Practical Residual Stress Measurement Methods, 2013. doi:10.1002/9781118402832.

[209] W. Elber, Effects of Shot-Peening Residual Stresses on the Fracture and Crack-Growth Properties of D6AC Steel, in: Fract. Toughness Slow-Stable Crack., 2009. doi:10.1520/stp38591s.

[210] J.Z. Zhou, S. Huang, L.D. Zuo, X.K. Meng, J. Sheng, Q. Tian, Y.H. Han, W.L. Zhu, Effects of laser peening on residual stresses and fatigue crack growth properties of Ti-6Al-4V titanium alloy, Opt. Lasers Eng. 52 (2014) 189–194. doi:10.1016/j.optlaseng.2013.06.011.

[211] E.J. Fairfax, M. Steinzig, A summary of failures caused by residual stresses, in: Conf. Proc. Soc. Exp. Mech. Ser., 2016. doi:10.1007/978-3-319-21765-9_26.

[212] F. Hosseinzadeh, P. Ledgard, P.J. Bouchard, Controlling the Cut in Contour Residual Stress Measurements of Electron Beam Welded Ti-6Al-4V Alloy Plates, Exp. Mech. 53 (2013) 829–839. doi:10.1007/s11340-012-9686-1.

[213] P. Xie, H. Zhao, B. Wu, S. Gong, Evaluation of Residual Stresses Relaxation by Post Weld Heat Treatment Using Contour Method and X-ray Diffraction Method, Exp. Mech. 55 (2015) 1329–1337. doi:10.1007/s11340-015-0040-2.

[214] P. Xie, H. Zhao, Y. Liu, Measuring residual stresses in linear friction welded joints composed by dissimilar titanium, Sci. Technol. Weld. Join. 21 (2016) 351–357. doi:10.1080/13621718.2015.1115158.

[215] R. Bandyopadhyay, J. Rotella, D. Naragani, J.S. Park, M. Eff, M.D. Sangid, Residual Strain Analysis in Linear Friction Welds of Similar and Dissimilar Titanium Alloys Using Energy Dispersive X-ray Diffraction, Metall. Mater. Trans. A Phys. Metall. Mater. Sci.

50A (2019) 704–718. doi:10.1007/s11661-018-5034-0.

[216] Y.A. Bahei-El-Din, G.J. Dvorak, Mechanics of hot isostatic pressing of a densified unidirectional SiC/Ti composite, Acta Metall. Mater. 43 (1995) 2531–2539. doi:10.1016/0956-7151(94)00477-Y.

[217] R.B. Parker, D.W. Brown, P. Rangaswamy, Residual stresses in an Inconel-718-clad Tungsten tube processed by hot iso-static pressing, Mater. Sci. Forum. 347 (2000) 229–234. doi:10.4028/www.scientific.net/msf.347-349.229.

[218] P. Angerer, W. Artner, E. Neubauer, L.G. Yu, K.A. Khor, Residual stress in spark-plasma-sintered and hot-pressed tantalum samples determined by X-ray diffraction methods, Int. J. Refract. Met. Hard Mater. 26 (2008) 312–317. doi:10.1016/j.ijrmhm.2007.08.002.

[219] P. Angerer, J. Wosik, E. Neubauer, L.G. Yu, G.E. Nauer, K.A. Khor, Residual stress of ruthenium powder samples compacted by spark-plasma-sintering (SPS) determined by X-ray diffraction, Int. J. Refract. Met. Hard Mater. 27 (2009) 105–110. doi:10.1016/j.ijrmhm.2008.04.002.

[220] M.B. Prime, A. Gonzales, The contour method: Simple 2-D mapping of residual stresses, in: Sixth Int. Conf. Residual Stress., Los Alamos National Laboratory, 2000: pp. 617–624.

[221] M.E. Fitzpatrick, A. Fry, P. Holdway, F. a Kandil, J. Shackleton, L. Suominen, Measurement Good Practice Guide No. 52. Determination of Residual Stresses by X-ray Diffraction, 2005. doi:10.1007/s00028-005-0194-y.

[222] P. Manda, R.M. Samudrala, M.K. Mohan, A.K. Singh, Microstructure, Texture, and Mechanical Properties of β Solution-Treated and Aged Metastable β Titanium Alloy, Ti-5Al-5Mo-5V-3Cr, Metall. Mater. Trans. A Phys. Metall. Mater. Sci. 48 (2017) 4539–4552. doi:10.1007/s11661-017-4217-4.

[223] N.G. Jones, R.J. Dashwood, M. Jackson, D. Dye, β Phase decomposition in Ti-5Al-5Mo-5V-3Cr, Acta Mater. 57 (2009) 3830–3839. doi:10.1016/j.actamat.2009.04.031.

[224] Y. Zheng, R.E.A. Williams, G.B. Viswanathan, W.A.T. Clark, H.L. Fraser, Determination of the structure of α-β interfaces in metastable β-Ti alloys, Acta Mater. 150 (2018)

25–39. doi:10.1016/j.actamat.2018.03.003.

[225] P. Manda, V. Singh, U. Chakkingal, A.K. Singh, Development of α precipitates in metastable Ti-5Al-5Mo-5V-3Cr and similar alloys, Mater. Charact. 120 (2016) 220–228. doi:10.1016/j.matchar.2016.09.005.

[226] B. Kedia, I. Balasundar, T. Raghu, Globularisation of α Lamellae in Titanium Alloy: Effect of Strain, Strain Path and Starting Microstructure, Trans. Indian Inst. Met. 71 (2018) 1791–1801. doi:10.1007/s12666-018-1323-y.

[227] S. Matsui, S. Ullah, A. Kubo, A. Fuji, Cutting force signal processing for machining bimetallic components, Proc. 8th Int. Conf. Lead. Edge Manuf. 21st Century, LEM 2015. (2015) 4–9. doi:10.1299/jsmelem.2015.8._1602-1_.

[228] A.S. Ullah, Machining Forces Due to Turning of Bimetallic Objects Made of Aluminum, Titanium, Cast Iron, and Mild/Stainless Steel, J. Manuf. Mater. Process. 2 (2018) 68. doi:10.3390/jmmp2040068.

[229] A.M.M. Sharif Ullah, A. Fuji, A. Kubo, J. Tamaki, M. Kimura, On the surface metrology of bimetallic components, Mach. Sci. Technol. 19 (2015) 339–359. doi:10.1080/10910344.2015.1018536.

[230] M. Uthayakumar, G. Prabhaharan, S. Aravindan, J. V. Sivaprasad, Machining studies on bimetallic pistons with CBN tool using the Taguchi method - Technical communication, Mach. Sci. Technol. 12 (2008) 249–255. doi:10.1080/10910340802067551.

[231] M. Uthayakumar, G. Prabhakaran, S. Aravindan, J. V. Sivaprasad, Influence of cutting force on bimetallic piston machining by a cubic boron nitride (CBN) tool, Mater. Manuf. Process. 27 (2012) 1078–1083. doi:10.1080/10426914.2012.677913.

[232] G. Manikandan, M. Uthayakumar, S. Aravindan, Machining and simulation studies of bimetallic pistons, Int. J. Adv. Manuf. Technol. 66 (2013) 711–720. doi:10.1007/s00170-012-4359-x.

[233] A. Saligheh, A. Hajialimohammadi, V. Abedini, Cutting forces and tool wear investigation for face milling of bimetallic composite parts made of aluminum and cast iron alloys, Int. J. Eng. Trans. C Asp. 33 (2020) 1142–1148.

doi:10.5829/ije.2020.33.06c.12.

[234] A. Malakizadi, I. Sadik, L. Nyborg, Wear mechanism of CBN inserts during machining of bimetal aluminum-grey cast iron engine block, Procedia CIRP. 8 (2013) 188–193. doi:10.1016/j.procir.2013.06.087.

[235] A. Cox, Understanding the effect of surface generation rates for finish milling of components, University of Sheffield, 2017.

[236] A. Cox, S. Herbert, J. Villain-chastre, S. Turner, M. Jackson, The effect of machining and induced surface deformation on the fatigue performance of a high strength metastable β titanium alloy, Int. J. Fatigue. 124 (2019) 26–33. doi:10.1016/j.ijfatigue.2019.02.033.

[237] P.-J. Arrazola, A. Garay, M. Armendia, S. Marya, F. Le Maitre, Machinability of titanium alloys (Ti6Al4V and Ti555.3), J. Mater. Process. Technol. 209 (2009) 2223–2230. doi:10.1016/j.jmatprotec.2008.06.020.

[238] N. Khanna, K.S. Sangwan, Interrupted machining analysis for Ti6Al4V and Ti5553 titanium alloys using physical vapor deposition ( PVD )– coated carbide inserts, Proc. Inst. Mech. Eng. Part B J. Eng. Manuf. 227 (2013) 465–470. doi:10.1177/0954405412472888.

[239] M. Nouari, H. Makich, On the Physics of Machining Titanium Alloys: Interactions between Cutting Parameters, Microstructure and Tool Wear, Metals (Basel). 4 (2014) 335–358. doi:10.3390/met4030335.

[240] A. Ugarte, R.M. Saoubi, A. Garay, P.J. Arrazola, Machining behaviour of Ti-6Al-4V and Ti-5553 alloys in interrupted cutting with PVD coated cemented carbide, Procedia CIRP. 1 (2012) 202–207. doi:doi.org/10.1016/j.procir.2012.04.035.

[241] A. Ikuta, K. Shinozaki, H. Masuda, Y. Yamane, Consideration of the adhesion mechanism of Ti alloys using a cemented carbide tool during the cutting process, J. Mater. Process. Technol. 127 (2002) 251–255. doi:10.1016/S0924-0136(02)00152-8.

[242] R.A.R. Rashid, S. Sun, G. Wang, M.S. Dargusch, Machinability of a near beta titanium alloy, Proc. Inst. Mech. Eng. Part B J. Eng. Manuf. 225 (2011) 2151–2162. doi:10.1177/2041297511406649.

[243] S.A. Niknam, R. Khettabi, V. Songmene, Machinability and Machining of Titanium Alloys : A Review, 1st ed., Springer, Berlin, Heidelberg, 2014. doi:10.1007/978-3-662-43902-9.

[244] C. Dredge, R. M'Saoubi, B. Thomas, O. Hatt, M. Thomas, M. Jackson, A low-cost machinability approach to accelerate titanium alloy development, Proc. Inst. Mech. Eng. Part B J. Eng. Manuf. 235 (2020) 1618–1632. doi:10.1177/0954405420937865.